Studying the interplay between ageing and Parkinson's disease using the zebrafish model

Oluwaseyi Anuoluwapo Pearce

A thesis submitted in partial fulfilment of the requirements for the degree of
Doctor of Philosophy

The University of Sheffield
Faculty of Medicine, Dentistry and Health
Department of Neuroscience

March 2023

Acknowledgements

I would like to thank the Battelle Memorial Institute for funding this PhD which has allowed me to further develop research and transferrable skills, and has increased my enthusiasm for scientific research.

My gratitude goes to my primary supervisor, Professor Oliver Bandmann, for selecting me for this PhD, and his guidance and support over the past 3.5 years. I am confident that the skills gained under his tutelage will help me as I advance in my career. I would like to thank my secondary supervisor, Professor Sherif El-Khamisy, for his ever-welcoming presence and his contributions to the DNA damage aspects of this PhD.

I would also like to express my thanks to my advisors, Drs Freek van Eeden and Julie Simpson, and my personal tutor, Professor Alison Gartland, for their kindness and words of counsel during this PhD.

Many thanks to Drs Ed Burton and Qing Bai for having me be part of their laboratory research group during my placement in the US; I learnt so much and equally had an amazing time. I would also like to thank past members of the Bandmann laboratory for the relevant training they provided, which allowed me to develop independence as a researcher, and for the laughs we shared. To Professor Heather Mortiboys, and Drs Scott Allen, Adrian Higginbottom, Noémie Hamilton, Heba Ismail and Freek van Eeden, thank you for your collaboration. I would also like to thank the aquarium teams at the University of Sheffield and the University of Pittsburgh for maintaining the zebrafish lines used.

I am deeply grateful to my undergraduate personal tutor, Professor Andrew Furley, for always believing in me, encouraging me and seeing my potential as a PhD student. I am also grateful to Dr Freek van Eeden for selecting me for a summer studentship back in 2018, which was my first experience of laboratory research. The rest, as they say, is history.

To all my friends at the Bateson Centre, particularly members of the van Eeden, El-Khamisy and Chico laboratory, thank you for the laughs, words of encouragement and for also being sounding boards when necessary. To my friends outside the laboratory, particularly Sinan and Olamide, thank you for your continued support and encouragement. It means the world to me.

My utmost gratitude goes to my mum, brother, aunty Bola and grandma. None of this would have been possible without their love and support. Last but most certainly not least, to my grandpa, Barrister Odetunde, who passed away during this PhD, thank you for loving me, believing in me and walking with me for as long as you could.

Abstract

Parkinson’s disease (PD) is a neurodegenerative disorder characterised by the loss of dopaminergic neurons in the substantia nigra. Ageing is the major risk factor for developing PD but the interplay between ageing and PD remains elusive.

To investigate the effect of ageing on PD-relevant pathological mechanisms, zebrafish mutant lines harbouring mutations in ageing-associated genes (*klotho*$^{-/-}$, *sirt1*$^{-/-}$, *satb1a*$^{-/-}$, *satb1b*$^{-/-}$ and *satb1a*$^{-/-}$;*satb1b*$^{-/-}$) were generated, using CRISPR/Cas9 gene editing. Likewise, a chemical model for *SIRT1* deficiency was utilised.

klotho$^{-/-}$ zebrafish displayed an accelerated ageing phenotype at 3mpf and reduced survival to 6mpf. Dopaminergic neuron number, MPP$^+$ susceptibility and microglial number were unaffected in *klotho*$^{-/-}$ larvae. NAD$^+$ levels were decreased in 6mpf *klotho*$^{-/-}$ brains. However, ATP levels and DNA damage were unaffected. *sirt1*$^{-/-}$ zebrafish did not display a phenotype through adulthood. *il-1β* and *il-6* were not upregulated in *sirt1*$^{-/-}$ larvae, and chemical inhibition of sirt1 did not increase microglial number. *cdkn1a*, *il-1β* and *il-6* were not upregulated in *satb1a*$^{-/-}$ and *satb1b*$^{-/-}$ larvae. Dopaminergic neuron number and MPP$^+$ susceptibility were unaffected in *satb1a*$^{-/-}$ larvae. However, *satb1b*$^{-/-}$ larvae demonstrated a moderate decrease in dopaminergic neuron number but equal susceptibility to MPP$^+$ as *satb1b*$^{+/+}$ larvae. Adult *satb1a*$^{-/-}$ but not adult *satb1b*$^{-/-}$ zebrafish were emaciated. *satb1a*$^{-/-}$;*satb1b*$^{-/-}$ zebrafish did not display a phenotype through adulthood.

Transgenic zebrafish expressing human wildtype α-Synuclein (Tg(*eno2*:hsa.*SNCA*-ires-EGFP)) were crossed with *klotho*$^{-/-}$ and *sirt1*$^{-/-}$ zebrafish, and treated with a sirt1-specific inhibitor. Neither genetic cross affected survival. The *klotho* mutation did not increase microglial number in Tg(*eno2*:hsa.*SNCA*-ires-EGFP) larvae. Likewise, sirt1 inhibition did not induce motor impairment or cell death in Tg(*eno2*:hsa.*SNCA*-ires-EGFP) larvae.

In conclusion, the suitability of zebrafish for studying ageing remains elusive, as only 1 ageing-associated mutant line displayed accelerated ageing. However, zebrafish remain an effective model for studying PD-relevant pathological mechanisms due to the availability of CRISPR/Cas9 gene editing, neuropathological and neurobehavioral tools.

Table of Contents

List of figures

List of tables

Declaration: I, Oluwaseyi Anuoluwapo Pearce, confirm that the Thesis is my own work. I am aware of the University's Guidance on the Use of Unfair Means (www.sheffield.ac.uk/ssid/unfair-means). This work has not been previously been presented for an award at this, or any other, university.

Abbreviations

-/- : Homozygous mutant

+/-: Heterozygous mutant

+/+: Wildtype

2^-ΔΔCt: 2^-delta-delta-Ct

2D: 2-dimensional

3D: 3-dimensional

5HT3aR: Ionotropic serotonin receptor

A: Adenine

Ac: Acetyl group

AceCS2: Acetyl-CoA-synthetase 2

ACMSD: 2-amino 3-carboxymuconate 6-semialdehyde decarboxylase

AD: Alzheimer's disease

ADAM: A disintegrin and metalloproteinase

ADHR: Autosomal dominant hypophosphataemic rickets

ADP: Adenosine diphosphate

Ala: Alanine

ALP: Autophagy-lysosome pathway

ALS: Amyotrophic lateral sclerosis

ANOVA: Analysis of variance

Anti-dsDNA: Anti-double stranded DNA

AO: Acridine orange

AP: Alkaline phosphatase

APOE4: Apolipoprotein e4

APP/PS1: Amyloid precursor protein/presenilin 1

APS: Ammonium persulfate

Arc: Activity-regulated cytoskeleton-associated protein

Areg: Amphiregulin

ARHR: Autosomal recessive hypophosphataemic rickets

ASD: Atrial septal defect

ATM: Ataxia telangiectasia mutated

ATP: Adenosine triphosphate

ATP13A2: ATPase cation transporting 13A2

Aβ: Amyloid-β

BA: Bulbus arteriosus

BBB: Blood-brain barrier

BCIP: 5-bromo-4-chloro-3-indolyl-phosphate

BDNF: Brain-derived neurotrophic factor

BER: Base excision repair

BFU-E: Erythroid burst colony forming units

BioFIND: Fox Investigation for New Discovery of Biomarkers

BLAST: Basic Local Alignment Search Tool

BLASTN: Nucleotide BLAST

BLASTP: Protein BLAST

bp: base pair(s)

BRASTO: Brain-specific Sirt1-overexpressing

BRG1: Brahma-related gene 1

BSA: Bovine serum albumin

BUR: Base unpairing region

C: Cytosine

Caenorhabditis elegans: *C.elegans*

Calb2: Calbindin 2

CCL2: C-C motif chemokine ligand 2

CDK: Cyclin-dependent kinase

CDKN1A: Cyclin-dependent kinase inhibitor 1A

cDNA: Complementary DNA

CFU-GEMM: Granulocyte-erythrocyte-monocyte-megakaryocyte colony forming units

CFU-GM: Granulocyte-monocyte colony forming units

CGE: Caudal ganglionic eminence

CKD: Chronic kidney disease

CNS: Central nervous system

COMT: Catechol-o-methyl-transferase

CoQ: Coenzyme Q

CPS1: Carbamoyl phosphate synthetase 1

CREB: cAMP-response element binding protein

Crh: Corticotropin-releasing hormone

CRISPR/Cas9: Clustered regularly interspaced short palindromic repeats/CRISPR-associated protein 9

CRISPR-STAT: CRISPR-somatic tissue activity test

crRNA: CRISPR RNA

CS: Corpuscles of Stannius

CSF: Cerebrospinal fluid

Csf3r: Colony stimulating factor 3 receptor

Ct: Cycle threshold

CUTL domain: CUT-like domain

CVD: Cardiovascular disease

Cyt c: Cytochrome c

DC: Diencephalic

DCF: Dichlorofluorescein

DDR: DNA-damage response

DIG: Digoxigenin

DMSO: Dimethyl sulfoxide

DNA: Deoxyribonucleic acid

dpf: Days post fertilisation

DSBs: Double-stranded breaks

dUTP: Deoxynucleotide triphosphate

e^-: Electron

ECL: Enhanced chemiluminescence

ECM: Extracellular matrix

EDTA: Ethylenediaminetetraacetic acid

EGCG: Epigallocatechin-3-gallate

Egr1: Early growth response 1

Egr2: Early growth response 2

EMT: Epithelial-to-mesenchymal transition

eno2: enolase 2

ENS: Enteric nervous system

EOPD: Early-onset PD

ER: Endoplasmic reticulum

ERC: Extrachromosomal rDNA circle

EST: Expressed sequence tag

EtBr: Ethidium bromide

ETC: Electron transport chain

EtOH: Ethanol

EX-527: 6-chloro-2,3,4,9-tetrahydro-1H-carbazole-1-carboxamide

FAD: Flavin adenine dinucleotide

$FADH_2$: Reduced flavin adenine dinucleotide

FGF23: Fibroblast growth factor 23

FGFR: FGF receptor

FOXO: Forkhead box transcription factors

FP: Forward primer

FTC: Familial tumoural calcinosis

G: Guanine

GAK: Cyclin G-associated kinase

GAPDH: Glyceraldehyde-3-phosphate dehydrogenase

GBA: β-glucocerebrosidase

GCH1: GTP cyclohydrolase 1

GCIP: Grap2 and cyclin D1 interacting protein

GDH: Glutamate dehydrogenase

GFP: Green fluorescent protein

Gly: Glycine

Gpx1: Glutathione peroxidase 1

gRNA: Guide RNA

GWAS: Genome-wide association studies

H^+: Proton

H+L: Heavy and light chains

H2AX: H2A histone family member X

H_2O: Water

H_2O_2: Hydrogen peroxide

HAT: Histone acetyltransferase

hbegfa: heparin-binding EGF-like growth factor a

hbegfb: heparin-binding EGF-like growth factor b

HD: Huntington’s disease

HDAC: Histone deacetylase

HERC4: HECT And RLD Domain Containing E3 Ubiquitin Protein Ligase 4

hESCs: Human embryonic stem cells

HGPS: Hutchinson-Gilford progeria syndrome

hpf: Hours post fertilisation

HR: Homologous recombination

HRP: Horseradish peroxidase

HSC: Haematopoietic stem cell

HSF1: Heat shock factor 1

Hsp70: Heat shock protein 70

IACUC: Institutional Animal Care and Use Committee

Iba-1: Ionised calcium-binding adapter molecule 1

Id3: Inhibitor of DNA binding 3

IDT: Integrated DNA Technologies

IEGs: Immediate early genes

IGF-1: Insulin-like growth factor 1

IGFBP7: Insulin-like growth factor binding protein 7

IgG: Immunoglobulin G

IHC: Immunohistochemistry

IL: Interleukin

Indel: Insertion/deletion

IRES: Internal ribosome entry site

kDa: Kilodaltons

KD: Knockdown

Kitl: Kit ligand

KO: Knockout

LAMP1: Lysosomal-associated membrane protein 1

LB: Lysogeny broth

LBs: Lewy bodies

LC3: Microtubule-associated protein 1A/1B-light chain 3

Leu: Leucine

LMA: Low melting agarose

LNs: Lewy neurites

LOPD: Late-onset PD

LPS: Lipopolysaccharide

LRRK2: Leucine-rich repeat kinase 2

Lys: Lysine

MANE: Matched annotation from NCBI and EMBL-EBI

MAO-B: Monoamine oxidase-B

MAR: Matrix attachment region

MATLAB: Matrix laboratory

MCC: 3-methylcrotonoyl-CoA carboxylase

MCCC1 : 3-methylcrotonoyl-CoA carboxylase subunit 1

MCP1: Monocyte chemoattractant protein 1

MDS-UPDRS: Movement Disorder Society-Sponsored Revision of the Unified Parkinson's Disease Rating Scale

Me: Methyl group

MEF: Mouse embryonic fibroblast

MeOH: Methanol

Met: Methionine

MGE: Medial ganglionic eminence

miR: MicroRNA

MMP: Matrix metalloproteinase

MMR: Mismatch repair

MPC: Muscle progenitor cell

mpeg1: macrophage expressed gene 1

MPP^+: 1-methyl-4-phenylpyridinium

MPTP: 1-methyl-4-phenyl-1,2,3,6-tetrahydropyridine

MQ: Milli-Q

mRNA: Messenger RNA

MS: Multiple sclerosis

MSA: Multiple system atrophy

mtDNA: Mitochondrial DNA

MW: Molecular weight

NAC: Non-amyloid-β-component

NAD^+: Nicotinamide adenine dinucleotide

NADH: Reduced nicotinamide adenine dinucleotide

NADT: NADtotal

NaOH: Sodium hydroxide

NBT: 4-nitro-blue-tetrazolium chloride

NCBI: National Centre for Biotechnology Information

NEB: New England Biolabs

NER: Nucleotide excision repair

NF-κB: Nuclear factor-kappa B

NHEJ: Non-homologous end joining

NHPs: Non-human primates

Nkx2-1: Nk2 homeobox 1

NLS: Nuclear localisation signal

NMD: Nonsense-mediated decay

NO: Nitric oxide

Non-Tg: Non-transgenic

Nos2: Nitric oxide synthase 2

NSCLC: Non-small cell lung cancer

O_2: Oxygen

OD: Optical density

OPC: Oligodendrocyte progenitor cell

Overnight: o/n

Ox2r: Orexin type 2 receptor

PAM : Protospacer adjacent motif

PAR: Poly (ADP-ribose)

PARP: Poly (ADP-ribose) polymerase

PARylation: Poly (ADP-ribosyl)ation

PBS: Phosphate buffered saline

PBT: Phosphate buffered saline with 0.1% Tween-20

PCAF: P300/CBP-associated factor

PCR: Polymerase chain reaction

PD: Parkinson’s disease

PDWBS: Web-based study of Parkinson’s disease

PET: Positron emission tomography

PFA: Paraformaldehyde

PFF: Preformed fibril

PGC-1α: PPARγ coactivator-1α

Phe: Phenylalanine

PINK1: Phosphatase and Tensin Homolog (PTEN)-Induced Putative Kinase 1

PKC: Protein kinase C

PLAC1: Placenta-specific 1

PolG: DNA polymerase γ

PPARγ: Peroxisome proliferator-activated receptor γ

PPMI: Parkinson’s Progression Markers Initiative

PSP: Progressive supranuclear palsy

PTH: Parathyroid hormone

PTM: Post-translational modification

PTU: Phenylthiourea

PV: Parvalbumin

qPCR: Quantitative PCR

Rag1: Recombination activating gene 1

RB: Retinoblastoma

RBA: Receptor binding arm

rDNA: Ribosomal DNA

REM: Rapid eye movement

RFLP: Restriction fragment length polymorphism

RNA: Ribonucleic acid

ROCK1: Rho-associated coiled-coil kinase 1

ROS: Reactive oxygen species

RP: Reverse primer

rpm: Revolutions per minute

RT: Room temperature

RT-PCR: Reverse transcription PCR

S100a8: S100 calcium binding protein a8

S100a9: S100 calcium binding protein a9

SASP: Senescence-associated secretory phenotype

SATB: Special AT-rich sequence-binding protein

SA-β-Gal: Senescence-associated β-galactosidase

SDS: Sodium dodecyl sulfate

SERPINs: Serine/cysteine proteinase inhibitors

SIR: Silent information regulator

slc27a2a: solute carrier family 27, member 2a

SNARE: Soluble N-ethylmaleimide-sensitive factor attachment protein receptor

SNpc: Substantia nigra pars compacta

SNP: Single nucleotide polymorphism

socs1a: suppressor of cytokine signalling 1a

SOCS2: Suppressor of cytokine signalling 2

Sod1: Superoxide dismutase 1

SOD2: Superoxide dismutase 2

SSRIs: Specific-serotonin reuptake inhibitors

SST: Somatostatin

T: Thymine

TAE: Tris-acetate-EDTA

TBC1D5: TBC1 Domain Family Member 5

TBST: Tris-buffered saline with 0.1% Tween-20

TDP1: Tyrosyl-DNA phosphodiesterase 1

TEMED: Thermo Scientific tetramethylethylenediamine.

Terc: Telomerase RNA component

Tg: Transgenic

TGF-β: Transforming growth factor-β

TH: Tyrosine hydroxylase

th1: tyrosine hydroxylase 1

TIO: Tumour-induced osteomalacia

TNF-α: Tumour necrosis factor-α

TORC1: CREB-regulated transcription coactivator 1

tracrRNA: Trans-activating CRISPR RNA

TARDBP: Transactive response DNA binding protein

tardbpl: tardbp-like

tRNA: Transfer RNA

TUNEL: Terminal deoxynucleotidyl transferase dUTP nick end labelling

U: Uracil

ULD: Ubiquitin-like domain

upf1: upstream frameshift 1

UPS: Ubiquitin-proteasome system

UV: Ultraviolet

VDR: Vitamin D receptor

vcla: vinculin a

vclb: vinculin b

VPS13C: Vacuolar Protein Sorting 13 Homolog C

VSD: Ventricular septal defect

WHO: World Health Organisation

WISH: Whole-mount in-situ hybridisation

WS: Werner Syndrome

WT: Wildtype

xg- Times gravity

XLH: X-linked hypophosphataemia

zebrin II: zII

ZFIN: Zebrafish Information Network

ZIRC: Zebrafish International Resource Centre

ZMPSTE24: Zinc metallopeptidase STE24

α: alpha

αα: amino acid(s)

β: beta

γ: gamma

Chapter 1: Introduction

1.1 Parkinson’s disease

1.1.1 Incidence, prevalence and societal burden

Parkinson’s disease (PD) is the second most common neurodegenerative disorder after Alzheimer’s disease (AD) (Marras *et al.*, 2018). According to the World Health Organisation (WHO), an estimated 8.5 million people were living with PD globally in 2019 (World Health Organisation, 2022). The WHO also estimates that in 2019, PD resulted in 5.8 million disability-adjusted life years and 329,000 deaths globally (World Health Organisation, 2022). Between 1990 and 2019, both PD incidence and prevalence increased by >150.0% globally with the highest increased incidence occurring in individuals ≥80 years old (**Figure 1.1**) (Ou *et al.*, 2021). PD-related death and disability are also rising faster than any neurological disorder (World Health Organisation, 2022).

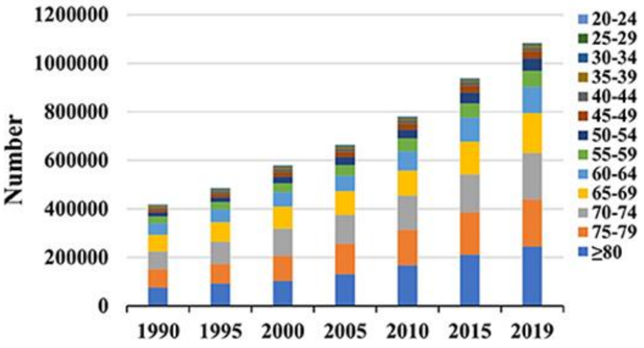

***Figure 1.1. PD incidence between 1990 and 2019 among different age groups.** From 1990 to 2019, PD incidence increased in individuals aged ≥ 45 years. The highest increased incidence was in individuals aged ≥ 80 years. PD, Parkinson’s disease. Reproduced from Ou et al., (2021).*

Many PD patients require either informal or formal care as their symptoms progress and this places an emotional and financial burden on families, as well as a healthcare and economic burden on countries (Parkinson’s UK, 2017; World Health Organisation, 2022).

In the UK, families with a single PD patient experience higher healthcare costs of £2,229/year, higher social care costs of £3,622/year, loss of livelihood worth £10,731/year, thereby losing a total of £16,582/year, all in addition to a reduction in the quality of life (Parkinson’s UK, 2017). The economic burden of PD also applies overseas (Yang *et al.*, 2020). Given the increased incidence and prevalence of PD, further research is needed to prevent socio-economic disruption in coming years.

1.1.2 PD pathology

The histopathological hallmarks of PD are the loss of dopaminergic neurons, and the presence of Lewy bodies (LBs) and Lewy neurites (LNs) (Geut *et al.*, 2020; Mackenzie, 2001).

At first glance, the brain of a PD patient has no evident pathology, with the exception of cerebral atrophy observed in the brains of PD patients with dementia. However, upon examining transverse brain sections of PD patients, loss of pigmentation is observed in the substantia nigra pars compacta (SNpc) and locus coeruleus (Mackenzie, 2001).

Microscopically, loss of pigmentation in the SNpc and locus coeruleus is directly proportional to the loss of dopaminergic and noradrenergic neurons, respectively (Dickson, 2012). The extent of dopaminergic neuron loss varies between different regions of the SNpc, with the lateral ventral tier being the most affected (Fearnley and Lees, 1991).

Aside the SNpc and locus coeruleus, neuronal loss is observed in the nucleus basalis of Meynert, the dorsal motor nucleus of the vagus nerve, the pedunculopontine nucleus, the raphe nuclei, the hypothalamus and olfactory bulb (Mackenzie, 2001; Giguère, Nanni and Trudeau, 2018). Likewise, other neuronal systems aside the dopaminergic system are affected in PD, including the cholinergic, noradrenergic and serotonergic systems (Giguère, Nanni and Trudeau, 2018).

LBs are intracytoplasmic neuronal inclusions which contain neurofilaments, ubiquitin and α-Synuclein, among others (Goldman *et al.*, 1983; Kuzuhara *et al.*, 1988; Spillantini *et al.*, 1997, 1998).

There are two types of LBs, namely brainstem and cortical LBs (Spillantini *et al.*, 1998). Brainstem LBs have a dense fibrillar and granular core surrounded by a halo, and are found in PD patients (Duffy and Tennyson, 1965; Spillantini *et al.*, 1998). Cortical LBs do not have a core or halo and are found in patients with dementia with LBs (Kosaka *et al.*, 1976; Spillantini *et al.*, 1998). LB distribution was used to develop a staging method for PD pathology called Braak staging (Braak *et al.*, 2003). However, the validity of this staging method is heavily debated (Jellinger, 2019).

1.1.3 Clinical presentation of PD

The cardinal features of PD are resting tremor, rigidity and bradykinesia. Bradykinesia refers to slow movement. Patients may also develop postural instability as the disease progresses. These motor symptoms are often unilateral at disease onset but become bilateral with disease progression (Clarke, 2007). Understandably, motor symptoms are often distressing and impact the quality of life of PD patients (Lubomski, Davis and Sue, 2021).

Motor symptoms are the result of dopaminergic neuron loss in the SNpc and are thought to present after 50-70% of these neurons are lost (Cheng, Ulane and Burke, 2010; Surmeier, 2018). Clinically, the Movement Disorder Society-Sponsored Revision of the Unified Parkinson's Disease Rating Scale (MDS-UPDRS) is used to assess disease progression and severity (Goetz *et al.*, 2008).

PD is also characterised by non-motor symptoms which include autonomic dysfunction, sleep disorders, sensory disorders and cognitive/neuropsychiatric disorders (Chaudhuri, Yates and Martinez-Martin, 2005); details are provided below (**Table 1.1**).

Neuropsychiatric symptoms	**Sleep disorders**	**Autonomic symptoms**	**Sensory and other symptoms**
Depression, apathy, anxiety	REM sleep behaviour disorder	Cardiovascular system: orthostatic hypotension, falls related to orthostatic hypotension, bradycardia, arrhythmia	Pain
Compulsive-obsessive behaviour, repetitive behaviour	Insomnia	Gastrointestinal system: sialorrhea, dysphagia and choking, reflux, vomiting, nausea, constipation, incontinence	Paraesthesia
Attention deficit	Excessive daytime somnolence	Urinary system: bladder disturbances, urgency and frequency, nocturia, incontinence	Olfactory disturbance
Hallucinations, illusion, delusions	Nightmares or vivid dreams	Reproductive system: sexual dysfunction, erectile dysfunction, hypersexuality	Fatigue
Delirium	Sleep apnea	Thermoregulation: sweating, heat or cold intolerance	Weight changes
Anxiety and panic attacks			

Dementia			

Table 1.1. A list of non-motor symptoms of PD. *PD, Parkinson's disease; REM, rapid eye movement. Modified from Chaudhuri, Yates and Martinez-Martin, (2005).*

Although they are common and can greatly impact quality of life, non-motor symptoms are often overlooked (Hou and Lai, 2007). More than half of PD patients suffer from autonomic dysfunction, with constipation occurring in up to 66% of patients (Pedrosa Carrasco, Timmermann and Pedrosa, 2018). Likewise, more than a third of patients experience sleep disorders (Lajoie, Lafontaine and Kaminska, 2021). Pain is reported by 40-85% of PD patients and hyposmia/anosmia is experienced by ≥80% of patients (Sveinbjornsdottir, 2016). In addition, 16-70% of patients develop neuropsychiatric symptoms, and 20-40% of patients suffer from cognitive deficits (Hou and Lai, 2007; Sveinbjornsdottir, 2016).

PD patients often develop non-motor symptoms before motor symptoms (Lee and Koh, 2015). For example, a case-control study found that 5 years prior to diagnosis, PD patients had a higher incidence of constipation, erectile dysfunction, urinary dysfunction, fatigue and depression, among others, compared to controls (Schrag *et al.*, 2015; Surmeier, 2018). Likewise, PD patients usually experience hyposmia/anosmia before the onset of motor symptoms (Sveinbjornsdottir, 2016).

1.1.4 Diagnosis

A correct diagnosis of PD could be challenging, due to clinical overlap with other movement disorders such as multiple system atrophy (MSA) and progressive supranuclear palsy (PSP). However, it is crucial for therapeutic management and improving the patient's quality of life (Tolosa *et al.*, 2021).

Clinical diagnosis is based on the presence of the previously listed cardinal features (**Section 1.1.3**) as well as the absence of atypical symptoms (Postuma *et al.*, 2015). For example, the presence of severe autonomic dysfunction would suggest a diagnosis of MSA while vertical supranuclear gaze palsy would suggest PSP (Williams-Gray and Worth, 2016). A good response to levodopa supports PD diagnosis (Postuma *et al.*, 2015). Although most PD diagnoses are correct, an autopsy remains the gold standard (Weiner, 2008).

1.1.5 Treatment

There is currently no cure or disease-modifying treatment available for PD (Mcdonald *et al.*, 2018). Current treatment options focus primarily on symptomatic relief, with levodopa being the most effective at relieving motor symptoms. Other therapeutics such as dopamine agonists, monoamine oxidase-B (MAO-B) inhibitors and catechol-o-methyl-transferase (COMT) inhibitors are also used to treat motor symptoms of PD (Williams-Gray and Worth, 2016). Although these drugs have different mechanisms of action, their end goal is to either restore dopamine levels in the striatum or to activate striatal dopamine receptors (Royal College of Physicians (UK), 2006).

Drugs such as specific-serotonin reuptake inhibitors (SSRIs), lubiprostone and atropine, are used to treat non-motor symptoms of PD. Lubiprostone and atropine are used to treat constipation and sialorrhea, respectively (Church, 2021).

1.1.6 Aetiology

PD aetiology is multifactorial, involving both genetic and environmental risk factors. However, ageing remains the single largest risk factor for developing PD (Pang *et al.*, 2019).

1.1.6.1 Genetics

Although the vast majority of PD cases are idiopathic, 5-10% are monogenic with Mendelian inheritance. PD genes are classified as PD-causing genes, that is, mutations in these genes cause PD, and PD-risk genes with single nucleotide polymorphisms (SNPs) that do not cause but rather increase the likelihood of developing PD (Deng, Wang and Jankovic, 2018).

Technological advances have facilitated the identification of PD-causing and PD-risk genes, namely through linkage analysis, candidate gene approaches and genome-wide association studies (GWAS) (Billingsley *et al.*, 2018). **Table 1.2** lists PD-causing genes studied in the Bandmann laboratory, using stable zebrafish mutant lines.

Gene	**Inheritance**	**Protein**	**Onset**	**Reference for where PD-causing gene was first identified**
SNCA	AD	α-Synuclein	EOPD and LOPD	(Polymeropoulos *et al.*, 1997)
Parkin	AR	Parkin	EOPD	(Kitada *et al.*, 1998)
PINK1	AR	PINK1	EOPD	(Valente *et al.*, 2004)
LRRK2	AD	LRRK2	LOPD	(Zimprich *et al.*, 2004)

DJ-1	AR	DJ-1	EOPD	(Bonifati *et al.*, 2003)
ATP13A2	AR	ATP13A2	EOPD	(Ramirez *et al.*, 2006)
VPS13C	AR	VPS13C	EOPD	(Lesage *et al.*, 2016)

Table 1.2. A list of PD-causing genes studied in the Bandmann laboratory, their inheritance, encoded protein, disease onset and references to their discovery. *α-Synuclein, alpha-synuclein; AD, autosomal dominant; AR, autosomal recessive; ATP13A2, ATPase cation transporting 13A2; EOPD, early-onset Parkinson's disease; LOPD, late-onset Parkinson's disease; LRRK2, leucine-rich repeat kinase 2; PD, Parkinson's disease; PINK1, phosphatase and tensin homolog (PTEN)-induced putative kinase 1; VPS13C, vacuolar protein sorting 13 Homolog C.*

The first mutation reported to cause autosomal dominant PD was the G209A missense mutation in *SNCA.* This mutation results in the substitution of alanine for threonine at amino acid 53 (A53T). *SNCA* encodes α-Synuclein and is further discussed below (**Section 1.1.10**).

Mutations in the *Parkin* gene were next identified as causing early onset autosomal recessive PD. The first mutations identified were deletions of exons 3-7. Parkin is an E3 ubiquitin ligase, which targets proteins for degradation by attaching ubiquitin molecules to lysine residues of target proteins (Kitada *et al.*, 1998; Seirafi, Kozlov and Gehring, 2015).

PINK1 mutations also cause early onset autosomal recessive PD. Together, Phosphatase and Tensin Homolog (PTEN)-Induced Putative Kinase 1 (PINK1) and Parkin promote the clearance of defective mitochondria in a process called mitophagy, thereby preventing oxidative stress (Ashrafi *et al.*, 2014).

PINK1 phosphorylation is required for PINK1-mediated mitochondrial recruitment of Parkin, and induces PINK1-mediated phosphorylation of Parkin, which stimulates Parkin's E3 ubiquitin ligase activity (Zhuang *et al.*, 2016).

LRRK2 mutations cause autosomal dominant PD, with the G2019S mutation being the most common genetic cause of PD (Zimprich *et al.*, 2004; Bouhouche *et al.*, 2017). Other *LRRK2* mutations have been confirmed to cause PD, namely I2020T, N1437H, R1441C, R1441G, R1441H and Y1699C (Tong *et al.*, 2009; Zimprich *et al.*, 2004; Di Fonzo *et al.*, 2005; Aasly *et al.*, 2010). These mutations increase LRRK2's kinase activity, resulting in phosphorylation and autophosphorylation of Rab GTPases which function as master regulators of intracellular trafficking. Hyperphosphorylation of Rab GTPases resulting from enhanced Lrrk2 kinase activity leads to defective autophagy (Nguyen *et al.*, 2020; Boecker *et al.*, 2021). *LRRK2* SNPs also increase PD risk (**Table 1.3**) (Satake *et al.*, 2009).

Mutations in *DJ-1* and *VPS13C* result in autosomal recessive PD (Bonifati *et al.*, 2003; Lesage *et al.*, 2016). Mutations in *ATP13A2* cause an autosomal recessive form of PD called Kufor-Rakeb syndrome (Ramirez *et al.*, 2006). DJ-1 prevents oxidative stress (Bonifati *et al.*, 2003; Kahle, Waak and Gasser, 2009), Vacuolar Protein Sorting 13 Homolog C (VPS13C) helps to maintain mitochondrial homeostasis (Lesage *et al.*, 2016) and ATPase Cation Transporting 13A2 (ATP13A2) maintains lysosomal function (Ramirez *et al.*, 2006).

Likewise, GWAS have been used to identify genes with SNPs which have a higher frequency in PD patients compared to controls and these genes have been designated PD-risk genes (Satake *et al.*, 2009; Nalls *et al.*, 2014, 2019; Chang *et al.*, 2017). **Table 1.3** lists PD-risk genes studied in the Bandmann laboratory, using stable zebrafish mutant lines.

Gene	**Protein**	**Reference for where SNPs were first identified, and protein function**
ACMSD	ACMSD	(Pucci *et al.*, 2007; Nalls *et al.*, 2014)
GAK	GAK	(C. X. Zhang *et al.*, 2005; Nalls *et al.*, 2014)
GBA	GBA	(Nalls *et al.*, 2014; Beutler *et al.*, 2017)
GCH1	GCH1	(Thöny, Auerbach and Blau, 2000; Nalls *et al.*, 2014)
LRRK2	LRRK2	(Zimprich *et al.*, 2004; Satake *et al.*, 2009)
MCCC1	MCCC1, α subunit	(Baumgartner *et al.*, 2001; Nalls *et al.*, 2014)
SATB1	SATB1	(Chang *et al.*, 2017; Riessland *et al.*, 2019)
SNCA	α-Synuclein	(Polymeropoulos *et al.*, 1997; Satake *et al.*, 2009)

VPS13C	VPS13C	(Nalls *et al.*, 2014; Lesage *et al.*, 2016)

Table 1.3. A list of PD-risk genes identified by GWAS and studied in the Bandmann laboratory, using stable zebrafish mutant lines. *α-Synuclein, alpha-synuclein; ACMSD, 2-amino 3-carboxymuconate 6-semialdehyde decarboxylase; GAK, Cyclin G-associated kinase; GBA, β-glucocerebrosidase; GCH1, GTP cyclohydrolase 1; GWAS, genome-wide association studies; LRRK2, leucine-rich repeat kinase 2; MCCC1, 3-methylcrotonoyl-CoA carboxylase subunit 1; PD, Parkinson's disease ; SATB1, special AT-rich sequence-binding protein 1; SNP, single nucleotide polymorphism; VPS13C, vacuolar Protein Sorting 13 Homolog C.*

ACMSD encodes an enzyme called 2-amino 3-carboxymuconate 6-semialdehyde decarboxylase (ACMSD), which is involved in tryptophan catabolism (Pucci *et al.*, 2007). *GAK* encodes Cyclin G-associated kinase (GAK) which is involved in clathrin-mediated endocytosis and clathrin-dependent trafficking (C. X. Zhang *et al.*, 2005). *GBA* encodes the lysosomal enzyme β-glucocerebrosidase (GBA), which hydrolyses glucocerebroside to glucose and ceramide (Beutler *et al.*, 2017). Homozygous mutations in *GBA* cause Gaucher disease which is a lysosomal storage disorder. The association between *GBA* mutations and PD was made following clinical observation of Gaucher disease patients. Approximately 5-15% of PD patients have mutations in *GBA*, making it the most common genetic risk factor for PD (Smith and Schapira, 2022).

GCH1 encodes GTP cyclohydrolase 1 (GCH1), which is required for the biosynthesis of tetrahydrobiopterin, an essential co-factor for tyrosine hydroxylase (TH) in catecholamine biosynthesis (Thöny, Auerbach and Blau, 2000). *MCCC1* encodes the α subunit of 3-methylcrotonoyl-CoA carboxylase (MCC), a biotin-dependent decarboxylase that catalyses leucine degradation (Baumgartner *et al.*, 2001). *SATB1* encodes Special AT-rich sequence binding protein 1 (SATB1), a global regulator of gene expression (Zelenka and Spilianakis, 2020). *SATB1* will be discussed further in chapter 5 of this thesis. *LRRK2* and *VPS13C* were previously discussed.

1.1.6.2 Environmental factors

Studies over the past 40 years have identified environmental factors associated with PD, including pesticides, herbicides, heavy metals and substance abuse (Jacobson *et al.*, 2019). An overview of toxins which induce parkinsonism is provided below (**Table 1.4**).

Toxin	**Product**	**Mechanism of action**	**Reference for where toxin was first associated with PD**
MPTP, specifically MPP$^+$	Illicit drug	Mitochondrial complex I inhibitor	(William Langston *et al.*, 1983)
Rotenone	Pesticide	Mitochondrial complex I inhibitor	(Heikkila *et al.*, 1985).
Paraquat	Herbicide	Oxidative stress in cytoplasmic proteins	(Hertzman *et al.*, 1990)

Table 1.4. An overview of toxins known to cause parkinsonism, the product each toxin can be found in, mechanism of action, and reference for where an association was first made between the toxin and PD. *MPP$^+$, 1-methyl-4-phenylpyridinium; MPTP, 1-methyl-4-phenyl-1,2,3,6-tetrahydropyridine; PD, Parkinson's disease.*

1-methyl-4-phenyl-1,2,3,6-tetrahydropyridine (MPTP) was first associated with PD in 1983 when 4 people developed parkinsonism following intravenous administration of a new "synthetic heroin" comprising mostly MPTP (William Langston *et al.*, 1983). In further studies, MPTP administration caused selective degeneration of dopaminergic neurons in the SNPc, resulting in a motor phenotype (Burns *et al.*, 1983; William Langston *et al.*, 1984). It is now known that MPTP crosses the blood-brain barrier (BBB) and is metabolised by MAO-B to form the active compound, 1-methyl-4-phenylpyridinium (MPP$^+$) which is a selective inhibitor of mitochondrial complex I (Chiba, Trevor and Castagnoli, 1984; Heikkila *et al.*, 1984; Langston *et al.*, 1984; Ramsay, Salach and Singer, 1986). MPP$^+$ is a substrate for the dopamine transporter which is responsible for dopamine reuptake, explaining its selectivity for dopaminergic neurons (Javitch and Snyder, 1984).

Both MPTP and MPP$^+$ are used to study PD in different model systems (Meredith and Rademacher, 2011; Christensen *et al.*, 2020), specifically MPP$^+$ in the Bandmann laboratory (Flinn *et al.*, 2009; Larbalestier *et al.*, 2022).

In 1985, another pesticide, rotenone was identified to induce parkinsonism (Heikkila *et al.*, 1985). Rotenone is lipophilic, so it is able to cross the BBB (Heikkila *et al.*, 1985). Like MPP$^+$, rotenone selectively inhibits mitochondrial complex I and selectively degenerates dopaminergic neurons in the SNPc, thereby inducing a motor phenotype (Heikkila *et al.*, 1985). However, unlike MPP$^+$, rotenone also induces the formation of α-Synuclein-containing LBs in the nigral region of rats (Betarbet *et al.*, 2000). Like MPP$^+$, rotenone is used to study toxin-induced PD (Greenamyre *et al.*, 2009).

The herbicide paraquat also causes degeneration of dopaminergic neurons in the SNPc and parkinsonism. (Brooks *et al.*, 1999) Paraquat also induces α-Synuclein aggregation (Manning-Bog *et* *al.*, 2002). Although paraquat has a similar chemical structure to MPP^+, it is not a substrate for the dopamine transporter (Richardson *et al.*, 2005) and it causes dopaminergic neuron death by inducing oxidative stress in cytosolic proteins, not by inhibiting mitochondrial complex I (Di Monte *et al.*, 1986; Ramachandiran *et al.*, 2007).

Heavy metals such as iron and manganese have also been suggested to induce parkinsonism through oxidative stress (Montgomery, 1995). Interestingly, caffeine and coffee consumption, as well as cigarette smoking reduce PD risk (Grandinetti *et al.*, 1994; Ross *et al.*, 2000).

Since MPP^+ exposure was utilised in this project, the impact of mitochondrial complex I inhibition on dopaminergic neurons needs to be understood.

1.1.7 Mitochondrial energy production and effect of complex I inhibition

Mitochondria are referred to as the powerhouse of the cell because they are responsible for energy production in a process called cellular respiration (Wills, 2009). Although cellular respiration begins in the cytoplasm with the anaerobic process called glycolysis, which produces two net ATP molecules, majority of ATP molecules are produced afterwards, in mitochondria. Mitochondrial cellular respiration is aerobic and is composed of two processes. First of which is the Krebs cycle, followed by oxidative phosphorylation. However, the Krebs cycle produces 2 ATP molecules, leaving the bulk of ATP production to oxidative phosphorylation; a total of 32-34 ATP molecules are produced by oxidative phosphorylation (Cooper, 2000).

Structurally, mitochondria are composed of an outer and an inner membrane, with an intermembrane space in between. While the outer membrane is permeable to proteins as large as 10 kilodaltons (kDa), the inner membrane is less permeable, thereby regulating the transport of molecules into and out of the mitochondrial matrix. The matrix contains enzymes involved in the Krebs cycle, as well as DNA and ribosomes. On the other hand, the inner membrane contains the electron transport chain (ETC) and ATP synthase (Wills, 2009).

The ETC is composed of transmembrane mitochondrial complexes I-IV, as well as electron transport carriers Coenzyme Q (CoQ) and cytochrome c (Cyt c). The ETC creates a proton gradient between the mitochondrial matrix and the intermembrane space, thereby driving ATP synthesis by ATP synthase. NADH molecules produced during glycolysis and the Krebs cycle, as well as $FADH_2$ molecules produced during the Krebs cycle are utilised in the ETC (Zhao *et al.*, 2019; Ahmad, Wolberg and Kahwaji, 2022). The ETC together with ATP synthase are responsible for oxidative phosphorylation (Wills, 2009). A schematic of oxidative phosphorylation is provided below (**Figure 1.2**).

Oxidative phosphorylation occurs as follows: NADH donates electrons to complex I, thereby becoming oxidised to NAD^+. As a result of this electron transfer, complex I becomes super-charged and pumps 4 protons from the mitochondrial matrix into the intermembrane space, thereby generating a proton-gradient between both mitochondrial compartments. Complex I then transfers its electrons to CoQ, also known as ubiquinone (Zhao *et al.*, 2019; Ahmad, Wolberg and Kahwaji, 2022).

Next, $FADH_2$ donates its electrons to complex II, thereby becoming oxidised to FAD. Unlike complex I, complex II cannot pump protons from the mitochondrial matrix into the inner mitochondrial membrane space. Instead, complex II transfers these electrons to CoQ (Zhao *et al.*, 2019; Ahmad, Wolberg and Kahwaji, 2022).

Electrons are then transferred from CoQ to complex III, thereby super-charging complex III. As a result, complex III pumps 4 protons from the mitochondrial matrix into the intermembrane space, further increasing the proton gradient between both mitochondrial compartments. Complex III then transfers its electrons to Cyt c, which in turn transfers these electrons to complex IV (Zhao *et al.*, 2019; Ahmad, Wolberg and Kahwaji, 2022).

Like with complexes I and III, electron transfer to complex IV super-charges it, resulting in the pumping of 2 protons from the mitochondrial matrix to the inner membrane space. Complex IV then transfers it's electrons to oxygen, the final electron carrier in the ETC, thereby splitting it into 2 oxygen ions. The addition of protons to these oxygen ions forms 2 water molecules. Now, a sufficient proton gradient for ATP synthesis has been generated between the mitochondrial matrix and the inner membrane space (Zhao *et al.*, 2019; Ahmad, Wolberg and Kahwaji, 2022).

Protons then flow down this gradient, from the intermembrane space back into the mitochondrial matrix, through ATP synthase. This migration of protons causes a conformational change within ATP synthase which results in the conversion of ADP to ATP (Zhao *et al.*, 2019; Ahmad, Wolberg and Kahwaji, 2022).

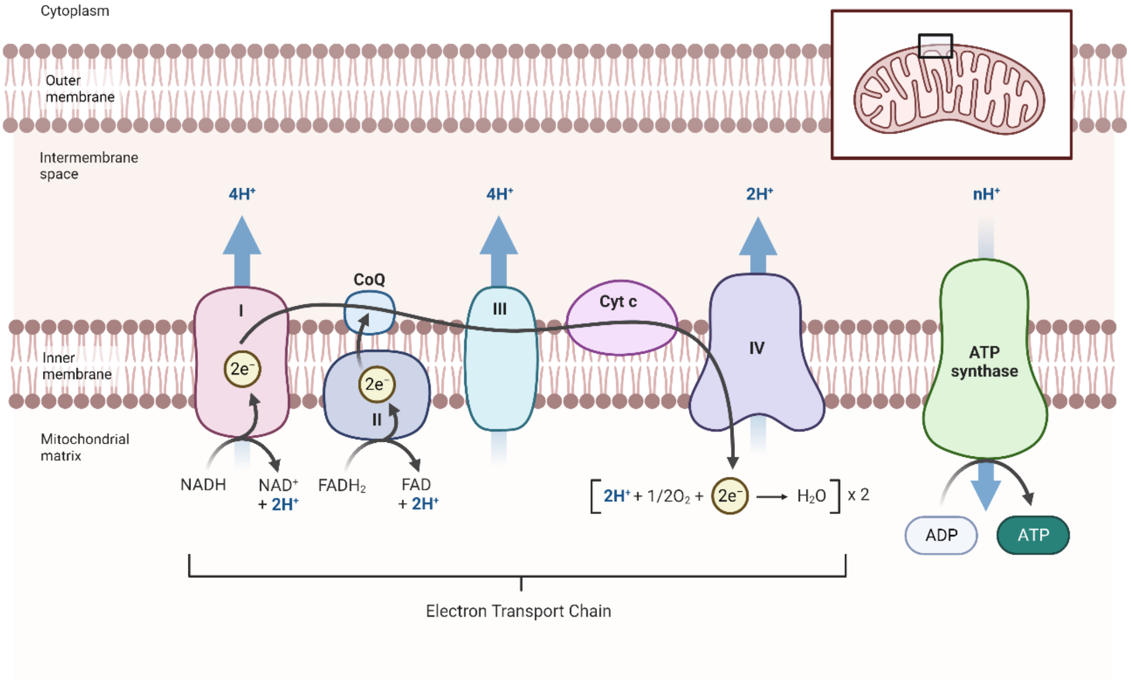

Figure 1.2. Oxidative phosphorylation. *Oxidative phosphorylation is the process by which mitochondria generate the majority of ATP molecules during cellular respiration, after glycolysis and the Krebs cycle. Oxidative phosphorylation involves 2 processes, the electron transport chain and ATP synthesis. NADH produced during glycolysis and the Krebs cycle donates its electrons to complex I, oxidising it to NAD*$^+$*. Complex I becomes super-charged and pumps protons from the mitochondrial matrix into the intermembrane space, thereby generating a proton gradient. Next, complex I transfers its electrons to CoQ. FADH*$_2$ *produced during the Krebs cycle donates its electrons to complex II, oxidising it to FAD. Complex II transfers its electrons to CoQ which then transfers these electrons to complex III, thereby super-charging it. Complex III then pumps protons from the mitochondrial matrix into the intermembrane space, increasing the already generated proton gradient. Next, complex III transfers its electrons to Cyt c which then transfers these electrons to complex IV, thereby super-charging complex IV. Complex IV also pumps protons from the mitochondrial matrix into the intermembrane space, increasing the already generated proton gradient. Complex IV transfers its electrons to the final electron acceptor in the ETC, oxygen. As a result, oxygen is split into two oxygen ions. The addition of protons to these oxygen ions generates 2 water molecules. ATP synthase then uses the established proton gradient to catalyse the conversion of ADP to ATP. ADP, adenosine diphosphate; ATP, adenosine triphosphate; CoQ, Coenzyme Q; Cyt c, cytochrome c; e*$^-$*, electron; FAD, flavin adenine dinucleotide; FADH*$_2$*, reduced flavin adenine dinucleotide; H*$^+$*, proton; H*$_2$*O, water; NAD*$^+$*, nicotinamide adenine dinucleotide; NADH, reduced nicotinamide adenine dinucleotide; O*$_2$*, oxygen. Reprinted from "Electron Transport Chain", by BioRender.com (2023). Retrieved from https://app.biorender.com/biorender-templates.*

MPP$^+$-mediated inhibition of complex I is thought to deplete cellular ATP levels and increase reactive oxygen species (ROS) production, thereby inducing dopaminergic neuron death (Schapira *et al.*, 1989; Meiser, Weindl and Hiller, 2013). ROS also damages mitochondrial DNA (mtDNA), which encodes the protein complexes involved in oxidative phosphorylation (except complex II), resulting in defective mitochondria within surviving dopaminergic neurons (Schapira *et al.*, 1989). This also promotes ROS production, resulting in a toxic positive-feedback loop (Van Houten, Woshner and Santos, 2006).

1.1.8 Pathogenesis

Several mechanisms are implicated in PD pathogenesis, including mitochondrial dysfunction, neuroinflammation, protein aggregation and glutamate-induced excitotoxicity (Jankovic and Tan, 2020). However, for the purpose of this thesis, mitochondrial dysfunction, neuroinflammation and protein aggregation will be discussed.

1.1.8.1 Mitochondrial dysfunction

The first evidence of mitochondrial dysfunction in PD pathogenesis was the discovery that mitochondrial complex I inhibitors, MPP^+ and rotenone, induce parkinsonism (William Langston *et al.*, 1983; Heikkila *et al.*, 1985). The effect of complex I inhibition on dopaminergic neurons was previously discussed (**Section 1.1.7**).

Likewise, a marked reduction of mitochondrial complex I activity has been reported in the substantia nigra and skeletal muscle of PD patients (Schapira *et al.*, 1989; Bindoff *et al.*, 1991), while a slight reduction has been reported in platelets (Krige *et al.*, 1992). This is likely due to brain and muscle tissue being richer in mitochondria than platelets, due to their high energy demand (Boengler *et al.*, 2017; Rango and Bresolin, 2018; Melchinger *et al.*, 2019). Complex I deficiency in mitochondria-rich tissues would produce more ROS than it would in tissues with lower energy demands. This would in turn lead to greater mtDNA damage, resulting in a greater reduction of complex I synthesis and activity.

Likewise, Parkin and PINK1 are both required for mitophagy, thereby preventing oxidative stress in neurons (Ashrafi *et al.*, 2014). *Parkin* mutant mice have reduced striatal mitochondrial respiratory activity (Palacino *et al.*, 2004). Also, *parkin* mutant *Drosophila* have defective locomotion arising from the disruption and disintegration of mitochondrial cristae (Greene *et al.*, 2003).

The livers of *Pink1* mutant mice are characterised by reduced complex I activity (Morais *et al.*, 2009). Both *Pink1* mutant and *Dj-1* mutant dopaminergic neurons have damaged mitochondria, specifically a reduction of cristae and cristae fragmentation, respectively (Shim *et al.*, 2011). *VPS13C* knockdown (KD) cells are also characterised by mitochondrial fragmentation (Lesage *et al.*, 2016).

1.1.8.2 Protein aggregation

Protein misfolding, aggregation and deposition are mechanisms shared among different neurodegenerative diseases, including PD (Soto and Pritzkow, 2018).

Protein homeostasis, also known as proteostasis, involves protein synthesis, trafficking, degradation and release (Morimoto and Cuervo, 2009). Neurons, particularly as post-mitotic cells, require protein clearance systems to remove damaged or abnormal proteins, thereby maintaining proteostasis (Yerbury *et al.*, 2016). The 2 cellular protein clearance systems are the ubiquitin-proteasome system (UPS) and the autophagy-lysosome pathway (ALP). Aggregated α-Synuclein is the major component of LBs and is involved in PD pathogenesis. α-Synuclein is further discussed below (**Section 1.1.10**) (Vilchez, Saez and Dillin, 2014).

1.1.8.3 Inflammation

The first evidence of inflammation in PD was reported in 1988 when reactive microglia were detected in the substantia nigra of PD patients (McGeer *et al.*, 1988). Likewise, activated microglia were observed in the substantia nigra of 3 patients exposed to MPTP (Langston *et al.*, 1999). Astrocyte activation was also detected in one of these patients (Langston *et al.*, 1999). Positron emission tomography (PET) imaging using PK11195, a radiotracer mostly selective for activated microglia, also showed microglial activation in PD patient brains (Banati, Myers and Kreutzberg, 1997; Gerhard *et al.*, 2006).

LRRK2 is highly expressed in peripheral blood mononuclear cells and macrophages (Moehle *et al.*, 2012). *LRRK2* mutations are also a risk factor for a type of inflammatory bowel disease called Crohn's disease (Barrett *et al.*, 2008). *Lrrk2* mutant mice are more susceptible to drug-induced colitis (Liu *et al.*, 2011). Likewise, intracranial lipopolysaccharide (LPS) injection induces microglial Lrrk2 expression within mouse SNpc (Moehle *et al.*, 2012). These suggest a role for *LRRK2* in neuro- and peripheral inflammation.

Systemic LPS treatment induces a greater reduction of dopaminergic neurons in the SNpc of *Parkin* mutant mice, compared to wildtype (WT) littermates (Frank-Cannon *et al.*, 2008). Also, LPS-induced *interleukin-1β* (*Il-1β*) expression is higher in activated macrophages of *Parkin* mutant mice (Tran *et al.*, 2011). Furthermore, *Dj-1* KD in microglia increases sensitivity to LPS, as shown by increased ROS production, nitric oxide (NO) production, as well as increased Il-1β and interleukin-6 (Il-6) expression (Trudler *et al.*, 2014).

In addition, *tumour necrosis factor-α* (*TNF-α*), *Il-1β* and *Il-6* expression is increased in cortical slices of *Pink1* mutant mice (Kim *et al.*, 2013) and aggregated α-Synuclein has been shown to induce microglial activation in a rat mesencephalic neuron-glia culture system (W. Zhang *et al.*, 2005).

1.1.9 Models of PD

PD has been modelled both *in vitro* and *in vivo* (Slanzi *et al.*, 2020; Razali *et al.*, 2021). Although *in vitro* models are informative of PD-related mechanisms, it is well documented that PD pathogenesis involves cell-extrinsic factors (Trudler *et al.*, 2014; Podbielska *et al.*, 2016; Ganjam *et al.*, 2019). *In vitro* models cannot recapitulate the complex cell-cell and cell-environment interactions occurring in an entire organism, both in homeostatic and disease states, thereby limiting the information they are capable of providing.

Three major animal groups have been used to model PD, namely rodents, non-human primates (NHPs) and non-mammalian species (Konnova and Swanberg, 2018). Rodent experiments utilised mostly mice and rats. Advantages of modelling PD in rodents include; the correlation between nigrostriatal degeneration and motor impairment, the availability of behavioural tests to assess both motor and non-motor symptoms of PD, genetic similarity between mice and humans, the ability to generate conventional and conditional knockout (KO) models, availability of transgenic (Tg) mouse strains for overexpression studies, relative ease of drug administration and relatively easy husbandry, among others (Hall, Limaye and Kulkarni, 2009; Vandamme, 2014; Konnova and Swanberg, 2018). Although an extensive amount of PD knowledge has been gained from rodents, a disadvantage of this model arises from physiological differences. For example, rats are resistant to systemic MPTP because their BBB is enriched in MAO-B which converts MPTP to MPP^+ within the BBB. Therefore, MPP^+ is unable to cross the BBB, thereby causing MPTP resistance (Riachi, LaManna and Harik, 1989).

NHPs have also be useful in PD research. An advantage of modelling PD in NHPs is the presence of a "unilateral syndrome" following intracarotid artery administration of MPTP. MPTP is taken up by dopaminergic neurons on the ipsilateral side of toxin administration, leaving a healthy contralateral midbrain. As a result, animals require minimal critical care during disease study. However, intracarotid artery administration of MPTP requires surgery and specialised training. Likewise, NHPs have long generation time and are expensive to maintain (Emborg, 2007).

Invertebrate models, such as *Caenorhabditis elegans* (*C.elegans*) and *Drosophila* have also been used to model PD. Advantages of using these organisms include short generation time, low maintenance cost, genetic tractability, well-defined neuropathology and behaviour, and drug discovery capabilities, among others. A major disadvantage of these models is their relatively simple nervous system, which makes them less compelling models for PD. The *C.elegans* nervous system contains 302 neurons, 8 of which are dopaminergic neurons while the *Drosophila* nervous system contains 135,000 neurons (Konnova and Swanberg, 2018). The human brain alone contains approximately 86 billion neurons (Herculano-Houzel, 2012).

1.1.9.1 Zebrafish as a model for PD

Another non-mammalian species used to model PD is zebrafish (*Danio rerio*). Zebrafish have a short generation time, can be bred frequently and have low maintenance cost. Zebrafish fertilisation is external, embryos are small and optically transparent, allowing intravital imaging. External fertilisation and the small size of zebrafish embryos allow for high through-put drug and phenotypic screens (Sakai, Ijaz and Hoffman, 2018; Choi *et al.*, 2021).

Furthermore, central nervous system (CNS) homology is conserved between humans and zebrafish (Panula *et al.*, 2010). Neurons projecting from the posterior tuberculum to the subpallium, called diencephalic (DC) neurons, are thought to be analogous to human dopaminergic neurons that project from the SNpc to the striatum (Rink and Wullimann, 2001, 2002) (**Figure 1.3**). DC neurons are detected as early at 30 hours post-fertilization (hpf) and axon projections are detected at 3 days post fertilisation (dpf) (Du *et al.*, 2016). DC neurons can be counted following in-situ hybridisation, as is later reported in this thesis.

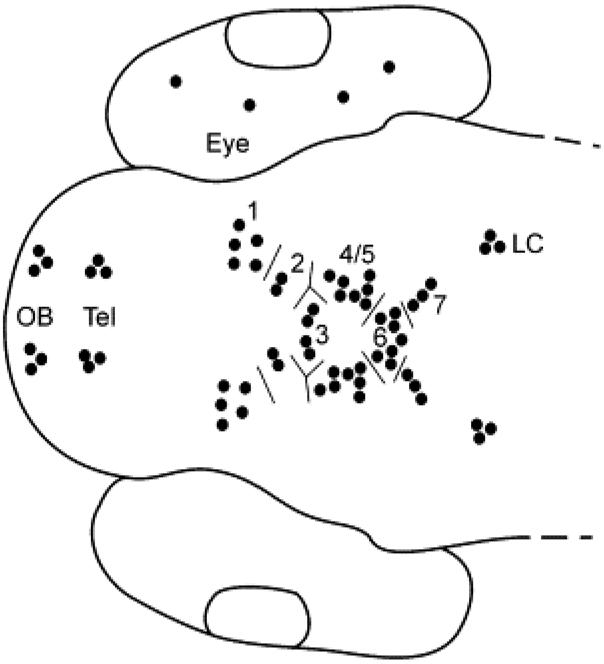

Figure 1.3. Th-positive neurons in zebrafish larvae at 5dpf. *DC neurons 1, 2, 4 and 5 were counted in this PhD because they are analogous to human dopaminergic neurons that project from the SNpc to the striatum. Reproduced from Rink and Wullimann, (2002). OB, olfactory bulb; DC, diencephalic; dpf, days post fertilisation; LC, locus coeruleus; SNpc, substantia nigra pars compacta; Tel, telencephalon; Th, tyrosine hydroxylase.*

Zebrafish also share genetic similarity with humans, with 87% homology with the human genome (Du *et al.*, 2016). Likewise, several PD-causing and PD-risk genes are conserved in zebrafish. Due to the genetic tractability of zebrafish, Tg zebrafish which fluorescently label proteins-of-interest can be generated. Also, zebrafish KO models of PD-causing and PD-risk genes can be easily generated (Razali *et al.*, 2021).

However, zebrafish do not express endogenous α-Synuclein (Milanese *et al.*, 2012). With α-Synuclein pathology being pivotal to both PD pathology and pathogenesis, this poses a possible disadvantage of modelling PD using zebrafish. However, the absence of α-Synuclein in zebrafish may enable the elucidation of the specific contributions of PD-causing and PD-risk genes to PD pathogenesis.

Common genetic techniques used to generate Tg zebrafish include Tol2- and I-SceI-mediated transgenesis, among others (Bai *et al.*, 2007; Ellett *et al.*, 2011). The most powerful gene KO technique is Clustered Regularly Interspaced Short Palindromic Repeats/CRISPR-associated protein 9 (CRISPR/Cas9) gene editing (Van Campenhout *et al.*, 2019), which was used to generate 5 of the stable zebrafish lines discussed in this thesis.

1.1.9.1.1 CRISPR/Cas9 gene editing

CRISPR/Cas9 technology allows researchers to edit the genome of living organisms at a specific region of DNA (Van Campenhout *et al.*, 2019). In nature, bacteria utilise the CRISPR/Cas9 system for adaptive immunity against viruses. During a viral infection, bacteria insert pieces of viral DNA into their own DNA sequence, creating CRISPR arrays. If reinfected, CRISPR arrays are transcribed into pre-CRISPR RNAs (crRNAs) which are processed to mature crRNAs. Mature crRNAs bind to trans-activating CRISPR RNAs (tracrRNA), forming guide RNAs (gRNAs). Cas9 protein then binds individual gRNAs, then Cas9/gRNA complexes bind viral DNA and ligate it (Arroyo-Olarte, Bravo Rodríguez and Morales-Ríos, 2021).

In research, a crRNA, a tracrRNA and the Cas9 protein are employed for CRISPR/Cas9 gene editing. The crRNA is a 17-20 nucleotide sequence complementary to the target DNA sequence and it must be directly upstream of a protospacer adjacent motif (PAM) site (5’ NGG). tracrRNA binds to the crRNA, forming a gRNA. The Cas9 protein uses the tracrRNA as a handle as it surveys the genome until the target DNA is found. crRNA binds its complementary DNA sequence, Cas9 recognises the PAM site and ligates DNA 3 base pairs (bp) upstream of the PAM site via double-stranded breaks (DSBs). Consequently, DNA-damage response (DDR) mechanisms are activated. In the absence of a repair template, DSBs are re-ligated through error-prone non-homologous end joining (NHEJ), thereby creating insertion/deletion (indel) mutations (Ran *et al.*, 2013; Van Campenhout *et al.*, 2019). This is summarised below (**Figure 1.4**).

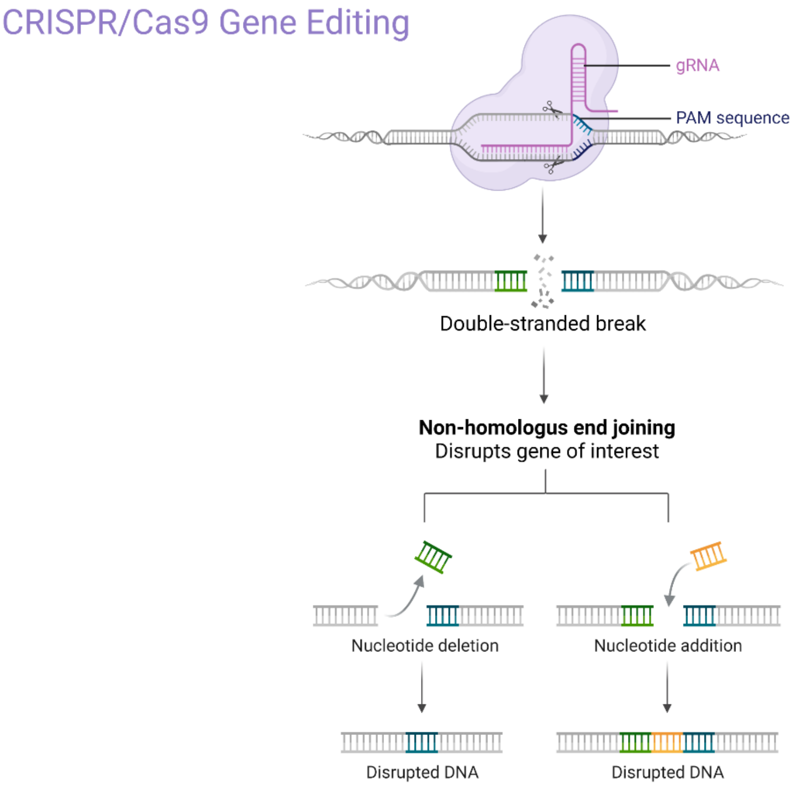

Figure 1.4. CRISPR/Cas9 gene editing. *The CRISPR/Cas9 gene editing technique utilises a crRNA, a tracrRNA and Cas9 protein. crRNA is a 17-20 nucleotide sequence complementary to target DNA, and it lies directly upstream of a PAM site (5' NGG). tracrRNA binds crRNA, forming gRNA. Cas9 protein surveys the genome, together with gRNA until the target DNA is found. crRNA then binds the target DNA sequence, Cas9 recognises the PAM site and induces DNA DSBs 3bp upstream of the PAM site. Consequently, DDR mechanisms are activated. In the absence of a repair template, DSBs are re-ligated through error-prone NHEJ, thereby creating indel mutations. bp, base pair; Cas9, CRISPR-associated protein 9; CRISPR, clustered regularly interspaced short palindromic repeats; crRNA, CRISPR RNA; DDR, DNA-damage response; DSBs, double-stranded breaks; gRNA, guide RNA; Indel, insertion/deletion; NHEJ, non-homologous end joining; PAM, protospacer adjacent motif; tracrRNA, trans-activating CRISPR RNA. Adapted from "CRISPR/Cas9 Gene Editing", by BioRender.com (2023). Retrieved from https://app.biorender.com/biorender-templates.*

1.1.10 *SNCA* and PD

A major focus of this thesis is to study the effect of ageing-related mechanisms on *SNCA*-mediated PD pathogenesis.

1.1.10.1 Background

SNCA is located on human chromosome 4 and has 6 exons, 5 of which encode α-Synuclein (Gámez-Valero and Beyer, 2018). *SNCA* mutations cause autosomal dominant PD (Meade, Fairlie and Mason, 2019), including the A53T mutation (Polymeropoulos *et al.*, 1997), the A30P mutation (Krüger *et al.*, 1998) and the E46K mutation (Zarranz *et al.*, 2004). Other *SNCA* mutations that cause autosomal dominant PD include the G51D mutation (Lesage *et al.*, 2013) and the recently identified A30G mutation (Liu *et al.*, 2021).

Likewise, duplication and triplication of the *SNCA* locus causes autosomal dominant PD (Singleton *et al.*, 2003; Chartier-Harlin *et al.*, 2004). A gene dosage effect exists as duplication of the *SNCA* locus causes late onset autosomal dominant PD (Chartier-Harlin *et al.*, 2004) while triplication of the *SNCA* locus causes early onset autosomal dominant PD (Singleton *et al.*, 2003). Both duplication and triplication increase α-Synuclein expression in PD patients (Miller *et al.*, 2004; Kim *et al.*, 2012). GWAS have also identified *SNCA* SNPs associated with increased PD risk (Nalls *et al.*, 2011, 2014, 2019).

1.1.10.2 α-Synuclein structure, function, post-translational modification and aggregation

α-Synuclein is a 140 amino acid protein expressed in pre-synaptic terminals of neurons, as well as glia and blood cells. α-Synuclein is composed of 3 distinct domains: the N-terminal domain (residues 1-60), the central hydrophobic non-amyloid-β-component (NAC) domain (residues 61-95) and the C-terminal domain (residues 96-140) (**Figure 1.5**). The N-terminal domain contains amphipathic repetitions and forms an α-helical structure, when bound to lipids. The NAC domain triggers β-sheet formation while the C-terminal domain has the tendency to prevent protein aggregation (Bisi *et al.*, 2021; Barba *et al.*, 2022).

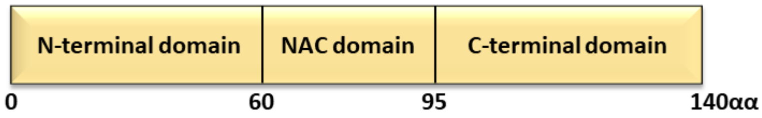

Figure 1.5. α-Synuclein structure. *α-Synuclein is a 140 amino acid protein composed of an N-terminal domain (residues 1-60), a NAC domain (residues 61-95) and a C-terminal domain (residues 96-140).*

α-Synuclein belongs to a family of synucleins which includes β- and γ-synuclein. β- and γ-synuclein are encoded by *SNCB* and *SNCG*, respectively. Although the N-terminal domain is highly conserved among these 3 synucleins, α-Synuclein is distinct in its NAC and C-terminal domains. Although, β-synuclein is reported to offer protection from α-Synuclein-mediated neurodegeneration, the role of γ-synuclein in α-Synuclein-mediated neurodegeneration is yet to be understood (Barba *et al.*, 2022).

α-Synuclein assists the assembly of the soluble N-ethylmaleimide-sensitive factor attachment protein receptor (SNARE) complex at synapses, thereby regulating neurotransmitter release (Barba *et al.*, 2022). α-Synuclein also modulates actin polymerisation and depolymerisation, thereby affecting synaptic function (Sousa *et al.*, 2009).

α-Synuclein can undergo post-translational modifications (PTMs) including but not limited to phosphorylation at serine 129, nitration, ubiquitination and truncation. These PTMs influence α-Synuclein aggregation and toxicity (Zhang, Li and Li, 2019). α-Synuclein aggregation refers to the progression of monomeric α-Synuclein to soluble oligomers, then to insoluble fibrils (Barba *et al.*, 2022). α-Synuclein aggregates are present in PD patient LBs and LNs (MacMahon Copas *et al.*, 2021). To maintain proteostasis, α-Synuclein is degraded by both the UPS and ALP (Stefanis *et al.*, 2019; Barba *et al.*, 2022).

However, α-Synuclein inhibits both the UPS and ALP (Snyder *et al.*, 2003; Xilouri *et al.*, 2009; Emmanouilidou, Stefanis and Vekrellis, 2010; Tang *et al.*, 2021), indicating a vicious cycle between the loss of proteostasis and α-Synuclein aggregation. Also, caspase-1 truncates α-Synuclein, thereby inducing α-Synuclein aggregation, implicating inflammation in α-Synuclein aggregation. Truncated α-Synuclein is thought to first aggregate then seed aggregation of full-length α-Synuclein (Wang *et al.*, 2016).

1.1.10.3 α-Synuclein-mediated neurotoxicity in animal models and PD patients

Although, α-Synuclein-mediated neurotoxicity has been modelled using *Drosophila* (Mizuno *et al.*, 2010) and yeast cells (Cooper *et al.*, 2006), among others, rodents remain the most extensively used model for α-Synuclein-mediated neurotoxicity (Recasens *et al.*, 2017).

Mice lacking α-Synuclein have reduced striatal dopamine levels (Abeliovich *et al.*, 2000). Interestingly, mice lacking α-Synuclein are resistant to MPTP-induced (Dauer *et al.*, 2002) and LPS-induced toxicity of SNPc dopaminergic neurons (Dauer *et al.*, 2002; Gao *et al.*, 2008). Likewise, MPTP treatment induces α-Synuclein nitration in the WT mouse striatum (Przedborski *et al.*, 2001), suggesting α-Synuclein involvement in mitochondrial dysfunction and inflammation in PD.

α-Synuclein is targeted to the mitochondria of dopaminergic neurons, using a signal in its N-terminal domain (Li *et al.*, 2007; Devi *et al.*, 2008). MPTP treatment causes nigral mitochondrial structural abnormalities specifically in mice overexpressing human WT α-Synuclein (Song *et al.*, 2004). Overexpression of human WT and A53T α-Synuclein inhibits complex I activity and increases ROS levels *in vitro* while overexpression of human WT α-Synuclein causes mitochondrial accumulation of α-Synuclein *in vitro* (Devi *et al.*, 2008).

Mitochondrial accumulation of α-Synuclein also occurs in the substantia nigra and striatum of PD patients. Likewise, there is a negative correlation between mitochondrial accumulation of α-Synuclein and mitochondrial complex I activity in the substantia nigra of PD patients (Devi *et al.*, 2008).

This is supported by another study where overexpression of human WT α-Synuclein caused fragmentation of neuronal mitochondria, increased ROS levels, decreased ATP levels and resulted in cell death. Interestingly, broad-spectrum caspase inhibitors rescued mitochondrial dysfunction and cell death, implicating inflammation in α-Synuclein-mediated mitochondrial dysfunction. A specific caspase-1 inhibitor also reduced cell death but its probable rescue effect on mitochondrial dysfunction was not investigated (Ganjam *et al.*, 2019).

LPS induces dopaminergic neuron loss in the SNPc of mice overexpressing human WT α-Synuclein (SYNO) and human A53T α-Synuclein (A53TSYNO), in the absence of murine α-Synuclein. A greater loss of dopaminergic neurons was reported in A53TSYNO mice compared to SYNO mice. LPS injection also induces α-Synuclein aggregation in SYNO and A53TSYNO mice, with greater aggregation in A53TSYNO mice. Nitrated and phosphorylated α-Synuclein were detected in LPS-treated SYNO and A53TSYNO mice only, indicating that glia-derived factors modified human α-Synuclein in these mice (Gao *et al.*, 2008). Likewise, human WT α-Synuclein has been shown to activate microglia (Béraud *et al.*, 2011). Overexpression of human WT α-Synuclein also inhibits dopamine release from mouse SNPc dopaminergic neurons (Nemani *et al.*, 2010).

Certain studies have investigated the effect of exogenous α-Synuclein preformed fibrils (PFFs) on neurodegeneration. For example, intracerebral injection of murine α-Synuclein PFFs induces brain-wide α-Synuclein aggregation, SNPc dopaminergic neuron loss, loss of striatal dopamine, and motor impairment in WT mice (Luk, V. Kehm, *et al.*, 2012).

Likewise, intracerebral injection of human α-Synuclein PFFs induces widespread α-Synuclein aggregation and motor deficits in Tg mice overexpressing human A53T α-Synuclein (Luk, V. M. Kehm, *et al.*, 2012).

Furthermore, intracerebral injection of LB fractions extracted from human PD brains induces loss of SNPc dopaminergic neurons, and α-Synuclein aggregation. These effects are thought to be the result of exogenous α-Synuclein inducing aggregation of endogenous α-Synuclein (Recasens *et al.*, 2014). It appears that the host mouse must express endogenous α-Synuclein because pathology is absent in α-Synuclein mutant mice (Recasens *et al.*, 2014). Further studies have utilised α-Synuclein PFFs to induce neurotoxicity (Gómez-Benito *et al.*, 2020). For example, inoculation of α-Synuclein PFFs into the gastric wall of WT mice induces phosphorylated α-Synuclein-positive LB-like aggregates in the dorsal motor nucleus of the vagus nerve (Uemura *et al.*, 2018). Likewise, intrastriatal injection of α-Synuclein PFFs induces phosphorylated α-Synuclein expression in the enteric nervous system (ENS) of WT mice (Earls *et al.*, 2019).

1.1.10.3.1 Zebrafish models of α-Synuclein-mediated neurotoxicity

Zebrafish have also been used to model α-Synuclein-mediated neurotoxicity but as previously stated, zebrafish do not have an *SNCA* orthologue and therefore do not express endogenous α-Synuclein. However, zebrafish have a single *SNCB* orthologue (*sncb*) and 2 *SNCG* orthologues (*sncg1* and *sncg2*). *sncb* expresses β-synuclein while *sncg1* and *sncg2* express γ1- and γ2-synuclein, respectively. *sncb* and *sncg1* are expressed in the CNS while *sncg2* is expressed in the notochord (Milanese *et al.*, 2012).

Zebrafish lacking endogenous synucleins were generated by Milanese *et al.*, (2012). Zebrafish lacking β-synuclein, γ1-synuclein or γ1- and γ2-synuclein showed no developmental defects but displayed motor impairment. This motor impairment was accompanied by an impaired dopamine system in zebrafish lacking β- and γ1-synuclein, which was rescued by exogenous human α-Synuclein expression (Milanese *et al.*, 2012).

Zebrafish have also been used to model α-Synuclein-mediated pathology by expressing exogenous human α-Synuclein under a neuronal promoter (Razali *et al.*, 2021). Exogenous human WT α-Synuclein is suggested to aggregate following expression in zebrafish (Weston *et al.*, 2021). Likewise, expression of exogenous human WT α-Synuclein is suggested to cause neuronal toxicity (Lopez *et al.*, 2022). However, neither Weston *et al.*, (2021) nor Lopez *et al.*, (2022) utilised a stable Tg zebrafish line with sustained α-Synuclein expression, thereby limiting reproducibility and relevance to age-related studies, respectively.

1.2 Ageing

Ageing is the progressive decline in cellular and tissue function which increases susceptibility to disease and death (Guo *et al.*, 2022).

The human population is ageing globally. Between 1990 and 2019, the proportion of adults aged ≥70 years old increased by more than 100% globally (**Figure 1.6**) (Kassebaum, 2022). Likewise, the proportion of the world's population over 60 years old is projected to nearly double between 2015 and 2050 (World Health Organisation, 2022).

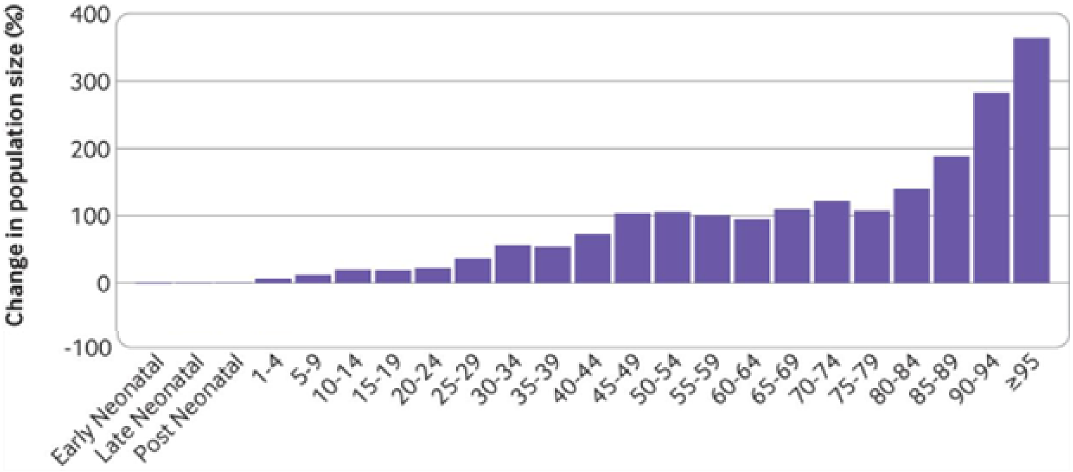

Figure 1.6. Trend in global ageing between 1990 and 2019. *The change in the population of different age brackets between 2019 and 1990 is expressed as a percentage. Reproduced from Kassebaum, (2022).*

Ageing is the major risk factor of several diseases, including cancer, cardiovascular disorders and neurodegenerative diseases, including PD (Niccoli and Partridge, 2012; Pang *et al.*, 2019). However, a detailed understanding of the interplay between ageing and PD remains elusive. The cellular and molecular changes associated with ageing, also known as the hallmarks of ageing, are discussed below.

1.2.1 Hallmarks of ageing

There are 9 hallmarks of ageing, namely genomic instability, telomere attrition, epigenetic alterations, loss of proteostasis, deregulated nutrient-sensing, mitochondrial dysfunction, cellular senescence, stem cell exhaustion and altered intercellular communication (**Figure 1.7**) (López-Otín *et al.*, 2013).

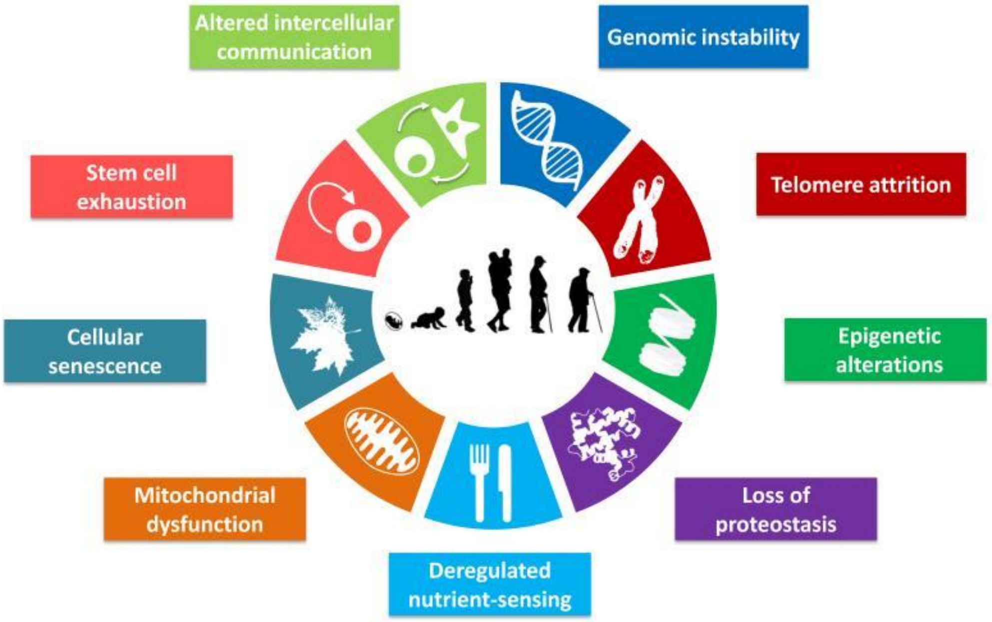

Figure 1.7. Hallmarks of ageing. *The hallmarks of ageing are genomic instability, telomere attrition, epigenetic alterations, loss of proteostasis, deregulated nutrient-sensing, mitochondrial dysfunction, cellular senescence, stem cell exhaustion and altered intercellular communication. Reproduced from López-Otín et al., (2013).*

For the purpose of this thesis, genomic instability, epigenetic alterations, loss of proteostasis, mitochondrial dysfunction, cellular senescence and altered intercellular communication will be discussed.

1.2.1.1 Genomic instability

Ageing is characterised by the accumulation of cellular DNA damage (Maynard *et al.*, 2015). DNA damage refers to alterations to the chemical structure of DNA and is caused by endogenous factors such as ROS and hydrolysis, and exogenous factors such as ultraviolet (UV) light and ionising radiation (Chen, Hales and Ozanne, 2007). Consequently, cells have DDR mechanisms to detect and promote DNA damage repair (Chatterjee and Walker, 2017). Highly conserved DNA repair systems include base excision repair (BER), nucleotide excision repair (NER), mismatch repair (MMR), homologous recombination (HR) and NHEJ (Chatterjee and Walker, 2017). DNA damage repair occurs in both nuclear DNA and mtDNA (Kazak, Reyes and Holt, 2012). However, mtDNA repair is less efficient than nuclear DNA repair (Blasiak *et al.*, 2013).

DNA mutations arise as a consequence of DNA replication errors or mutagenesis, such as in CRISPR/Cas9 gene editing (**Section 1.1.9.1.1**) (Brown, 2002). Examples of DNA mutations include point mutations, indel mutations, transposition and inversion mutations, among others (Loewe and Hill, 2010).

Indel mutations of a number of nucleotides not divisible by 3 may cause frameshift mutations, thereby altering the open reading frame. When frameshift mutations are encountered by a translating ribosome, variant amino acids encoded by the alternative reading frame are incorporated into the translated protein. However, a stop codon (TAA, TAG or TGA) in the alternative reading frame usually causes premature termination of translation, thereby truncating the protein (**Figure 1.8**) (Harfe and Jinks-Robertson, 1999; Old, 2013). Mutant mRNA may also be degraded by nonsense-mediated decay (NMD), thereby preventing the translation of an aberrant protein (Dyle *et al.*, 2020).

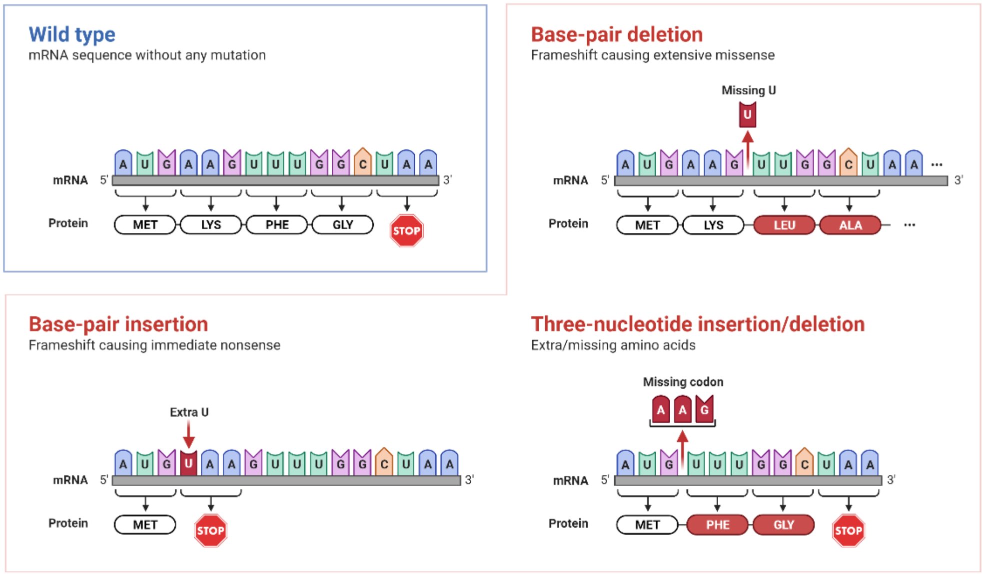

Figure 1.8. Frameshift mutations. *Indel mutations with multiples not divisible by 3bp change the reading frame of the nucleotide sequence. As a result, variant amino acids are translated, giving a variant protein. Indel mutations also induce a premature stop codon, in this case UAA, which truncates the translated protein. A, adenine; Ala, alanine; C, cytosine; G, guanine; Gly, glycine; Indel, Insertion/deletion; Leu, leucine; Lys, lysine; Met, methionine; mRNA, messenger RNA; Phe, phenylalanine; STOP, stop codon, U, uracil;. Reprinted from "Frameshift Mutations", by BioRender.com (2023). Retrieved from https://app.biorender.com/biorender-templates.*

A link between genomic instability and ageing is supported by accelerated ageing in mice with deficient DNA repair mechanisms (Murga *et al.*, 2009; Gregg *et al.*, 2012). Likewise, mice expressing proof-reading deficient mtDNA polymerase (Polγ) have increased levels of mtDNA mutations and display accelerated ageing (Trifunovic *et al.*, 2004; Kujoth *et al.*, 2005; Vermulst *et al.*, 2008). Furthermore, defective DNA mechanisms underlie progeroid syndromes in humans, including Cockayne's syndrome, trichothiodystrophy and xeroderma pigmentosum (Hoeijmakers, 2009). Progeroid syndromes refer to rare human diseases such as Hutchinson-Gilford progeria syndrome (HGPS) or Werner Syndrome (WS), which mimic ageing (Kõks *et al.*, 2016).

1.2.1.2 Epigenetic alterations

Epigenetics refers to gene expression changes not caused by changes to DNA. Epigenetic changes are thought to influence gene expression majorly at the level of transcription and involve cytosine methylation, chromatin remodelling and RNA-mediated mechanisms (Gibney and Nolan, 2010). For the purpose of this thesis, chromatin remodelling will be discussed.

Chromatin remodelling refers to conformational changes in chromatin structure at specific regions, allowing cellular processes such as transcription, differentiation and DNA repair to occur (Alberts et al., 2002). The primary factors responsible for chromatin remodelling are histone-modifying enzymes and ATP-dependent chromatin remodelling complexes (Swygert and Peterson, 2014).

Histones are conserved proteins around which DNA is coiled (**Figure 1.9**) (Gibney and Nolan, 2010). Each histone has an N-terminal tail that acts as a site for PTMs, such as methylation, acetylation, ubiquitination, phosphorylation (Bowman and Poirier, 2015).

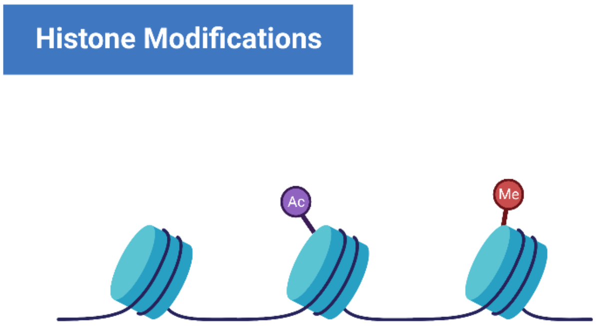

Figure 1.9. Histone modifications. *This nucleosome consists of a DNA molecule and 8 histone proteins (3 of which are depicted in this figure); one histone is unmodified while one is acetylated and the other is methylated. Ac, acetyl group; Me, methyl group. Adapted from "Histone Modifications", by BioRender.com (2023). Retrieved from https://app.biorender.com/biorender-templates.*

The DNA-protein complex formed by the coiling of DNA around 8 histone proteins is called a nucleosome (Ettig *et al.*, 2011). Multiple nucleosomes condense to form chromatin. This packaging of DNA presents a challenge for important elements, such as DNA repair enzymes to access DNA when needed (Alberts *et al.*, 2002; Simpson, Tupper and Al Aboud, 2022).

Through PTMs, histone-modifying enzymes, such as sirtuins can induce conformational changes in nucleosomes, thereby exposing transcription factor-binding sites (Feige and Johan, 2008). Sirtuins will be discussed in chapter 4 of this thesis.

An example of histone modification is the phosphorylation of H2A histone family member X (H2AX) at serine 139 by the tumour suppressor gene, ataxia telangiectasia mutated (ATM), in response to DSB.

This modification forms γH2AX which then facilitates chromatin remodelling and the recruitment of DNA repair enzymes to the site of DNA damage (Nakamura *et al.*, 2010). Like histone-modifying enzymes, ATP-dependent chromatin remodelling complexes induce chromatin remodelling but in an ATP-dependent manner (Swygert and Peterson, 2014). Age-associated accumulation of γH2AX has been reported in human fibroblasts as well as mouse liver, testis, kidney, lung and brain (Sedelnikova *et al.*, 2004).

1.2.1.3 Loss of proteostasis

Proteostasis and its maintenance were previously explained (**Section 1.1.8.2**).

Evidence for loss of proteostasis in ageing includes, the decreased expression of the molecular chaperone heat shock protein 70 (hsp70) in response to heat shock in rat livers, lymphocytes, and skin and lung fibroblasts (Fargnoli *et al.*, 1990; Pahlavani *et al.*, 1995; Hall *et al.*, 2000). This is also thought to occur in rhesus monkeys (Pahlavani *et al.*, 1995).

Likewise, the activity of the 20S core of the UPS is reduced in the skeletal muscle of aged rats (Ferrington, Husom and Thompson, 2005). Also, intralysosomal accumulation of lipofuscin impairs autophagy and is characteristic of ageing (Moreno-García *et al.*, 2018).

1.2.1.4 Mitochondrial dysfunction

Mitochondrial dysfunction was also previously explained (**Section 1.1.8.1**).

A popular theory, the free radical theory of ageing, suggests that ageing may in part result from the accumulation of ROS (Harman, 1956). Although increased ROS levels have been reported in the elderly (Radak *et al.*, 2011) and oxidative stress is involved in the pathogenesis of several age-associated diseases, including cancer, diabetes and neurodegenerative diseases (Tan *et al.*, 2018), longevity is unaffected in mice with increased ROS levels (Van Remmen *et al.*, 2003). Likewise, longevity is unaffected in mice that overexpress anti-oxidant enzymes (Pérez *et al.*, 2009), thereby prompting a review of the free radical theory of ageing.

1.2.1.5 Cellular senescence

Cellular senescence is the irreversible cell cycle arrest that occurs in response to triggers such as telomere shortening, DNA damage and increased ROS levels (Van Deursen, 2014). First described in 1961 (Hayflick and Moorhead, 1961), cellular senescence is implicated in multiple biological processes aside ageing, including embryonic development, wound healing, tissue repair and cancer (Collado, Blasco and Serrano, 2007; Krizhanovsky *et al.*, 2008; Jun and Lau, 2010; Muñoz-Espín *et al.*, 2013; Storer *et al.*, 2013).

There are 3 types of cellular senescence, namely replicative senescence, as described in 1961, oncogene-induced senescence and stress-induced premature senescence (Hayflick and Moorhead, 1961; De Magalhães *et al.*, 2002; Collado, Blasco and Serrano, 2007). Senescent cells can be detected in situ, using senescence-associated β-galactosidase (SA-β-Gal) staining (Dimri *et al.*, 1995). Under normal conditions, senescent cells prevent tissue damage (Jun and Lau, 2010) and are subsequently destroyed by natural killer cells (Krizhanovsky *et al.*, 2008). Therefore, age-associated accumulation of senescent cells (Dimri *et al.*, 1995; Hudgins *et al.*, 2018), suggests an imbalance between the production and degradation of these cells.

At the molecular level, senescence is induced by DNA damage as follows: DSBs are detected by ATM which then stabilises p53, a tumour suppressor protein. In turn, p53 promotes *cyclin dependent kinase inhibitor 1A* (*CDKN1A*) transcription. The protein encoded by *CDKN1A* is p21, a cyclin-dependent kinase (CDK) inhibitor. As implied by its name, p21 inhibits downstream kinases, resulting in the hypophosphorylation of the retinoblastoma (RB) protein. Hypophosphorylated RB binds E2F transcription factors and RB-E2F complexes arrest the cell cycle by downregulating the transcription of cell cycle genes. This is called the p53-p21-RB signalling pathway (**Figure 1.10**). In addition, p16 interacts with p21 in a p53-independent manner to promote RB hypophosphorylation (Crouch *et al.*, 2022; Engeland, 2022).

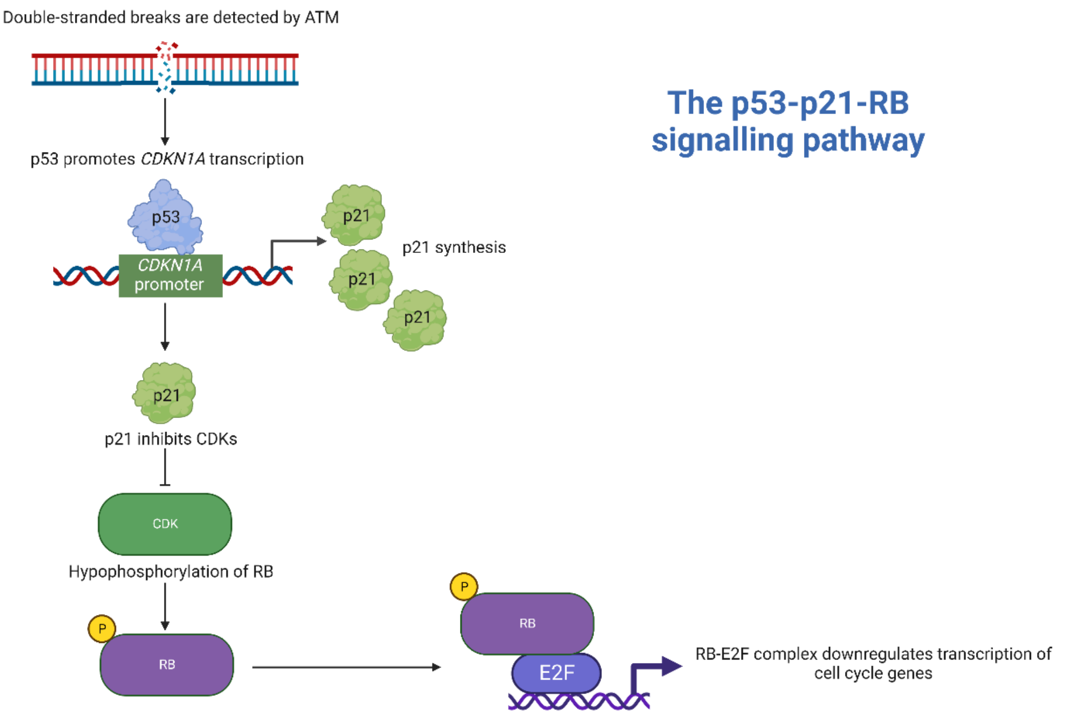

Figure 1.10. The p53-p21-RB signalling pathway. *DSBs are detected by ATM. Next, ATM stabilises p53. In turn, p53 promotes CDKN1A transcription, thereby promoting p21 synthesis. Downstream, p21 inhibits CDKs, resulting in the hypophosphorylation of RB. Hypophosphorylated RB binds E2F transcription factors and RB-E2F complexes arrest the cell cycle by preventing the transcription of cell cycle genes. ATM, ataxia telangiectasia mutated; CDKN1A, CDK inhibitor 1A; CDK, cyclin-dependent kinase; p, phosphate; RB, retinoblastoma. Created with BioRender.com.*

Likewise, the transcriptional program of senescent cells changes to induce the transcription of genes encoding pro-inflammatory cytokines, chemokines, growth factors and extracellular matrix (ECM) proteases. As a result, these cells secrete a collection of toxic factors called the senescence-associated secretory phenotype (SASP) factors. Specifically, SASP factors include IL-1β, IL-6, interleukin-8 (IL-8), monocyte chemoattractant protein 1 (MCP1), matrix metalloproteinases (MMPs), serine/cysteine proteinase inhibitors (SERPINs), insulin-like growth factor binding protein 7 (IGFBP7), among others (Coppé *et al.*, 2010; Di Micco *et al.*, 2020).

Senescent cells have emerged as an attractive target for age and disease. This is because the selective elimination of senescent cells mitigated disease and increased lifespan in mice (Childs *et al.*, 2017). However, this is a relatively new research field and a considerable number of studies need to be completed to assess safety, efficacy and tolerability in humans (Chaib, Tchkonia and Kirkland, 2022).

1.2.1.6 Altered intercellular communication

Altered intercellular communication refers to neuroendocrine dysfunction, inflammageing, immunosenescence and the bystander effect. For the purpose of this thesis, inflammageing, immunosenescence and the bystander effect are discussed below.

Inflammation was previously discussed (**Section 1.1.8.3**). Inflammageing refers to chronic inflammation with ageing (de Magalhães, Curado and Church, 2009; Salminen, Kaarniranta and Kauppinen, 2012; Ferrucci and Fabbri, 2018). Inflammatory cytokines secreted in inflammageing include interleukin-1 (IL-1), IL-1β, IL-6, interleukin-13 (IL-13), TNF-α, transforming growth factor-β (TGF-β), among others (Csiszar *et al.*, 2003; Ferrucci and Fabbri, 2018). Anti-inflammatory cytokines IL-13 and TGF-β are likely secreted as an attempt to counteract the effects of pro-inflammatory cytokines such as IL-1β, IL-6 and TNF-α. Likewise, age-associated gene expression changes result in the overexpression of immune response genes (de Magalhães, Curado and Church, 2009). Inflammageing is a risk factor for several chronic diseases, including cardiovascular disease, cancer, chronic kidney disease, diabetes, depression, dementia and more (Ferrucci and Fabbri, 2018).

Immunosenescence refers to the age-associated decline in the proficiency of the immune system, particularly adaptive immunity (Larbi *et al.*, 2008), thereby increasing the susceptibility of the elderly to pathogens. Lastly, the bystander effect refers to the ability of senescent cells to induce senescence in neighbouring cells via cell-cell contact (Nelson *et al.*, 2012).

1.2.2 Models of ageing

In vitro and *in vivo* models of ageing helped to elucidate the hallmarks of ageing (López-Otín *et al.*, 2013). *In vitro* models include cultured fibroblasts and yeast cells, among others (Sedelnikova *et al.*, 2004; Taormina *et al.*, 2019). *In vitro* models pose the advantage of generating personalised data as human fibroblasts can be used for experiments (Sedelnikova *et al.*, 2004). Likewise, yeast cells have a short generation time and genetic similarity with humans, are cheap to maintain, and are short-lived (Taormina *et al.*, 2019). However, *in vitro* models are less suitable for recapitulating cell-extrinsic factors influencing ageing, such as altered intercellular communication. Likewise, the mechanisms of ageing are likely different between tissues, meaning that results obtained from a certain cell type may not be reproducible in another.

In vivo models of ageing include invertebrates and vertebrate models. Invertebrate models include *C.elegans* and *Drosophila*; both are short-lived and have short generation times. *C.elegans* are hermaphrodites, so they can be in-bred by self-fertilisation, in addition to regular breeding. *C.elegans* are also transparent, allowing intravital cell tracking (Taormina *et al.*, 2019).

Although there is genetic similarity between *Drosophila* and humans, as well as shared organ systems (Taormina *et al.*, 2019), a risk of modelling ageing with *Drosophila*, as with other invertebrates is that certain mechanisms of ageing, such as cellular senescence and inflammageing, are vertebrate-specific (P. P. Singh *et al.*, 2019).

Vertebrates used to study ageing include mice and NHPs, among others. Like humans, these animals are mammals, suggesting reproducibility of results obtained from them in human clinical trials. However, these animals have long lifespans ranging from 3-20 years, as well as long generation times (Taormina *et al.*, 2019). Therefore, ageing studies would be considerably costly, as well as slow. Ethical issues also pose another challenge of modelling ageing using NHPs.

1.2.2.1 Mice as a model for ageing

Extensive research into the mechanisms underlying ageing has been conducted using the mouse model (Kõks *et al.*, 2016). A list of mouse models of ageing is provided below (**Table 1.5**).

Mouse model	**Phenotype**	**Age of onset**	**Model for Progeroid syndrome?**	**Reference**
Lmna^{HG}	Loss of subcutaneous fat, hair loss and osteoporosis	6-8 weeks	Yes, HGPS	(Yang *et al.*, 2005, 2008)
Lmna^{G609G}	Growth retardation, curvature in the spine, vascular calcification, infertility, decreased insulin-like growth factor levels	3 weeks	Yes, HGPS	(Osorio *et al.*, 2011; Villa-Bellosta *et al.*, 2013)
Zmpste24$^{-/-}$	Growth retardation, alopecia, muscle weakness, bone fractures, dilated cardiomyopathy, muscular dystrophy and lipodystrophy	6–8 weeks	Yes, HGPS	(Bergo *et al.*, 2002; Pendás *et al.*, 2002)
Wrn$^{-/-}$	Hypertriglyceridemia, insulin resistance, elevated levels ROS,	5 months	Yes, WS	(Lebel and Leder, 1998; Massip *et al.*, 2006)

	DNA damage and increased incidence of cancer			
Wrn$^{-/-}$;*Terc*$^{-/-}$	Shortening of telomeres, hair graying, alopecia, osteoporosis, type 2 diabetes, cataracts and cancer	Late-generation mice	Yes, WS	(Chang *et al.*, 2004)
PolG	Kyphosis, alopecia, anaemia, weight loss, reduced lifespan, sarcopenia, hearing loss, reduced fat mass and bone mineral density, cardiomyopathy,	Onset strain dependent (~25 weeks and ~9 months)	No	(Trifunovic *et al.*, 2004; Kujoth *et al.*, 2005; Vermulst *et al.*, 2008)
Klotho$^{-/-}$	Infertility, arteriosclerosis, skin atrophy, osteoporosis, hyperphosphataemia, emphysema, motor impairment, cognitive decline	4 weeks	No	(Kuro-o *et al.*, 1997; Nagai *et al.*, 2003)
Sirt1$^{-/-}$	Growth retardation, reduced lifespan	Embryonic	No	(Cheng *et al.*, 2003; Wang *et al.*, 2008)
Satb1$^{-/-}$	Growth retardation, reduced lifespan, defective T-cell development, autoimmunity	3 days	No	(Alvarez *et al.*, 2000; Kondo *et al.*, 2016)

Table 1.5. A list of multiple mouse models of ageing, their phenotypes, age of onset, whether or not these mice model human progeroid syndrome and references. *Modified from Kõks et al., (2016). HGPS, Hutchinson-Gilford progeria syndrome; PolG, DNA polymerase γ, Satb1, special AT-rich sequence-binding protein 1; Terc, telomerase RNA component; WS, Werner Syndrome; Zmpste24, zinc metallopeptidase ste24.*

HGPS is caused by sporadic, autosomal dominant mutations in the *LMNA* gene. *LMNA* encodes lamins A/C, which are components of the nuclear laminae. Nuclear laminae are important for cellular processes such as cell division, chromatin organisation, nuclear shape, DNA replication and transcription. The most common *LMNA* mutation found in HGPS is the C1824T mutation. Although this substitution does not induce a change in the encoded amino acid (Gly608Gly), it causes aberrant splicing in *LMNA* pre-mRNA, resulting in the translation of an aberrant protein called progerin, which lacks 50 amino acids near its C-terminus. The C1824T mutation deletes a farnesylated proteolytic cleavage site for zinc metallopeptidase STE24 (ZMPSTE24). Therefore, patients accumulate farnesylated progerin which causes structural changes to the nuclear envelope (Lamis *et al.*, 2022).

Mouse models of HGPS include *Lmna*^{HG} mice, *Lmna*^{G609G} mice and *Zmpste24*$^{-/-}$ mice (Bergo *et al.*, 2002; Pendás *et al.*, 2002; Yang *et al.*, 2005, 2008; Osorio *et al.*, 2011; Villa-Bellosta *et al.*, 2013). Both *Lmna*^{HG} and *Lmna*^{G609G} mice express progerin. However, *Lmna*^{HG} mice harbour a deletion of the last 150 nucleotides in exon 11 of *Lmna* while *Lmna*^{G609G} mice harbour a C1827T mutation (Gly609G) which is equivalent to the human C1824T mutation (Yang *et al.*, 2005, 2008; Osorio *et al.*, 2011; Villa-Bellosta *et al.*, 2013). *Zmpste24*$^{-/-}$ mice are deficient in *Zmpste24* and accumulate farnesylated prelamin A, the precursor to Lamin A (Bergo *et al.*, 2002; Pendás *et al.*, 2002).

WS is caused by null mutations in the *WRN* gene, which encodes WRN, an ATP-dependent DNA helicase that is part of the RECQ family of DNA helicases (David *et al.*, 2017). *Wrn*$^{-/-}$ mice were generated to model WS (Lebel and Leder, 1998; Massip *et al.*, 2006). However, only double-mutant mice lacking *Wrn* and *telomerase RNA component* (*Terc*) developed progeria similar to WS (Chang *et al.*, 2004).

Likewise, mice expressing proof-reading-deficient mtDNA Polγ display accelerated ageing (Trifunovic *et al.*, 2004; Kujoth *et al.*, 2005), as previously stated (**Section 1.2.1.1**). *Klotho*$^{-/-}$ mice, *Sirt1*$^{-/-}$ mice and *Satb1*$^{-/-}$ mice also display accelerated ageing and will be further discussed in chapters 3, 4 and 5 of this thesis. Henceforth, *Klotho*$^{-/-}$ mice, *Sirt1*$^{-/-}$ mice and *Satb1*$^{-/-}$ mice will be referred to as *Klotho* mutant mice, *Sirt1* mutant mice and *Satb1* mutant mice. Due to the expensive and time-consuming nature of ageing research in mice (Kõks *et al.*, 2016), it would be beneficial to develop another ageing model.

1.2.2.2 Zebrafish as a model for ageing

Zebrafish are another vertebrate model used to study ageing. Zebrafish research is affordable compared to other vertebrates. Likewise, zebrafish have short generation time and an average lifespan of approximately 3 years in laboratory conditions, making ageing studies feasible (Kishi *et al.*, 2009).

Also, zebrafish demonstrate age-related spinal curvature and age-related decline in motor function, like humans (Gerhard *et al.*, 2002; Gilbert, Zerulla and Tierney, 2013). Furthermore, age-related increased SA-β-Gal staining is observed in zebrafish (Kishi *et al.*, 2003).

In addition, zebrafish genetic models of ageing display accelerated ageing (Henriques *et al.*, 2013; A. P. Singh *et al.*, 2019; Ogura *et al.*, 2021), including a zebrafish line in the Bandmann laboratory. **Table 1.6** lists ageing-associated genes studied in this PhD, using stable zebrafish mutant lines.

Gene	Protein	Zebrafish mutant line published by another group?	Publication
KLOTHO	KLOTHO	Yes	(A. P. Singh *et al.*, 2019; Ogura *et al.*, 2021)
SIRT1	SIRT1	Yes	(Kim *et al.*, 2019)
SATB1	SATB1	Yes	(Thyme *et al.*, 2019)

Table 1.6. A list of ageing-associated genes modelled using zebrafish for the purpose of this PhD. *SATB1, special AT-rich sequence binding protein 1.*

Zebrafish models of *KLOTHO*, *SIRT1* and *SATB1* deficiency will be discussed in chapters 3, 4 and 5 of this thesis.

1.3 Shared mechanisms between ageing and PD

Mechanisms of ageing, such as mitochondrial dysfunction and inflammation increase the likelihood of dopaminergic neuron loss. Although dopaminergic neuron loss is accompanied by ageing, the rate of neurodegeneration in ageing cannot account for the dopaminergic neuron loss observed in PD. It is thought that genetic and environmental factors contribute to the increased risk of developing PD with age (Pang *et al.*, 2019).

Nigral neurons are preferentially susceptible to age-associated loss, with an estimated 9.8% decrease in SNpc dopaminergic neurons per decade (Ma *et al.*, 1999; Buchman *et al.*, 2012). Likewise, the highest age-associated accumulation of brain mtDNA deletion is found in the substantia nigra (Soong *et al.*, 1992). It was recently suggested that the deleterious effect of age-associated accumulation of nigral mtDNA deletion is rescued by an age-associated increase in mtDNA copy number (Dölle *et al.*, 2016). However, this is not supported by the age-associated decrease in nigral mitochondrial complex I activity, which causes oxidative damage (Venkateshappa *et al.*, 2012). There is also an age-associated increase in nigral neuroinflammation (Venkateshappa *et al.*, 2012).

ROS generation damages mtDNA and promotes further ROS generation (Schapira *et al.*, 1989; Van Houten, Woshner and Santos, 2006). ROS-induced neuronal damage also leads to the secretion of microglial-activation factors (Langston *et al.*, 1999; Podbielska *et al.*, 2016). Activated microglia then secrete pro-inflammatory factors which further damage neurons (Podbielska *et al.*, 2016).

The pro-inflammatory phenotype generated by inflammageing (Csiszar *et al.*, 2003; Ferrucci and Fabbri, 2018), as well as the secretion of SASP factors by senescent cells (Di Micco *et al.*, 2020) could also increase neuronal damage. The bystander effect (Nelson *et al.*, 2012), coupled with immunosenescence (Larbi *et al.*, 2008) would in theory, contribute to increased neuronal damage. Furthermore, age-associated epigenetic changes promoting the expression of immune response genes (de Magalhães, Curado and Church, 2009) could worsen the previously mentioned neuronal damage.

There is an age-associated increase in nigral α-Synuclein expression that is accompanied by a decrease in nigral dopaminergic neurons containing α-Synuclein. However, α-Synuclein expressed in aged substantia nigra is not aggregated like that found in PD patients (Chu and Kordower, 2007). Regardless, age-associated loss of proteostasis (Pahlavani *et al.*, 1995; Ferrington, Husom and Thompson, 2005; Moreno-García *et al.*, 2018) could be involved in protein aggregation in PD.

These shared mechanisms between ageing and PD, together with ageing being the major risk factor for developing PD (Pang *et al.*, 2019) are plausible reasons to investigate the interplay between ageing and PD.

1.4 Aim, Hypothesis and Objectives

1.4.1 Aim

The aim of this PhD is to study the interplay between mechanisms linked to ageing and PD, using the zebrafish model.

1.4.2 Hypothesis

The underlying hypothesis is that PD-relevant pathological mechanisms will be enhanced by mechanisms of ageing, namely mitochondrial dysfunction and inflammation.

1.4.3 Objectives

The main objectives of this PhD were:

1. **To further validate the zebrafish as an effective model for ageing (chapters 3-5).**

   Zebrafish mutant lines harbouring mutations in ageing-associated genes, namely the *klotho*$^{-/-}$ (generated by Dr Marcus Keatinge), *sirt1*$^{-/-}$, *satb1a*$^{-/-}$, *satb1b*$^{-/-}$ and *satb1a*$^{-/-}$;*satb1b*$^{-/-}$ lines were investigated for accelerated ageing, by monitoring zebrafish viability, morphology, morbidity and mortality.

2. **To characterise zebrafish models of ageing for PD-relevant pathological mechanisms (chapters 3-5).**

   The *klotho*$^{-/-}$, *sirt1*$^{-/-}$, *satb1a*$^{-/-}$ and *satb1b*$^{-/-}$ lines were assessed for PD-relevant pathological mechanisms such as loss of dopaminergic neurons, mitochondrial function, inflammation and DNA damage. Microglial activation was also investigated in larvae treated with a sirt1-specific chemical inhibitor.

3. **To characterise a novel zebrafish line expressing human WT α-Synuclein; the Tg(*eno2*:hsa.*SNCA*-ires-EGFP) line (chapters 3 and 4).**

   To investigate a potential pathological effect of human WT α-Synuclein expression in zebrafish, motor function and microglial activation of Tg(*eno2*:hsa.*SNCA*-ires-EGFP) larvae were assessed.

4. **To investigate the effect of accelerated ageing on PD-relevant pathological mechanisms, using the zebrafish model (chapters 3 and 4).**

   Microglial activation was investigated in Tg(*eno2*:hsa.*SNCA*-ires-EGFP);*klotho*$^{+/+}$ and Tg(*eno2*:hsa.*SNCA*-ires-EGFP);*klotho*$^{-/-}$ larvae. Likewise, motor function and cell death were investigated using untreated and sirt1-inhibited Tg(*eno2*:hsa.*SNCA*-ires-EGFP) larvae.

Chapter 2: Materials and methods

Unless stated otherwise, all restriction enzymes were obtained from New England Biolabs (NEB), all primers were designed using the online Primer3Plus tool (https://www.primer3plus.com/) and supplied by Integrated DNA Technologies (IDT) Ltd.

2.1 Zebrafish

2.1.1 Zebrafish husbandry

Experiments detailed in this thesis utilised zebrafish housed either at the University of Sheffield (Bateson Centre) or the University of Pittsburgh.

The aquarium at the University of Sheffield uses a semi-closed system with approximately 10% entry of fresh water per 24-hour period. This system operates on a 14-hour light 10-hour dark cycle with a stocking density of no more than 60 fish per tank. Both adults and larvae were kept at 28^{o}C.

All experiments at the University of Sheffield were performed in accordance with the Animals (Scientific Procedures) Act 1986 under the Project Licence of Professor Oliver Bandmann (70/8437) and the Personal Licence of Oluwaseyi Pearce (I22289923).

The aquarium at the University of Pittsburgh uses a similar system to that at the University of Sheffield. All experiments at the University of Pittsburgh were performed with approval from the University of Pittsburgh Institutional Animal Care and Use Committee (IACUC), in accordance with the NIH *Guide for the Care and Use of Laboratory Animals*. Unless stated otherwise, experiments were performed at the University of Sheffield.

2.1.2 Zebrafish lines

Unless stated otherwise, WT zebrafish were obtained from the AB strain and zebrafish lines were generated using CRISPR/Cas9 gene editing. Mutant zebrafish lines were maintained as heterozygous colonies. With the exception of mutant lines crossed with the Tg(*eno2*:hsa.*SNCA*-ires-EGFP) line, homozygous mutant embryos were obtained by in-crossing heterozygous mutant adults, with age-matched WT siblings serving as control. All mutant zebrafish lines were viable to adulthood.

2.1.2.1 klotho$^{-/-}$ line

The *klotho*$^{-/-}$ line harbours a loss-of-function mutation in the *klotho* gene. The *klotho*$^{-/-}$ allele has a 10bp deletion of TCTCACTGGA in exon 2 of *klotho* and can be genotyped by digesting polymerase chain reaction (PCR) products with BsrI (**Sections 2.2.2 and 2.2.3**). The 10bp deletion creates a premature stop codon (TAA) immediately after 855bp and the predicted protein is truncated within its kl1 domain

(**Section 3.2.1**). The *klotho*$^{-/-}$ line was utilised for experiments at the University of Sheffield only. As previously stated (**Section 1.4.3**), the *klotho*$^{-/-}$ line was generated by Dr Marcus Keatinge.

2.1.2.2 *sirt1*$^{-/-}$ line

The *sirt1*$^{-/-}$ line was generated using the following gRNA sequence targeting exon 1 of *sirt1*; TGGACGAGAAACCGGCGCGGA, which was obtained from Kim *et al.*, (2019). The *sirt1*$^{-/-}$ allele has a 10bp deletion of CGGATGGACG in exon 1 and can be genotyped by digesting PCR products with BccI. This mutation creates a premature stop codon (TAA) immediately after 234bp and the predicted truncated protein lacks its conserved catalytic domain. The *sirt1*$^{-/-}$ line was utilised for experiments at the University of Sheffield only. Further details concerning the generation of the *sirt1*$^{-/-}$ line are provided below (**Sections 2.3.4.2 and 4.2.3**).

2.1.2.3 *satb1a*$^{-/-}$ and *satb1b*$^{-/-}$ lines

The *satb1a*$^{-/-}$ line was generated using the following gRNA sequence targeting exon 7 of *satb1a*; GTAAATTTCAGGTGACACGT. The *satb1a*$^{-/-}$ allele has an 11bp deletion of GACGTGTCACC in exon 7 and can be genotyped by digesting PCR products with MslI. This 11bp deletion creates a premature stop codon (TGA) immediately after 987bp and the predicted protein is truncated within its CUT1 domain. The *satb1a*$^{-/-}$ line was utilised for experiments at the University of Sheffield only. Further details concerning the generation of the *satb1a*$^{-/-}$ line are provided below (**Sections 2.3.4.1 and 5.2.4**).

The *satb1b*$^{-/-}$ line was generated using the following gRNA sequence targeting exon 5; TGTCCGCCGACATCTACCAG. The *satb1b*$^{-/-}$ allele contains a 4bp deletion of TACC in exon 5 and can be genotyped by digesting PCR products with BsrI. This 4bp deletion induces a premature stop codon (TGA) immediately 1113bp and the predicted protein is truncated within its CUT1 domain. The *satb1b*$^{-/-}$ line was used for experiments at the University of Sheffield only. Further details concerning the generation of the *satb1b*$^{-/-}$ line are provided below (**Sections 2.3.4.1 and 5.2.5**).

To investigate double-mutant zebrafish, the *satb1a*$^{+/-}$ line was crossed with the *satb1b*$^{+/-}$ line and offspring were genotyped for each allele to identify *satb1a*$^{+/-}$;*satb1b*$^{+/-}$ zebrafish. The *satb1a*$^{+/-}$;*satb1b*$^{+/-}$ line was utilised for further studies at the University of Sheffield only.

2.1.2.4 *Tg(eno2:hsa.SNCA-ires-EGFP)* line

This line expresses human WT α-Synuclein under the neuronal *enolase 2* (*eno2*) promoter. IRES technology was utilised to simultaneously express human WT α-Synuclein and green fluorescent protein (GFP). The construct is [12kb *eno2* promoter]:[human *SNCA*]-[IRES]-[GFP]-[PolyA] and its insertion site is unknown. Human WT *SNCA* cDNA was inserted in frame at the ATG codon in exon 2 of *eno2*, exon 1 is not translated (**Figure 2.1A**). This line was generated in the Burton laboratory at the

University of Pittsburgh, using I-Sce1 meganuclease-mediated transgenesis and the transgene is inherited in a homozygous dominant fashion (**data not published**).

Internal ribosome entry site (IRES) technology enables co-expression of human WT α-Synuclein and GFP, allowing selection of Tg embryos by GFP sorting in the caudal fin at 2dpf or the pectoral fin at 8dpf (**Figure 2.1B**). Human α-Synuclein expression was confirmed in the CNS of adult Tg(*eno2*:hsa.*SNCA*-ires-EGFP) zebrafish, indicating sustained α-Synuclein expression (**Figure 2.1C**). The *eno2* promoter was previously characterised and used to generate a Tg zebrafish model of tauopathy (Bai *et al.*, 2007).

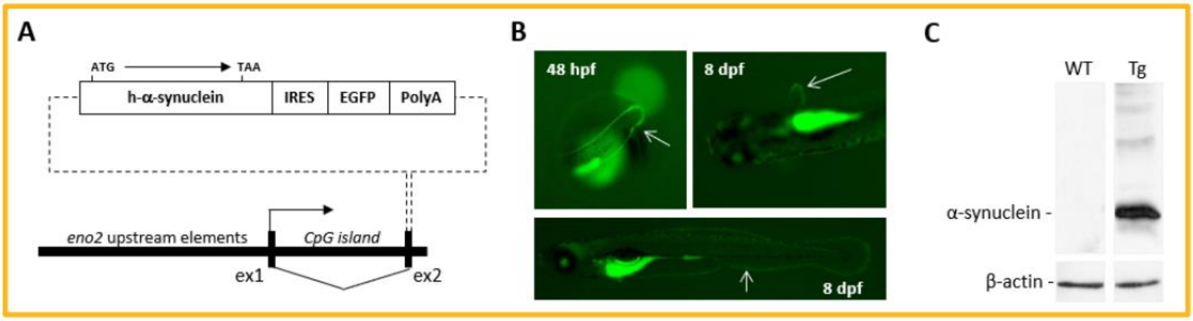

Figure 2.1. Generation and characterisation of the Tg(eno2:hsa.SNCA-ires-EGFP) zebrafish line. *The Tg(eno2:hsa.SNCA-ires-EGFP) zebrafish line expresses human WT α-Synuclein under the neuronal eno2 promoter. IRES technology was utilised to co-express human WT α-Synuclein and GFP. The construct is [12kb eno2 promoter]:[human SNCA]-[IRES]-[GFP]-[PolyA] and its genomic insertion site is unknown. Human WT SNCA cDNA was inserted in frame at the ATG codon in exon 2 of eno2; exon 1 is not translated (A). This line was generated using I-Sce1 meganuclease-mediated transgenesis and the transgene is inherited in a homozygous dominant fashion. Tg embryos can be sorted for GFP expression in the caudal fin at 48hpf, or the pectoral and caudal fins at 8dpf (B). Expression of human α-Synuclein in the Tg(eno2:hsa.SNCA-ires-EGFP) zebrafish line was confirmed in the adult CNS, using a western blot (C). Data is unpublished and was generated by Dr Qing Bai. Figure was obtained from the Burton laboratory. eno2, enolase 2; GFP, green fluorescent protein; IRES, internal ribosome entry site; Tg, transgenic; WT, wildtype.*

Adult monoallelic Tg(*eno2*:hsa.*SNCA*-ires-EGFP) zebrafish were out-crossed for experiments. Tg embryos and non-transgenic (Non-Tg) siblings were identified by sorting embryos for GFP expression (**Section 2.1.7**) in the caudal fin at 2dpf. Alternatively, Tg offspring were identified by PCR, using primers which amplify human *SNCA* (**Section 3.2.6**). The Tg(*eno2*:hsa.*SNCA*-ires-EGFP) line was supplied by the Burton laboratory and utilised for experiments both at the University of Sheffield and the University of Pittsburgh.

2.1.2.5 Tg(eno2:hsa.SNCA-ires-EGFP);klotho$^{-/-}$ *line*

This line was obtained by crossing adult monoallelic Tg(*eno2*:hsa.*SNCA*-ires-EGFP) zebrafish with adult *klotho*$^{-/-}$ zebrafish. Offspring were sorted for GFP expression at 2dpf and GFP-positive offspring were raised to adulthood, thereby establishing a Tg(*eno2*:hsa.*SNCA*-ires-EGFP);*klotho*$^{+/-}$ colony.

Adult Tg(*eno2*:hsa.*SNCA*-ires-EGFP);*klotho*$^{+/-}$ zebrafish were crossed with adult *klotho*$^{+/-}$ zebrafish and offspring were utilised in subsequent experiments where they were genotyped for both *SNCA* and *klotho* to identify Tg(*eno2*:hsa.*SNCA*-ires-EGFP);*klotho*$^{+/+}$, Tg(*eno2*:hsa.*SNCA*-ires-EGFP);*klotho*$^{-/-}$, Non-Tg;*klotho*$^{+/+}$ and Non-Tg;*klotho*$^{-/-}$ offspring.

For the purpose of this thesis, Tg(*eno2*:hsa.*SNCA*-ires-EGFP);*klotho*$^{+/+}$ zebrafish and Tg(*eno2*:hsa.*SNCA*-ires-EGFP);*klotho*$^{-/-}$ zebrafish will be referred to as Tg;*klotho*$^{+/+}$ zebrafish and Tg;*klotho*$^{-/-}$ zebrafish, respectively. The Tg;*klotho*$^{-/-}$ line was utilised for experiments at the University of Sheffield only.

2.1.2.6 Tg(eno2:hsa.SNCA-ires-EGFP);sirt1$^{-/-}$ line

This line was obtained by crossing adult monoallelic Tg(*eno2*:hsa.*SNCA*-ires-EGFP) zebrafish with adult *sirt1*$^{+/-}$ zebrafish. Offspring were sorted for GFP expression at 2dpf. GFP-positive offspring were raised to adulthood, and adult zebrafish were genotyped for the *sirt1* allele, thereby establishing a Tg(*eno2*:hsa.*SNCA*-ires-EGFP);*sirt1*$^{+/-}$ colony.

Adult Tg(*eno2*:hsa.*SNCA*-ires-EGFP);*sirt1*$^{+/-}$ zebrafish were crossed with adult *sirt1*$^{+/-}$ zebrafish and offspring were utilised in a subsequent experiment where they were genotyped for both *SNCA* and *sirt1* to identify Tg(*eno2*:hsa.*SNCA*-ires-EGFP);*sirt1*$^{+/+}$, Tg(*eno2*:hsa.*SNCA*-ires-EGFP);*sirt1*$^{-/-}$, Non-Tg;*sirt1*$^{+/+}$ and Non-Tg;*sirt1*$^{-/-}$ offspring.

For the purpose of this thesis, Tg(*eno2*:hsa.*SNCA*-ires-EGFP);*sirt1*$^{+/+}$ zebrafish and Tg(*eno2*:hsa.*SNCA*-ires-EGFP);*sirt1*$^{-/-}$ zebrafish will be referred to as Tg;*sirt1*$^{+/+}$ zebrafish and Tg;*sirt1*$^{-/-}$ zebrafish, respectively. The Tg;*sirt1*$^{-/-}$ line was utilised for experiments at the University of Sheffield only.

2.1.2.7 Tg(mpeg1:EGFP) line

This line fluorescently labels macrophages; this is because GFP expression is under the control of the macrophage-specific *mpeg1* promoter. The Tg(*mpeg1*:EGFP) zebrafish line was generated by Ellett *et al.*, (2011), using Tol2-mediated recombination. Adult Tg Tg(*mpeg1*:EGFP) zebrafish were out-crossed with Casper zebrafish. Tg offspring were identified by sorting 2dpf embryos for GFP expression in the head and yolk sac. The Tg(*mpeg1*:EGFP) line was utilised for experiments at the University of Pittsburgh only.

2.1.3 Zebrafish mating

Mating tanks were utilised, as follows:

On the evening before spawning, adult male and female zebrafish were placed in tanks filled with system water and were separated by a divider. Mating tanks contained an insert with a gridded bottom which eggs fall through after laying; thereby preventing ingestion of eggs by zebrafish. The insert did not prevent fertilisation of eggs by male zebrafish. Zebrafish were left in tanks overnight (o/n) and spawning was stimulated on the following morning by the initiation of the aquarium light cycle. Use of mating tanks meant that spawning was dictated by the removal of dividers from mating tanks, allowing for protocols such as micro-injection into one-cell stage embryos. Also, the use of mating tanks allowed for the collection of clutches of embryos from multiple pairs of zebrafish at a given time.

2.1.4 Embryo collection and maintenance

Embryos were collected from mating tanks with a tea-strainer and transferred to a clean 9 cm petri-dish, using a wash-bottle containing system water. System water was replaced with ~40.0 ml 1X E3 media (500.0 µM NaCl, 17.0 µM KCl, 33.0 µM $CaCl_2$ and 33.0 µM MgSO4, 1 drop per litre methylene blue antifungal agent) and embryos were incubated at 28°C with a maximum density of 60 embryos per petri-dish at the University of Sheffield, and 30 embryos per petri-dish at the University of Pittsburgh. At 8hpf, dead and unfertilised embryos were discarded. Unless stated otherwise, 1X E3 media utilised in this PhD contained methylene blue.

2.1.5 Depigmentation

At 8hpf, 12.0 µl phenylthiourea (PTU) (0.50 M) was added to ~40.0 ml 1X E3 media containing embryos, giving a final concentration of 0.15 mM. PTU was administered to prevent pigment formation and embryos were treated with PTU ahead of fixation (**Section 2.1.9**).

2.1.6 Bleaching

To prevent a potential spread of pathogens, embryos obtained from quarantined zebrafish were bleached at 24hpf by 2x successive 5 minute incubations in 10% bleach (sodium hypochlorite), system water. Embryos were agitated for the first minute of both bleach incubations, to ensure the removal of parasites from chorions, if present. After bleaching, embryos were transferred to a new petri-dish with fresh ~40.0 ml 1X E3 media, then returned to a 28°C incubator.

2.1.7 Sorting for GFP expression

2dpf embryos were sorted for GFP expression using either the Leica M165 FC microscope at the University of Sheffield or the Olympus MVX-10 zoom stereoscope at the University of Pittsburgh.

2.1.8 Dechorionation

Chorions were removed manually, using two pairs of forceps. Both pairs were used to pull the chorion apart from opposite ends, releasing the embryo/larva within. Embryos/larvae which were dechorionated include, embryos bleached at 24hpf (**Section 2.1.6**), embryos used in drug treatment experiments (**Section 2.10**) and 3dpf larvae genotyped using tail clips (**Section 2.2.1.2**).

2.1.9 Fixation

Larvae were transferred from petri-dishes to 2.0 ml microcentrifuge tubes at a maximum density of 20 larvae per tube. 1X E3 media was replaced with 4% paraformaldehyde (PFA) in phosphate buffered saline (PBS) and larvae were incubated for 2 hours at room temperature (RT). Next were 2x 5 minute 1X phosphate buffered saline with 0.1% Tween-20 (PBT) washes followed by a 15 minute incubation in 100% methanol (MeOH). This last solution was replaced with fresh 100% MeOH and larvae were stored at -20°C. Fixation was required ahead of whole-mount in-situ hybridisation (WISH) (**Section 2.11**) and whole-mount immunohistochemistry (IHC) (**Section 2.12.1**).

2.1.10 Anaesthesia and culling

Tricaine (MS-222) was available at a stock concentration of 0.4% in deionised water. Larvae were anaesthetised in petri-dishes by immersion in tricaine solution (~40.0 ml 1X E3 media + 1.0 ml tricaine) while adult zebrafish were anaesthetised in beakers containing 95.8 ml system water + 4.2 ml tricaine. Larvae under 5.2dpf were culled by disposal in bleach while larvae over 5.2dpf were culled in accordance with schedule 1 methods using an overdose of tricaine (30.0 ml tricaine per 100.0 ml 1X E3 media), with cessation of circulation serving as confirmation of death. Adult zebrafish were also culled using an overdose of tricaine (30.0 ml tricaine per 100.0 ml system water). Destruction of the brain served as confirmation of death for zebrafish not needed for brain extraction (**Section 2.1.11**).

2.1.11 Adult brain extraction

Adult zebrafish were overdosed with tricaine one at a time. Once the absence of gill movement and loss of stimulus-evoked movement were observed, adult zebrafish were placed on a flat surface and decapitated, using a scalpel with a clean blade (in line with regulated procedures). The decapitated head was transferred to a petri-dish under a dissecting microscope (Leica). A pair of forceps was used to expose and extract the brain. Zebrafish brains and bodies were transferred into separate clean 1.5 ml microcentrifuge tubes and stored in dry ice until transfer to a -80°C freezer. Brain extraction was done in a timely manner to prevent tissue degradation.

2.2 Zebrafish genotyping

2.2.1 Genomic DNA extraction

To determine the genotype of zebrafish, biological samples were obtained as detailed below (**Sections 2.2.1.1, 2.2.1.2 and 2.2.1.3**). Genomic DNA was extracted from each type of biological sample by boiling in sodium hydroxide (NaOH) (50.0 mM) at 98°C for 10 minutes. After boiling, the solution was vortexed, then one-tenth volume of Tris pH 8.0 was added to the NaOH solution, followed by another vortex.

2.2.1.1 From whole embryos/larvae

Whole embryos/larvae were transferred from a petri-dish to wells of a 96-well PCR plate (StarLab UK) with one embryo per well. 1X E3 media was removed from wells and replaced with 100.0 µl NaOH for genomic DNA extraction.

2.2.1.2 From larval tail clips

Wilkinson *et al.*, (2013)'s protocol was followed. 3dpf larvae were anaesthetised (**Section 2.1.10**) then transferred to the flat surface of a petri-dish reinforced by four layers of white-labelled laboratory tape. Under a dissecting microscope (Leica), tails of anaesthetised larvae were cut distal to circulating blood using a clean scalpel (**Figure 2.2**). Tail clips were collected using 2.0 µl of 1X E3 media and pipetted into wells of a 96-well PCR plate, each containing 20.0 µl NaOH. Following clipping, anaesthetised larvae were transferred to corresponding wells of a 96-well plate (Greiner) containing 400.0 µl 1X E3 media for recovery from anaesthesia and larvae were sorted accordingly after genotyping.

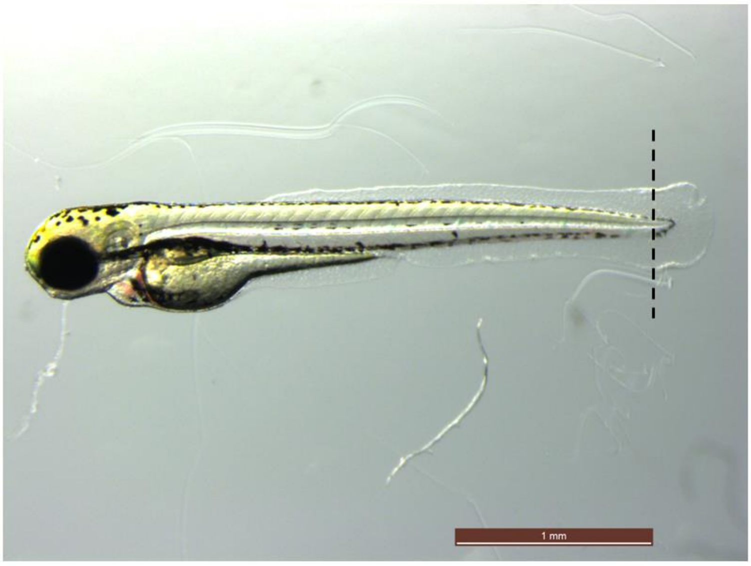

Figure 2.2. Tail clipping of 3dpf larvae. *Tails of 3dpf larvae were clipped distal to circulating blood and DNA was extracted from tail clips for genotyping purposes. dpf, days post fertilisation.*

2.2.1.3 From adult fin clips

Adult fin clipping followed Home Office guidelines and fin clips were transferred to wells of a 96-well plate containing 100.0 µl NaOH. Adult zebrafish were transferred to corresponding grids (FishGridPool) and zebrafish were sorted accordingly after genotyping.

2.2.2 PCR

PCR is a technique used to rapidly amplify a specific DNA sequence. A PCR reaction requires template DNA, a pair of single-stranded DNA molecules called primers, nucleotides, a temperature-resistant DNA polymerase and a thermal cycler to run the PCR reaction.

A PCR reaction involves 3 stages, namely, denaturation, annealing and elongation stages. During denaturation, double-stranded DNA is separated into single strands. Next, the temperature is reduced for the annealing stage where forward and reverse primers bind to specific DNA sequences. Next, the temperature is increased for the elongation phase which is where DNA polymerase binds the primer-DNA hybrid and synthesises a complementary DNA strand. These 3 stages are repeated for multiple cycles, producing several copies of a specific DNA sequence.

Once supplied, primers were resuspended to a 100.0 µM working concentration, using ultrapure deionised water (Milli-Q (MQ)). The optimum annealing temperature of primers was determined by running a gradient PCR reaction with annealing temperatures ranging from 55-65^{o}C as follows:

Per 10.0 µl reaction, PCR mix contained 0.1 µl forward primer, 0.1 µl reverse primer, either 5.0 µl Biomix Red (2X) or 2.0 µl FirePol Green (5X) and MQ to 9.0 µl. 9.0 µl PCR mix was added to wells of a 96-well PCR plate, then 1.0 µl DNA was added to the PCR mix. PCR plates were sealed then placed in a thermal cycler (Labnet Multigene Optimax) for the following reaction:

1. 94^{o}C for 5 minutes
2. 94^{o}C for 30 seconds
3. 55-65^{o}C for 30 seconds
4. 72^{o}C for 30 seconds
5. GOTO step 2, 39x
6. 72^{o}C for 10 minutes
7. 4^{o}C for infinity

Subsequent PCR reactions were run using the optimised annealing temperature, which often confirmed *in silico* data obtained from Primer3Plus. PCR master mixes were prepared for reactions involving multiple DNA samples. A list of genotyping primers used in this PhD is provided below (**Table 2.1**).

Gene	Forward primer (5’-3’)	Reverse primer (5’-3’)
klotho	CCTGGCACCTGTATGACGAG	CGTTCACATACGCGCTCTC
sirt1	GGCGGACGGCGAAAATAAAC	CCCGGGTTCAGTCGGTCTA
satb1a	CAGCCCTCTTCTTCCAGTCA	TCCTGTTAATGGCCACTCGT
satb1b	TCCTGTTAATGGCCACTCGT	GTCTTCAGGAACAGGCTTGG
SNCA	GTGGCTGCTGCTGAGAAAAC	TGCTCCCTCCACTGTCTTCT

Table 2.1. A list of genotyping primers used in this PhD.

2.2.3 Restriction digest

Restriction digest was used to genotype zebrafish lines, as well as to determine the efficiency of CRISPR/Cas9 gene editing (**Section 2.3**).

The enzyme of interest was diluted 1:1 using MQ. 1.0 µl diluted enzyme was added to 4.0 µl PCR product and the restriction digest mixture was incubated at the appropriate temperature for 2 hours and 30 minutes in a thermal cycler (**Table 2.2**).

Enzyme	Zebrafish line	Incubation temperature (°C)
BccI	*sirt1*$^{-/-}$	37
BsrI	*klotho*$^{-/-}$ and *satb1b*$^{-/-}$	65
MslI	*satb1a*$^{-/-}$	37

Table 2.2. A list of enzymes used to genotype the different zebrafish lines used in this PhD, and their incubation temperatures.

2.2.4 Gel electrophoresis

Gel electrophoresis is a technique used to separate DNA, RNA and proteins according to molecular size. Under an electric current, molecules migrate through the pores of a gel, with smaller molecules migrating further through the gel than larger molecules. A ladder which contains markers of known molecular size is included to determine the molecular size of samples.

PCR and restriction digest products were visualised using DNA gel electrophoresis. Mass of agarose powder (Appleton Woods) and volume of 1X Tris-acetate-EDTA (TAE) buffer (Lonza Bioscience) differed depending on the desired gel concentration. Agarose solution was heated till boiling and mixed at intervals until agarose was fully dissolved. Molten agarose was cooled under running tap water, then 1 drop of ethidium bromide (EtBr) (Insight Biotechnology) per 50.0 ml 1X TAE buffer was added to molten agarose and mixed carefully. Molten agarose was then poured into a gel mould with combs.

After the gel had set, combs were removed and depressions made by combs served as DNA-loading wells. The gel was transferred into an electrophoresis tank (GeneFlow) containing fresh 1X TAE buffer. 1.5 µl ladder (Hyperladder Bioline) was added into the first and last wells, as a size reference. This was followed by loading 3.0 µl PCR and/or 5.0 µl restriction digest products. Samples were electrophoresed at 150 volts for 30 minutes. DNA bands were visualised under UV light using the BioDoc-It Imaging System.

2.3 CRISPR/Cas9 gene editing

CRISPR/Cas9 gene editing was previously explained (**Section 1.1.9.1.1**).

2.3.1 gRNA design

DNA sequences of target genes were downloaded from Ensembl genome browser (https://www.ensembl.org/index.html) and gRNAs were designed using SnapGene Software, being careful to ensure that the Cas9 cut site overlapped a restriction enzyme site. Thereby, gRNA efficiency was inferred from restriction digest efficiency in CRISPR-injected embryos.

2.3.2 Preparation of CRISPR mix

CRISPR mix constituted 1.0 µl tracrRNA (20.0 µM) (Sigma-Aldrich), 1.0 µl crRNA (20.0 µM) (Sigma-Aldrich), 1.0 µl Cas9 protein (7.0 µM) (NEB), 0.3 µl phenol red (0.5%) (Sigma-Aldrich) and 0.7 µl nuclease-free water. While testing gRNA efficiency, no more than 4 crRNAs were included in the same CRISPR mix for micro-injection. However, once highly efficient gRNAs were identified, only 1 crRNA was included per CRISPR mix.

2.3.3 Micro-injection of CRISPR mix

Needles were pulled from borosilicate glass capillaries (Kwik-Fil, World Precision Instruments, Inc., Hertfordshire, UK), using a micropipette puller (Model P-97, Sutter Instrument Co., USA) and CRISPR mix was loaded into needles, using a gel-loading pipette tip. The needle was inserted into the injection rig of a pneumatic picopump (World Precision Instruments) then lowered to a 45° angle. The tip of the needle was broken using a pair of tweezers and the injection volume was determined as follows:

The needle was placed over the surface of an oil-covered graticule (Pyser) and the pedal connected to the pneumatic pump was tapped, thereby ejecting a volume of CRISPR mix which was monitored under a microscope (Leica). The ejection pressure was adjusted until a single tap of the pedal ejected

0.5 nl CRISPR mix. 1.0 nl CRISPR mix was micro-injected into one-cell stage embryos by tapping the pedal twice.

2.3.4 Determination of gRNA efficiency

Determination of gRNA efficiency is important for assessing gRNA mutagenic ability as well as the germline transmission efficiency of CRISPR-injected zebrafish.

2.3.4.1 Restriction Fragment Length Polymorphism

DNA was extracted from individual embryos (4 uninjected and 8 CRISPR-injected) at 24hpf (**Section 2.2.1.1**). DNA samples were amplified using PCR (**Section 2.2.2**) and PCR products were digested (**Section 2.2.3**). PCR and restriction digest products of uninjected embryos, as well as restriction digest products of CRISPR-injected embryos were electrophoresed (**Section 2.2.4**) and gRNA efficiency was determined by visually assessing the intensities of undigested and digested bands of CRISPR-injected embryos.

Efficiencies of gRNAs targeting *satb1a* and *satb1b* are provided below (**Tables 2.3 and 2.4**). Due to poor digestion of PCR products obtained from both uninjected and CRISPR-injected embryos, efficiencies of the following gRNAs could not be determined, *satb1a* exon 3b, *satb1a* exon 7b and *satb1b* exon 2a. Likewise, gRNA efficiency of *satb1a* exon 5 was not investigated as poor restriction digestion with MwoI was previously observed.

gRNA name	**gRNA sequence (5'-3')**	**gRNA efficiency**	**Overlapping restriction enzyme site**	**Forward primer (5'-3')**	**Reverse primer (5'-3')**
satb1a exon 3	GCGATGTCCCACCATCCGAA	Medium	BslI	AGAGATCTGCCTGTACCTGG	GCTGCGGTGTGTGTGTATC
satb1a exon 3a	ACCGCTTCCCTTCGGATGGT	Medium	BccI		
satb1a exon 3b	ACCATCCGAAGGGAAGCGGT	Undetermined	MwoI		
satb1a exon 5	GAATGAGTCCATTGCTCAGC	Undetermined	MwoI	GTTGGCCATTGGAACCCTG	GCCAATGTGCTCTGATTCATCT
satb1a exon 6	GATGTCAAGAGTTCGGCCAG	Medium	BsrI	CATCAGTGGTAAACGGCACTT	CCTGTATTGTCAAAATTACATCCAT

satb1a exon 7	GGTGTTGTCCAGATGCAGGC	Zero	XcmI	CAGCCCTCTTCTTCCAGTCA	TCCTGTTAATGGCCACTCGT
satb1a exon 7a	GTAAATTTCAGGTGACACGT	High	MslI		
satb1a exon 7b	TCAGCTCCTCGCGCACCCAG	Undetermined	DraIII		

Table 2.3. A list of gRNAs targeting satb1a, respective gRNA efficiencies, as well as the restriction enzymes and genotyping primers used to determine gRNA efficiency. *gRNA, guide RNA.*

gRNA name	**gRNA sequence (5'-3')**	**gRNA efficiency**	**Overlapping restriction enzyme site**	**Forward primer (5'-3')**	**Reverse primer (5'-3')**
satb1b exon 2	CTTCAACCAGCTCATCGAGA	Low	MslI	GCTCAAGTGTTAAGCCTGCTG	CCTCTTTCCTTTCGACGTGC
satb1b exon 2a	CTCGCACAGTTCAGCCGCAC	Undetermined	MwoI		
satb1b exon 4	ATGTCCCTTATCACAGGTGC	Medium	AlwNI	GACCTTCCTCCAGAGCAGTG	ACTGCTGCAAGAGCATCAAA
satb1b exon 5	TCGCACGCGTGGCCTTCAAC	Low	EcoNI	TCAACCAGCAGTACGCAGTC	GTCTTCAGGAACAGGCTTGG
satb1b exon 5a	TGTCCGCCGACATCTACCAG	High	BsrI		
satb1b exon 6	GAAAGAGGAAGACCCCAAAA	Medium	BslI	AGGGTCCATTGTTGCACTTGA	GCATGTGCAAGTGTGTTTTCC
satb1b exon 6a	TTGACTGCAGCCTCAGCCAT	Medium	BtgI		

Table 2.4. A list of gRNAs targeting satb1b, respective gRNA efficiencies, as well as the restriction enzymes and genotyping primers used to determine gRNA efficiency. *gRNA, guide RNA.*

2.3.4.2 CRISPR-Somatic Tissue Activity Test

CRISPR-Somatic Tissue Activity Test (CRISPR-STAT), published by Carrington *et al.*, (2015), was employed to determine the efficiency of the gRNA published by Kim *et al.*, (2019) which targets exon 1 of *sirt1* (TGGACGAGAAACCGGCGCGGA). gRNA efficiency could not be determined using restriction fragment length polymorphism (RFLP) because the Cas9 cut site does not overlap any suitable restriction enzyme site. CRISPR-STAT, including analysis was conducted by Dr Heba Ismail.

CRISPR-STAT determines gRNA efficiency by comparing peak profiles of fluorescent PCR products. Genotyping primers published by Kim *et al.*, (2019) were used for CRISPR-STAT. The forward primer was tagged with an M13F-adapter (5'-TGTAAAACGACGGCCAGT-3') while the reverse primer was tagged with a PIGtail adapter (5'-GTGTCTT-3') (**Table 2.5**).

Forward primer (5'-3')	**Reverse primer (5'-3')**
TGTAAAACGACGGCCAGTCGAAAATAAACGGGCCGAA	AGATCTCGGGCTCCGGGTC**GTGTCTT**

Table 2.5. M13F-tagged forward and PIGtail-tagged reverse sirt1 genotyping primers used to determine gRNA efficiency. *Primer sequences were obtained from Kim et al., (2019). M13F and PIGtail tags are bolded. gRNA; guide RNA.*

6.0 µl of a 3 primer mix containing equimolar ratios of the M13F-tagged forward primer, the PIGtail-tagged reverse primer and fluorescently labelled M13F (M13F-FAM) was added to 100.0 µl of PCR mix containing $MgCl_2$, AmpliTaq-Gold, buffer, dNTPs and MQ to prepare "PCR brew". 5.0 µl PCR brew was added to separate wells of a 96-well PCR plate (StarLab UK). DNA samples extracted from 8 uninjected and 8 CRISPR-injected embryos at 24hpf (**Section 2.2.1.1**) were diluted 1:10 using MQ and PCR reactions were prepared by adding 1.5 µl diluted DNA samples to 5.0 µl PCR brew, ensuring each DNA sample was added to a separate well, giving a final volume of 6.5 µl per well. The following PCR reaction was run:

1. 94°C for 12 minutes
2. 94°C for 30 seconds
3. 57°C for 30 seconds
4. 72°C for 30 seconds
5. GOTO step 2, 34x
6. 72°C for 10 minutes
7. 4°C for infinity

PCR products were electrophoresed (**Section 2.2.4**) to confirm successful amplification. 10.0 µl of 1:50 mixture of 400HD ROX size standard (GeneScan) and HiDi-Formamide (ThermoFisher Scientific) was added to 2.0 µl PCR products. Samples were denatured at 95°C for 5 minutes then run on the Genetic Analyser (Applied Biosystems 3130xl). Results were analysed using Geneious Prime.

2.4 Sanger sequencing

For each sample, a 30.0 µl PCR reaction was run (**Section 2.2.2**) and 3.0 µl of the resulting PCR product was electrophoresed (**Section 2.2.4**) to confirm the amplification of a single DNA band. The remaining PCR product (27.0 µl) as well as the relevant forward primer (20.0 µl per 8 samples, 10.0 µM) were transferred to separate 1.5 ml microcentrifuge tubes, and shipped at RT to Genewiz /Azenta for PCR purification and DNA sequencing.

2.5 RNA extraction

Between 7-20 dechorionated larvae were collected into a 1.5 ml microcentrifuge tube. All 1X E3 media was removed and replaced with 250.0 µl TRIzol reagent (Sigma). Larvae were homogenised by 15 passages through a 25 g needle and 1.0 ml syringe. Homogenised samples were incubated for 3 minutes at RT. 50.0 µl chloroform (Sigma) was added to samples and tubes were gently inverted 10 times to mix. Samples were further incubated for 3 minutes at RT.

Each sample was centrifuged for 15 minutes at maximum speed at 4°C. The top aqueous layer was collected, being careful to not include the bottom layer. Same volume isopropanol was added to the top layer and inverted gently to mix. Each sample was incubated at RT for 15 minutes then centrifuged for 15 minutes at maximum speed to collect the pellet. Each pellet was washed by adding 150.0 µl 70% ethanol (EtOH) (diluted using nuclease-free water) and centrifuging for 5 minutes at 7000 xg at 4°C. Supernatant was removed and a brief centrifugation step was made to remove remaining 70% EtOH. Pellet was air-dried for a few minutes then resuspended in 15.0 µl nuclease-free water. Purity and concentration of RNA samples were determined using a nanodrop spectrophotometer and samples were stored at -80°C.

2.6 RNA clean-up

In cases of RNA contamination, 30.0 µl nuclease-free water and 25.0 µl LiCl precipitation solution (7.5 M LiCl and 50.0 mM EDTA pH 8.0) (Invitrogen) were added to the RNA sample, mixed and incubated at -20°C for 30 minutes. Following incubation, this mixture was centrifuged at 13,000 xg for 15 minutes at 4°C. The resulting supernatant was discarded and the pellet washed with 100.0 µl 75% EtOH. Washed pellet was centrifuged at 13,000 xg for 5 minutes at 4°C. Supernatant was discarded, the pellet was resuspended in 15.0 µl nuclease-free water and RNA purity was checked using a nanodrop spectrophotometer.

2.7 Complementary DNA synthesis

RNA was reverse transcribed into complementary DNA (cDNA) using either the Verso cDNA synthesis kit or the ProtoScript II First Strand cDNA Synthesis Kit, according to manufacturer's instructions. For the Verso kit, a 10.0 µl reaction contained 2.0 µl cDNA synthesis buffer (5X), 1.0 µl dNTP mix (5.0 mM), 0.5 µl RNA primer, 0.5 µl Verso enzyme mix, 0.5 µl anchored oligo dT (500.0 ng/µl) and a volume of RNA (500.0 ng) made up to 5.5 µl, using nuclease-free water. The reaction mixture was incubated for 30 minutes at 42°C followed by 2 minutes at 95°C, in a thermal cycler.

For the ProtoScript kit, a 20.0 µl reaction contained 2.0 µl $d(T)_{23}$, 10.0 µl ProtoScript II Reaction Mix (2X), 2.0 µl ProtoScript II Enzyme Mix (10X), and a volume of RNA (500.0 ng) made up to 6.0 µl, using nuclease-free water. The reaction was incubated for 60 minutes at 42°C followed by 5 minutes at 80°C, in a thermal cycler.

2.8 Quantitative PCR

Quantitative PCR (qPCR) is used to quantitatively determine the amount of specific mRNA in a sample. Unlike conventional PCR, a qPCR reaction requires template cDNA, not genomic DNA. A qPCR reaction also requires a pair of primers which amplify a specific region of cDNA, a probe or an intercalating dye, nucleotides, a heat-resistant DNA polymerase and a specialised thermal cycler for detecting fluorescence.

Like conventional PCR, double-stranded DNA is denatured. Next, primers bind to their target sequence and DNA polymerase uses the template strand to synthesise a new DNA strand, thereby doubling the amount of double-stranded DNA with each cycle. In qPCR, cDNA amplification is detected using fluorescent reporters, therefore, with each cycle, product amplification is detected as an increase in fluorescence. The fluorescent dye SYBR Green which binds to newly synthesised double-stranded DNA was used in this project. Signal intensity must exceed a threshold for fluorescence to be detected above background. The number of cycles for fluorescence to exceed said threshold is the Ct value.

qPCR primers were designed to flank introns, ensuring specific amplification of cDNA. Once supplied, qPCR primers were diluted to 20.0 µM working concentration, using MQ. qPCR primers were optimised for annealing temperature by running a gradient PCR using WT cDNA (similar to **Section 2.2.2**). qPCR primers were also optimised for concentration and efficiency. Primer and cDNA concentrations were used to generate a standard curve. The lowest primer concentration to achieve an efficiency close to 100% was used for subsequent reactions. The melt curve was also used to re-confirm primer specificity.

Per 20.0 µl reaction, 19.0 µl qPCR reaction mix (50.0% SYBR Green (Agilent), primers at optimised concentration and 5.0% DMSO made up to 19.0 µl, using nuclease-free water) was pipetted into wells of a 96-well qPCR plate (Bio-Rad), followed by the addition of 1.0 µl cDNA. The plate was centrifuged to ensure mixing then transferred into Bio-Rad's CFX96 Real-Time System C1000 Touch Thermal Cycler where it underwent the following amplification cycles:

1. 95°C for 3 minutes
2. 95°C for 5 seconds
3. 60-63°C for 10 seconds
4. Plate read
5. GOTO step 2, 39x
6. 95°C for 1 minute
7. 55°C for 30 seconds
8. Melt curve: 55°C to 95°C, increments of 0.5°C at 5.0 second intervals

Data was analysed using the double-delta Ct method. Ct values of the gene-of-interest were subtracted from that of the reference gene (*β-actin*) to give the delta-Ct value. The delta-delta-Ct value was calculated by subtracting the delta-Ct value of each sample from the average delta-Ct value of the control group. Fold change was calculated as 2^-delta-delta-Ct (2^-ΔΔCt).

A list of qPCR primers used in this PhD is provided below (**Table 2.6**). Note that *il-6* and *cdkn1a* qPCR primer sequences were obtained from Xie *et al.*, (2019) and Laranjeiro *et al.*, (2013), respectively. *β-actin* primer sequences were obtained from Dr Nan Li. All 3 primer pairs were re-optimised for use in this PhD by myself. *il-1β* qPCR primer sequences were obtained from López Nadal *et al.*, (2018) and re-optimised for use in the Bandmann laboratory by Dr Emma Fargher.

Gene	**Forward primer (5'-3')**	**Reverse primer (5'-3')**	**Primer concentration (nM)**
β-actin	ATGGATGAGGAAATCGCTGC	AGTCTTTCTGTCCCATGCCA	250.0
cdkn1a	CCGCATGAAGTGGAGAAAAC	ACGCTTCTTGGCTTGGTAGA	250.0
il-1β	TGCGGGCAATATGAAGTC	TTCGCCATGAGCATGTCC	500.0
il-6	CGCTAAGGCAACTGGAAGAC	CCAGACCACTGGGAAACACT	250.0

satb1a (1)	TGCATTGCAAGAGCTGGGAT	AGAGCCACAGGGTTCCAATG	100.0
satb1a (2)	AAGCTCACCTCTGCCCATTC	GCTCGCCTCATTTCTTGCTG	250.0
satb1b (1)	GCCGAGTTCGTCCTGGTC	CGTAGGAAAGAGGCACTGGG	100.0
satb1b (2)	CCCAGAATTCCAGTGGGCAT	TCCTGCTGGATCTCGTCGTA	100.0
sirt1 (2)	TGCTGGACAAGAAGGGAAGG	AAAAGACCCGTGGCACTGAA	250.0

Table 2.6. List of qPCR primers and concentrations used to detect mRNA expression in this PhD. *β-actin, beta-actin; il-1β, interleukin-1β; il-6, interleukin-6.*

2.9 Reverse transcription PCR through development

RNA was extracted from 0-5dpf WT zebrafish (**Section 2.5**). 0dpf refers to embryos at the 30% epiboly developmental stage. RNA was reverse transcribed to cDNA (**Section 2.7)** and a PCR reaction was run (**Section 2.2.2**). With the exception of *sirt1*, primers used for reverse transcription PCR (RT-PCR) were also used for qPCR experiments. *sirt1* RT-PCR primers were obtained from Kim *et al.*, (2019) and optimised for annealing temperature (**Section 2.2.2**).

A 10.0 µl reaction contained 3.8 µl MQ, 5.0 µl Biomix Red (2X), 0.1 µl forward primer, 0.1 µl reverse primer, 1.0 µl cDNA. 3.0 µl PCR products were loaded into wells and electrophoresed (**Section 2.2.4**). *β-actin* served as loading control. A list of primers used for RT-PCR in this PhD is provided below (**Table 2.7**).

Gene	**Forward primer (5'-3')**	**Reverse primer (5'-3')**
β-actin	ATGGATGAGGAAATCGCTGC	AGTCTTTCTGTCCCATGCCA
satb1a (1)	TGCATTGCAAGAGCTGGGAT	AGAGCCACAGGGTTCCAATG
satb1b (1)	GCCGAGTTCGTCCTGGTC	CGTAGGAAAGAGGCACTGGG
sirt1 (1)	ATGGCGGACGGCGAAAATAA	CGGTCTAGTGTTGTTGTTGTTG

Table 2.7. List of qPCR primers used to detect mRNA expression through development in this PhD. *β-actin, beta-actin.*

2.10 Drug treatment

Drug treatment experiments were performed to determine the susceptibility of mutant zebrafish lines to MPP^+, to investigate the effect of chemical inhibition of sirt1 in Tg(*eno2*:hsa.*SNCA*-ires-EGFP) larvae and to obtain a positive control for western blot experiments.

2.10.1 MPP^+ exposure

The neurotoxic effect of MPP^+ was previously detailed (**Sections 1.1.6.2 and 1.1.7**). MPP^+ was handled with care, in a fume-hood.

At 24hpf, PTU-treated embryos (**Section 2.1.5**) were transferred to 6-well plates (CytoOne) (20 embryos per well). 1X E3 media transferred with embryos was replaced with 2.7 ml 1X E3 media (without methylene blue) containing PTU. Next, 300.0 µl MPP^+ (30.0 mM) was added to wells assigned to MPP^+-treated embryos, giving a final concentration of 3.0 mM MPP^+ while 300.0 µl MQ was added to wells assigned to untreated embryos. Due to the light-sensitive nature of MPP^+, 6-well plates were protected from light throughout this protocol. At 48hpf, media was replaced for both experiment groups. At 72hpf, MPP^+ media was discarded, followed by 2x successive washes in 1X E3 media (without methylene blue) containing PTU. Both MPP^+-treated and untreated larvae were transferred to 2.0 ml microcentrifuge tubes for fixation (**Section 2.1.9**).

2.10.2 6-chloro-2,3,4,9-tetrahydro-1H-carbazole-1-carboxamide exposure

6-chloro-2,3,4,9-tetrahydro-1H-carbazole-1-carboxamide (EX-527) is a sirt1-specific inhibitor which will be further discussed in chapter 4 of this thesis. EX-527 exposure was completed at the University of Pittsburgh.

EX-527 was prepared to a stock concentration of 25.0 mM using DMSO. EX-527 working concentrations were prepared by diluting EX-527 (25.0 mM) in 1X E3 media (without methylene blue). 2dpf embryos were manually dechorionated (**Section 2.1.8**) and transferred to 6-well plates (VWR International) (12 embryos per well). 1X E3 media transferred with embryos was replaced with 3.0 ml EX-527 ranging from 0-25.0 µM. 0 µM EX-527 contained DMSO diluted 1:1000 in 1X E3 media (without methylene blue). Media was replaced at 3-, 4- and 5dpf, followed by 3x successive washes in 1X E3 media (without methylene blue) at 6dpf before subsequent experiments.

2.10.3 Hydrogen peroxide exposure

Hydrogen peroxide (H_2O_2) causes oxidative stress (Luo and Lee Kraus, 2012). Here, H_2O_2 treatment was used to obtain a positive control for western blot experiments (**Section 2.15**).

H_2O_2 and MRC cells were obtained from the El-Khamisy laboratory. Culture media was discarded and cells were briefly washed in 1X PBS at RT. Next, a master mix was prepared by adding 1.0 µl H_2O_2 (10.0 mM) per 1.0 ml 1X PBS, giving a final concentration of 10.0 µM H_2O_2. This master mix was kept on ice and protected from light, due to the temperature- and light-sensitive nature of H_2O_2. Cells were then incubated in 2.0 ml H_2O_2 (10.0 µM) on ice for 10 minutes in the dark. Following incubation, cells were returned to RT, H_2O_2 solution was discarded and cells were briefly washed in 1X PBS. Next, 1X PBS was replaced with 50.0 µl 1X sodium dodecyl sulfate (SDS) buffer and cells were scraped into a 1.5 ml microcentrifuge tube. Scraped cells were briefly vortexed then incubated at RT for 15 minutes. Next, cells were boiled at 95°C for 5 minutes then left at RT.

2.11 WISH

WISH was utilised to investigate the spatial expression of mRNAs. In WISH, the larval cell membrane is permeabilised, allowing the migration of a digoxigenin (DIG)-labelled RNA probe into the cell where it hybridises to a specific mRNA sequence. An alkaline phosphatase (AP)-conjugated antibody binds to the RNA probe and upon the addition of the 5-bromo-4-chloro-3-indolyl-phosphate/ 4-nitro-blue-tetrazolium chloride (BCIP/NBT) substrate, AP catalyses the dephosphorylation of BCIP and converts NBT to a purple product.

2.11.1 Synthesis of DIG-labelled WISH probes

2.11.1.1 From plasmid (satb1a only)

To synthesise DIG-labelled *satb1a* RNA probes, the pBlueScript II SK (+) plasmid (**Figure 2.3**) containing the “cb955” clone was obtained from the Zebrafish International Resource Centre (ZIRC). cb955 is an expressed sequence tag (EST) clone which contains *satb1a* cDNA.

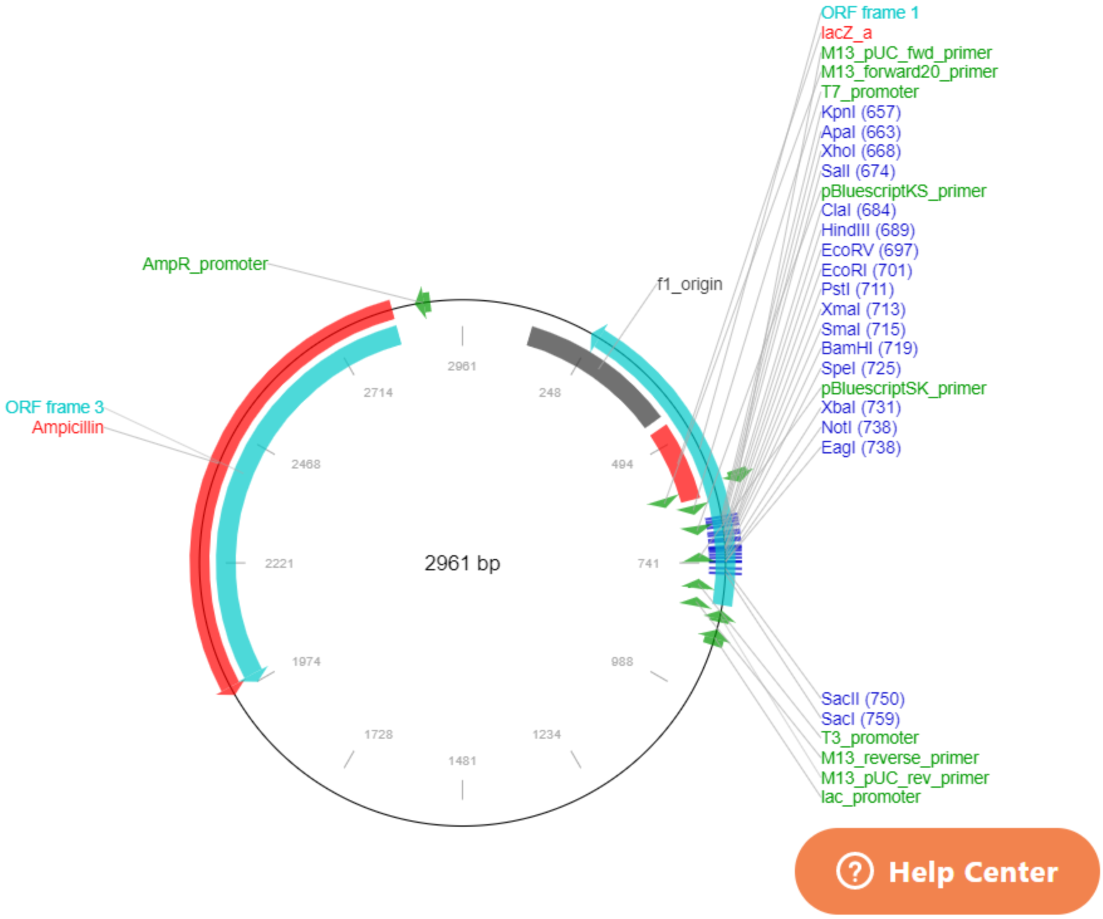

Figure 2.3. Map of the pBlueScript II SK (+) plasmid which contains satb1a's cDNA sequence used to synthesise the satb1a WISH probe. *cDNA, complementary DNA; WISH, whole-mount in-situ hybridisation.*

A pair of scissors was dried with 100% EtOH and used to cut the filter paper on which the pBlueScript II SK (+) plasmid was delivered. The filter paper was soaked in 50.0 µl MQ enclosed in an microcentrifuge tube and incubated for 30 minutes at RT. Next, the filter paper was drained and removed from the tube, using a pair of tweezers previously dried with 100% EtOH, thereby leaving a plasmid solution. Plasmid concentration was determined using a nanodrop spectrophotometer.

The plasmid was transformed according to manufacturer's instructions as follows:

2.0 µl plasmid (36.2 ng) was pipetted into 50.0 µl of C3019H cell solution (supplied by the van Eeden laboratory), followed by gentle swirling of the plasmid-cell mixture, then a 30 minute incubation on ice. Next, this mixture was incubated at 42°C for 40 seconds, followed by a 2 minute incubation on ice. 1.0 ml pre-heated lysogeny broth (LB) solution (supplied by the van Eeden laboratory) was added to the mixture, followed by shaking for 60 minutes at 250 rpm at 37°C. The sample was centrifuged for 5 minutes at 2000 rpm, then 800.0 µl supernatant was discarded and a cell-rich volume was made by mixing pellet with the remaining 200.0 µl supernatant. 100.0 µl cell-rich volume was pipetted and spread on the surface of an LB agar plate (supplied by the van Eeden laboratory) containing carbenicillin (50.0 µg/µl) (supplied by the van Eeden laboratory). Although the pBlueScript II SK (+) plasmid is resistant to ampicillin (**Figure 2.3**), ampicillin was substituted with carbenicillin due to stability. The agar plate was incubated o/n at 37°C and the remaining cell-rich volume was stored at 4°C.

Plasmid DNA was extracted using a MidiPrep Kit (QIAGEN). 100.0 ml LB solution was transferred into a 500.0 ml conical flask and 50.0 µl carbenicillin (100.0 mg/ml) was pipetted into LB solution. Using a pipette, a single colony was selected from the carbenicillin-resistant agar plate and dropped into the LB solution containing carbenicillin. The conical flask was incubated o/n at 200 rpm at 37 °C. Following plasmid DNA extraction, concentration was measured using a nanodrop spectrophotometer.

Following its extraction, DNA plasmid was linearised as follows: 200.0 µl linearisation mixes were prepared (20.0 µl buffer, 6.0 µl enzyme, 15.0 µg extracted DNA plasmid, MQ) for both the sense and anti-sense probe, and incubated for 3 hours at 37°C. To confirm linearisation, 2.0 µl linearised plasmids were electrophoresed on a 1% gel, with 2.0 µl non-linearised plasmid serving as control. ApaI and NotI were used to linearise plasmid in preparation of the sense and anti-sense probe, respectively (**Table 2.8**). This is because cb955 was cloned between EcoRI and XhoI (**Figure 2.3**). NotI was used to linearise the plasmid ahead of transcription of the anti-sense probe (**Table 2.8**), as stated in the ZIRC database.

Linearised plasmids were purified by adding 200.0 µl phenol:chloroform (25:24) (Sigma) and centrifuging at 13,300 rpm for 5 minutes. Supernatants were collected then same volume chloroform was pipetted to supernatants and samples were centrifuged at 13,300 rpm for 5 minutes. The subsequent supernatants were collected, then NaAc 3 M pH 5.2 1/10th of the supernatant volume and 100% EtOH 2.5x the supernatant volume were added to sense and anti-sense supernatants. Samples were precipitated for 1 hour at -80°C. Samples were centrifuged at 13,300 rpm for 30 minutes at 4°C and supernatant was discarded. Next, 70% EtOH 1x the supernatant volume was added to samples and samples were incubated for 2 minutes on ice. Samples were centrifuged for 10 minutes at 4°C and supernatant was discarded. Pellet was air-dried for 5 minutes, then reconstituted with 10.0 µl nuclease-free water. The concentration of purified plasmids was determined using a nanodrop spectrophotometer.

Purified linearised plasmids were then transcribed in a 2 hour incubation with the following mix at 37°C: 2.0 µg DNA template, 2.0 µl DTT (100.0 mM), 4.0 µl 5X transcription buffer, 2.0 µl DIG-labelled oligonucleotides (10X), 1.0 µl rRNAse inhibitor (40.0 U/µl), 2.0 µl RNA polymerase (T3, sense probe and T7, anti-sense probe- **Table 2.8**), nuclease-free water to 20.0 µl.

WISH probe	Plasmid	Enzyme	Incubation temperature (°C)	RNA Polymerase
satb1a sense	pBlueScript II SK (+)	ApaI	37	T3
satb1a anti-sense		NotI	37	T7

Table 2.8. List of enzymes and RNA polymerases used to synthesise satb1a sense and anti-sense WISH probes. *WISH, whole-mount in-situ hybridisation.*

Next, 2.0 µl DNAse (TURBO) was added to the reaction mix, followed by a 15 minute incubation at 37°C; this was done to remove template DNA. NH_4Ac (10.0 M) 1/10th of the reaction mix volume as well as isopropanol 1X the reaction mix volume were added to the reaction mix, then samples were precipitated for 30 minutes at -20°C. Samples were centrifuged for 30 minutes at 4°C, supernatants were discarded, 70% EtOH was added to pellets and samples were further centrifuged for 5 minutes at 4°C. 70% EtOH was discarded and pellets were air-dried for 5 minutes, then resuspended in 10.0 µl nuclease-free water. Purity and concentration of probes were determined using a nanodrop spectrophotometer. Probes were diluted (1:10) using nuclease-free water and incubated for 10 minutes at 70°C, to break intramolecular RNA bonds. To further confirm transcription, diluted probes were mixed with Gel loading dye (ThermoFisher Scientific) and electrophoresed on a 1% gel. Probes were stored at -20°C.

2.11.1.2 From PCR product (satb1b, sirt1 and th1)

Primers were designed to amplify WT cDNA. Two sets of the same primer pair were designed as follows: The forward primer was tagged with the T7 promoter (**TAATACGACTCACTATAGGG**) in the first set while the reverse primer was tagged with the T7 promoter in the second set. The first set of primers was used to synthesise the anti-sense probe while the second set was used to synthesise the sense probe (**Table 2.9**). Once provided, primers were reconstituted and optimised for annealing temperature (**Section 2.2.2**). Again, subsequent PCR reactions were run using the optimised annealing temperature.

Per primer set, a 100.0 µl PCR reaction was run in the same thermal cycler with the following PCR mix: 1.0 µl forward primer, 1.0 µl reverse primer, either 50.0 µl Biomix Red (2X) or 20.0 µl FirePol Green (5X) and 10.0 µl cDNA obtained from WT larvae. 3.0 µl PCR product obtained using each primer set was electrophoresed on a 1% gel to confirm a successful PCR reaction.

Next, the remaining 97.0 µl PCR product obtained using each primer set was purified using GeneJet's PCR purification kit, according to manufacturer's instructions. The concentration of purified PCR product was measured using a nanodrop spectrophotometer. 200-400.0 ng purified PCR product was transcribed, as previously detailed. Purity and concentration of probes were determined using a nanodrop spectrophotometer. Probes were diluted (1:10) as previously detailed (**Section 2.11.1.1**) and incubated for 10 minutes at 70°C. Probes were electrophoresed and stored at -20°C, as previously detailed (**Section 2.11.1.1**).

WISH probe	**Forward primer (5'-3')**	**Reverse primer (5'-3')**
satb1b sense	TGGAGCATCTCAGCGAAACA	**TAATACGACTCACTATAGGG** CCACTCTATCAAACTCTGGGCA
satb1b anti-sense	**TAATACGACTCACTATAGGG** TGGAGCATCTCAGCGAAACA	CCACTCTATCAAACTCTGGGCA
sirt1 sense (1)	TTCAGTGCCACGGGTCTTTT	**TAATACGACTCACTATAGGG** TCTCGATATGTTCAGCATCAGCA
sirt1 anti-sense (1)	**TAATACGACTCACTATAGGG** TTCAGTGCCACGGGTCTTTT	TCTCGATATGTTCAGCATCAGCA
sirt1 sense (2)	CCGAAGAAACCGAGGCTTCT	**TAATACGACTCACTATAGGG** AAAGGCCTGGGATCTCTCCT
sirt1 anti-sense (2)	**TAATACGACTCACTATAGGG** CCGAAGAAACCGAGGCTTCT	AAAGGCCTGGGATCTCTCCT
sirt1 sense (3)	GGCGGACGGCGAAAATAAAC	**TAATACGACTCACTATAGGG** GCCTGGGATCTCTCCTGAAGTA
sirt1 anti-sense (3)	**TAATACGACTCACTATAGGG** GGCGGACGGCGAAAATAAAC	GCCTGGGATCTCTCCTGAAGTA
th1 sense	AGTGCACCTGTCGGATGTTA	**TAATACGACTCACTATAGGG** GCGTCCACAAAGCTTTCTGA

th1 anti-sense	**TAATACGACTCACTATAGGG** AGTGCACCTGTCGGATGTTA	GCGTCCACAAAGCTTTCTGA

Table 2.9. List of primer sequences used to synthesise satb1b, sirt1 and th1 WISH probes from PCR products. *T7 promoter is bolded. th1, tyrosine hydroxylase 1; WISH, whole-mount in-situ hybridisation.*

2.11.2 WISH protocol

On day 1, fixed larvae (**Section 2.1.9**) were rehydrated by successive 5 minute incubations in 75% MeOH/1X PBT, 50% MeOH/1X PBT and 25% MeOH/1X PBT. This was followed by 4x 5 minute washes in 100% 1X PBT. Larvae were digested by incubating in 10.0 µg/ml proteinase K for 30 minutes for 3-5dpf larvae. Larvae were refixed in 4% PFA in PBS for 20 minutes then washed 5 times in 1X PBT, for 5 minutes each. Following 1X PBT washes, larvae were pre-hybridised in preheated HybA buffer (5X SSC (750.0 mM NaCl and 75.0 mM trisodium citrate), Heparin, 0.1% Tween-20, 500.0 µg/ml tRNA, ddH2O, 50% Formamide, 1.0 M Citric acid to pH 6.0) for 3 hours at 68°C. Following pre-hybridisation, HybA buffer was replaced with 0.5 ng/µl DIG-labelled probe and larvae were left o/n at 68°C.

On day 2, DIG-labelled probe was recycled and larvae were washed in HybB (no Heparin or tRNA) for 5 minutes. This was followed by successive 15 minute washes in 75% HybB/2X SSC, 50% HybB/2X SSC, 25% HybB/2X SSC and 2X SSC at 68°C. Next was 2x 30 minute washes in 0.2X SSC at 68°C. The last wash was replaced with successive 10 minute washes in 75% 0.2X SSC/1X PBT, 50% 0.2X SSC/1X PBT, 25% 0.2X SSC/1X PBT and 100% 1X PBT. Larvae were blocked for 2 hours (blocking solution was 2.0 mg/ml BSA, 2% sheep serum, 1X PBT), then incubated o/n with anti-DIG-AB FAB antibody (Roche) diluted in blocking solution (1:5000) at 4°C. Larvae were protected from light from this antibody incubation step.

On day 3, larvae were briefly washed in 1X PBT for 5 minutes, followed by 6x 15 minute washes in 1X PBT. Next was 3x 5 minute washes in NTMT (0.1 M Tris pH 9.5, 50.0 mM $MgCl_2$, 0.1 M NaCl, 0.1% Tween-20). Larvae were transferred to a 12-well plate and the last wash solution was replaced with staining solution (3.5 µl BCIP and 4.5 µl NBT per ml NTMT). BCIP and NBT were purchased from Roche. Staining was monitored using a dissection microscope. Once stain was satisfactory, staining solution was removed, followed by 3x 5 minute 1X PBT washes. If background staining was observed, larvae were incubated in 50% MeOH/1X PBT for 5 minutes, then 100% MeOH incubation for 5 minutes, followed by 50% MeOH/1X PBT for 5 minutes. Next, was 3x 5 minute 1X PBT washes. Larvae were returned to microcentrifuge tubes, refixed in 4% PFA in PBS for 20 minutes, followed by 3x 5 minute 1X PBT washes. Next, larvae were transferred to glycerol for storage through successive incubation in 25%, 50% and 75% glycerol. Larvae were stored at 4°C until imaging. Note that unless stated otherwise, washes and incubations were at RT.

2.11.3 Imaging WISH samples

With the exception of *tyrosine hydroxylase 1* (*th1*), WISH samples were suspended in 100% glycerol and imaged using the Leica M165 FC microscope at 5.0x magnification for lateral images and 10.0x magnification for dorsal images.

2.11.4 Counting of *th1*-positive neurons

The purpose of running a *th1* WISH was to assess the effect of genetic mutations on the number of dopaminergic neurons and susceptibility to MPP$^+$.

Following the 3rd 1X PBT wash preceding the refixing step on day 3 of the WISH protocol, larvae were decapitated right above the yolk sac, using a clean scalpel. Heads were transferred to wells of a 96-well PCR plate (StarLab UK) containing 100.0 µl 1X PBT while bodies were transferred to corresponding wells of another 96-well PCR plate (StarLab UK) containing 20.0 µl NaOH (50.0 mM) for DNA extraction (**Section 2.2.1.2**).

Larval heads were transferred to the aperture of slides containing 100% glycerol and mounted dorsally; heads were secured in position with a coverslip. *th1*-positive neurons belonging to DC groups 1, 2, 4 and 5 on both hemispheres were visualised using the Axiophot2 microscope (Zeiss) at 20.0x magnification and counted manually (**Figure 2.4**). These neuronal groups were selected because they are analogous to human dopaminergic neurons that project from the SNpc to the striatum (Rink and Wullimann, 2001, 2002). In parallel, bodies were used to genotype larvae (**Figure 2.5**). Counting of *th1*-positive neurons was done blindly using 3 independent clutches of larvae.

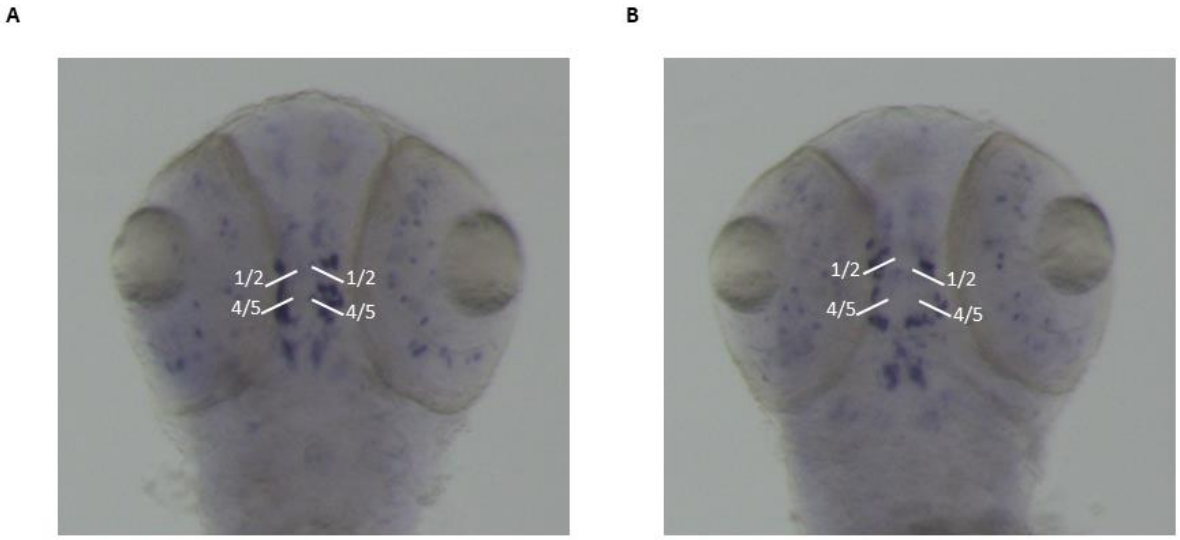

Figure 2.4. Representative image of 3dpf WT larvae following th1 WISH. *DC1, DC2, DC4 and DC5 neurons on both hemispheres (indicated by white lines) were counted because they are analogous to human dopaminergic neurons that project from the SNPc to the striatum. A higher number of DC1, DC2, DC4 and DC5 neurons were observed in untreated larvae (A) compared to MPP$^+$-treated larvae (B). DC, diencephalic; dpf, days post fertilisation; MPP$^+$, 1-methyl-4-phenylpyridinium; SNPc, substantia nigra pars compacta; th1, tyrosine hydroxylase 1; WT, wildtype.*

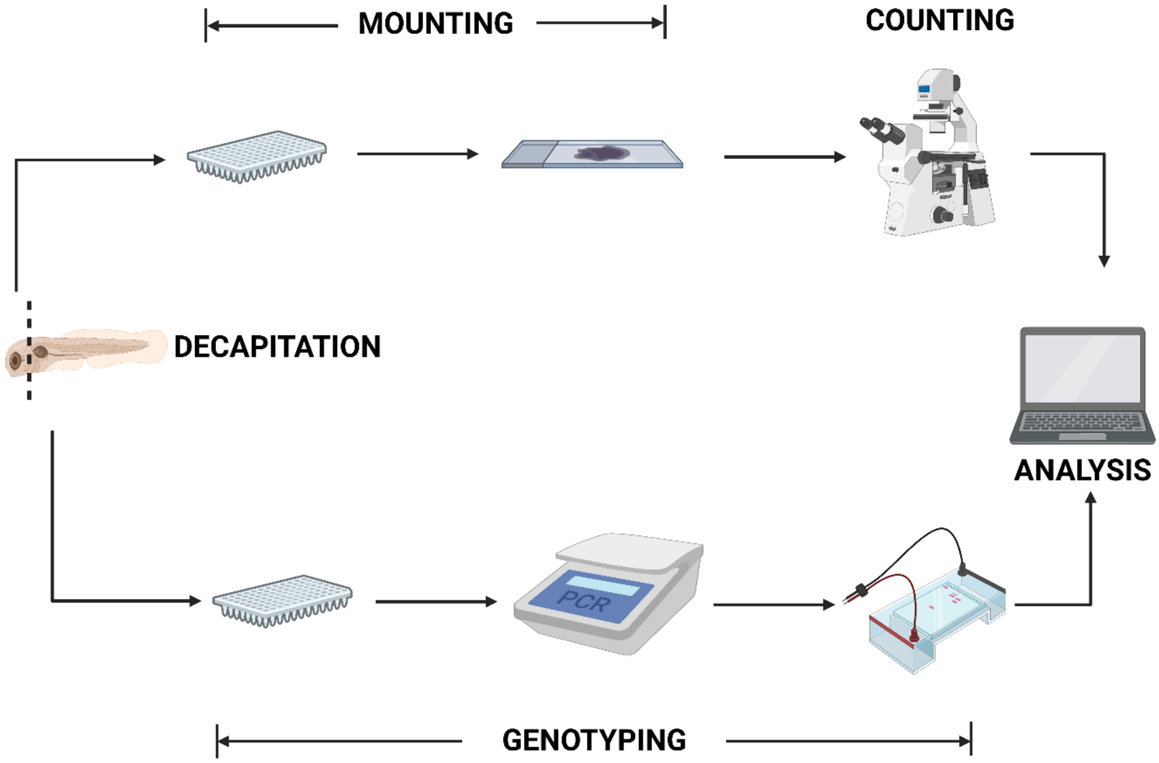

Figure 2.5. ***Schematic showing the work-flow of th1-positive neuron counting.*** *Larvae were decapitated then heads were mounted on microscope slides for blind th1-positive neuron counting. In parallel, DNA was extracted from larval bodies for genotyping purposes. Following both counting and genotyping, data were analysed using GraphPad Prism. th1, tyrosine hydroxylase 1. Created with BioRender.com.*

2.12 Microglial analysis

Microglial analysis comprised of microglial counting only. To do this, microglia were visualised either by whole-mount IHC (**Section 2.12.1**) or by intravital imaging of Tg(*mpeg1*:EGFP) larvae (**Section 2.1.2.7**).

2.12.1 Whole-mount IHC

IHC is a technique used to detect an antigen within a tissue sample, using an antigen-specific antibody. There are two types of IHC, namely direct and indirect IHC. In direct IHC, the primary antibody binds to the epitope of its antigen. Here, the primary antibody itself is conjugated to a label, thereby giving spatial information of protein expression. In indirect IHC, the primary antibody binds to the epitope of its antigen, like with direct IHC. However, in indirect IHC either a labelled secondary antibody binds to the primary antibody or a labelled tertiary antibody binds to the secondary antibody, giving spatial protein expression. Indirect IHC was used in this project.

2.12.1.1 Whole-mount IHC protocol

Fixed larvae (**Section 2.1.9**) were rehydrated by successive 5 minute washes in 75% MeOH/1X PBT, 50% MeOH/1X PBT and 25% MeOH/1X PBT, followed by 4x 5 minute washes in 1X PBT. Next, larvae were incubated for 5 minutes with 150.0 mM Tris HCl (pH 9.0) then 15 minutes at 70°C, for antigen retrieval. This was followed by 2x 5 minute washes in 1X PBT, then 2x 5 minute washes in MQ. MQ was replaced with 100% acetone and larvae were incubated for 20 minutes at -20°C. Next was 2x 5 minute washes in 1X PBT followed by 3x 5 minute washes in 1X PBT. Larvae were blocked o/n at 4°C (blocking solution was 10% sheep serum, 0.8% Triton X-100, 1% BSA, 1X PBT) then incubated for 3 nights with the primary antibody, 4c4 (supplied by the Hamilton laboratory) diluted 1:100 in modified blocking solution (1% sheep serum, 0.8% Triton X-100, 1% BSA, 1X PBT) at 4°C. Note that larvae were protected from light from the primary antibody incubation step onwards.

Primary antibody incubation was followed by 3x 1 hour washes in 10% sheep serum, 0.1% Triton X-100, PBS. Next were 2x 10 minute washes in 0.1% Triton X-100 in PBS. Larvae were then incubated for 3 nights with the secondary antibody (ms488) diluted 1:200 in 1X PBT at 4°C. Secondary antibody incubation was followed by 3x 1 hour washes in 1X PBT.

Following the 3rd 1X PBT wash, larvae were decapitated (**Section 2.11.4**). Heads and bodies were transferred to corresponding wells of 96-well PCR plates (StarLab UK) and DNA was extracted from bodies for genotyping purposes, as previously detailed (**Section 2.11.4**). However, heads were mounted ventrally in a clear bottomed 96-well black µclear microplate (Greiner) using 1% low melting agarose (LMA).

2.12.1.2 Imaging and counting of microglia

Microglia were imaged using Perkin Elmer's Opera Phoenix High Content Screening System, at 20.0x magnification. Microglia in the fore- and midbrain were counted blindly in ImageJ by scrolling through Z stacks, ensuring deep-tissue microglia were counted as well as surface microglia (**Figure 2.6**). Likewise, grids were implemented to prevent a single microglia from being counted more than once. Microglia in the forebrain and midbrain were counted, then added to obtain the number of microglia in the "total brain".

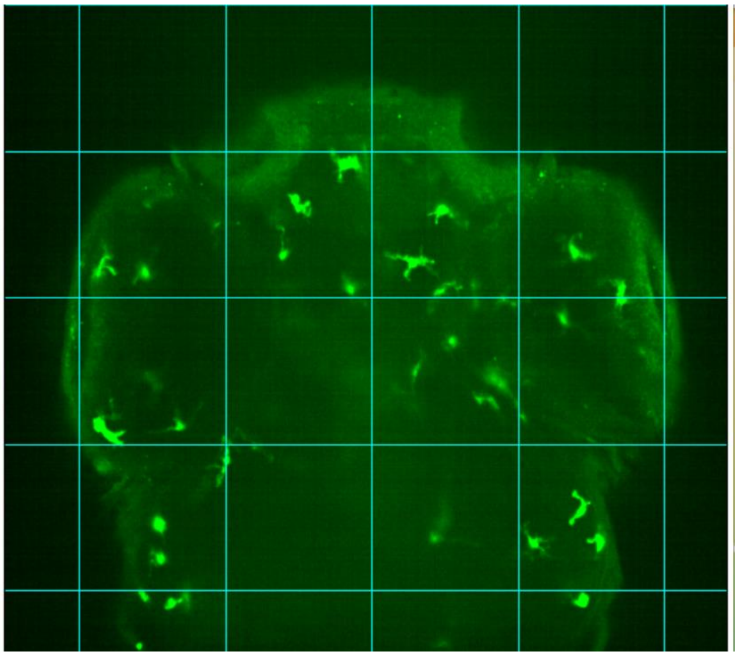

Figure 2.6. Microglial counting in larvae following 4c4 whole-mount IHC. *Microglia were counted in ImageJ by scrolling through Z stacks, ensuring deep-tissue microglia were counted as well as surface microglia. Grids were also employed to prevent multiple counts of a single microglia. IHC, immunohistochemistry.*

2.12.2 Intravital imaging of Tg(*mpeg1*:EGFP) larvae

Intravital imaging was completed at the University of Pittsburgh, using the Tg(*mpeg1*:EGFP) line which fluorescently labels macrophages with GFP (**Section 2.1.2.7**).

Tg parents were out-crossed with adult Casper zebrafish and 2dpf offspring were sorted for GFP in the head and yolk sac (**Section 2.1.7**). Tg offspring were anaesthetised (**Section 2.1.10**) then mounted ventrally in 1.5% LMA against the coverslip glass of a dish (MatTek) for intravital imaging.

2.12.2.1 Imaging and counting of microglia

Microglia were imaged using a Nikon Eclipse Ti2 inverted microscope, at 20.0x and 40.0x magnification. Microglia were counted using an algorithm developed in the Burton laboratory that counts the total number of macrophages in the zebrafish brain, including deep-tissue macrophages (**Figure 2.7**).

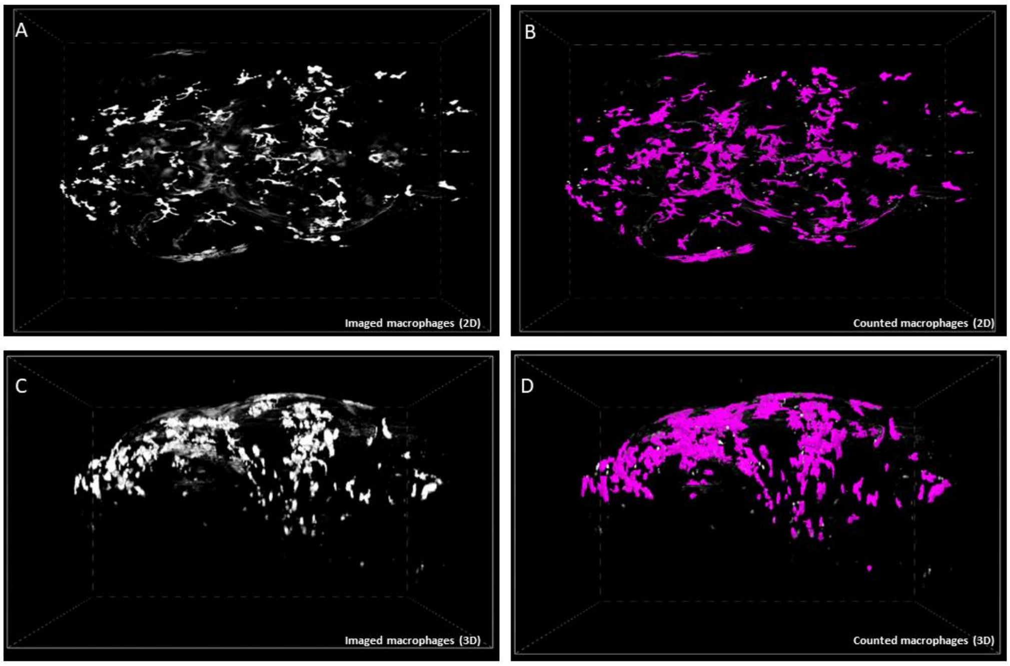

Figure 2.7. Microglial counting in Tg(mpeg1:EGFP) larvae. *Microglia were counted using an algorithm developed in the Burton laboratory. A and C show macrophages imaged in the larval brain and surrounding tissues, 2D and 3D, respectively. B and D show the macrophages counted by the algorithm (highlighted in magenta), 2D and 3D, respectively. 3D images are provided to show that the algorithm included deep-tissue macrophages during counting. 2D, 2-dimensional; 3D, 3-dimensional.*

2.13 Acridine orange staining

Acridine orange (AO) is a DNA intercalating dye that labels degenerating cells due to their permeable plasma membranes (Xie *et al.*, 2020).

A master mix was prepared by adding 1.0 µl AO (5.0 µg/ml) per 1.0 ml 1X E3 media (without methylene blue). This master mix was protected from light, due to the light-sensitive nature of AO. Larvae were transferred to a flat-bottomed 6-well plate (VWR International) (12 larvae per plate) and incubated in 2.0 ml AO master mix solution at RT for 30 minutes in the dark. To prevent photo-bleaching of AO staining, subsequent steps of this protocol were completed in the dark.

Incubation was followed by 3x brief washes in 1X E3 media (without methylene blue) then larvae were anaesthetised (**Section 2.1.10**). Next, larvae were mounted laterally in 1.5% LMA against the coverslip glass of a dish (MatTek) and imaged using an inverted epifluorescence microscope (Olympus IX-71). AO-stained spinal cord cells were counted manually.

2.14 Zebrafish morphology, morbidity and mortality

2.14.1 Larval zebrafish

Larvae were monitored for morphological abnormalities under a dissecting microscope (Leica). Larvae which showed signs of morbidity were culled immediately for DNA extraction (**Sections 2.1.10 and 2.2.1.1**).

2.14.2 Adult zebrafish

To avoid variability in results, zebrafish were housed in equal-density tanks prior to morphological studies. Adult zebrafish were also monitored for morbidity and mortality.

2.14.2.1 Weight recordings

Adult zebrafish were anaesthetised one at a time by immersion in tricaine (**Section 2.1.10**). To avoid variability in weight recordings, each zebrafish was first dried on absorbent laboratory roll. Next, each zebrafish was placed on a Precision Laboratory Scale (Kern) and weight was recorded.

2.14.2.2 Size measurements

Each adult zebrafish was transferred to a flat and transparent surface immediately after weight recording then imaged using the camera of a Samsung Galaxy A5 (2017), with a metre rule included in each image to establish a scale.

Size was analysed using ImageJ. A scale was set by extrapolating distance in pixels to distance in centimetre, using the imaged metre rule. For length measurements, a straight line was drawn across the rostro-caudal axis of the zebrafish, originating from the mouth and ending just before the caudal fin (**Figure 2.8**). For width measurements, a straight line was drawn across the dorso-ventral axis of the zebrafish, at its midline (**Figure 2.8**).

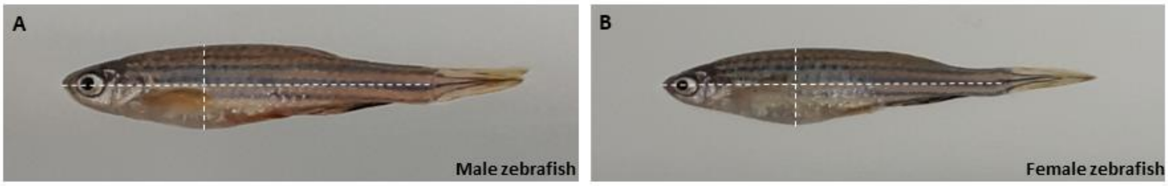

Figure 2.8. Size measurements in adult zebrafish. *Size was measured in male (A) and female (B) zebrafish. Length was measured by drawing a straight line across the rostro-caudal axis of the zebrafish, originating from the mouth and ending just before the caudal fin while width was measured by drawing a straight line across the dorso-ventral axis of the zebrafish, at its midline. Distance in pixels was extrapolated to distance in centimetre, using a metre rule imaged together with zebrafish.*

2.15 Western blotting

Western blotting is a technique used to detect specific proteins. Here, samples are loaded into wells of an SDS gel and electrophoresed. Proteins migrate through this gel based on molecular weight (MW), with high MW proteins migrating less through the gel compared to low MW proteins. Following electrophoresis, proteins are transferred to a nitrocellulose membrane. Next, the nitrocellulose membrane is incubated with a primary antibody which specifically binds to the protein-of-interest. Western blotting also utilises an enzyme-conjugated secondary antibody which specifically binds the primary antibody. The secondary antibody is usually conjugated to horseradish peroxidase (HRP). To detect the protein-of-interest, a substrate is added to the blot which results in a chemiluminescence reaction, thereby enabling the visualisation of the protein-of-interest in the form of a band on the nitrocellulose membrane. During this PhD, western blot experiments were performed in the El-Khamisy laboratory, with reagents supplied by the El-Khamisy laboratory, with the exception of the γH2AX antibody which was supplied by the van Eeden laboratory. Western blot experiments were used to detect Poly (ADP-ribose) (PAR) and γH2AX expression.

2.15.1 Western blot protocol

4% and 15% separating SDS gels were prepared (**Table 2.10**), mixed together in a serological pipette and loaded into a gel cassette, then topped-up with isopropanol and left for 30 minutes to solidify.

Components	**Volume (µl)**	
	4% gel	**15% gel**
MQ	1,800.0	840.0
30% acrylamide	390.0	1,500.0
1.5 M Tris pH 8.8	750.0	750.0
10% SDS	30.0	30.0
10% APS	30.0	30.0
TEMED	2.4	1.2

Table 2.10. Components of 4% and 15% separating gels used in this PhD. *APS, ammonium persulfate; MQ, Milli-Q; SDS, sodium dodecyl sulfate; TEMED, Thermo Scientific Tetramethylethylenediamine.*

Next, isopropanol was gently discarded and a stacking gel was prepared (**Table 2.11**) then loaded into the gel cassette. A comb was placed into the stacking gel and the gel was left for 30 minutes to solidify.

Components	**Volume (µl)**
MQ	2,700.0
30% acrylamide	670.0
1.0 M Tris pH 6.8	500.0
10% SDS	40.0
10% APS	40.0
TEMED	10.0

Table 2.11. Components of the stacking gel used in this PhD. *APS, ammonium persulfate; MQ, Milli-Q; SDS, sodium dodecyl sulfate; TEMED, Thermo Scientific Tetramethylethylenediamine.*

While the stacking gel was solidifying, previously extracted brains (**Section 2.1.11**) were thawed from -80°C then washed with 1X PBS. Next, brains were homogenised by 100 passages in 50.0 µl 2X SDS buffer (containing basemuncher, ab270049, 1:1000), using a Dounce homogeniser (supplied by the Ismail laboratory). SDS buffer also contained β-mercaptoethanol.

0.5 µl and 2.0 µl brain homogenates were topped-up to 10.0 µl using 2X SDS buffer (containing basemuncher, 1:1000) for γH2AX and PAR western blots, respectively. 10.0 µl homogenates were boiled at 95°C for 5 minutes, then centrifuged. Sample preparation was carefully timed to ensure that it's completion coincided with the end of the 30 minutes allocated to the solidification of the stacking gel.

Next, the gel cassette was inserted into a gel tank containing 1X SDS running buffer (25.0 mM Tris, pH 8.3, 192.0 mM glycine, 0.1% w/v SDS). The comb was removed and 10.0 µl samples were loaded into wells with a gel-loading pipette tip, with 3.0 µl Precision Plus Protein Dual Colour Standard (Bio-Rad, 1610374) serving as a reference for MW. Samples were first electrophoresed at 60 volts for 40 minutes to allow migration through the stacking gel, followed by 120 volts for 60 minutes for migration through the separating gel, using the Bio-Rad Mini-PROTEAN Tetra electrophoresis cell (Bio-Rad, 1658004).

Protein was transferred from the gel to a nitrocellulose membrane (Bio-Rad, 170-4271) using the Trans-Blot Turbo transferTM system (Bio-Rad, 17001915). Following transfer, the nitrocellulose membrane was blocked with 5% milk solution, that is, milk powder (Marvel) dissolved in 20.0 ml 1X TBST (20.0 mM Tris, 150.0 mM NaCl and 0.1% Tween-20 pH 7.6) for 1 hour at RT. Next, blot was incubated with primary antibody solution o/n at 4°C. This was followed by 3x 5 minute washes in 1X TBST at RT. The blot was then incubated with the secondary antibody solution for 1 hour at RT. This was also followed by 3x 5 minute washes in 1X TBST at RT. A list of antibodies and concentrations used in this PhD is provided below (**Table 2.12**).

Antibody	Primary/secondary antibody	Host species	Supplier	Concentration used
PAR	Primary	Mouse	Tulip Biolabs (1020)	1:1000
γH2AX		Rabbit	Genetex (GTX127342)	
GAPDH		Rabbit	Genetex (GTX100118)	
Anti-mouse IgG (H + L)-HRP Conjugate	Secondary	Goat	Bio-rad (1706516)	1:4000
Anti-rabbit IgG (H + L)-HRP Conjugate		Goat	Bio-rad (1706515)	

Table 2.12. A list of antibodies utilised in western blot experiments in this PhD, as well as their host species, suppliers and the concentrations used. *γH2AX, gammaH2AX; GAPDH, glyceraldehyde-3-phosphate dehydrogenase; H, heavy chain; HRP, horseradish peroxidase; IgG, immunoglobulin G; L, light chain; PAR, poly (ADP-ribose).*

2.15.2 Imaging and stripping of blot

Following the 3rd 1X TBST wash, ECL luminol: peroxide solution (1:1) (Bio-Rad) was added to the surface of the blot and the blot was dark adapted for 1 minute. Bands were detected using the ChemiDoc MP imaging system (Bio-Rad, 17008280).

When needed, a blot was stripped following imaging, as follows: the blot was first washed in 1X TBST for 5 minutes at RT. Next, the blot was incubated in stripping buffer (ThermoFisher Scientific) for 15 minutes at RT, followed by a second wash in 1X TBST for 5 minutes at RT. The blot was then re-blocked with 5% milk solution in preparation for the next primary antibody incubation.

2.15.3 Densitometry

Protein expression in each brain sample was quantified using ImageLab. Protein expression was normalised by dividing the band intensities of proteins-of-interest by the band intensities of the loading control.

2.16 Protein quantification

Prior to running ATP and NAD/NADH assays (**Sections 2.17 and 2.18**), brain protein concentration was determined using a Bradford assay as follows:

Supernatants obtained from brain lysates were diluted 1:5, 1:10 and 1:15 using 1X PBS then BSA standards ranging from 1000.0 µg/ml to 0 µg/ml (1X PBS only) were prepared by diluting 2000.0 µg/ml BSA (supplied by the Allen laboratory) in 1X PBS. Blank samples were prepared by diluting lysis buffer 1:5, 1:10 and 1:15 in 1X PBS, like with supernatants.

BSA standards (supplied by the Allen laboratory), supernatant- and blank dilutions were vortexed, then 5.0 µl BSA standards, supernatant- and blank dilutions were pipetted into respective wells of a flat-bottomed 96-well microplate (Greiner), each in triplicate. 195.0 µl Bradford reagent (ThermoFisher Scientific) (supplied by the Allen laboratory) was pipetted into each well and the microplate was shook in the dark for 5 minutes at RT. Next, absorbance was measured at OD 595 nm, using a microplate reader (PheraStar).

A standard curve was plotted using absorbance readings obtained from wells designated for standards. Protein concentrations for supernatant- and blank dilutions were extrapolated from absorbance readings, using the standard curve. Extrapolated blank protein concentrations were subtracted from supernatant protein concentrations of the same dilution factor. Next, blank-corrected supernatant protein concentrations were multiplied by their respective dilution factors to obtain protein concentrations in µg/ml which were then averaged per brain. Averaged protein concentrations were divided by 1000 to obtain protein concentrations in µg/µl.

2.17 ATP assay

PerkinElmer's ATPlite Luminescence ATP Detection System (6016941) was used, according to manufacturer's instructions. This kit relies on the production of light when ATP reacts with luciferase and D-luciferin, it's substrate; emitted light is proportional to ATP within certain limits. The lysis solution supplied with this kit inactivates endogenous ATPases, by raising the pH of the reaction mixture. Substrate solution lowers the pH, allowing the luminescence reaction to occur.

Freshly dissected adult zebrafish brains (**Section 2.1.11**) were homogenised in 300.0 µl lysis solution by 30 passages through a large bore needle followed by a further 30 passages through a fine bore needle. Homogenate was centrifuged at maximum speed at 4°C for 5 minutes, supernatant was collected and 20.0 µl supernatant was used for protein quantification (**Section 2.16**).

Following protein quantification, master mixes containing 18.0 µg brain lysates were prepared using lysis solution, then added to wells of a white flat-bottomed 96-well microplate (Greiner) designated for sample readings and background readings (triplicate wells each), with 100.0 µl master mix per well. Next, ATP standards ranging from 0-0.6 mM were prepared using MQ. 100.0 µl lysis solution was added to wells designated for standards (duplicate wells per concentration) and “no protein” control (6 wells). Then 10.0 µl standards were added to wells designated for standards only and the microplate was shook at 700 rpm at RT for 5 minutes.

Next, 50.0 µl lysis solution was added to every well and the plate was shook at 700 rpm at RT for 5 minutes. This was followed by the addition of 50.0 µl substrate solution to wells designated for sample readings, standards and 3 “no protein” control wells. Then 50.0 µl MQ was added to wells designated for background readings and 3 “no protein” control wells. The microplate was shook at 700 rpm at RT for 5 minutes. Lastly, the microplate was dark adapted for 10 minutes then luminescence was measured using a microplate reader (PheraStar).

To generate robust data, background luminescence was subtracted from reaction luminescence. Blank luminescence was disregarded because it was lower than the luminescence detected in wells designated for 0 mM standard. Luminescence readings were normalised by protein concentration compared between brains.

2.18 NAD/NADH assay

Abcam’s NAD/NADH assay kit was used (ab65348), according to manufacturer’s instructions. This kit detects NADH only; it’s NAD Cycling Enzyme Mix converts existing NAD^+ in samples to NADH. To determine the NAD^+ level and NAD/NADH of a sample, the sample must be split into halves, one NAD^+-decomposed and the other unperturbed. In the presence of the NAD Cycling Enzyme Mix, the NAD^+-decomposed half of the sample would be used to detect NADH only while the unperturbed half of the sample would be used to detect NADtotal (NADT), that is, NAD^+ + NADH. NAD^+ levels were obtained by subtracting NADH levels from NADT levels. Also, NAD/NADH was obtained by dividing NAD^+ levels by NADH levels.

Fresh brain samples were first washed with cold 1X PBS. Cold 1X PBS was replaced with 400.0 µl NADH/NAD extraction buffer and per experiment group, 3 brains were homogenised in 400.0 µl

NADH/NAD extraction buffer by 50 passages using a Dounce homogeniser. Homogenate was centrifuged for 5 minutes at maximum speed at 4°C and supernatant was collected. 20.0 µl supernatant was collected for protein quantification (**Section 2.16**). Remaining supernatant was centrifuged for 2 hours 30 minutes at maximum speed at 4°C, using a 10 kDa spin column (ab93349) to remove NADH consuming enzymes.

Next, per sample, supernatant was split into two. Half of the supernatant was incubated for 30 minutes at 60°C to decompose NAD$^+$ while the other half was kept on ice. Master mixes of NAD$^+$-decomposed (NADH) and unperturbed samples (NADT; NAD$^+$+NADH) were prepared using NADH/NAD extraction buffer, ensuring that each well of the flat-bottomed 96-well microplate (Greiner) contained 25.0 µg protein per sample.

Likewise, reaction (NAD cycling buffer and NAD cycling enzyme mix) and background (NAD cycling buffer only) master mixes were prepared for the detection of sample and background readings (**Table 2.13**).

Component	Reaction mix (µl)	Background mix (µl)
NAD Cycling Buffer	98.0	100.0
NAD Cycling Enzyme Mix	2.0	0.0

Table 2.13. Components of reaction and background master mixes prepared for the NAD/NADH assay. *100.0µl reaction mix (98.0 µl NAD Cycling Buffer + 2.0 µl NAD Cycling Enzyme Mix) was added to each well designated for sample readings (triplicate) while 100.0 µl background mix (100.0 µl NAD Cycling Buffer) was added to each well designated for background readings. To prevent variability between wells, reaction and background master mixes were prepared, accordingly. NAD, nicotinamide adenine dinucleotide.*

Also, NADH standards ranging from 0-100.0 pmol/well were prepared, by diluting 10.0 pmol/µl NADH standard in NADH/NAD extraction buffer. 50.0 µl NADH and NADT master mixes, as well as 50.0 µl NADH standards were added to designated wells (triplicate wells for NADH and NADT, and duplicate wells per standard concentration), followed by the addition of 100.0 µl reaction mix to wells designated for standards and sample readings, and the addition of 100.0 µl background mix to wells designated for background readings only. The flat-bottomed 96-well plate was incubated for 5 minutes at RT to convert NAD$^+$ to NADH, then 10.0 µl NADH developer was added to each well. Absorbance was measured at OD 450 nm with 15-minute intervals for 210 minutes, using a microplate reader (PheraStar).

Data was analysed by extrapolating NADH concentrations at 105 minutes (during the linear phase of the reaction) from absorbance readings, using NADH standards. Sample background NADH readings were subtracted from sample NADH readings, if necessary, thereby correcting sample NADH readings.

Readings were also normalised by protein concentration. NAD^+ and NAD/NADH values were calculated, as previously detailed.

2.19 Zebrafish movement assay

Zebrafish behaviour is an important assay used to assess the effect of genetic mutations and/or pharmacological agents on spontaneous and stimulus-evoked movements.

2.19.1 Larval movement assay protocol

Larval behaviour assays were completed at the University of Pittsburgh, using a protocol designed and published by the Burton laboratory in Zhou *et al.*, (2014). Here, zebrafish movement is tracked using a matrix laboratory (MATLAB) application called *LSRtrack* while movement is analysed using either *LSRanalyze* or *VMRanalyze*.

To acclimate embryos to a light cycle, they were incubated in a 28°C light cycle incubator (14-hour light: 10-hour dark) from 0dpf until the time of the assay, with no more than 30 embryos per petri-dish.

To run this assay, 6dpf larvae were first transferred into wells of a black 96-well plate (CoStar) and each well was filled with 1X E3 media (without methylene blue) till a convex meniscus was obtained at the top of each well. Next, the 96-well plate was transferred to a 28°C incubator and larvae were habituated to dark:light cycles by exposing them to 3x 5-minute dark: 5-minute light cycles. Following habituation, larvae were exposed to 3x 10-minute dark: 10-minute light cycles followed by 1 hour light exposure (**Figure 2.9**) and movement during the entire 2-hour period was recorded using a *Flea3* camera (Point Grey Research).

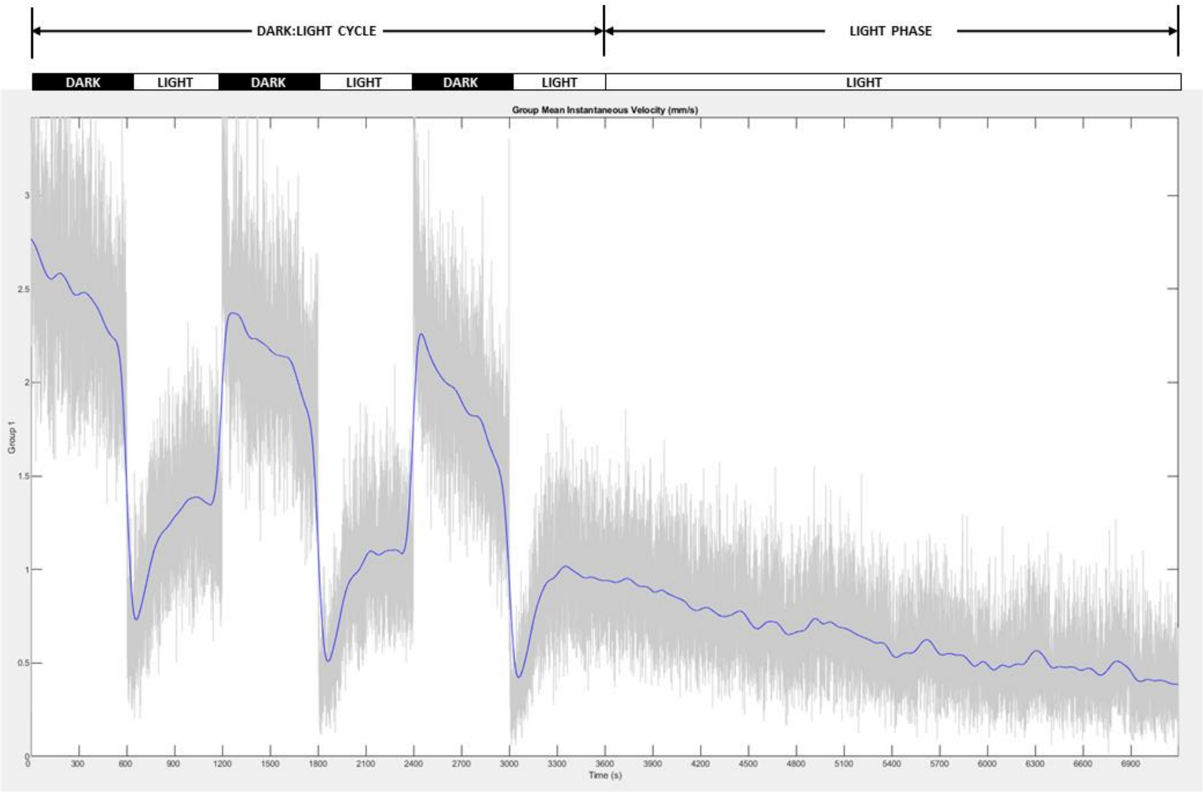

Figure 2.9. Demarcation of the dark:light cycle and the light phase used to analyse larval movement in this PhD. *The dark:light cycle refers to the 3x 10-minute dark: 10-minute light cycles while light exposure refers to 1 hour where larvae are exposed to light.*

2.19.2 Tracking and analysis of larval movement

LSRtrack was used to track zebrafish movement for the 2-hour period. *VMRanalyze* was used to analyse movement in the 3x 10-minute dark: 10-minute light cycles while analysis of movement in the light phase was done using *LSRanalyze*. The single parameter used to analyse movement in the dark:light cycles was mean speed while mean speed, active speed, % time moving, active duration and rest duration were used to analyse movement in the light phase.

To analyse larval movement in the dark:light cycle, larval speeds at each minute were averaged across all 3 cycles. Larval movement in the light phase was analysed using the mean speed, active speed, % time moving, active duration and rest duration data generated using *LSRanalyze*.

Mean speed refers to the average speed of a larva for the duration of the recording. Active speed refers to the mean speed of a larva for the duration which it moved during the recording. % time moving is the amount of time a larva moved during the recording, expressed as a %. Active duration is the mean duration of movement events of a larva during the recording while rest duration of a larva is the mean time interval between movement events during the recording (**Figure 2.10**).

Figure 2.10. Schematic illustrating the difference between % time moving, active duration and rest duration. *Assume each rectangle shown in 1, 2 and 3 refers to the duration of a larva during a movement recording. Active duration refers to the mean duration of movement events during the recording while rest duration refers to the mean time interval between movement events during the recording. % time moving refers to the duration of movement during the recording, expressed as a %. In 1, there are 9 equal-sized green and red rectangles, representing movement and rest periods, respectively. Therefore, active and rest duration are equal. In this case, 10 s was arbitrarily assigned to both active and rest duration, and 50% was arbitrarily assigned to % time moving because half of the rectangles are green while the other half are red. In 2, there are 6 smaller green rectangles and 6 larger red rectangles. The larger red rectangles signify longer rest periods. 10 s was arbitrarily assigned to active duration. However, due to longer rest periods and therefore a longer mean time interval between movement events, 20 s was arbitrarily assigned to rest duration. Likewise, 33% was arbitrarily assigned to % time moving because of longer rest periods. In 3, there are 12 equal-sized green and red rectangles. Therefore, 10 s was arbitrarily assigned to active and rest duration and 50% was arbitrarily assigned to % time moving, like in 1.*

This protocol has marked advantages over its commercial equivalents. To name a few, the *LSRtrack*, *LSRanalyse* and *VMRanalyze* applications are free, can be used with a variety of suitable cameras and behaviour analysis chambers. Also, *LSRtrack* reports zebrafish tracking errors.

2.19.3 Adult movement assay protocol and data analysis

Adult zebrafish movement assay and data analysis were conducted by Dr Deepak Ailani. Adult zebrafish were placed in individual tanks containing system water. Movement was recorded for 7 hours using a ViewPoint camera and tracked using the ViewPoint software. The first hour of recording served as the habituation period and was not included in data analysis. Normality was assessed using D'Agostino & Pearson test and statistical significance was tested using a two-tailed unpaired t-test.

2.20 *In silico* analysis

Zebrafish orthologues of human genes were identified using Ensembl's "orthologues" tool. Human transcripts with a "Matched Annotation from NCBI and EMBL-EBI (MANE) Select" tag and zebrafish transcripts with an "Ensembl Canonical" tag were selected as biologically relevant transcripts. Basic Local Alignment Search Tool (BLAST) programs were used to align human sequences with zebrafish sequences. BLASTN was used to align human *cDNA* sequences against the zebrafish transcriptome. BLASTP was used to align human protein sequences against the zebrafish proteome. In concert, CLUSTAL was used to align human protein sequences against the protein sequences of their zebrafish homologues. The National Centre for Biotechnology Information (NCBI) online alignment tool was used to align a query cDNA sequence with the zebrafish or human transcriptome. DNA sequences were edited to account for CRISPR-induced mutations, using SnapGene. Resulting truncated proteins were also predicted using SnapGene. Protein domains were identified using the Superfamily, SMART, Pfam, PROSITE profiles databases available on Ensembl.

2.21 Statistical analysis

Statistical analysis was performed using GraphPad Prism 9. Graphs are presented as mean ± standard error of the mean. Unless stated otherwise, normality was assessed using D'Agostino & Pearson test. Larval experiments were conducted in at least triplicate. A clutch of embryos from a single set of parents represented a biological replicate with the exception of dopaminergic neuron counting experiments where 2 clutches of embryos were combined to obtain a biological replicate. For larval experiments, statistical difference between the control groups of different biological replicates was investigated before combining datasets. Each zebrafish served as a biological replicate for adult experiments. Significance was set at 0.05.

Chapter 3: Zebrafish as a model for *KLOTHO* deficiency

3.1 Introduction

3.1.1 Background

Named after the Greek goddess of destiny who spins the thread of life, *Klotho* is an ageing-suppressor gene (Kuro-o *et al.*, 1997). First reported in 1997, *Klotho* mutant mice developed normally and were indistinguishable from their littermates, until 4 weeks after birth, when they displayed an accelerated ageing phenotype characterised by growth retardation, motor impairment, infertility, thymic atrophy, arteriosclerosis, ectopic calcification, osteoporosis, skin atrophy, emphysema, an abnormal pituitary gland, and a moderate increase in serum calcium and phosphate. This accelerated ageing phenotype was confirmed to be the result of Klotho deficiency, as it was rescued by exogenous expression of *Klotho* cDNA. *Klotho* mutant mice died between 8-9 weeks after birth (Kuro-o *et al.*, 1997).

Although predominantly expressed in the kidneys, the mouse *Klotho* transcript is also expressed in the brain, placenta, skeletal muscle, urinary bladder, aorta, pancreas, testis, ovary, colon and thyroid gland (Kuro-o *et al.*, 1997), explaining the phenotype displayed by *Klotho* mutant mice.

The human *KLOTHO* gene has 5 exons, all of which are protein-coding, and is located on chromosome 13 (Matsumura *et al.*, 1998). The resulting protein is a 1,012 amino acid single-pass transmembrane protein with an intracellular and an extracellular domain (Kuro-o *et al.*, 1997; Matsumura *et al.*, 1998). This extracellular domain contains 2 domains, namely KL1 and KL2 domains, which are homologous to family 1 glycoside hydrolases, also known as glycosidases. The extracellular domain also contains a signal peptide which is responsible for the translocation of Klotho from the cytosol to the cell membrane (**Figure 3.1**) (Matsumura *et al.*, 1998; Mian, 1998).

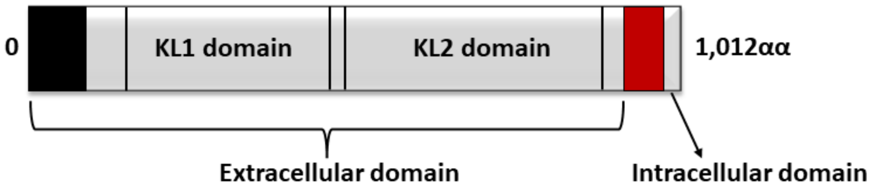

Figure 3.1. Full-length transmembrane KLOTHO protein structure. *KLOTHO protein is a single-pass transmembrane protein comprised of an extracellular and an intracellular domain. The extracellular domain contains a signal peptide (black box) for protein translocation from the cytosol to the cell membrane, and 2 glycoside hydrolase domains, namely KL1 and KL2. The red box indicates the transmembrane domain.*

Human *KLOTHO* mRNA expression is reported in the kidneys, prostate, small intestine and placenta (Matsumura *et al.*, 1998). Human KLOTHO is expressed in the kidneys, cerebral cortex, cerebellum, spinal cord, renal artery, aorta, epigastric artery, keratinocytes and mammary epithelial cells (Lim *et al.*, 2015).

KLOTHO's transmembrane domain can be cleaved by α-secretases, β-secretase and γ-secretase to release its extracellular domain; this process is called ectodomain shedding. α-secretases involved in ectodomain shedding include, a disintegrin and metalloproteinase 10 (ADAM10) and ADAM17 (Chen *et al.*, 2007; Bloch *et al.*, 2009). Shed KLOTHO, called soluble KLOTHO, is circulated in serum and cerebrospinal fluid (CSF) (Imura *et al.*, 2004).

Likewise, a splice variant of *KLOTHO* mRNA encodes an alternate protein that contains the signal peptide and KL1 domain only, called secreted klotho (Matsumura *et al.*, 1998; Shiraki-Iida *et al.*, 1998). However, transmembrane and soluble KLOTHO are the 2 forms of the protein consistently detected *in vivo* (Xu and Sun, 2015).

A homologous protein to KLOTHO, called βKLOTHO is also expressed in humans (Ito *et al.*, 2000; Dongiovanni *et al.*, 2020), causing the nomenclature change of the initially discovered KLOTHO protein to αKLOTHO. However, for the purpose of this thesis, KLOTHO refers to αKLOTHO.

Physiologically, KLOTHO acts as a co-receptor for fibroblast growth factor 23 (FGF23), an endocrine factor. KLOTHO binds directly to FGF receptor 1c (FGFR1c), one of FGF23's receptors, by extending a receptor binding arm (RBA). FGF23 then binds to both FGFR1c and KLOTHO, using it's N- and C-terminus, respectively. Downstream, this FGFR1c-FGF23-KLOTHO complex stimulates FGFR1c's kinase activity; this pathway is implicated in phosphate and calcium homeostasis (Chen *et al.*, 2018). KLOTHO also binds to other FGF23 receptors, namely FGFR3c and FGFR4 (Kurosu *et al.*, 2006). The formation of this FGFR1c-FGF23-KLOTHO complex and the stimulation of FGFR1c's kinase activity are both heparan-sulfate dependent (Chen *et al.*, 2018).

FGF23 is secreted from osteocytes and osteoblasts in response to elevated serum phosphate, that is, hyperphosphataemia, active vitamin D and parathyroid hormone (PTH) (Feng *et al.*, 2006; Masuyama *et al.*, 2006; Barthel *et al.*, 2007; Lavi-Moshayoff *et al.*, 2010). FGF23 reduces mRNA and protein expression of NaPi-IIa, a type IIa sodium-phosphate cotransporter (Shimada *et al.*, 2004). NaPi-IIa is predominantly expressed in the proximal tubules of the kidneys, a major site for phosphate reabsorption (Murer, Forster and Biber, 2004). Consequently, FGF23-induced reduction of NaPi-IIa expression decreases serum phosphate levels, resulting in hypophosphataemia (Shimada *et al.*, 2001, 2004).

Active vitamin D and PTH are key regulators of calcium homeostasis; they promote calcium absorption from the intestine and calcium release from bones, respectively ('Guyton and Hall Textbook of Medical

Physiology', 2016). The binding of active vitamin D to the vitamin D receptor (VDR) triggers a signalling pathway that induces FGF23 production (Barthel *et al.*, 2007). Likewise, binding of PTH to the PTH receptor activates a signalling pathway that results in FGF23 production (Lavi-Moshayoff *et al.*, 2010). In contrast, FGF23 reduces serum levels of active vitamin D and PTH (Shimada *et al.*, 2004; Ben-Dov *et al.*, 2007), thereby preventing continuous FGF23 secretion.

While it is assumed that FGF23-mediated mineral homeostasis is dependent on KLOTHO, parathyroid-specific deletion of *Klotho* did not affect Fgf23's ability to reduce PTH secretion in rats (Olauson *et al.*, 2013), indicating that FGF23 may exert some of the above effects independent of KLOTHO.

In addition to FGF23, KLOTHO expression is also regulated by active vitamin D (Forster *et al.*, 2011). Therefore, the regulation of FGF, vitamin D and PTH, as well as KLOTHO, is required for mineral homeostasis.

Increased serum FGF23 is observed in patients with hereditary phosphate-wasting syndromes, such as autosomal dominant hypophosphataemic rickets (ADHR), X-linked hypophosphataemia (XLH) and autosomal recessive hypophosphataemic rickets (ARHR), as well as in patients with tumour-induced osteomalacia (TIO) (White *et al.*, 2000; Shimada *et al.*, 2001; Yu and White, 2005; Feng *et al.*, 2006).

Likewise, increased serum FGF23 is observed in patients with chronic kidney disease (CKD) (Isakova *et al.*, 2011). In contrast, decreased serum FGF23 is observed in patients with familial tumoural calcinosis (FTC), which is characterised by ectopic calcification and hyperphosphataemia (Garringer *et al.*, 2006). Hyperphosphataemia is also implicated in macrophage activation (Smith *et al.*, 2013). Interestingly, decreased serum KLOTHO is also observed in CKD patients (Zou *et al.*, 2018).

3.1.2 Model systems

Since 1997, further *Klotho* models have been generated. *klotho*'s role in ageing is conserved in *C.elegans*, as *klotho* KD reduces survival (Château *et al.*, 2010). Conversely, klotho overexpression increases the lifespan of Tg mice, beyond that of WT mice (Kurosu *et al.*, 2005). Klotho's effect on ageing and longevity is reported to result from high serum levels of active vitamin D as well as inhibition of the insulin and insulin-like growth factor-1 (IGF-1) signalling (Tsujikawa *et al.*, 2003; Kurosu *et al.*, 2005).

NaPi-IIa is translocated to the apical plasma membrane of renal proximal tubules in *Klotho* mutant mice (Li *et al.*, 2004), explaining hyperphosphataemia in these mice. In addition to the accelerated ageing phenotype reported by Kuro-o *et al.*, (1997), *Klotho* mutant mice display age-associated decline in cognitive ability, as well as increased oxidative stress and apoptosis in the hippocampus. This phenotype was rescued by administering an anti-oxidant, α-tocopherol (Nagai *et al.*, 2003). Treatment with exogenous Klotho also improves cognition in young and old WT mice (Leon *et al.*, 2017).

Klotho KD in WT mouse muscle progenitor cells (MPCs) alters mitochondrial structure, decreases mitochondrial function and increases mtDNA damage. Likewise, MPCs isolated from *Klotho* heterozygous mice have reduced mitochondrial function and increased mtDNA damage. Muscle regeneration is also impaired in *Klotho* heterozygous mice. Exogenous expression of Klotho rescues impaired muscle regeneration in old WT mice (Sahu *et al.*, 2018).

With regards to microglial activation, selective *Klotho* KO in the mouse choroid plexus enhances microglial activation in the hippocampus following LPS injection. The effect of selective *Klotho* KO on microglial activation without LPS injection was not investigated (Zhu *et al.*, 2018).

3.1.3 The role of *KLOTHO* in human disease

3.1.3.1 Role in non-neurological diseases

Mutations in or near *KLOTHO* have also been reported in 2 patients. The first patient harboured a homozygous missense mutation (H193R) in KL1 which resulted in ectopic calcification, tumoral calcinosis, and increased serum levels of PTH and FGF23 (Ichikawa *et al.*, 2007). The second patient harboured a *de novo* translocation between chromosomes 9 and 13; the translocation breakpoint was in close proximity to *KLOTHO*, which is located on chromosome 13. This patient had hypophosphataemic rickets, hyperparathyroidism, hypercalcaemia, and increased serum levels of KLOTHO and FGF23 (Brownstein *et al.*, 2008). An effect of these mutations on lifespan was not reported in either patient (Ichikawa *et al.*, 2007; Brownstein *et al.*, 2008).

Likewise, a variant *KLOTHO* allele harbouring 6 SNPs with perfect linkage disequilibrium has been identified and named the KL-VS haplotype. Two of these SNPs, rs9536314 and rs9527025 cause amino acid substitutions, F352V and C370S, respectively (Arking *et al.*, 2002; Freathy *et al.*, 2006). Individuals heterozygous for KL-VS have increased serum KLOTHO levels, increased lifespan and decreased risk of cardiovascular disease (CVD) (Arking *et al.*, 2002, 2005; Dubal *et al.*, 2014). Individuals homozygous for KL-VS have decreased lifespan and increased risk of CVD (Arking *et al.*, 2005; Dubal *et al.*, 2014).

3.1.3.2 Role in neurodegenerative diseases

To model multiple sclerosis (MS), oligodendrocyte apoptosis and demyelination were induced in Klotho-overexpressing and WT mice by including the neurotoxic agent-, cuprizone in animal feed. Mice were also treated with rapamycin, to inhibit the proliferation of oligodendrocyte progenitor cells (OPCs), thereby inhibiting the differentiation of new oligodendrocytes (Zeldich *et al.*, 2015).

Remyelination was observed in the corpus callosum of Klotho-overexpressing and WT mice 3 weeks after cuprizone and rapamycin treatment. The number of myelinated axons per unit length of the corpus callosum was 1.88 times higher in Klotho-overexpressing mice compared to WT mice. Also, the density of myelinated axons per unit area was 1.76 fold higher in Klotho-overexpressing mice compared to WT mice (Zeldich *et al.*, 2015).

Intracerebral Klotho overexpression was induced in Amyloid Precursor Protein/Presenilin 1 (APP/PS1) mice by the injection of a lentivirus containing murine *Klotho* cDNA. Klotho overexpression ameliorated amyloid-β (Aβ) burden, neuronal loss and cognitive deficits in APP/PS1 mice (Zhao *et al.*, 2020). Likewise, heterozygosity for the KL-VS haplotype is associated with reduced AD risk in carriers of the *Apolipoprotein e4* (*APOE4*) allele (Belloy *et al.*, 2020).

3.1.3.3 Role in PD

The number of dopaminergic neurons in the SNPc of *Klotho* mutant mice is reduced, in an age-dependent manner. This reduction in dopaminergic neuron number is accompanied by reduced cytoplasmic volume of dopaminergic neurons and reduced striatal dopamine, indicating dopaminergic neuron degeneration. This neurological phenotype is rescued by dietary restriction of vitamin D (Kosakai *et al.*, 2011), indicating that high serum levels of vitamin D play a role in dopaminergic neuron degeneration in *Klotho* mutant mice.

While Kuro-o *et al.*, (1997) reported motor impairment in *Klotho* mutant mice and a decrease in the number of cerebellar Purkinje cells, they did not examine the SNPc. Kosakai *et al.*, (2011) reported a 25% reduction of dopaminergic neurons in *Klotho* mutant mice. However, a previous MPTP study showed that a minimum reduction of 43.2% of dopaminergic neurons is required to observe a motor phenotype in monkeys (Bezard *et al.*, 2001). Therefore, it is plausible that *Klotho* mutant mice die before PD onset and the reported motor impairment is the result of cerebellar dysfunction (Kosakai *et al.*, 2011).

Klotho protects cells from oxidative stress by inhibiting forkhead box transcription factor (FOXO) phosphorylation, thereby promoting nuclear translocation where FOXO increases the expression of an anti-oxidant, superoxide dismutase 2 (SOD2) (Yamamoto *et al.*, 2005). This proved relevant as *Klotho* is expressed in the mouse substantia nigra and Klotho overexpressing mice are resistant to MPTP-induced dopaminergic neuron toxicity (Brobey *et al.*, 2015). Treatment with exogenous Klotho improves cognition and rescues motor impairment in mice overexpressing human WT α-Synuclein (Leon *et al.*, 2017).

Additional studies have investigated the role of KLOTHO in PD patients. Zimmermann *et al.*, (2021) analysed 2 longitudinal cohorts of PD patients; cohort 1, the Tuebingen Parkinson cohort, comprised of 459 PD patients who were stratified for the KL-VS haplotype. A subgroup of cohort 1 comprised of 125 PD patients and 50 age-matched healthy controls without evidence of neurodegenerative diseases. All participants in this subgroup were stratified for the KL-VS haplotype, and CSF levels of KLOTHO and FGF23 were measured. Cohort 2, the Parkinson's Progression Markers Initiative (PPMI) cohort, comprised of 297 PD patients who were also stratified for the KL-VS haplotype. Results for Cohorts 1 and 2 but not the subgroup of cohort 1 were stratified for sex. Only patients heterozygous for the KL-VS haplotype were included in this study.

While there was no difference in age of PD onset and disease duration between PD patients heterozygous for the KL-VS haplotype (n = 108) and PD patients with WT *KL* (n = 351) in cohort 1, PD patients with the KL-VS haplotype had an earlier onset of cognitive impairment. The same applied to PD patients in cohort 2 (n; KL-VS haplotype = 79 patients, WT *KL* = 218 patients) (Zimmermann *et al.*, 2021).

Effect of the KL-VS haplotype on cognitive impairment was gender-specific with female patients having an earlier onset in cohort 1 (n; female KL-VS haplotype = 45 patients, male KL-VS haplotype = 63 patients, female WT *KL* = 131 patients, male WT *KL* = 220 patients) while male patients had an earlier onset of cognitive impairment in cohort 2 (n; female KL-VS haplotype = 24 patients, male KL-VS haplotype = 55 patients, female WT *KL* = 73 patients, male WT *KL* = 145 patients) (Zimmermann *et al.*, 2021).

PD patients in the cohort 1 subgroup had motor impairment which was absent in controls, as expected. Patients heterozygous for the KL-VS haplotype also had worse motor impairment in cohort 2 but the KL-VS haplotype had no effect on motor impairment in cohort 1 (Zimmermann *et al.*, 2021).

Analysis of the cohort 1 subgroup revealed that PD patients had reduced CSF levels of KLOTHO and FGF23 compared to control. However, patients heterozygous for the KL-VS haplotype had increased CSF KLOTHO levels compared to patients with WT *KL* and the KL-VS haplotype had no effect on CSF FGF23 levels (n; KL-VS haplotype = 29 patients, WT *KL* = 96 patients) (Zimmermann *et al.*, 2021). These results are summarised below (**Table 3.1**). Although these results are somewhat confusing, KLOTHO mitigates oxidative stress (Yamamoto *et al.*, 2005), therefore, reduced CSF KLOTHO levels in PD patients further implicate KLOTHO as a potential PD biomarker. Furthermore, CSF KLOTHO levels decrease in normal ageing (Semba *et al.*, 2014).

Parameter	Cohort 1- Main group (KL-VS versus WT *KL*; 108 versus 351 patients, respectively)	Cohort 1- Subgroup (PD patients versus healthy control; 125 versus 50 healthy controls)	Cohort 1- Subgroup (KL-VS versus WT *KL*; 29 versus 96 patients, respectively)	Cohort 2 (KL-VS versus WT *KL*; 79 versus 218 patients, respectively)
Age of PD onset	Unaffected	Unaffected	Unaffected	Unaffected
Disease duration	Unaffected	Unaffected	Unaffected	Unaffected
Onset of cognitive impairment	Earlier in female participants	N/A	N/A	Earlier in male participants
Motor impairment	Unaffected	Present	Unaffected	Worse
CSF KLOTHO levels	N/A	Reduced	Increased	N/A
CSF FGF23 levels	N/A	Reduced	Unaffected	N/A

Table 3.1. Summary of results reported by Zimmermann et al., (2021). *Using 2 longitudinal cohorts, Zimmermann et al., (2021) investigated KLOTHO's effect on PD. N/A refers to parameters not investigated in a cohort. CSF, cerebrospinal fluid; FGF23, fibroblast growth factor 23; PD, Parkinson's disease.*

Sancesario *et al.*, (2021) investigated CSF and serum KLOTHO levels in 26 and 22 PD patients, respectively. 9 age-matched healthy individuals without neurodegenerative diseases served as control. Patients were not stratified for the KL-VS haplotype.

CSF KLOTHO levels were increased in PD patients compared to control while serum KLOTHO levels were reduced in PD patients compared to control. These results were unaffected by the age and sex of participants. CSF KLOTHO levels were also inversely associated with CSF α-Synuclein levels (Sancesario *et al.*, 2021).

Kakar *et al.*, (2021) analysed the KLOTHO levels of 122 plasma samples from the Fox Investigation for New Discovery of Biomarkers (BioFIND) cohort. 61 plasma samples were obtained from PD patients while another 61 plasma samples were obtained from age- and sex-matched healthy controls.

Although there was no difference in plasma KLOTHO levels between PD patients and control, plasma KLOTHO levels were higher in female compared to male PD patients (Kakar *et al.*, 2021).

In conclusion, although peripheral KLOTHO levels in PD patients are conflicting, CSF KLOTHO levels reported by Sancesario *et al.*, (2021) and Zimmermann *et al.*, (2021) were measured in patients with a mean disease duration of 4 and 7 years, respectively, suggesting that CSF KLOTHO levels may increase at PD onset to mitigate neurodegeneration but eventually decrease with disease progression. The reason for increased CSF KLOTHO levels in PD patients with the KL-VS haplotype compared to PD patients with WT *KL* remains unknown and further studies are needed to elucidate this matter.

Also, Sancesario *et al.*, (2021) and Zimmermann *et al.*, (2021) measured CSF and serum levels of soluble KLOTHO while Kakar *et al.*, (2021) measured plasma levels of full-length KLOTHO. Therefore, differences in fluids as well as the type of KLOTHO measured could explain the conflicting result obtained by Kakar *et al.*, (2021).

3.1.4 *klotho* mutant zebrafish

Zebrafish have also been used to study *klotho* and *fgf23*. Both *klotho* and *fgf23* are conserved in zebrafish, with each having a single zebrafish orthologue on chromosome 10 and 4, respectively (Itoh and Konishi, 2007; Sugano and Lardelli, 2011; Mangos *et al.*, 2012). Both KL1 and KL2 protein domains are conserved in zebrafish klotho (Mangos *et al.*, 2012). *klotho* expression is detected as early as 5hpf and is expressed in the brain, kidneys, pancreas and liver of zebrafish larvae. *klotho* is also expressed in the brain, gill, heart, kidneys, testis, ovary and intestine of adult zebrafish (Sugano and Lardelli, 2011; Mangos *et al.*, 2012). *fgf23* expression is first detected between 24-48hpf in the corpuscles of Stannius (CS), an endocrine gland involved in maintaining calcium and phosphate homeostasis (Mangos *et al.*, 2012; Lin, Hu and Hwang, 2017). *fgf23* expression in the CS persists to adulthood (Mangos *et al.*, 2012).

There are currently 2 published *klotho* mutant zebrafish lines (A. P. Singh *et al.*, 2019; Ogura *et al.*, 2021). Singh *et al.*, (2019) generated both *klotho* and *fgf23* mutant zebrafish lines and showed that both are morphologically indistinguishable from WT siblings until 5mpf when they develop the same phenotype; emaciation, tattered fins and reduced survival. However, motor impairment occurs as early as 2mpf and continues after the onset of the accelerated ageing phenotype in both *klotho* and *fgf23* mutants. Importantly, *klotho* and *fgf23* mutations do not induce a survival disadvantage, until adulthood (A. P. Singh *et al.*, 2019).

klotho mutant zebrafish have ectopic calcification, particularly in the bulbus arteriosus (BA) which is the outflow tract of the zebrafish heart. *klotho* mutant zebrafish BA also has high osteoclast activity, indicating bone remodelling. *fgf23* mutant zebrafish also have severe BA calcification (A. P. Singh *et al.*, 2019).

Although there was no morphological change in the kidneys of 5mpf *klotho* mutant zebrafish, there was an upregulation of genes involved in heme metabolism. Also, there was an upregulation of genes involved in ECM reorganisation in gills of 5mpf *klotho* mutant zebrafish. Gene expression changes in gills are likely important to ectopic calcification observed in *klotho* mutant zebrafish, as gills are the major site for calcium uptake in adult fish (Flik, Verbost and Bonga, 1995; A. P. Singh *et al.*, 2019).

Furthermore, there was an upregulation of genes involved in bone formation and remodelling in the hearts of 5mpf *klotho* mutant zebrafish (A. P. Singh *et al.*, 2019). Unfortunately, gene expression of zebrafish brain tissue was not investigated.

The second publication also reported that *klotho* mutant zebrafish are indistinguishable from WT siblings until 5mpf when they become emaciated. Survival was reduced in *klotho* mutant zebrafish to 9mpf. Importantly, the *klotho* mutation did not induce a survival disadvantage until adulthood. *klotho* mutant zebrafish also displayed motor impairment at 4mpf, before the onset of the accelerated ageing phenotype (Ogura *et al.*, 2021). This indicates that the cellular and molecular mechanisms driving accelerated ageing in *klotho* mutant zebrafish begin before the onset of the accelerated ageing phenotype.

In this chapter, the Bandmann *klotho* mutant zebrafish line (referred to as the *klotho*$^{-/-}$ zebrafish line in this thesis) will be discussed. Chapter-specific aims are provided below (**Section 3.1.5**).

3.1.5 Chapter-specific aims

This chapter describes:

- The systematic assessment of *klotho*$^{-/-}$ zebrafish for PD-relevant pathological mechanisms, namely loss of dopaminergic neurons, mitochondrial dysfunction, DNA damage and microglial activation.
- Whether *klotho* deficiency alters microglial activation in Tg(*eno2*:hsa.*SNCA*-ires-EGFP) zebrafish.

3.2 Methods

3.2.1 Generation of the stable *klotho*$^{-/-}$ zebrafish line

Prior to the start of this PhD, the *klotho*$^{-/-}$ zebrafish line was generated by Dr Marcus Keatinge, using CRISPR/Cas9 gene editing.

The *klotho*$^{-/-}$ allele harbours a 10bp deletion of TCTCACTGGA in exon 2 which deletes a BsrI restriction enzyme site. Therefore, the *klotho*$^{-/-}$ zebrafish line can be genotyped, using BsrI digest. PCR products obtained from *klotho*$^{+/+}$ zebrafish were digested giving 75- and 177bp bands, while PCR products obtained from *klotho*$^{-/-}$ zebrafish were undigested, giving a single 242bp band. Due to the presence of a single copy of the WT and mutant allele, PCR products obtained from *klotho*$^{+/-}$ zebrafish were both digested and undigested, giving 75-, 177- and 242bp bands (**Figure 3.2A**).

This 10bp deletion induces a premature stop codon (TAA) immediately after 855bp. The predicted protein is truncated within its kl1 domain, having 285 instead of 990 amino acids. Therefore, the predicted protein lacks most of the kl1 domain and all of the kl2 domain (**Figure 3.2B**).

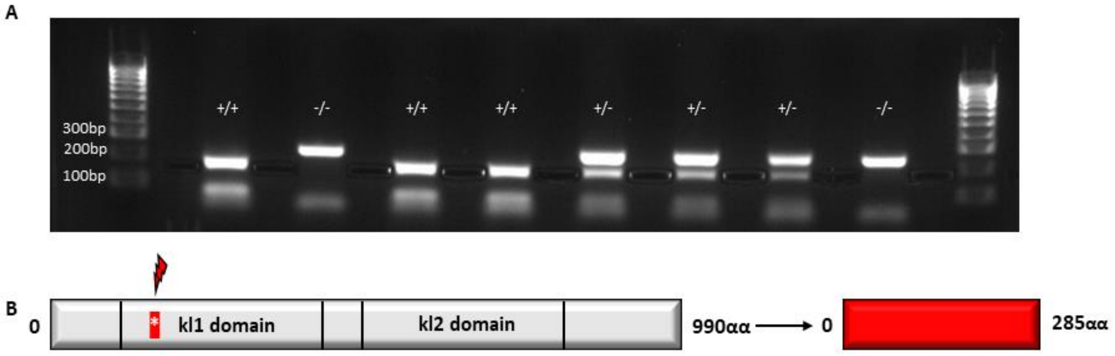

Figure 3.2. Generation of the stable klotho$^{-/-}$ zebrafish line using CRISPR/Cas9 gene editing. *The klotho mutation is a 10bp deletion of TCTCACTGGA in exon 2 which can be genotyped using BsrI digest. PCR products obtained from klotho$^{+/+}$ zebrafish were digested giving 75- and 177bp bands, while PCR products obtained from klotho$^{-/-}$ zebrafish were undigested, giving a single 242bp band. Due to the presence of a single copy of the WT and mutant allele, PCR products obtained from klotho$^{+/-}$ zebrafish were both digested and undigested, giving 75-, 177- and 242bp bands (A). This 10bp deletion induces a premature stop codon immediately after 885bp. The predicted protein is truncated, having 285 instead of 990αα, and lacks most of the kl1 domain and all of the kl2 domain (B). αα, amino acids; bp, base pairs; CRISPR, clustered regularly interspaced short palindromic repeats; Cas9, CRISPR-associated protein 9; PCR, polymerase chain reaction; WT, wildtype.*

3.2.2 ATP assay optimisation

To investigate *klotho*'s effect on mitochondrial function, ATP levels were measured in adult *klotho*$^{-/-}$ brains, using PerkinElmer's ATPlite Luminescence ATP Detection System (6016941) (**Section 2.17**). First, this system was optimised for adult zebrafish brain tissue because it had not been used to measure zebrafish ATP levels prior to this PhD.

Two fresh adult WT zebrafish brains were used for optimisation. Prior to running this assay, the protein concentration of each brain was determined using a Bradford assay (**Section 2.16**). Each brain was serially diluted to 1/8 dilution, using lysis solution and the µg protein of each brain dilution is provided below (**Table 3.2**).

Dilution Factor	**µg protein**	
	Brain 1	**Brain 2**
1/8 Dilution	4.3 µg	4.9 µg
1/4 Dilution	8.7 µg	9.7 µg
1/2 Dilution	17.4 µg	19.4 µg
1x Protein	34.7 µg	38.8 µg

Table 3.2. µg protein of adult WT zebrafish brains used for the optimisation of PerkinElmer's ATPlite luminescence ATP detection system. *ATP, adenosine triphosphate; WT, wildtype.*

MQ was added to serial dilutions in lieu of substrate solution, which according to PerkinElmer is required for ATP detection. To assess the protein concentration needed to detect robust ATP signals, background readings were compared to sample readings, per dilution. To ensure the luminescence detected was proportional to brain ATP levels, ATP standards were included during optimisation.

There was a significant difference between background and sample readings in 1/4 dilution, 1/2 dilution and 1x brain lysates, that is, undiluted, but not in 1/8 dilution of brain lysate (1/8 dilution- MQ = 0.0101, Substrate solution = 0.0110, $p = 0.0695$; 1/4 dilution- MQ = 0.0101, Substrate solution = 0.0119, $p = 0.0010$; 1/2 dilution- MQ = 0.0102, Substrate solution = 0.0137, $p<0.0001$; 1x protein- MQ = 0.0102, Substrate solution = 0.0179, $p<0.0001$, **Figure 3.3**).

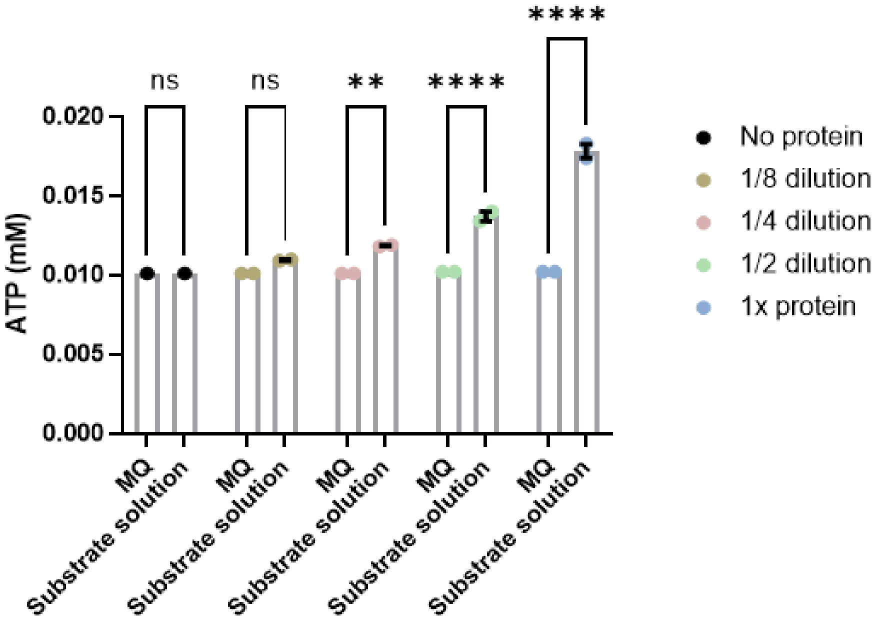

Figure 3.3. Optimisation of PerkinElmer's ATPlite luminescence ATP detection system for adult zebrafish brain tissue (ATP). *Optimisation experiment utilised 2 fresh adult WT zebrafish brains. Brains were homogenised using ATP lysis solution and protein concentrations were determined using a Bradford assay. Serial dilutions of brain lysates were prepared, using ATP lysis solution. To assess the amount of protein needed to detect robust ATP signal, that is ATP signal which is significantly higher than background signal, serial dilutions were incubated in either MQ or substrate solution. Error bars represent standard error of the mean. Data was analysed using a two-way ANOVA with Šídák's multiple comparisons. n; brain = 2. p>0.9999 (No protein MQ-Substrate solution), p = 0.0695 (1/8 dilution MQ-Substrate solution), p = 0.0010 (1/4 dilution MQ-Substrate solution), p<0.0001 (1/2 dilution MQ-Substrate solution), p<0.0001 (1x protein MQ-Substrate solution). ANOVA, analysis of variance; ATP, adenosine triphosphate; MQ, Milli-Q; WT, wildtype.*

Although ATP appeared to be detected in background wells (**Figure 3.3**), luminescence was undetectable (**Figure 3.4**), indicating that the accuracy of the ATP standard curve plotted for this optimisation experiment was reduced at low ATP concentrations. However, luminescence was directly proportional to ATP concentration for the range of ATP standards tested (**Figure 3.5**) and brain ATP levels were within the range of ATP standards tested, indicating that brain ATP levels were not above the detection limit of this assay. Thereby, ATP standards were not included in the subsequent experiment. 18.0 µg brain protein was utilised for the subsequent experiment, because this is within the range of protein concentrations in 1/2 dilution brain lysate used during optimisation (**Table 3.2**).

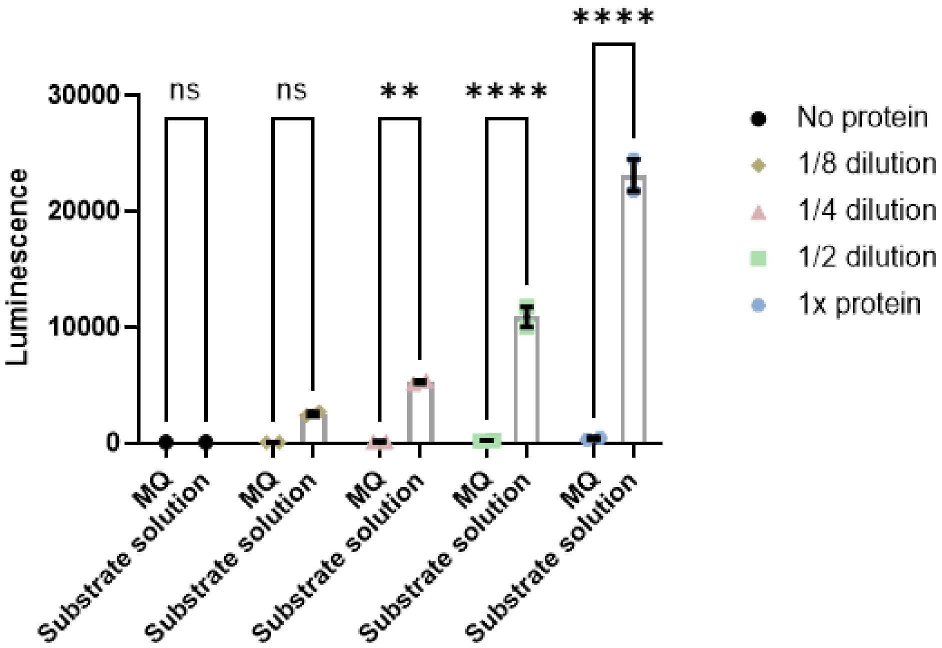

__Figure 3.4. Optimisation of PerkinElmer's ATPlite luminescence ATP detection system for adult zebrafish brain tissue (luminescence).__ Optimisation experiment utilised 2 fresh adult WT zebrafish brains. Brains were homogenised using ATP lysis solution and protein concentrations were determined using a Bradford assay. Serial dilutions of brain lysates were prepared, using ATP lysis solution. To assess the amount of protein needed to detect robust ATP signal, that is ATP signal which is significantly higher than background signal, serial dilutions were incubated in either MQ or substrate solution. Error bars represent standard error of the mean. Data was analysed using a two-way ANOVA with Šídák's multiple comparisons. n; brain = 2. p>0.9999 (No protein MQ-Substrate solution), p = 0.0827 (1/8 dilution MQ-Substrate solution), p = 0.0013 (1/4 dilution MQ-Substrate solution), p<0.0001 (1/2 dilution MQ-Substrate solution), p<0.0001 (1x protein MQ-Substrate solution). ANOVA, analysis of variance; ATP, adenosine triphosphate; MQ, Milli-Q; WT, wildtype.

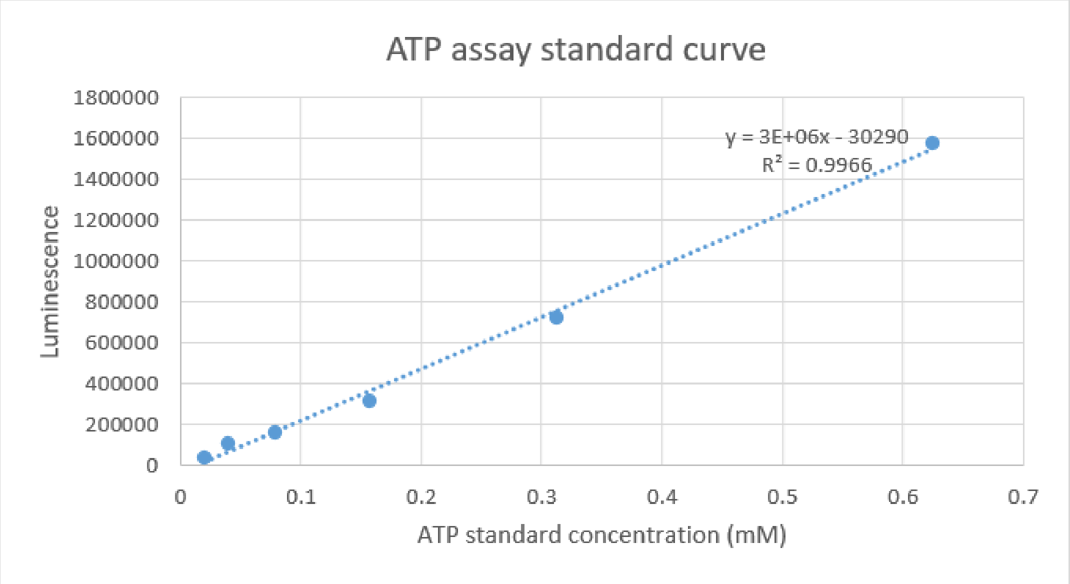

Figure 3.5. ATP assay standard curve. *To obtain the standard curve of the ATP optimisation assay, luminescence detected in wells containing ATP standards with known concentrations (0-0.6 mM) was plotted against ATP standard concentrations. Luminescence was directly proportional to ATP concentration.* $R^2 = 0.9966$. *ATP, adenosine triphosphate.*

3.2.3 NAD/NADH assay optimisation

NAD^+, NADH, NADT and NAD/NADH levels were measured, using Abcam's NAD/NADH assay kit (ab65348) (**Section 2.18**). This kit was first optimised for adult zebrafish brain tissue because it had not been used to measure zebrafish NAD^+, NADH, NADT and NAD/NADH levels prior to this PhD.

Two fresh adult WT zebrafish brains were used for this optimisation experiment; pilot data showed that NAD^+, NADH, NADT and NAD/NADH levels are undetectable using frozen brain tissue. Before running this NAD/NADH assay, the protein concentration of each brain was determined using a Bradford assay (**Section 2.16**). 25.0 µg, 15.0 µg and 10.0 µg protein were utilised for this optimisation experiment because pilot data showed that robust NADH results cannot be obtained from brain protein concentrations lower than 10.0 µg. Abcam recommends measuring absorbance at OD 450 nm for a duration of 1-4 hours to ensure that absorbance readings are robust and within the linear range of detection, that is, before absorbance plateaus. Measurement within this linear range is important because absorbance is proportional to NADT and NADH levels only within this linear range. Pilot data showed that absorbance readings plateau after 210 minutes. Therefore, absorbance readings were measured for 210 minutes in subsequent assays, including this optimisation experiment.

To detect background signal, background mix (which lacks NAD Cycling Enzyme Mix) was added to wells in lieu of reaction mix (which contains NAD Cycling Enzyme Mix). NAD Cycling Enzyme Mix is required for the detection of NADH and the determination of NAD^+, NADH, NADT and NAD/NADH levels.

In the presence of the reaction mix, NADT and NADH absorbance readings (OD 450 nm) were linear for the duration of measurement, with a concentration and time-dependent increase in absorbance, indicating the detection of robust NADT and NADH signals (**Figure 3.6**). 105 minutes was chosen as the timepoint at which NADT and NADH absorbance readings would be analysed, as it is the midpoint of 210 minutes. Comparable NADT and NADH results were obtained by analysing NADT and NADH absorbance readings measured at 165 minutes, further supporting the robustness of the results generated using this assay.

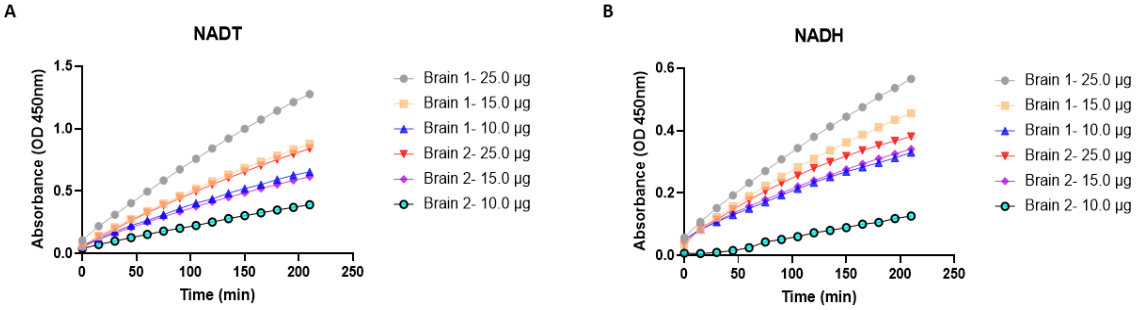

Figure 3.6. Brain NADT and NADH absorbance readings measured at OD 450 nm for 210 minutes. *Assay optimisation utilised 2 fresh adult WT zebrafish brains. Brains were homogenised using Abcam's NADH/NAD extraction buffer and protein concentrations were determined using a Bradford assay. Brain homogenates were diluted to obtain 25.0 µg, 15.0 µg and 10.0 µg protein. NADT and NADH absorbances were measured at OD 450 nm for 210 minutes. Robust signals were detected at 105 minutes and this timepoint was chosen for future analyses. NAD$^+$, nicotinamide adenine dinucleotide; NADH, reduced nicotinamide adenine dinucleotide; NADT, NADtotal; OD, optical density; WT, wildtype.*

To further assess the protein concentration needed to detect robust NADT and NADH signals at 105 minutes, background readings were compared to sample readings per brain protein concentration.

There was a significant difference between background and sample readings in wells containing 25.0 µg and 15.0 µg brain homogenate only (NADT; 25.0 µg- Background mix = 0.33 pmol, Reaction mix = 23.76 pmol, p = 0.0019; 15.0 µg- Background mix = 0.10 pmol, Reaction mix = 16.82 pmol, p = 0.0107; 10.0 µg- Background mix = 1.24 pmol, Reaction mix = 12.62, p = 0.0585, **Figure 3.7A**. NADH; 25.0 µg- Background mix = 0.07 pmol, Reaction mix = 11.36 pmol, p = 0.0015; 15.0 µg- Background mix = 0.14 pmol, Reaction mix = 9.62 pmol, p = 0.0038; 10.0 µg- Background mix = 1.96 pmol, Reaction mix = 7.15 pmol, p = 0.0604, **Figure 3.7B**). 25.0 µg brain protein was utilised for the subsequent experiment.

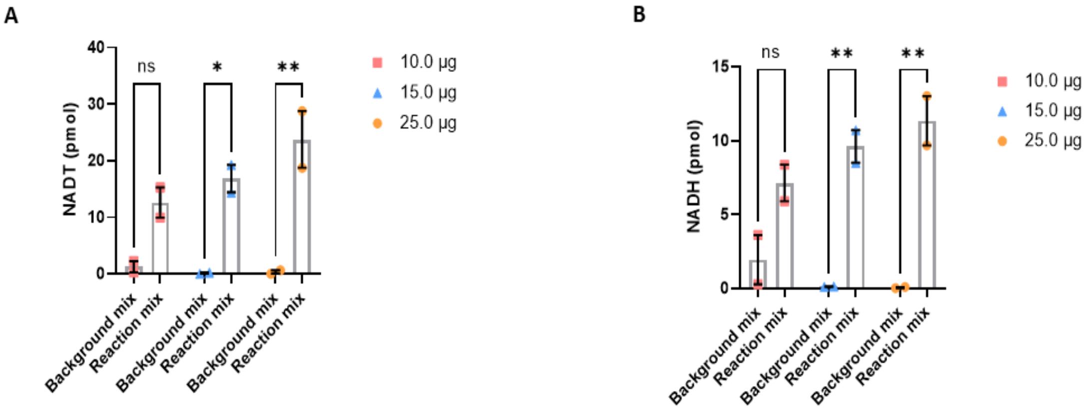

Figure 3.7. Optimisation of Abcam's NAD/NADH assay kit for adult zebrafish brain tissue. *Optimisation utilised 2 fresh adult WT zebrafish brains. Brains were homogenised using Abcam's NADH/NAD extraction buffer and protein concentrations were determined using a Bradford assay. Brain homogenates were diluted to obtain 25.0 µg, 15.0 µg and 10.0 µg brain protein. To further assess the protein concentration needed to detect robust NADT and NADH signals, brain homogenates were incubated in either background mix or reaction mix. Error bars represent standard error of the mean. Data was analysed using a two-way ANOVA with Šídák's multiple comparisons. n; brain = 2. p = 0.0585 (10.0 µg background mix-reaction mix; NADT), p = 0.0107 (15.0 µg background mix-reaction mix; NADT), p = 0.0019 (25.0 µg background mix-reaction mix; NADT), p = 0.0604 (10.0 µg background mix-reaction mix; NADH), p = 0.0038 (15.0 µg background mix-reaction mix; NADH), p = 0.0015 (25.0 µg background mix-reaction mix; NADH).*

3.2.4 PAR western blot optimisation

To investigate DNA damage in adult *klotho*$^{-/-}$ zebrafish brains, PAR expression was detected using a western blot (**Section 2.15**). First, PAR western blotting was optimised for adult zebrafish brain tissue because this had not been done prior to this PhD.

Two frozen brains extracted from 20mpf WT zebrafish were used for optimisation. Brains were homogenised in 2X SDS buffer (containing basemuncher, 1:1000) because robust PAR expression was detected in a pilot experiment, using this homogenisation method. Due to homogenisation in SDS buffer, brain protein concentration could not be quantified using a Bradford assay. Therefore, serial dilutions were used for this optimisation experiment, with the assumption that the volume of brain homogenate would be directly proportional to PAR expression, provided brain tissue from different zebrafish were of equal mass. Also, the presence of a loading control, glyceraldehyde-3-phosphate dehydrogenase (GAPDH), allows for the normalisation of PAR expression. H_2O_2-treated MRC cells (**Section 2.10.3**) served as positive control because H_2O_2 treatment increases PAR expression (Luo and Lee Kraus, 2012).

PAR expression was detected in both adult zebrafish brains and H_2O_2-treated MRC cells (**Figure 3.8**). The high MW protein detected in adult brains is likely tyrosyl-DNA phosphodiesterase 1 (TDP1), a DDR gene with a MW of 68.5 kDa (Kawale and Povirk, 2018) while the low MW proteins are likely histones (Pardridge *et al.*, 1989; Fulton *et al.*, 2021). The smear observed in H_2O_2-treated MRC cells is likely due to the addition of PAR moieties to proteins of different MWs (Campigli *et al.*, 2013). The nitrocellulose membrane was stripped then re-probed for GAPDH detection.

Following optimisation, 1.0 µl brain homogenate was utilised in the subsequent experiment because it was the lowest volume that detected robust PAR expression.

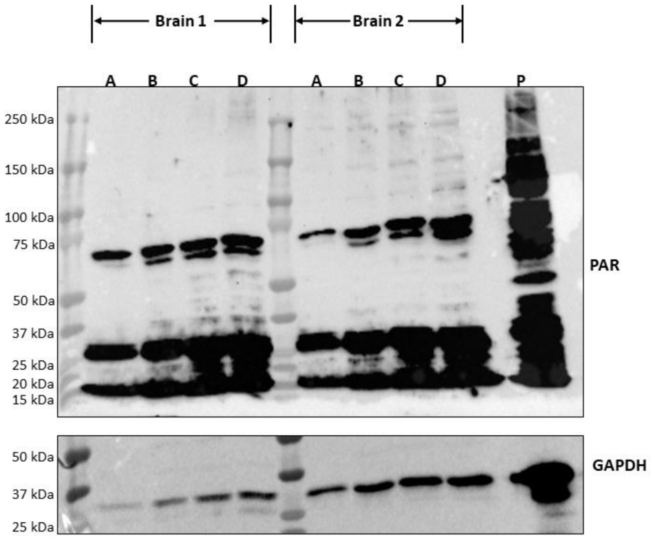

Figure 3.8. Optimisation of PAR western blot for adult zebrafish brain tissue. *Optimisation experiment utilised 2 frozen adult WT zebrafish brains (20mpf). Brains were homogenised using 2X SDS buffer. Serial dilutions were prepared by topping up 0.5 µl (A), 1.0 µl (B), 1.5 µl (C) and 2.0 µl (D) of brain homogenates to 10.0 µl, using 2X SDS buffer (containing basemuncher, 1:1000). 10.0 µl lysate of* H_2O_2*-treated MRC cells served as positive control (P). GAPDH served as loading control (MW of 36 kDa). This blot was stripped then re-probed for GAPDH detection. A 4-15% gradient gel was prepared to allow proper protein separation during electrophoresis. GAPDH, glyceraldehyde-3-phosphate dehydrogenase;* H_2O_2*, hydrogen peroxide; kDa, kilodaltons; mpf, months post fertilisation; MW, molecular weight; PAR, poly (ADP-ribose); SDS, sodium dodecyl sulfate; WT, wildtype.*

3.2.5 γH2AX western blot optimisation

To further investigate DNA damage in *klotho*$^{-/-}$ brains, γH2AX expression was detected, using a western blot (**Section 2.15**). γH2AX western blotting was first optimised for adult zebrafish brain tissue because it had not been done prior to this PhD.

Two frozen brains extracted from 20mpf WT zebrafish were used for optimisation. Brains were homogenised and homogenates were diluted as previously detailed (**Section 3.2.4**). GAPDH and H_2O_2-treated MRC cells served as loading and positive control (Li, Yang and Huang, 2006), respectively. γH2AX expression was detected in both brain homogenates and positive control (**Figure 3.9**). The portion of the blot corresponding to GAPDH's MW was previously cut. As a result, the cut portions of the blot were reassembled for GAPDH detection.

Following optimisation, 0.5 µl brain homogenate was utilised in the subsequent experiment because γH2AX expression detected using higher volumes appeared saturated.

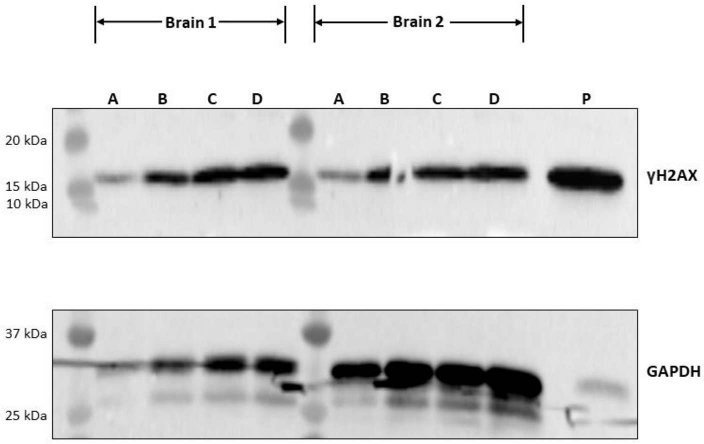

Figure 3.9. Optimisation of γH2AX western blot for adult zebrafish brain tissue. *Optimisation experiment utilised 2 frozen adult WT zebrafish brains (20mpf). Brains were homogenised using 2X SDS buffer (containing basemuncher, 1:1000). Serial dilutions were prepared by topping up 0.5 µl (A), 1.0 µl (B), 1.5 µl (C) and 2.0 µl (D) of brain homogenates to 10.0 µl, using 2X SDS buffer (containing basemuncher, 1:1000). 10.0 µl lysate of* H_2O_2*-treated MRC cells served as positive control (P). γH2AX (MW of 15 kDa) expression was detected in both brain samples and positive control. GAPDH served as loading control (MW of 36 kDa). A 4-15% gradient gel was prepared to allow proper protein separation during electrophoresis. γH2AX, gammH2AX; GAPDH, glyceraldehyde-3-phosphate dehydrogenase;* H_2O_2*, hydrogen peroxide; kDa, kilodaltons; mpf, months post fertilisation; MW, molecular weight; SDS, sodium dodecyl sulfate; WT, wildtype.*

3.2.6 Design and optimisation of genotyping primers for Tg(*eno2*:hsa.*SNCA*-ires-EGFP) zebrafish

The investigation into whether the mechanisms of ageing in *klotho*$^{-/-}$ zebrafish enhance PD-relevant pathological mechanisms required crossing monoallelic Tg(*eno2*:hsa.*SNCA*-ires-EGFP) zebrafish supplied by the Burton laboratory (**Section 2.1.2.4**) with the *klotho*$^{-/-}$ zebrafish line. Upon arrival at the Bateson Centre, monoallelic Tg(*eno2*:hsa.*SNCA*-ires-EGFP) embryos were raised to adulthood and the genotype of adult monoallelic Tg(*eno2*:hsa.*SNCA*-ires-EGFP) zebrafish was first confirmed before subsequent genetic crosses.

To confirm the genotype of adult monoallelic Tg(*eno2*:hsa.*SNCA*-ires-EGFP) zebrafish in a more efficient manner, genotyping primers were designed to amplify human *SNCA*. First, the sequence of the construct used to generate this Tg line (**Section 2.1.2.4**) was aligned with human *SNCA* cDNA sequence, using NCBI's online alignment tool. Results showed that this construct contains exons 2-6 of human *SNCA*. To prevent non-specific amplification, a pair of genotyping primers was designed to amplify exons 2-4 of human *SNCA* (**Figure 3.10B**).

Primer specificity was tested by out-crossing adult monoallelic Tg(*eno2*:hsa.*SNCA*-ires-EGFP) zebrafish, then amplifying DNA extracted from whole Tg offspring and Non-Tg siblings sorted by GFP fluorescence, and from whole unrelated WT embryos (n = 4 each) in a PCR reaction (**Section 2.2.2**). A bright 210bp band and a faint 100bp band were observed in PCR products of Tg offspring only (**Figure 3.10C**). No bands were observed in PCR products of Non-Tg siblings while a band was observed in the PCR product of a single WT embryo, albeit higher than 210bp (**Figure 3.10C**), thereby confirming primer specificity. This and subsequent PCR experiments were run using an annealing temperature of 65 °C, because non-specific amplification in unrelated WT embryos was observed in a pilot PCR experiment run using an annealing temperature of 60 °C.

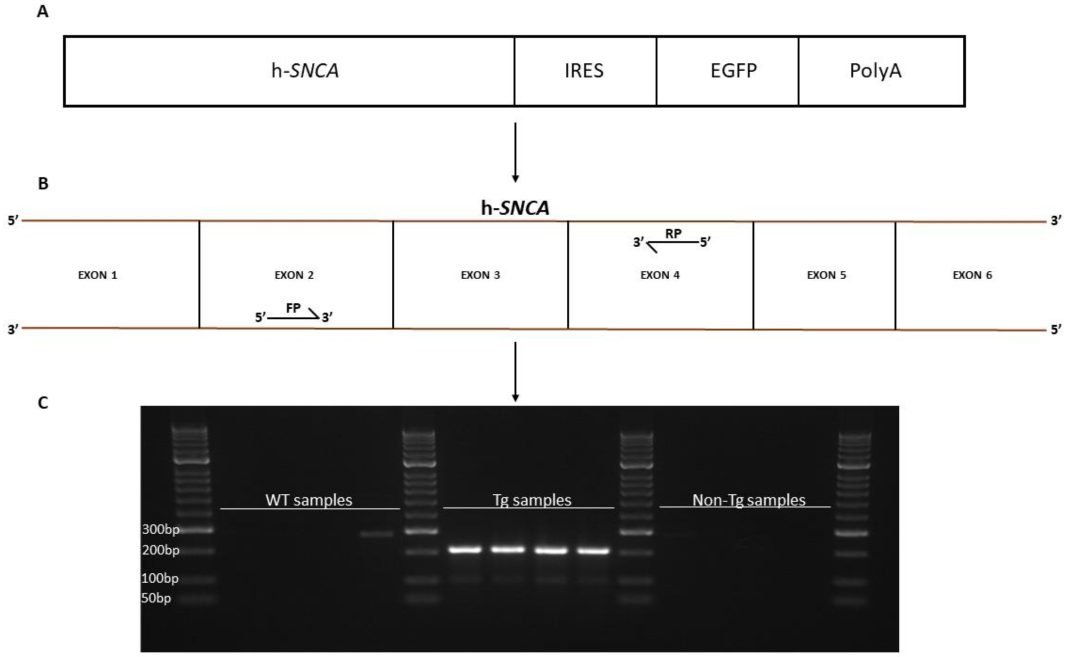

*Figure 3.10. **Design of genotyping primers for the Tg(eno2:hsa.SNCA-ires-EGFP) zebrafish line.** The human SNCA-containing construct, [12kb eno2 promoter]:[human SNCA]-[IRES]-[GFP]-[PolyA] (A) was aligned with human SNCA cDNA sequence, using NCBI's online alignment tool. Results showed that this construct contains exons 2-6 of human SNCA. To prevent non-specific amplification, genotyping primers were designed to amplify exons 2-4 of human SNCA (B). Primer specificity was tested by outcrossing monoallelic Tg(eno2:hsa.SNCA-ires-EGFP) zebrafish, then amplifying DNA extracted from Tg offspring and Non-Tg siblings sorted by GFP fluorescence, and from unrelated WT embryos (n = 4 each) in a PCR reaction run using an annealing temperature of 65 °C. A bright 210bp band and a faint 100bp band were observed in PCR products of Tg offspring only. No bands were observed in PCR products of Non-Tg siblings while a band was observed in the PCR product of a single WT embryo, albeit higher than 210bp (C), thereby confirming primer specificity. cDNA, complementary DNA; GFP, green fluorescent protein; NCBI, national centre for biotechnology information; Non-Tg, non-transgenic; PCR, polymerase chain reaction; Tg, transgenic; WT, wildtype.*

Following the confirmation of primer specificity, *SNCA* primers were used to confirm the genotype of all adult Tg(*eno2*:hsa.*SNCA*-ires-EGFP) zebrafish shipped from the University of Pittsburgh (**Figure 3.11**).

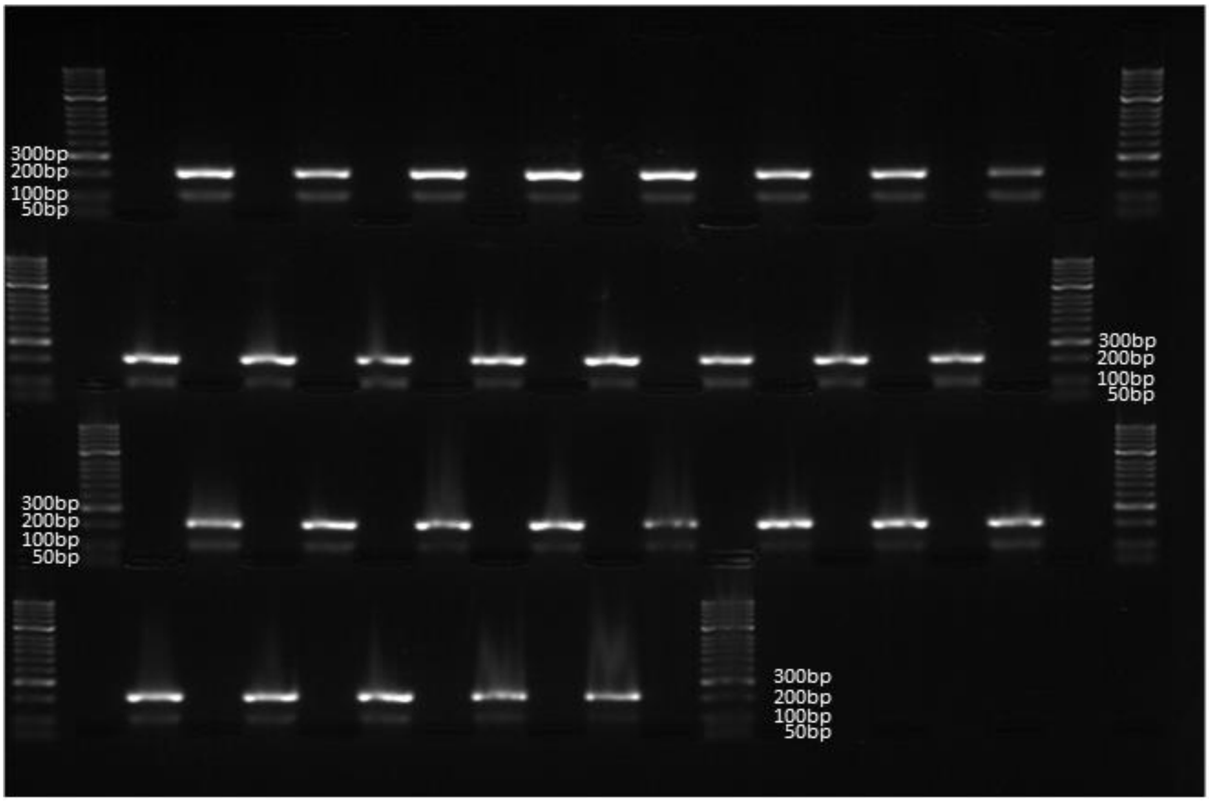

Figure 3.11. Genotyping of adult Tg(eno2:hsa.SNCA-ires-EGFP) zebrafish shipped from the University of Pittsburgh. *Adult Tg(eno2:hsa.SNCA-ires-EGFP) zebrafish were genotyped using SNCA primers. Genotyping confirmed that all 29 zebrafish shipped from the University of Pittsburgh were Tg(eno2:hsa.SNCA-ires-EGFP) zebrafish.*

3.2.7 Generation of the Tg;*klotho*$^{-/-}$ line

Following confirmation that zebrafish supplied by the Burton laboratory were monoallelic Tg(*eno2*:hsa.*SNCA*-ires-EGFP) zebrafish, they were crossed with adult *klotho*$^{-/-}$ zebrafish. Offspring were sorted for GFP expression at 2dpf (**Section 2.1.7**) and GFP-positive offspring were raised to adulthood, thereby generating a colony of Tg(*eno2*:hsa.SNCA-ires-EGFP);*klotho*$^{+/-}$ zebrafish (**Figure 3.12**).

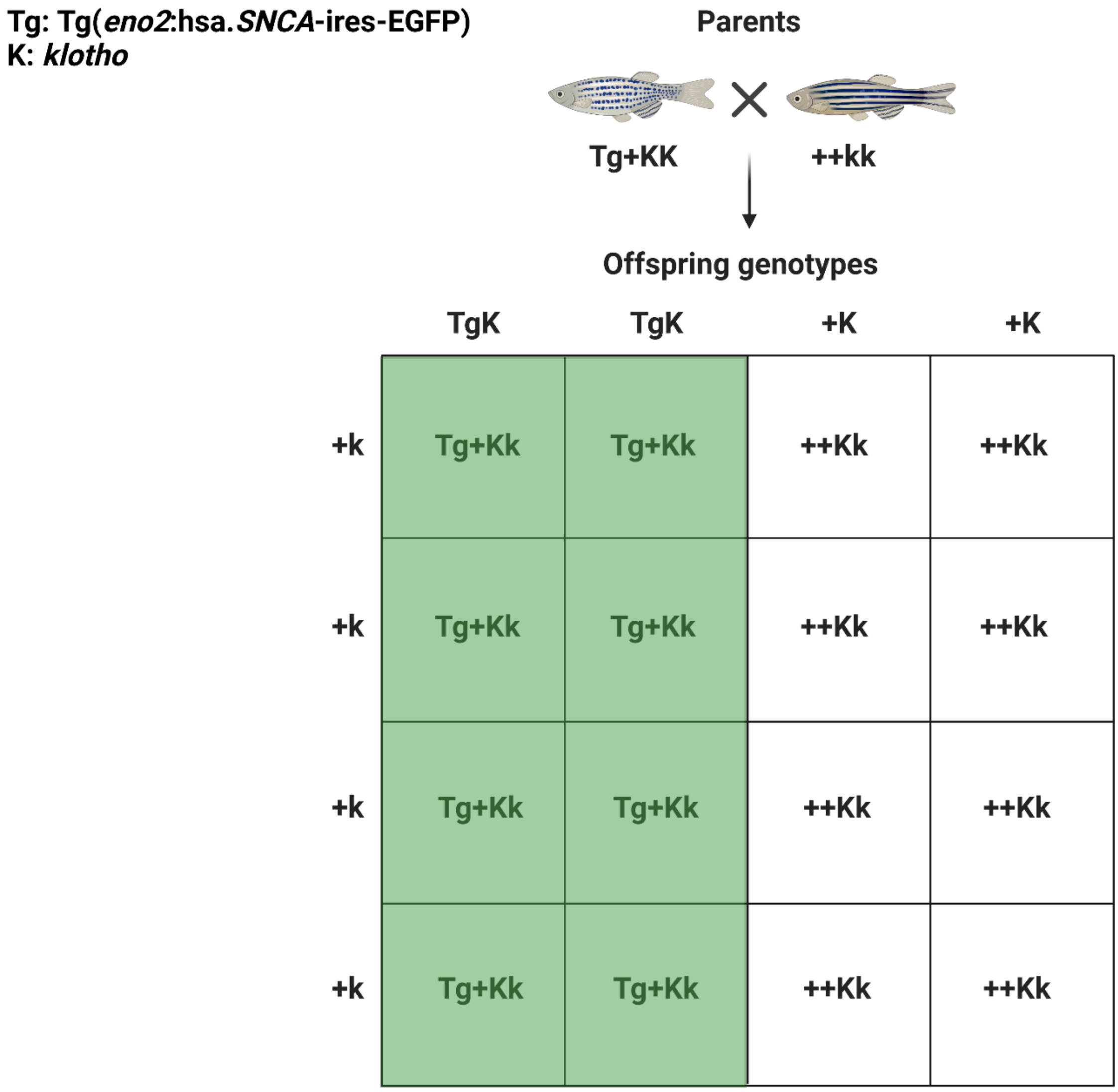

	TgK	TgK	+K	+K
+k	Tg+Kk	Tg+Kk	++Kk	++Kk
+k	Tg+Kk	Tg+Kk	++Kk	++Kk
+k	Tg+Kk	Tg+Kk	++Kk	++Kk
+k	Tg+Kk	Tg+Kk	++Kk	++Kk

Figure 3.12. A Punnett square of the Tg(eno2:hsa.SNCA-ires-EGFP) x klotho$^{-/-}$ cross. *Adult monoallelic Tg(eno2:hsa.SNCA-ires-EGFP) zebrafish were crossed with adult klotho$^{-/-}$ zebrafish. 1/2 of the offspring from this cross expressed GFP (highlighted in green, confirmed by microscopy at 2dpf) but all offspring were heterozygous for the klotho allele. GFP-positive embryos were raised to adulthood, generating a colony of Tg(eno2:hsa.SNCA-ires-EGFP);klotho$^{+/-}$ zebrafish. GFP, green fluorescent protein; k, klotho; Tg, Tg(eno2:hsa.SNCA-ires-EGFP). Adapted from "Zebrafish Punnett Square (Layout 4x4)", by BioRender.com (2023). Retrieved from https://app.biorender.com/biorender-templates.*

Next, adult monoallelic Tg(*eno2*:hsa.*SNCA*-ires-EGFP);*klotho*$^{+/-}$ zebrafish were crossed with adult *klotho*$^{+/-}$ zebrafish. Offspring were raised to adulthood and genotyped for both *SNCA* and *klotho* to identify Non-Tg;*klotho*$^{+/+}$, Non-Tg;*klotho*$^{-/-}$, Tg;*klotho*$^{+/+}$ and Tg;*klotho*$^{-/-}$ zebrafish (**Figure 3.13**).

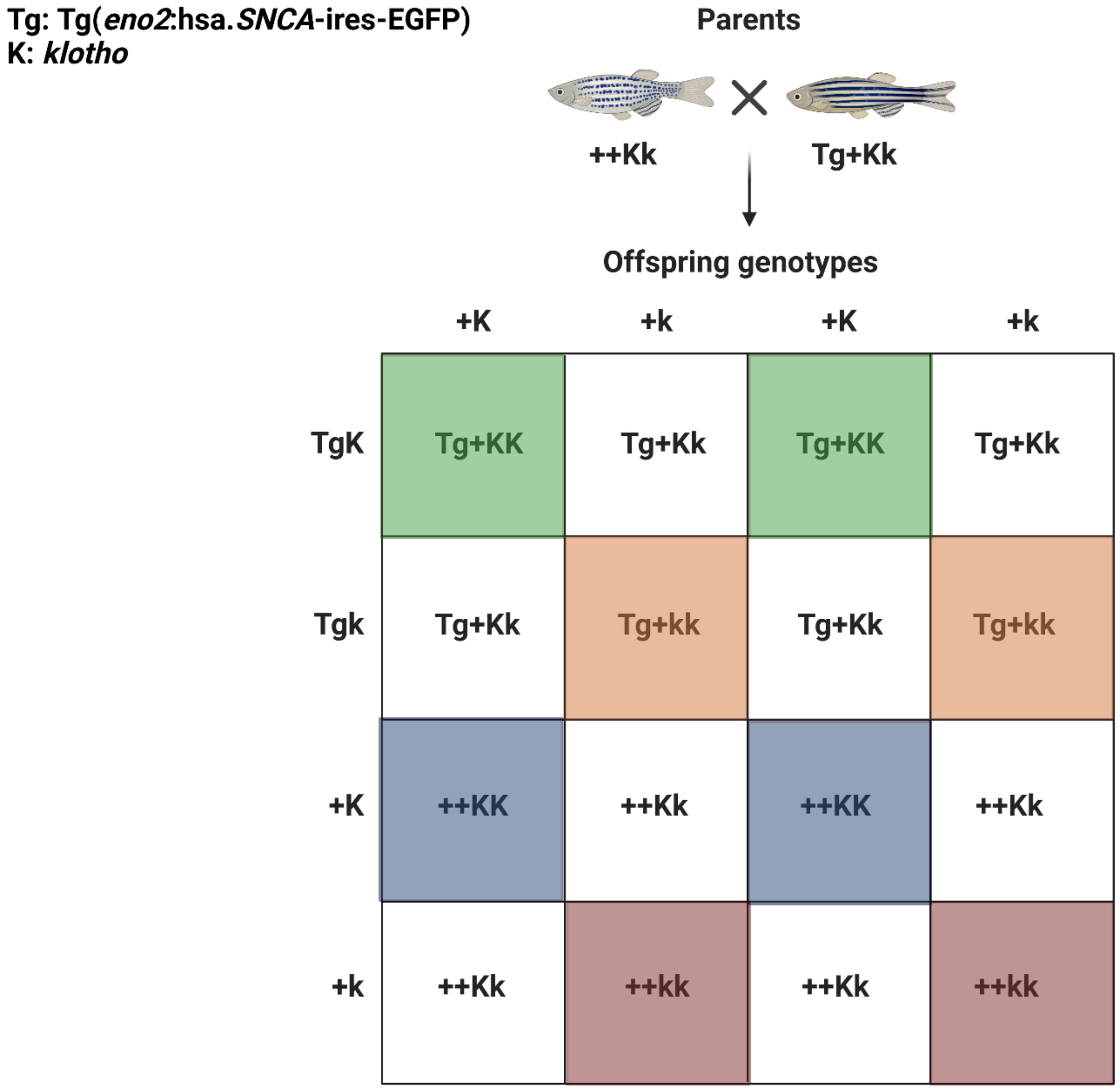

	+K	+k	+K	+k
TgK	Tg+KK	Tg+Kk	Tg+KK	Tg+Kk
Tgk	Tg+Kk	Tg+kk	Tg+Kk	Tg+kk
+K	++KK	++Kk	++KK	++Kk
+k	++Kk	++kk	++Kk	++kk

Figure 3.13. A Punnett square of the Tg(eno2:hsa.SNCA-ires-EGFP);klotho$^{+/-}$ x klotho$^{+/-}$ cross. *Adult monoallelic Tg(eno2:hsa.SNCA-ires-EGFP);klotho$^{+/-}$ zebrafish were crossed with adult klotho$^{+/-}$ zebrafish. 1/8 of the offspring from this cross were either Non-Tg;klotho$^{+/+}$ (highlighted in dark blue), Non-Tg;klotho$^{-/-}$ (highlighted in red), Tg;klotho$^{+/+}$ (highlighted in green) or Tg;klotho$^{-/-}$ (highlighted in orange). k, klotho; Non-Tg, non-transgenic; Tg, Tg(eno2:hsa.SNCA-ires-EGFP). Adapted from "Zebrafish Punnett Square (Layout 4x4)", by BioRender.com (2023). Retrieved from https://app.biorender.com/biorender-templates.*

3.3 Results

3.3.1 NMD, morphology, survival and motor function of *klotho*$^{-/-}$ zebrafish

klotho mRNA undergoes NMD in *klotho*$^{-/-}$ zebrafish (**Figure 3.14A**). Also, *klotho*$^{-/-}$ zebrafish are indistinguishable from WT siblings until 3mpf when they become emaciated and develop tattered fins (**Figure 3.14B**). Survival of *klotho*$^{-/-}$ zebrafish is also reduced to about 6mpf (**Figure 3.14C**). However, surviving *klotho*$^{-/-}$ zebrafish display motor impairment at 7mpf (**Figure 3.14D**). This dataset confirms the presence of an accelerated ageing phenotype in our *klotho*$^{-/-}$ zebrafish line which mirrors that reported by Singh *et al.*, (2019) and Ogura *et al.*, (2021). NMD result was provided by Dr Sarah Brown. Morphology and survival results were provided by Dr Marcus Keatinge. Adult movement result was provided by Dr Deepak Ailani.

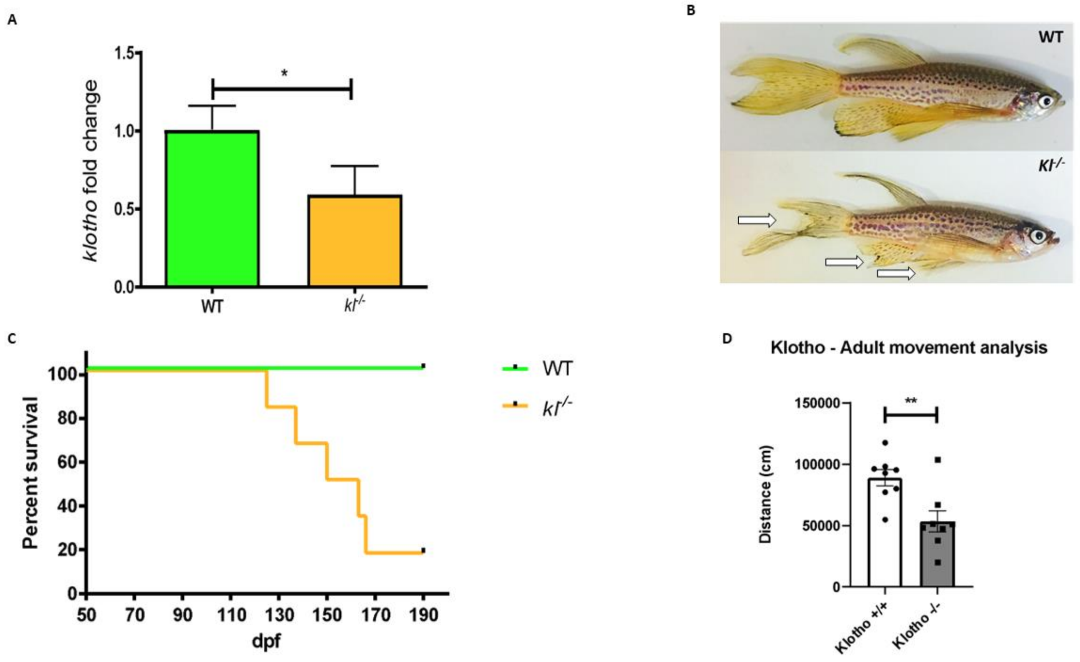

*Figure 3.14. Characterisation of **klotho**$^{-/-}$ **zebrafish.** klotho mRNA undergoes NMD in klotho$^{-/-}$ zebrafish (A). klotho$^{-/-}$ zebrafish are indistinguishable from klotho$^{+/+}$ siblings until 3mpf when they become emaciated and develop tattered fins (B). Most klotho$^{-/-}$ zebrafish die at 6mpf (C). Surviving adult klotho$^{-/-}$ zebrafish also develop motor impairment (D). NMD data (A) was generated by Dr Sarah Brown. Morphology (B) and survival data (C) were generated by Dr Marcus Keatinge. Adult movement data (D) was generated by Dr Deepak Ailani.*

3.3.2 Dopaminergic neuron number and MPP$^+$ susceptibility in *klotho*$^{-/-}$ larvae

Adult *klotho*$^{+/-}$ zebrafish were in-crossed and offspring were exposed to either 3.0 mM MPP$^+$ or MQ from 1-3 dpf (**Section 2.10.1**). 3dpf *klotho*$^{+/-}$ in-cross larvae were fixed (**Section 2.1.9**) and dopaminergic neurons were visualised using *th1* WISH (**Section 2.11.2**). DC1, DC2, DC4 and DC5 neurons were counted on both hemispheres at 20.0x magnification while larvae were genotyped in parallel (**Section 2.11.4**).

There was no significant difference in the number of dopaminergic neurons between untreated *klotho*$^{+/+}$ and untreated *klotho*$^{-/-}$ larvae (*klotho*$^{+/+}$ = 24.14, *klotho*$^{-/-}$ = 22.46, p = 0.3983, **Figure 3.15**). Likewise, there was no significant difference in MPP^{+} susceptibility between *klotho*$^{+/+}$ and *klotho*$^{-/-}$ larvae (*klotho*$^{+/+}$ = 45.84% reduction in dopaminergic neuron number, *klotho*$^{-/-}$ = 39.26% reduction in dopaminergic neuron number, p = 0.9217, **Figure 3.15**).

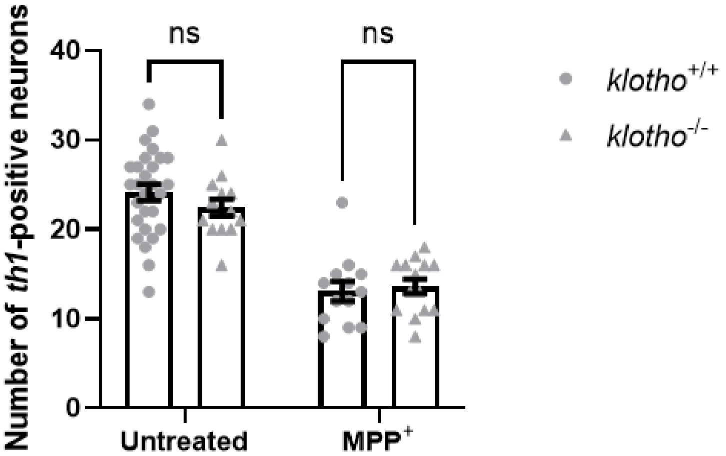

Figure 3.15. Dopaminergic neuron count of 3dpf klotho$^{+/+}$ and klotho$^{-/-}$ larvae with and without MPP^{+} exposure. *Dopaminergic neurons were counted in 3dpf untreated and MPP^{+}-treated klotho$^{+/+}$ and klotho$^{-/-}$ larvae. There was no significant difference in the number of dopaminergic neurons between klotho$^{+/+}$ and klotho$^{-/-}$ larvae, with and without MPP^{+} exposure. Error bars represent standard error of the mean. Data was analysed using a two-way ANOVA with Šídák's multiple comparisons. Larvae were obtained from 3 biological replicates of klotho$^{+/-}$ in-cross embryos. n; untreated klotho$^{+/+}$ = 28, untreated klotho$^{-/-}$ = 13, MPP^{+}-treated klotho$^{+/+}$ = 13 and MPP^{+}-treated klotho$^{-/-}$ = 14. p = 0.3983 (Untreated klotho$^{+/+}$-klotho$^{-/-}$), p = 0.9217 (MPP^{+} klotho$^{+/+}$-klotho$^{-/-}$). ANOVA, analysis of variance; dpf, days post fertilisation; MPP^{+}, 1-methyl-4-phenylpyridinium; th1, tyrosine hydroxylase 1.*

3.3.3 ATP levels in adult *klotho*$^{-/-}$ brains

ATP levels were measured in adult *klotho*$^{+/+}$ and *klotho*$^{-/-}$ brains at 6mpf, that is, the age at which most *klotho*$^{-/-}$ zebrafish die. There was no significant difference in ATP levels between *klotho*$^{+/+}$ and *klotho*$^{-/-}$ zebrafish brains at 6mpf (*klotho*$^{+/+}$ = 1467.29/µg, *klotho*$^{-/-}$ = 1111.23/µg, p = 0.2268, **Figure 3.16**).

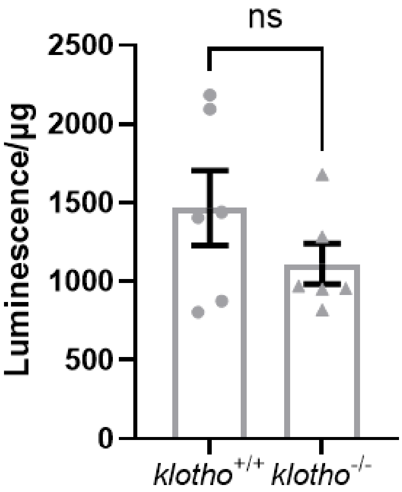

Figure 3.16. ATP levels in klotho$^{+/+}$ and klotho$^{-/-}$ brains at 6mpf. *ATP was measured in klotho$^{+/+}$ and klotho$^{-/-}$ zebrafish brains at 6mpf, using PerkinElmer's ATPlite Luminescence ATP Detection System. 18.0µg brain protein was utilised for experiments. Luminescence served as a readout for ATP, because 18.0µg brain lysate is within the linear range of detection of PerkinElmer's ATPlite Luminescence Assay Kit. There was no significant difference in ATP levels between klotho$^{+/+}$ and klotho$^{-/-}$ zebrafish. Measurements were normalised to µg brain protein. Error bars represent standard error of the mean. Normality was assessed using a Shapiro-Wilk test and data was analysed using a two-way unpaired t-test with Welch's correction. n = 6. p = 0.2268. ATP, adenosine triphosphate; mpf, months post fertilisation.*

3.3.4 NAD$^+$, NADH, NADT and NAD/NADH levels in adult *klotho*$^{-/-}$ brains

NAD$^+$, NADH, NADT and NAD/NADH levels were measured in adult *klotho*$^{+/+}$ and *klotho*$^{-/-}$ brains at 6mpf. NAD$^+$ levels were lower in *klotho*$^{-/-}$ brains compared to *klotho*$^{+/+}$ brains (*klotho*$^{+/+}$ = 1.95 pmol/µg, *klotho*$^{-/-}$ = 1.58 pmol/µg, p = 0.0126, **Figure 3.17A**). Likewise, NADT levels were significantly lower in *klotho*$^{-/-}$ brains compared to *klotho*$^{+/+}$ brains (*klotho*$^{+/+}$ = 4.31 pmol/µg, *klotho*$^{-/-}$ = 3.88 pmol/µg, p = 0.0300, **Figure 3.17B**). However, there was no significant difference in NADH levels between *klotho*$^{+/+}$ and *klotho*$^{-/-}$ brains (*klotho*$^{+/+}$ = 2.36 pmol/µg, *klotho*$^{-/-}$ = 2.30 pmol/µg, p = 0.6338, **Figure 3.17C**) or in NAD/NADH levels between *klotho*$^{+/+}$ and *klotho*$^{-/-}$ brains (*klotho*$^{+/+}$ = 0.82, *klotho*$^{-/-}$ = 0.69, p = 0.1002, **Figure 3.17D**).

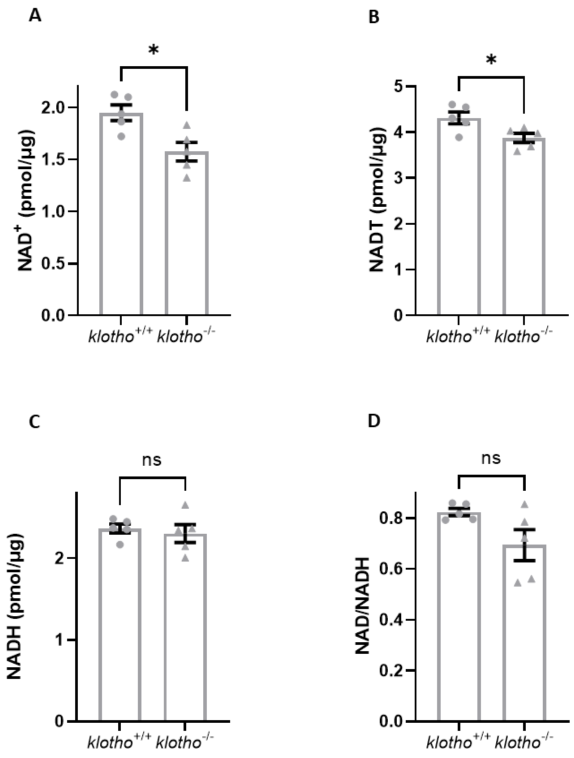

Figure 3.17. NAD$^+$, NADH, NADT and NAD/NADH levels of 6mpf klotho$^{+/+}$ and klotho$^{-/-}$ brains. *NAD$^+$ (A) and NADT (B) levels were significantly lower in klotho$^{-/-}$ brains compared to klotho$^{+/+}$ brains. There was no significant difference in NADH levels between klotho$^{+/+}$ and klotho$^{-/-}$ brains (C) or in NAD/NADH levels between klotho$^{+/+}$ and klotho$^{-/-}$ brains (D). Normality was assessed using a Shapiro-Wilk test; NAD$^+$, NADT, NADH and NAD/NADH datasets were analysed using a two-tailed unpaired t-test with Welch's correction. n = 5. p = 0.0126 (A), p = 0.0300 (B), p = 0.6338 (C), p = 0.1002 (D). mpf, months post fertilisation; NAD$^+$, nicotinamide adenine dinucleotide; NADH, reduced nicotinamide adenine dinucleotide; NADT, NADtotal.*

After obtaining these results, I hypothesised that the pathway reported by Braidy *et al.*, (2011) was responsible for decreased NAD$^+$ levels in *klotho*$^{-/-}$ brains. Using heart, lung, liver and kidney tissue of female wistar rats, Braidy *et al.*, (2011) showed that age-associated accumulation of DNA damage results in the activation of the DNA repair enzyme, poly (ADP-ribose) polymerase 1 (PARP1). Being NAD$^+$-dependent, PARP1 activation reduces NAD$^+$ levels and ATP levels. Downstream, reduced NAD$^+$ levels reduce the activity of another NAD$^+$-dependent enzyme, Sirt1. Consequently, Sirt1-mediated deacetylation of the tumour suppressor gene, p53 is inhibited, leading to apoptosis. This pathway is summarised below (**Figure 3.18**).

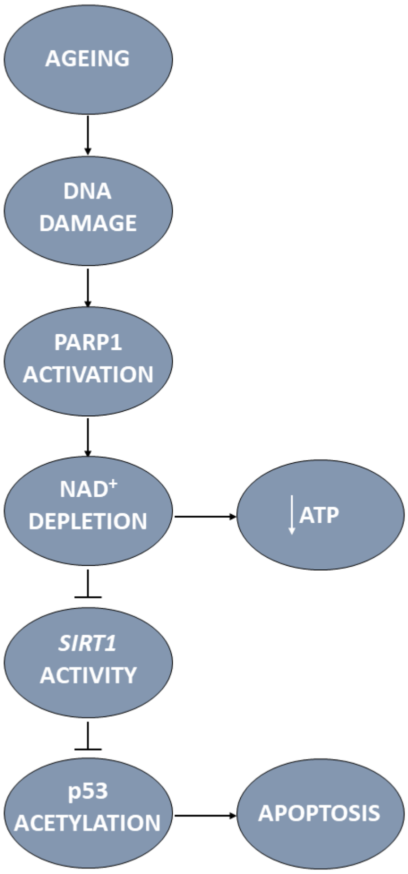

Figure 3.18. Schematic showing the pathway identified by Braidy et al., (2011) which aided the formulation of my hypothesis for premature death in klotho$^{-/-}$ zebrafish. *Ageing causes DNA-damage accumulation which activates the NAD$^+$-dependent DNA repair enzyme, PARP1. PARP1 activity depletes NAD$^+$ levels, thereby reducing ATP levels and the activity of another NAD$^+$-dependent enzyme, Sirt1. Normally, Sirt1 acts to inhibit p53 through deacetylation. However, with reduced Sirt1 activity, p53 is activated resulting in apoptosis. ATP, adenosine triphosphate; NAD$^+$, nicotinamide adenine dinucleotide; PARP1, poly (ADP-ribose) polymerase 1.*

If correct, accelerated ageing would trigger the above pathway in *klotho*$^{-/-}$ brains. The absence of a statistically significant reduction in the ATP levels of 6mpf *klotho*$^{-/-}$ brains could be due to the large variation in ATP levels between replicates (**Figure 3.16**).

3.3.5 PARylation in adult *klotho*$^{-/-}$ brains

To test the above hypothesis, PAR expression was detected in adult *klotho*$^{+/+}$ and *klotho*$^{-/-}$ brains at 6mpf. This is because PARP1 activity causes the production of PAR moieties in a process called Poly (ADP-ribosyl)ation (PARylation), making PARylation a suitable read-out for PARP1 activity (D'amours *et al.*, 1999).

There was no significant difference in PARylation between *klotho*$^{+/+}$ and *klotho*$^{-/-}$ brains at 6mpf (*klotho*$^{+/+}$ = 0.37, *klotho*$^{-/-}$ = 0.17, p = 0.1075, **Figure 3.19**). Due to oversaturation, low MW histones were excluded from densitometry. Likewise, brains 1 and 3 were excluded from densitometry because of the absence of PARylation in high MW proteins in *klotho*$^{+/+}$ brains.

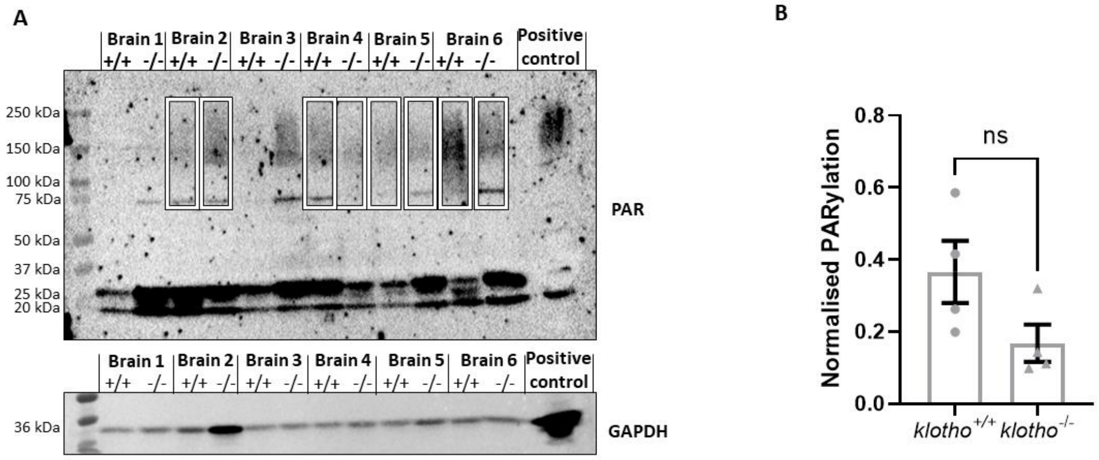

Figure 3.19. PARylation in klotho$^{+/+}$ and klotho$^{-/-}$ brains at 6mpf. *PARylation was investigated in klotho$^{+/+}$ and klotho$^{-/-}$ zebrafish brains at 6mpf, using a PAR western blot. GAPDH served as loading control and H$_2$O$_2$-treated MRC cells served as positive control. Following detection of PARylation, the blot was stripped then re-probed for GAPDH detection. The blot showed genotype-independent changes in PARylation. However, this could be due to unequal protein loading as seen by GAPDH expression (A). Brains 1 and 3 were excluded from analysis due to the absence of PARylation in high MW proteins in klotho$^{+/+}$ brains. Following densitometry and normalisation of PAR band intensities with that of GAPDH (MW of 36kD), no significant difference in PARylation was found between klotho$^{+/+}$ and klotho$^{-/-}$ brains (B). Error bars represent standard error of the mean. Normality was assessed using a Shapiro-Wilk test and data was analysed using a two-tailed unpaired t-test with Welch's correction. n = 4. p = 0.1075. GAPDH, glyceraldehyde-3-phosphate dehydrogenase; H$_2$O$_2$, hydrogen peroxide; kDa, kilodaltons; mpf, months post fertilisation; MW, molecular weight; PAR, poly (ADP-ribose); PARylation, poly (ADP-ribosyl)ation.*

3.3.6 γH2AX expression in adult *klotho*$^{-/-}$ brains

There was no significant difference in γH2AX expression between *klotho*$^{+/+}$ and *klotho*$^{-/-}$ brains at 6mpf (*klotho*$^{+/+}$ = 0.80, *klotho*$^{-/-}$ = 1.51, p = 0.2361, **Figure 3.20**). Brains 4 and 5 were excluded from analysis due to poor protein transfer from the gel to the nitrocellulose membrane.

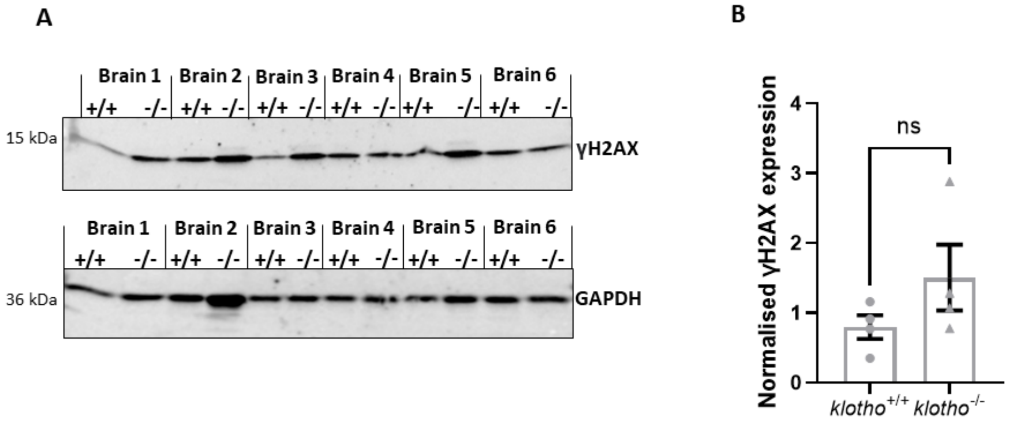

Figure 3.20. γH2AX expression in klotho$^{+/+}$ and klotho$^{-/-}$ brains at 6mpf. *γH2AX expression was investigated in klotho$^{+/+}$ and klotho$^{-/-}$ zebrafish brains at 6mpf, using a western blot. GAPDH (MW of 36kD) served as loading control and shows unequal loading among brain samples (A). Brains 4 and 5 were excluded from analysis as a result of poor protein transfer from the gel to the nitrocellulose membrane. Densitometry showed no significant difference in γH2AX expression between klotho$^{+/+}$ and klotho$^{-/-}$ brains (B). Error bars represent standard error of the mean. Normality was assessed using a Shapiro-Wilk test and data was analysed using a two-tailed unpaired t-test with Welch's correction. n = 4. p = 0.2361. γH2AX, gammaH2AX; GAPDH, glyceraldehyde-3-phosphate dehydrogenase; kDa, kilodaltons; mpf, months post fertilisation; MW, molecular weight.*

3.3.7 Microglial analysis in Tg;*klotho*$^{-/-}$ larvae

Adult monoallelic Tg(*eno2*:hsa.*SNCA*-ires-EGFP);*klotho*$^{+/-}$ zebrafish were crossed with adult *klotho*$^{+/-}$ zebrafish, as previously detailed (**Section 3.2.7**). All offspring were fixed at 5dpf for 4c4 whole-mount IHC (**Section 2.12.1.1**). Microglia were visualised using Perkin Elmer's Opera Phoenix High Content Screening System (**Section 2.12.1.2**) and larvae were genotyped for both *SNCA* and *klotho* in parallel (**Section 2.11.4**). Representative images of microglia in 5dpf Non-Tg;*klotho*$^{+/+}$, Non-Tg;*klotho*$^{-/-}$, Tg;*klotho*$^{+/+}$ and Tg;*klotho*$^{-/-}$ larvae are provided below (**Figure 3.21**).

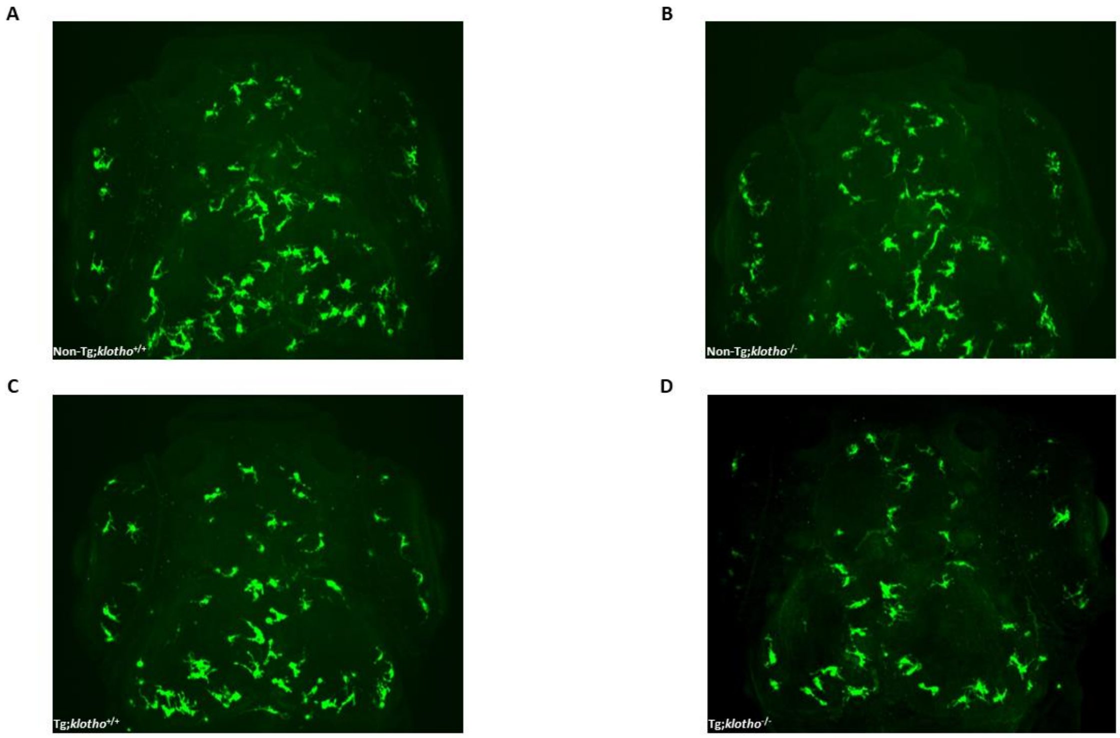

Figure 3.21. Representative microglial images of Non-Tg;klotho*$^{+/+}$*, Non-Tg;klotho*$^{-/-}$*, Tg;klotho*$^{+/+}$ *and Tg;klotho*$^{-/-}$ *larvae at 5dpf. *Microglia of 5dpf Non-Tg;klotho*$^{+/+}$ *(A), Non-Tg;klotho*$^{-/-}$ *(B), Tg;klotho*$^{+/+}$ *(C) and Tg;klotho*$^{-/-}$ *(D) larvae were stained, using 4c4 IHC. Larvae were imaged using Perkin Elmer's Opera Phoenix High Content Screening System and genotyped for both SNCA and klotho in parallel. dpf, days post fertilisation; IHC, immunohistochemistry; Non-Tg, non-transgenic; Tg, transgenic.*

Microglia were counted blindly and counting results were cross-referenced against genotyping results. There was no significant difference between the microglial number of Non-Tg;*klotho*$^{+/+}$ larvae and Tg;*klotho*$^{+/+}$ larvae (Forebrain- Non-Tg;*klotho*$^{+/+}$ = 25.17, Tg;*klotho*$^{+/+}$ = 22.90, p = 0.1780, **Figure 3.22A**; Midbrain- Non-Tg;*klotho*$^{+/+}$ = 60.61, Tg;*klotho*$^{+/+}$ = 54.95, p = 0.1259, **Figure 3.22C**; Total brain- Non-Tg;*klotho*$^{+/+}$ = 85.78, Tg;*klotho*$^{+/+}$ = 77.63, p = 0.0649, **Figure 3.22E**).

Likewise, there was no significant difference between the microglial number of Non-Tg;*klotho*$^{-/-}$ larvae and Tg;*klotho*$^{-/-}$ larvae (Forebrain- Non-Tg;*klotho*$^{-/-}$ = 24.44, Tg;*klotho*$^{-/-}$ = 23.79, p = 0.9045, **Figure 3.22A**; Midbrain- Non-Tg;*klotho*$^{-/-}$ = 57.56, Tg;*klotho*$^{-/-}$ = 54.84, p = 0.7161, **Figure 3.22C**; Total brain- Non-Tg;*klotho*$^{-/-}$ = 82.00, Tg;*klotho*$^{-/-}$ = 78.63, p = 0.7150, **Figure 3.22E**). Together, these results indicate that expression of human WT α-Synuclein has no effect on microglial number in both *klotho*$^{+/+}$ and *klotho*$^{-/-}$ larvae at 5dpf.

Also, there was no significant difference in microglial number between Non-Tg;*klotho*$^{+/+}$ and Non-Tg;*klotho*$^{-/-}$ larvae (Forebrain- Non-Tg;*klotho*$^{+/+}$ = 25.17, Non-Tg;*klotho*$^{-/-}$ = 24.44, p = 0.8871, **Figure 3.22B**; Midbrain- Non-Tg;*klotho*$^{+/+}$ = 60.61, Non-Tg;*klotho*$^{-/-}$ = 57.56, p = 0.6605, **Figure 3.22D**; Total brain- Non-Tg;*klotho*$^{+/+}$ = 85.78, Non-Tg;*klotho*$^{-/-}$ = 82.00, p = 0.6614, **Figure 3.22F**), indicating that the *klotho* mutation has no effect on microglial number at 5dpf.

Furthermore, the *klotho* mutation had no effect on the microglial number of larvae expressing human WT α-Synuclein (Forebrain- Tg;*klotho*$^{+/+}$ = 22.89, Tg;*klotho*$^{-/-}$ = 23.79, p = 07487, **Figure 3.22B**; Midbrain- Tg;*klotho*$^{+/+}$ = 54.95, Tg;*klotho*$^{-/-}$ = 54.85, p = 0.9992, **Figure 3.22D**; Total brain- Tg;*klotho*$^{+/+}$ = 77.63, Tg;*klotho*$^{-/-}$ = 78.63, p = 0.9546, **Figure 3.22F**), suggesting that the *klotho* mutation does not promote microglial activation in the presence of human WT α-Synuclein at 5dpf.

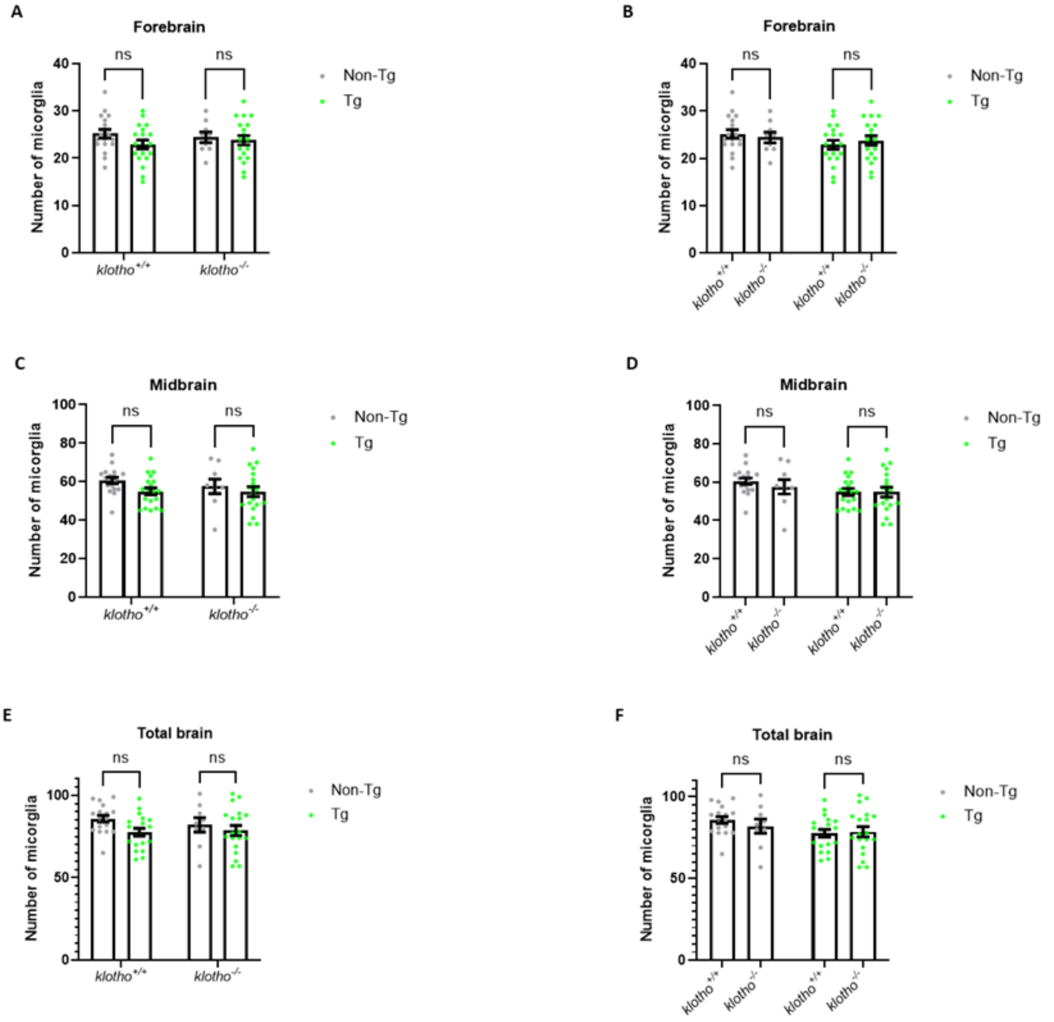

Figure 3.22. Microglial number in Non-Tg;klotho$^{+/+}$, Non-Tg;klotho$^{-/-}$, Tg;klotho$^{+/+}$ and Tg;klotho$^{-/-}$ larvae at 5dpf. *Microglia in the forebrain and midbrain were added to give the number of microglia in the total brain. The expression of human WT α-Synuclein had no effect on the number of microglia in the fore-, mid- and total brains of both klotho$^{+/+}$ and klotho$^{-/-}$ larvae, at 5dpf (A, C and E). Likewise, the klotho mutation had no effect on the number of microglia in the fore-, mid- and total brains of both Non-Tg siblings and Tg larvae expressing human WT α-Synuclein at 5dpf (B, D and F). Error bars represent standard error of the mean. Data was analysed using a two-way ANOVA with Šídák's multiple comparisons. n; Non-Tg;klotho$^{+/+}$ = 18, Non-Tg;klotho$^{-/-}$ = 9, Tg;klotho$^{+/+}$ = 19, Tg;klotho$^{-/-}$ = 19. p = 0.1780 (klotho$^{+/+}$ Non-Tg-Tg; forebrain), p = 0.9045 (klotho$^{-/-}$ Non-Tg-Tg; forebrain), p = 0.8871 (Non-Tg klotho$^{+/+}$-klotho$^{-/-}$; forebrain), p = 0.7487 (Tg klotho$^{+/+}$-klotho$^{-/-}$; forebrain). p = 0.1259 (klotho$^{+/+}$ Non-Tg-Tg larvae; midbrain), p = 0.7161 (klotho$^{-/-}$ Non-Tg-Tg; midbrain), p = 0.6605 (Non-Tg klotho$^{+/+}$-klotho$^{-/-}$; midbrain), p = 0.9992 (Tg klotho$^{+/+}$-klotho$^{-/-}$; midbrain). p = 0.0649 (klotho$^{+/+}$ Non-Tg-Tg; total brain), p = 0.7150 (klotho$^{-/-}$ Non-Tg-Tg; total brain), p = 0.6614 (Non-Tg klotho$^{+/+}$-klotho$^{-/-}$; total brain), p = 0.9546 (Tg klotho$^{+/+}$-klotho$^{-/-}$; total brain). α-Synuclein, alpha-synuclein; ANOVA, analysis of variance; dpf, days post fertilisation; Non-Tg, non-transgenic; Tg, transgenic; WT, wildtype.*

3.3.8 Morphology, morbidity and mortality of Tg;*klotho*$^{-/-}$ zebrafish

Adult Tg;*klotho*$^{-/-}$ zebrafish did not display an overt phenotype (weight and size were not investigated). The number of adult Non-Tg;*klotho*$^{+/+}$, Non-Tg;*klotho*$^{-/-}$, Tg;*klotho*$^{+/+}$ and Tg;*klotho*$^{-/-}$ zebrafish identified by genotyping was in accordance with Mendelian inheritance (**Table 3.3**), indicating equal viability of Tg;*klotho*$^{+/+}$ and Tg;*klotho*$^{-/-}$ zebrafish to adulthood. Survival was also unaffected in Tg;*klotho*$^{-/-}$ zebrafish and controls which were monitored until ~5mpf.

Total number of Tg(*eno2*:hsa.*SNCA*-ires-EGFP);*klotho*$^{+/-}$ x *klotho*$^{+/-}$ zebrafish = 107				
Zebrafish	**Non-Tg;*klotho*$^{+/+}$**	**Non-Tg;*klotho*$^{-/-}$**	**Tg;*klotho*$^{+/+}$**	**Tg;*klotho*$^{-/-}$**
Mendelian inheritance	1/8	1/8	1/8	1/8
Number of zebrafish predicted by Mendelian inheritance	13	13	13	13
Number of zebrafish identified by genotyping	9	12	9	10

Table 3.3. Viability of Tg;klotho$^{-/-}$ zebrafish to adulthood. *Genotyping of 107 adult Tg(eno2:hsa.SNCA-ires-EGFP);klotho$^{+/-}$ x klotho$^{+/-}$ zebrafish revealed that 9 were Non-Tg;klotho$^{+/+}$ zebrafish, 12 were Non-Tg;klotho$^{-/-}$ zebrafish, 9 were Tg;klotho$^{+/+}$ zebrafish and 10 were Tg;klotho$^{-/-}$ zebrafish, which was in accordance with Mendelian inheritance. Therefore, Tg;klotho$^{-/-}$ zebrafish are viable to adulthood. Non-Tg, non-transgenic; Tg, transgenic.*

3.4 Discussion

3.4.1 Overview

The major aims of this chapter were to systematically assess *klotho*$^{-/-}$ zebrafish for PD-relevant pathological mechanisms and to investigate whether *klotho* deficiency alters microglial activation in Tg(*eno2*:hsa.*SNCA*-ires-EGFP) zebrafish.

Prior to starting this PhD, the *klotho*$^{-/-}$ zebrafish line was generated by Dr Marcus Keatinge. The *klotho*$^{-/-}$ line displays an accelerated ageing phenotype identical to the phenotype reported by Singh *et al.*, (2019) and (Ogura *et al.*, 2021), thereby validating our *klotho*$^{-/-}$ zebrafish line as a model for accelerated ageing and providing a unique opportunity to investigate ageing-related mechanisms which may contribute to PD pathogenesis.

The majority of *in vivo SNCA* studies have utilised rodents. To date, mice remain the only model in which the interaction between Klotho and α-Synuclein has been investigated. Peripheral administration of Klotho ameliorated cognitive and motor impairment in mice overexpressing human WT α-Synuclein (Leon *et al.*, 2017). Recently, human CSF and serum KLOTHO levels were suggested as potential PD biomarkers (Sancesario *et al.*, 2021; Zimmermann *et al.*, 2021). A negative effect of KLOTHO on α-Synuclein expression was also suggested (Sancesario *et al.*, 2021). Although zebrafish do not express endogenous α-Synuclein (Milanese *et al.*, 2012), Tg zebrafish lines that express human α-Synuclein can be generated, making it possible to study the interplay between ageing and PD.

To assess *klotho*$^{-/-}$ zebrafish for PD-relevant pathological mechanisms, dopaminergic neuron count and MPP^{+} susceptibility, and microglial count were investigated in larvae while mitochondrial function and DNA damage were investigated in adult brain tissue.

3.4.2 Characterisation of *klotho*$^{-/-}$ zebrafish

There was no significant difference in the number of dopaminergic neurons between *klotho*$^{+/+}$ and *klotho*$^{-/-}$ larvae at 3dpf, suggesting that the mechanisms which trigger accelerated ageing in *klotho*$^{-/-}$ zebrafish are inactive at 3dpf. *klotho*$^{-/-}$ zebrafish may develop an age-related decrease in dopaminergic neurons, as reported in mice (Kosakai *et al.*, 2011). Age-related neurotoxicity could be the result of mitochondrial dysfunction in adult *klotho*$^{-/-}$ brains which will be discussed below. An age-related decrease in dopaminergic neurons might also explain the motor impairment observed in 7mpf *klotho*$^{-/-}$ zebrafish. However, it is also possible that motor impairment is caused by a loss of cerebellar Purkinje cells, not dopaminergic neurons, as suggested by mice data (Kosakai *et al.*, 2011). For this reason, cerebellar Purkinje cells should be examined in *klotho*$^{-/-}$ zebrafish to determine the cause of motor impairment. This can be achieved by immunostaining brain sections for parvalbumin (pv) or zebrin II (zII) which are markers of cerebellar Purkinje cells (Bae *et al.*, 2009; Furlan *et al.*, 2020).

Klotho is implicated in oxidative stress (Nagai *et al.*, 2003; Yamamoto *et al.*, 2005; Brobey *et al.*, 2015; Sahu *et al.*, 2018). Equal susceptibility to MPP^+ between *klotho*$^{+/+}$ and *klotho*$^{-/-}$ larvae at 3dpf suggests the absence of oxidative stress in *klotho*$^{-/-}$ larvae at 3dpf.

Also, results showed no significant difference in microglial number between *klotho*$^{+/+}$ and *klotho*$^{-/-}$ larvae at 5dpf, suggesting the absence of microglial activation in *klotho*$^{-/-}$ larvae. This result supports equal susceptibility to MPP^+ between *klotho*$^{+/+}$ and *klotho*$^{-/-}$ larvae, because if present, oxidative stress should trigger microglial activation in *klotho*$^{-/-}$ larvae. Although microglial morphology was not investigated by counting the number of ameboid microglia, it is now known that microglia have intermediate forms of activation characterised by morphological subtleties (Karperien, Ahammer and Jelinek, 2013). To further investigate microglial activation in *klotho*$^{+/+}$ and *klotho*$^{-/-}$ larvae, susceptibility to LPS could been investigated.

Furthermore, the generation of a *klotho*$^{-/-}$;*fgf23*$^{-/-}$ zebrafish line may quicken the onset of accelerated ageing mechanisms in zebrafish, thereby allowing the modelling of ageing in larvae. However, this is unlikely given the equal severity of *Klotho* KO and *Klotho/Fgf23* double KO in mice (Nakatani *et al.*, 2009).

To study mechanisms driving accelerated ageing in adult *klotho*$^{-/-}$ zebrafish, mitochondrial function was investigated in *klotho*$^{-/-}$ brains at 6mpf, that is, the timepoint when most *klotho*$^{-/-}$ zebrafish die. Specifically, brain ATP and NAD/NADH levels were investigated because of their relevance to ageing and PD (Schniertshauer, Gebhard and Bergemann, 2018; Covarrubias *et al.*, 2020).

Although there was no significant difference in ATP levels between *klotho*$^{+/+}$ and *klotho*$^{-/-}$ brains at 6mpf, there was a moderate decrease in NAD^+ and NADT levels in *klotho*$^{-/-}$ brains. The absence of a significant decrease in the NAD/NADH levels of *klotho*$^{-/-}$ brains compared to control is likely due to the variation in NAD/NADH values obtained from *klotho*$^{-/-}$ brains. Together, these results suggest mitochondrial dysfunction in *klotho*$^{-/-}$ brains at 6mpf but perhaps not to the extent of significantly affecting ATP production. Due to the non-significant difference in ATP levels between *klotho*$^{+/+}$ and *klotho*$^{-/-}$ brains and only a moderate decrease in NAD^+ and NADT levels in *klotho*$^{-/-}$ brains, mitochondrial respiratory chain activity was not investigated.

Importantly, because whole brains were used for the ATP assay, it is possible that altered ATP levels in dopaminergic neurons of adult *klotho*$^{-/-}$ zebrafish were concealed by unaltered ATP levels in other brain regions, due to the heterogeneity of the CNS. For this same reason, dopaminergic neurons may not contribute to decreased NAD^+ levels detected in 6mpf *klotho*$^{-/-}$ brains. Since decreased NAD^+ levels may be the result of mitochondrial complex I deficiency, investigation of MPP^+ susceptibility in *klotho*$^{+/+}$ and *klotho*$^{-/-}$ zebrafish at 6mpf may help elucidate the contribution of dopaminergic neurons to this dataset.

NAD/NADH results led to the formulation of the hypothesis that decreased NAD^+ levels in 6mpf *klotho*$^{-/-}$ brains was caused by increased PARP1 activity in response to DNA damage accumulation. PARylation served as a read-out for PARP1 activity and there was no significant difference in PARylation between *klotho*$^{+/+}$ and *klotho*$^{-/-}$ brains at 6mpf.

Following an initial western blot experiment, the spots on the PAR blot were thought to be the result of a dirty nitrocellulose membrane. However, these spots were observed after stripping and re-probing the blot for PAR but not for GAPDH, suggesting an issue with the PAR antibody solution. These spots were likely caused by insoluble particles in the PAR antibody solution, resulting from undissolved milk solution.

The PAR western blot experiment was not repeated due to the clear evidence of a non-significant difference in PARylation between *klotho*$^{+/+}$ and *klotho*$^{-/-}$ brains at 6mpf, as well as time constraints. Although other members of the PARP family, namely PARP2 and PARP3 consume NAD^+ (Wilk *et al.*, 2020), PARP1 is the major NAD^+-consuming member of the PARP family (Hurtado-Bagès *et al.*, 2020). Therefore, PARP1 activity remains the best read-out for NAD^+ consumption in response to DNA damage. Alternatively, PARP1 activity in adult *klotho*$^{+/+}$ and *klotho*$^{-/-}$ brains could be determined using a commercial kit. However, this method would not give information regarding PARP1 activity in dopaminergic neurons and to date has not been utilised in zebrafish.

γH2AX expression was not increased in 6mpf *klotho*$^{-/-}$ brains. This was surprising because an age-associated increase in γH2AX expression was reported in the lung, spleen, dermis, liver and gut of WT mice (Wang *et al.*, 2009). Since different neuronal groups have different vulnerabilities to oxidative stress (Salim, 2017), double immunostaining adult brain slices for Th and γH2AX may reveal evidence of DNA damage within dopaminergic neurons.

3.4.3 Characterisation of Tg(*eno2*:hsa.*SNCA*-ires-EGFP) zebrafish and the effect of *klotho* deficiency on Tg(*eno2*:hsa.*SNCA*-ires-EGFP) zebrafish

Microglial counting was used to investigate whether the mechanisms of ageing in *klotho*$^{-/-}$ zebrafish enhance microglial activation in Tg(*eno2*:hsa.*SNCA*-ires-EGFP) zebrafish. Morphology, morbidity and mortality of adult Tg;*klotho*$^{-/-}$ zebrafish was also investigated. Due to delays in the shipment of monoallelic Tg(*eno2*:hsa.*SNCA*-ires-EGFP) embryos from the University of Pittsburgh caused by the coronavirus pandemic and subsequent lockdowns, these were the only experiments run to investigate whether the mechanisms of ageing in *klotho*$^{-/-}$ zebrafish enhance PD-relevant pathological mechanisms in Tg(*eno2*:hsa.*SNCA*-ires-EGFP) zebrafish. Dopaminergic neuron number was not investigated in Tg(*eno2*:hsa.*SNCA*-ires-EGFP) larvae because the reporter is not expressed in zebrafish neurons.

Expression of human WT α-Synuclein in Tg(*eno2*:hsa.*SNCA*-ires-EGFP) larvae had no effect on microglial number at 5dpf. This could be due to low expression of α-Synuclein in larval brains. Although *eno2* expression is restricted to the nervous system (Bai *et al.*, 2007), ectopic GFP expression is observed in the caudal and pectoral fins of Tg(*eno2*:hsa.*SNCA*-ires-EGFP) larvae. Although, high level α-Synuclein expression was detected in the CNS of adult Tg(*eno2*:hsa.*SNCA*-ires-EGFP) zebrafish, CNS α-Synuclein expression was not systematically investigated in larvae.

The *klotho* mutation did not increase microglial number in Tg(*eno2*:hsa.*SNCA*-ires-EGFP) larvae. As previously stated, it is likely that the mechanisms which trigger accelerated ageing in *klotho*$^{-/-}$ zebrafish are inactive in larvae. This combined with a potential low expression of α-Synuclein in the brains of Tg(*eno2*:hsa.*SNCA*-ires-EGFP) larvae further emphasises the need for adult experiments. For example, the expression of pro-inflammatory genes in adult Tg;*klotho*$^{+/+}$ and Tg;*klotho*$^{-/-}$ brains could be investigated using RNAseq. The absence of an overt phenotype in ~5mpf Tg;*klotho*$^{-/-}$ zebrafish, and equal viability and survival of ~5mpf Tg;*klotho*$^{-/-}$ zebrafish to controls also suggest the absence of pathogenesis in Tg;*klotho*$^{-/-}$ zebrafish. However, Tg;*klotho*$^{-/-}$ zebrafish were expected to develop a phenotype at 6mpf but were culled (together with controls) before reaching this timepoint for brain extraction for a western blot comparing α-Synuclein expression between adult Tg;*klotho*$^{+/+}$ and Tg;*klotho*$^{-/-}$ brains. Due to a delayed shipment of these brain samples to the University of Pittsburgh, they perished in transit and this western blot experiment could not be conducted.

3.4.4 Future work

Matsui and Matsui, (2017) generated a Tg zebrafish line expressing human α-Synuclein in the CNS, which did not display α-Synuclein aggregation even in adulthood. However, CSF injection of human α-Synuclein fibrils induced α-Synuclein aggregation within adult zebrafish brains, suggesting prion-like propagation of α-Synuclein aggregation. The reason why endogenous human α-Synuclein in this published Tg line was insufficient to induce α-Synuclein aggregation remains unknown. It may be that β- and γ1-synuclein compensate for endogenous α-Synuclein expression but this compensation is insufficient when α-Synuclein expression is increased by injecting exogenous fibrils. Therefore, experiments utilising our Tg(*eno2*:hsa.*SNCA*-ires-EGFP) zebrafish line may also require injection of human α-Synuclein fibrils into one-cell stage embryos to induce α-Synuclein-mediated pathology and promote PD mechanisms in larvae. Alternatively, Tg zebrafish expressing a mutated form of human α-Synuclein, for example A53T α-Synuclein may develop a phenotype in the larval stage.

The mechanisms which trigger accelerated ageing in the *klotho*$^{-/-}$ zebrafish line are presumably inactive in larvae. Therefore, adult zebrafish are needed for subsequent experiments. Microglial activation was not detected in Tg(*eno2*:hsa.*SNCA*-ires-EGFP) larvae, suggesting the absence of α-Synuclein-mediated toxicity. Injection of human α-Synuclein fibrils might be needed to circumvent this and promote the activation of PD-relevant mechanisms in larvae. However, the requirement for adult *klotho*$^{-/-}$ zebrafish would limit studies investigating the interplay between the mechanisms of ageing and PD-relevant pathological mechanisms to utilising adult zebrafish, thereby increasing research time, costs, and limiting high through-put studies, such as chemical screens.

Chapter 4: Zebrafish as a model for *SIRT1* deficiency

4.1 Introduction

4.1.1 Background

The yeast silent information regulator (*SIR*) complex comprises of *Sir2*, *Sir3* and *Sir4* and is responsible for gene silencing at mating-type loci and telomeres. However, only *Sir2* is responsible for gene silencing at ribosomal DNA (rDNA) (Shore, Squire and Nasmyth, 1984; Gottlieb and Esposito, 1989; Blander and Guarente, 2004). Sir2, the first sirtuin described, is an NAD$^+$-dependent histone deacetylase (HDAC) (Imai *et al.*, 2000; Landry *et al.*, 2000).

Deacetylation of each lysine residue by Sir2 is coupled to the cleavage of NAD$^+$ to produce nicotinamide and O-acetyl-ADP ribose (**Figure 4.1**). The acetyl group is transferred from the lysine residue to the ADP-ribose moiety of NAD$^+$ (Tanner *et al.*, 2000; Tanny and Moazed, 2001).

$$\mathbf{NAD^{+} + acetyl\text{-}lysine\text{-}histone \xrightarrow{Sir2} Nicotinamide + O\text{-}acetyl\text{-}ADP\text{-}ribose + lysine\text{-}histone}$$

Figure 4.1. Sir2-mediated histone deacetylation. *Sir2-mediated histone deacetylation is coupled to the cleavage of NAD$^+$ to produce nicotinamide and O-acetyl-ADP ribose. NAD$^+$, nicotinamide adenine dinucleotide; Sir2, silent information regulator 2.*

Sir2 is the only yeast SIR protein that is highly conserved from prokaryotes to humans (Frye, 1999). There are 7 mammalian Sir2 homologues, namely SIRT1-7. However, SIRT1 has the highest homology to Sir2, is the best studied mammalian sirtuin and deacetylates histones in the same manner as Sir2 (**Figure 4.1**) (Frye, 1999, 2000; Outeiro, Marques and Kazantsev, 2008).

In humans, HDACs are divided into 4 classes based on sequence similarity, classes I, II, III and IV. Class I HDACs are homologous to yeast Rpd3, class II HDACs are homologous to yeast Hda1. There is a single class IV HDAC and it shares sequence similarity with both class I and class II HDACs. SIRT1-7 are class III HDACs (Seto and Yoshida, 2014).

Mammalian sirtuins differ in subcellular localisation, target specificity, function and catalytic activity. For example, SIRT1, SIRT6 and SIRT7 are localised to the nucleus, SIRT3, SIRT4 and SIRT5 are localised to the mitochondria and SIRT2 can be found in the cytoplasm and nucleus. (Frye, 1999, 2000; Outeiro, Marques and Kazantsev, 2008). A list of mammalian sirtuins, their subcellular localisation, targets and functions is provided below (**Table 4.1**). However, the focus of this thesis chapter is SIRT1.

Mammalian sirtuin	**Subcellular localisation**	**Targets**	**Function**	**Reference**
SIRT1	Nucleus	p53, Ku70, PPARγ, PGC-1α, NF-κB, FOXO, HSF1, LC3	Regulation of cell survival and metabolism, stress response control	(Luo *et al.*, 2001; Sawada *et al.*, 2003; Brunet *et al.*, 2004; Cohen *et al.*, 2004; Yeung *et al.*, 2004; Motta *et al.*, 2004; Picard *et al.*, 2004; Nemoto, Fergusson and Finkel, 2005; Gerhart-Hines *et al.*, 2007; Westerheide *et al.*, 2009; Guo *et al.*, 2016)
SIRT2	Cytoplasm/nucleus	α-tubulin, histone H4	Regulation of microtubule stability, cell cycle regulation	(North *et al.*, 2003; Vaquero *et al.*, 2006)
SIRT3	Mitochondria	AceCS2, GDH, mitochondrial complex I	Thermogenesis regulation, ATP production	(Shi *et al.*, 2005; Schwer *et al.*, 2006; Lombard *et al.*, 2007; Ahn *et al.*, 2008; Schlicker *et al.*, 2008)
SIRT4	Mitochondria	GDH	Downregulation of insulin secretion in response to amino acids	(Haigis *et al.*, 2006)
SIRT5	Mitochondria	CPS1	Ammonia detoxification	(Nakagawa *et al.*, 2009)

SIRT6	Nucleus (associated with heterochromatin)	GCIP, Histone H3, NF-κB	DNA repair, regulation of inflammation	(Michishita et al., 2005; Mostoslavsky et al., 2006; Ma et al., 2007; Kawahara et al., 2009; Van Gool et al., 2009)
SIRT7	Nucleus (concentrated in nucleoli)	RNA polymerase I	Regulation of rRNA synthesis and ribosome production	(Michishita et al., 2005; Ford et al., 2006)

Table 4.1. List of mammalian sirtuins, their subcellular localisation, targets, functions and relevant references. *Reproduced from Outeiro, Marques and Kazantsev, (2008) and Haigis and Sinclair, (2010). α-tubulin, alpha-tubulin; AceCS2, acetyl-CoA-synthetase 2; CPS1, carbamoyl phosphate synthetase 1; FOXO, forkhead box transcription factors; GCIP, Grap2 and cyclin D1 interacting protein; GDH, glutamate dehydrogenase; LC3, microtubule-associated protein 1A/1B-light chain 3; NF-κB, nuclear factor-kappa B; PPARγ, peroxisome proliferator-activated receptor γ; PGC-1α, PPARγ coactivator-1alpha.*

SIRT1 is encoded by the *SIRT1* gene which is located on chromosome 10 and contains 9 exons (Yang et al., 2022). SIRT1 is composed of 747 amino acids, is ubiquitously expressed in human tissues, and contains an N-terminal domain, a catalytic domain and a C-terminal domain (**Figure 4.2A**).

The catalytic domain of all sirtuins, including SIRT1, consists of a Rossmann-fold domain, a zinc-binding domain and loops connecting both domains. These loops form a cleft; the amino acids responsible for SIRT1's catalytic activity are located within this cleft. NAD^+ and the acetyl-lysine group of the protein substrate access SIRT1 from opposite ends of this cleft then bind to SIRT1 (**Figure 4.2B**). Binding induces cleft closure and a structural change in the "cofactor binding loop" from being highly flexible to being ordered. During the catalytic reaction, nicotinamide and an alkylimidate intermediate are formed. This intermediate is hydrolysed to O-acetyl-ADP-ribose and deacetylated lysine (Sanders, Jackson and Marmorstein, 2010; Gertz *et al.*, 2013).

Chemical modifiers of SIRT1's catalytic activity exploit the above stated mechanism. For example, EX-527, a SIRT1-specific inhibitor, stabilises the "cofactor binding loop" in a closed conformation, thereby preventing product release (Napper *et al.*, 2005; Gertz *et al.*, 2013). Consequently, resveratrol (a polyphenol) is thought to activate SIRT1 by promoting a conformational change which increases substrate affinity to SIRT1 (Borra, Smith and Denu, 2005). Polyphenols are naturally occurring compounds with antioxidant effects (Pandey and Rizvi, 2009).

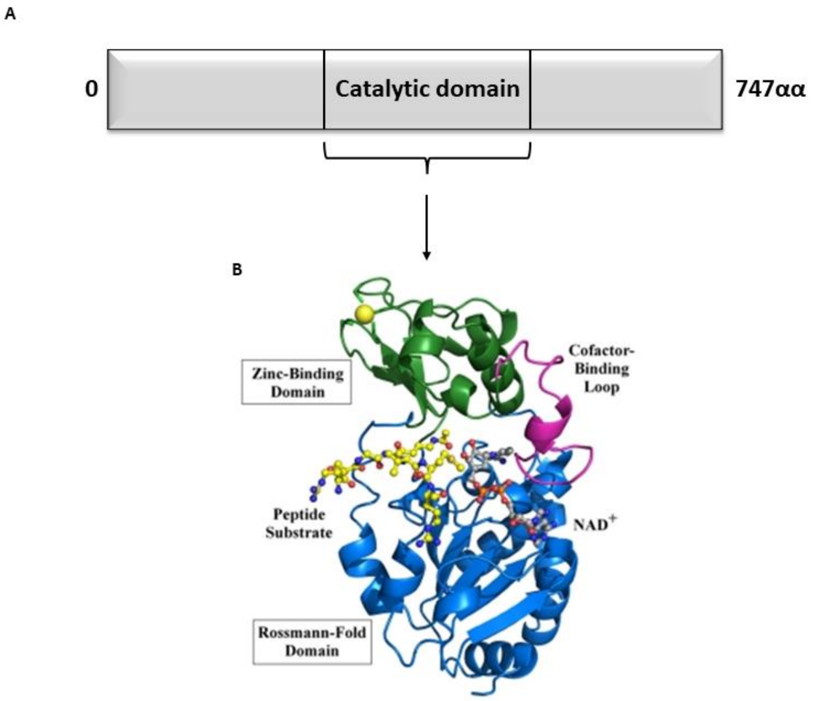

Figure 4.2. SIRT1 structure. *SIRT1 is a 747αα protein which contains a conserved catalytic domain (A). This catalytic domain consists of a Rossmann-fold domain, a zinc-binding domain and loops connecting both domains (B).* NAD^+ *and the acetyl-lysine group of the protein substrate access SIRT1 from opposite ends of a cleft formed by the loops connecting the Rossmann-fold and zinc-binding domains, then bind SIRT1. Binding induces cleft closure and the "cofactor-binding loop" becomes ordered. Following the completion of the catalytic reaction within this cleft, nicotinamide, O-acetyl-ADP-ribose and lysine are produced. Figure 4.2B was reproduced from Moniot, Weyand and Steegborn, (2012). αα, amino acid;* NAD^+*, nicotinamide adenine dinucleotide.*

4.1.2 Role in ageing

Sir2 regulates longevity in yeast by decreasing the rate of extrachromosomal rDNA circle (ERC) formation; Fob1 promotes ERC formation. The lifespan of *Sir2* mutant yeast is decreased by 50% compared to the lifespan of WT yeast while the lifespan of *Fob1* mutant yeast is higher than the lifespan of WT yeast. The lifespan of *Sir2*;*Fob1* double mutant yeast is comparable to that of WT yeast, but slightly decreased compared to the lifespan of *Fob1* mutant yeast, suggesting that Sir2 and Fob1 act in the same pathway. Contrastingly, Sir2 overexpression rescues the decreased lifespan of *Sir2* mutant yeast and increases the lifespan of WT yeast by 30%. However, Sir2 overexpression does not increase the lifespan of *Fob1* mutant yeast, suggesting that Fob1 acts downstream of Sir2 (Kaeberlein, McVey and Guarente, 1999).

Overexpression of sir2.1 (the *C.elegans* homologue of yeast Sir2) in *C.elegans* was reported to increase lifespan beyond that of controls. This was attributed to sir2.1's interaction with the insulin and IGF-1 signalling pathway, and endoplasmic reticulum (ER) stress response (Tissenbaum and Guarente, 2001; Viswanathan *et al.*, 2005; Berdichevsky *et al.*, 2006). However, out-crossing of sir2.1 overexpressing *C.elegans* abolished increased longevity while maintaining sir2.1 overexpression, indicating that the increased longevity reported in sir2.1 overexpressing *C.elegans* is due to genetic background. Likewise, *sir2.1* KD in sir2.1 overexpressing *C.elegans* did not affect longevity, despite reduction of sir2.1 expression to WT levels (Burnett *et al.*, 2011). *sir2.1* mutant *C.elegans* are also more susceptible to paraquat (Guo and García, 2014).

There are conflicting reports in the literature concerning resveratrol's effect on lifespan in model organisms. For example, while resveratrol was reported to increase *C.elegans* lifespan under normal biological conditions (Viswanathan *et al.*, 2005), Chen, Rezaizadehnajafi and Wink, (2013) reported that resveratrol only increases *C.elegans* lifespan under oxidative stress conditions. This discrepancy could be due to different experimental conditions; Viswanathan *et al.*, (2005) treated *C.elegans* with higher resveratrol doses compared to Chen, Rezaizadehnajafi and Wink, (2013). Also, Viswanathan *et al.*, (2005) dissolved resveratrol in EtOH but added DMSO to treatment media, because DMSO is necessary for resveratrol efficacy. However, Chen, Rezaizadehnajafi and Wink, (2013) dissolved resveratrol in DMSO, therefore, treatment media utilised by Viswanathan *et al.*, (2005) contained an extra compound which may have affected the reproducibility of results.

Ubiquitous and neuron-specific overexpression of the *Drosophila* homologue of yeast Sir2, dSir2, were reported to increase lifespan beyond that of controls (Rogina and Helfand, 2004). However, results obtained using *Drosophila* ubiquitously overexpressing dSir2 were unsupported by another study (Burnett *et al.*, 2011) but supported by a further study (Whitaker *et al.*, 2013). Validation of the effect of neuron-specific dSir2 overexpression on longevity has not been investigated.

Mutant mice expressing catalytically-inactive Sirt1 (*Sirt1*$^{ci/ci}$ mice) develop perinatal lethality; despite the number of *Sirt1*$^{ci/ci}$ embryos being in accordance to Mendelian inheritance during late gestation, they constitute 10% of pups born and 67% of these pups die during their first week after birth. *Sirt1*$^{ci/ci}$ mice are characterised by small size compared to littermate controls, occasional exencephaly, reduced sperm numbers, cardiac abnormalities such as a ventricular septal defect (VSD), atrial septal defect (ASD) and elongated atrioventricular valves. Cardiac abnormalities were not observed in *Sirt1*$^{ci/ci}$ mice which survived to adulthood (Cheng *et al.*, 2003).

Sirt1$^{ci/ci}$ mice also develop eye defects such as abnormal closure of the optic fissure in embryos, thin and disorganised retinal cell layers in adults. *Sirt1*$^{ci/ci}$ mouse embryonic fibroblasts (MEFs) are more susceptible to DNA damage-induced p53 acetylation. *Sirt1* mutant mice develop a similar phenotype to *Sirt1*$^{ci/ci}$ mice (Cheng *et al.*, 2003).

According to Wang *et al.*, (2008), *Sirt1* mutant mice display embryonic lethality, supporting McBurney *et al.*, (2003). Some *Sirt1* heterozygous mice develop exencephaly, reminiscent of *Sirt1*$^{ci/ci}$ mice. *Sirt1* mutant MEFs have impaired chromosome condensation, impaired heterochromatin formation and impaired DNA damage repair (Wang *et al.*, 2008).

Interestingly, the *Sirt1* mutant phenotype is not rescued in *Sirt1;P53* double mutant mice, suggesting that the *Sirt1* mutant phenotype is not mediated by P53 (Kamel *et al.*, 2006; Wang *et al.*, 2008). Adult *Sirt1;P53* double heterozygous mice develop tumours (primarily sarcomas, lymphomas, teratomas and carcinomas) more rapidly compared to *Sirt1* heterozygous and *P53* heterozygous mice. Resveratrol treatment reduces spontaneous tumour formation in *Sirt1;P53* double heterozygous mice, and the few tumours in resveratrol-treated *Sirt1;P53* double heterozygous mice do not express Sirt1, thereby implicating Sirt1 in cancer (Wang *et al.*, 2008). Resveratrol treatment of *P53* heterozygous mice, as well as Sirt1 overexpression in lymphocytes of *P53* heterozygous mice increase survival following exposure to ionising radiation by reducing the frequency of malignant thymic lymphomas (Oberdoerffer *et al.*, 2008).

Lifespan is not increased in Sirt1 overexpressing mice (Herranz *et al.*, 2010). However, Sirt1 overexpressing mice have a lower incidence of metabolic syndrome, osteoporosis, motor impairment, DNA damage and liver cancer (Bordone *et al.*, 2007; Banks *et al.*, 2008; Pfluger *et al.*, 2008; Herranz *et al.*, 2010).

Brain-specific Sirt1-overexpressing (BRASTO) mice have increased lifespan which is thought to be caused by Sirt1-mediated upregulation of orexin type 2 receptor (*Ox2r*) in the dorsomedial and lateral hypothalamic nuclei via deacetylation of Nk2 homeobox 1 (Nkx2-1) (A. Satoh *et al.*, 2013). Interestingly, sirtuin function is often associated with caloric restriction (Grabowska, Sikora and Bielak-Zmijewska, 2017).

4.1.3 Role in neurodegenerative diseases

Sirt1 overexpression and NAD^+ treatment promote α-secretase activity and attenuate Aβ peptide generation in Tg2576 mouse neuronal cultures (a model for AD), by reducing the expression of the serine/threonine Rho kinase, Rho-associated coiled-coil kinase 1 (ROCK1), thereby promoting non-amyloidogenic processing of APP (Qin *et al.*, 2006).

Sirt1 expression is also increased in the cortex but decreased in the hippocampus of 3xTg-AD mice (another AD model) at 6 months after birth, which is when cognitive deficits begin in 3xTg-AD mice, thereby associating Sirt1 expression with the development of AD (Torres-Lista *et al.*, 2014). Likewise, studies utilising 10-12 AD patients and age-matched controls have shown that SIRT1 expression is decreased in the frontal and temporal cortices, and hippocampus of AD patient brains (Singh, Hanson and Morris, 2017; Cao *et al.*, 2018). Likewise, SIRT1 activity is decreased in the frontal and temporal cortices of AD patients (Singh, Hanson and Morris, 2017).

Brain-specific KO of *Sirt1* enhances Huntington's disease (HD) phenotypes in R6/2 mice such as motor impairment, atrophy of striatal neurons and aggregation of mutant huntingtin protein while overexpression of Sirt1 ameliorates HD phenotypes (Jeong *et al.*, 2011), supporting Jiang *et al.*, (2011). Sirt1 deacetylates and activates cAMP-response element binding protein (CREB)-regulated transcription coactivator 1 (TORC1), thereby promoting TORC1's interaction with CREB, resulting in the transcription of the neuroprotective factor, *brain-derived neurotrophic factor* (*BDNF*) in R6/2 mice (Jeong *et al.*, 2011).

Sirt1-mediated upregulation of *BDNF* also inhibits microglial activation in the hippocampus of a mouse model of type-2-diabetes (Lang *et al.*, 2020). Also, increase in NAD^+ improves motor function and expression of mitochondrial ETC genes in mice deficient for mitochondrial complex IV (Cerutti *et al.*, 2014).

4.1.3.1 Role in PD

Increased Sirt1 expression is associated with the rescue of neuronal death, decreased ROS levels and upregulation of antioxidant genes such as *superoxide dismutase 1* (*Sod1*) and *glutathione peroxidase 1* (*Gpx1*) in MPP^+-treated PC12 cells, pre-treated with the polyphenol, Epigallocatechin-3-gallate (EGCG) (Du *et al.*, 2012; Ye *et al.*, 2012). Although 2.5µM EGCG rescued neuronal death following MPP^+ exposure, Ye *et al.*, (2012) utilised 10.0µM EGCG in the subsequent experiment which showed increased Sirt1 expression in MPP^+-treated PC12 cells, pre-treated with EGCG. It is possible that the use of a higher than necessary EGCG concentration elicited non-specific effects unaccounted for by Ye *et al.*, (2012).

Exposure of PC12 cells to exogenous α-Synuclein downregulates *sirt1* mRNA expression, and promotes ROS formation and cell death (Motyl *et al.*, 2018). Overexpression of WT SIRT1 ameliorates cell death, decreases the expression of the pro-inflammatory transcription factor NF-κB (Liu *et al.*, 2017), decreases the expression of phosphorylated α-Synuclein and decreases the expression of cleaved PARP1 (a marker of caspase-dependent apoptosis) in rotenone-treated SH-SY5Y cells (Singh, Hanson and Morris, 2017). SIRT1-mediated protection from rotenone is not solely due to SIRT1's catalytic activity, as overexpression of catalytically inactive SIRT1 also ameliorates rotenone's effects, however, to a smaller degree when compared to overexpression of WT SIRT1 (Singh, Hanson and Morris, 2017).

Exposure to resveratrol ameliorates motor impairment, rescues SNpc dopaminergic neuron loss, attenuates the reduction of striatal dopamine levels, decreases striatal levels of cleaved caspase 3, and decreases α-Synuclein expression in the striatum and substantia nigra of MPTP-treated mice. In response to resveratrol exposure, SIRT1 deacetylates microtubule-associated protein 1A/1B-light chain 3 (LC3), thereby promoting LC3 translocation from the nucleus to the cytoplasm and α-Synuclein clearance through autophagy (Guo *et al.*, 2016). Resveratrol's effects were confirmed to be SIRT1-specific because they were abolished by EX-527 treatment.

Sirt1 expression is decreased in the SNpc of hm^{2}α-SYN-39 Tg mice which express a double-mutant form of human α-Synuclein, containing the A30P and A53T mutations. Sirt1 expression is also decreased in the SNpc of MPTP-treated WT mice and is due to Sirt1 degradation through the UPS, which is regulated by Cdk5 (Zhang *et al.*, 2018).

Sirt1 mutant mice develop worse MPTP-induced motor impairment compared to WT mice, suggesting increased susceptibility to MPTP (Zhang *et al.*, 2018). However, neuronal and CNS-specific overexpression of Sirt1 do not confer protection against MPTP-induced neurodegeneration in mice (Kakefuda *et al.*, 2009; Kitao *et al.*, 2015). Interestingly, resveratrol ameliorates MPTP-mediated neurodegeneration of SNPc dopaminergic neurons, suggesting that resveratrol-mediated protection from MPTP is Sirt1-independent. Also, brain-specific overexpression of Pgc-1α (a target of Sirt1) protects SNpc dopaminergic neurons from MPTP-mediated neurodegeneration (Mudò *et al.*, 2012). A PubMed search did not reveal any publications detailing MPTP experiments utilising ubiquitous Sirt1 overexpressing mice. Therefore, it remains unknown if ubiquitous overexpression of Sirt1 protects SNpc dopaminergic neurons from MPTP-induced neurodegeneration.

Studies have investigated the role of SIRT1 in PD such as, Chen *et al.*, (2019) who evaluated 222 PD patients and 161 age-matched controls, and reported an association between the *SIRT1* SNP, rs12778366, and PD risk, with a p-value of 0.0221. PD patients homozygous for rs12778366 had decreased *SIRT1* mRNA levels in peripheral blood leukocytes compared to controls.

Also, Maszlag-Török *et al.*, (2021) evaluated 177 PD patients and 171 age-matched controls for an association between *SIRT1* SNPs and PD risk. They reported an association between 2 *SIRT1* SNPs, rs3740051 and rs3818292, and PD risk, with p-values of 0.0212 and 0.0097, respectively. A further evaluation of 84 PD patients and 52 age-matched controls revealed lower *SIRT1* mRNA levels in peripheral venous blood samples of PD patients compared to controls. Other PD GWAS studies have not identified an association between *SIRT1* SNPs and PD risk (Nalls *et al.*, 2019).

Singh, Hanson and Morris, (2017) investigated SIRT1 expression in 12 PD patients and 12 age-matched controls, and reported increased SIRT1 expression in the frontal cortex of PD patients compared to controls but decreased SIRT1 expression in the temporal cortex of PD patients, compared to controls.

However, SIRT1 activity was decreased in both the frontal and temporal cortices of PD patients compared to controls.

Zhu *et al.*, (2021) evaluated 58 PD patients and 91 age-matched controls and reported lower serum SIRT1 levels in PD patients. Low serum SIRT1 levels were associated with cognitive impairment, age of disease onset, disease duration and motor impairment.

4.1.4 *sirt1* mutant zebrafish

sirt1 is ubiquitously expressed in zebrafish embryos, like in human tissues (Potente *et al.*, 2007). Kim *et al.*, (2019) generated a *sirt1* mutant zebrafish line which is characterised by increased ROS levels in larvae, inflammation marked by upregulation of *il-1β*, *il-6*, *il-8*, *nitric oxide synthase 2* (*nos2*), *tnf-α* and *suppressor of cytokine signalling 1a* (*socs1a*) in larvae and/or adult tissues, intestinal inflammatory cell infiltration and apoptosis in adult zebrafish. Survival of *sirt1* mutant zebrafish is similar to that of WT siblings until 5mpf when it begins to decrease progressively. However, some *sirt1* mutant zebrafish survive to 18mpf.

In this chapter, the Bandmann *sirt1* mutant zebrafish line (referred to as the *sirt1*$^{-/-}$ zebrafish line in this thesis) and a chemical model for *SIRT1* deficiency will be discussed. Chapter-specific aims are provided below (**Section 4.1.5**).

4.1.5 Chapter-specific aims

This chapter describes:

- The generation and characterisation of the *sirt1*$^{-/-}$ line to study ageing-related mechanisms and PD-relevant pathological mechanisms, namely *il-1β* and *il-6* mRNA expression.
- Microglial activation in a chemical model for *SIRT1* deficiency.
- Whether chemical inhibition of sirt1 induces/enhances motor impairment and cell death in Tg(*eno2*:hsa.*SNCA*-ires-EGFP) zebrafish.

4.2 Methods

4.2.1 Confirmation of the zebrafish orthologue of human *SIRT1*

Ensembl describes *SIRT1* (ENSG00000096717) as a protein-coding gene located on human chromosome 10 (**Figure 4.3B**). Ensembl's "orthologues" tool identified a single zebrafish orthologue, *sirt1* (ENSDARG00000068064), with 50.07% of the genomic sequence of *SIRT1* matching the genomic sequence of *sirt1* (**Figure 4.3A**). *sirt1* is located on zebrafish chromosome 13 and synteny is conserved between *SIRT1* and *sirt1*, with *HERC4/herc4* located on a nearby locus in both humans and zebrafish (**Figure 4.3B**).

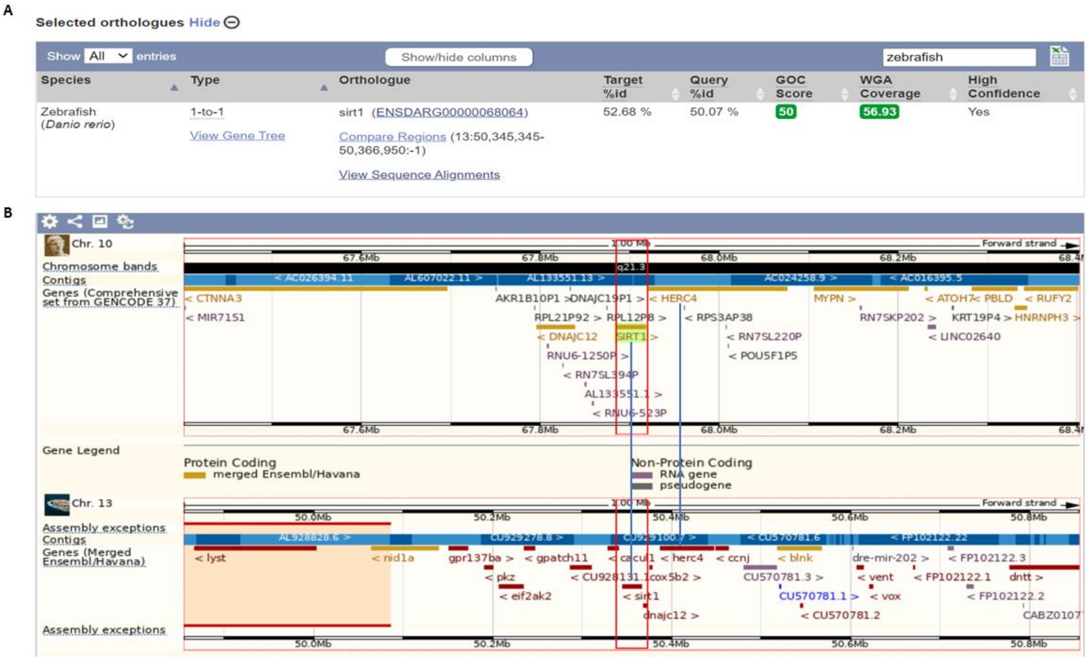

Species	Type	Orthologue	Target %id	Query %id	GOC Score	WGA Coverage	High Confidence
Zebrafish (*Danio rerio*)	1-to-1 View Gene Tree	sirt1 (ENSDARG00000068064) Compare Regions (13:50,345,345-50,366,950:-1) View Sequence Alignments	52.68 %	50.07 %	50	56.93	Yes

__Figure 4.3. Zebrafish have a single SIRT1 orthologue.__ sirt1 is the single zebrafish orthologue of human SIRT1 with 50.07% of the genomic sequence of human SIRT1 matching the genomic sequence of zebrafish sirt1 (A). Also, synteny is conserved between human SIRT1 and zebrafish sirt1, as shown by the localisation of HERC4/herc4 in a nearby locus to SIRT1/sirt1 (B). HERC4, HECT And RLD Domain Containing E3 Ubiquitin Protein Ligase 4.

SIRT1 is alternatively spliced, giving 6 transcripts (**Table 4.2**), 4 of which are protein-coding. However, the most biologically relevant transcript identified by Ensembl is *SIRT1-201* (ENST00000212015.11). In contrast, *sirt1* has a single annotated protein-coding transcript, *sirt1-201* (**Table 4.2**). Thereby, *SIRT1-201* and *sirt1-201* were used for subsequent *in silico* analyses.

To validate the above analyses (**Figure 4.3**), *SIRT1's* cDNA sequence (ENST00000212015.11) was aligned against the zebrafish transcriptome, using Ensembl's BLASTN tool. *sirt1* (ENSDART00000098209.5) was the top hit with 84.74% identity to *SIRT1* (**data not shown**). Both *SIRT1* and *sirt1* transcripts have 9 exons, with the *SIRT1* transcript containing 4,107bp while the *sirt1* transcript contains 6,340bp (**Table 4.2**).

Next, SIRT1’s protein sequence (ENSP00000212015.6) was aligned against the zebrafish proteome, using Ensembl’s BLASTP tool. sirt1 (ENSDARP00000088981.3) was the top hit with 60.21% identity to SIRT1 (**data not shown**). SIRT1 contains 747 amino acids while sirt1 contains 710 amino acids. However, the catalytic domain is conserved in both proteins (**Table 4.2**).

Pertinent Information	**Gene**	
	SIRT1 **(Human)**	***sirt1*** **(Zebrafish)**
Location	Chromosome 10	Chromosome 13
Number of exons	9	9
Length of cDNA	4,107bp	6,340bp
Length of protein	747 amino acids	710 amino acids
Catalytic domain present	Yes	Yes

Table 4.2. Comparison between SIRT1 and sirt1 with regards to their respective genomic locations, number of exons in relevant transcripts, length of cDNA and protein in relevant transcripts, and conservation of its catalytic domain. *bp, base pairs; cDNA, complementary DNA.*

Likewise, the amino acid sequences of SIRT1 and sirt1 were aligned, using CLUSTAL. There is a 47.0% identity between SIRT1 and sirt1, with yellow highlighting identical amino acids and green highlighting conservative substitution (**Figure 4.4**). The difference in % identities between Ensembl BLASTP and CLUSTAL alignment is likely due to differences in programming software.

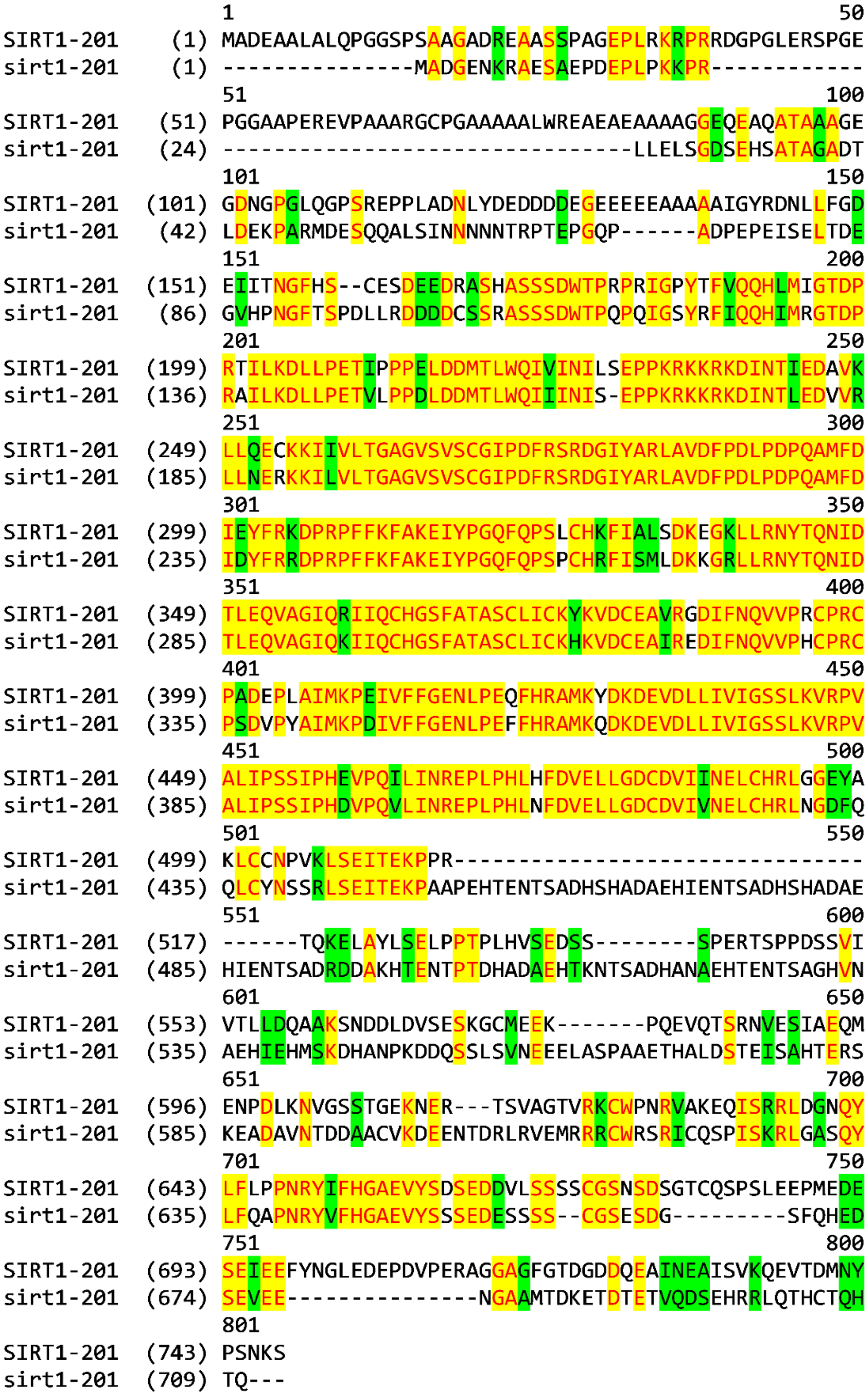

```
                  1                                                50
SIRT1-201     (1) MADEAALALQPGGSPSAAGADREAASSPAGEPLRKRPRRDGPGLERSPGE
sirt1-201     (1) ---------------MADGENKRAESAEPDEPLPKKPR------------
                  51                                              100
SIRT1-201    (51) PGGAAPEREVPAAARGCPGAAAAALWREAEAEAAAAGGEQEAQATAAAGE
sirt1-201    (24) --------------------------------LLELSGDSEHSATAGADT
                  101                                             150
SIRT1-201   (101) GDNGPGLQGPSREPPLADNLYDEDDDDEGEEEEEAAAAAIGYRDNLLFGD
sirt1-201    (42) LDEKPARMDESQQALSINNNNNTRPTEPGQP------ADPEPEISELTDE
                  151                                             200
SIRT1-201   (151) EIITNGFHS--CESDEEDRASHASSSDWTPRPRIGPYTFVQQHLMIGTDP
sirt1-201    (86) GVHPNGFTSPDLLRDDDDCSSRASSSDWTPQPQIGSYRFIQQHIMRGTDP
                  201                                             250
SIRT1-201   (199) RTILKDLLPETIPPPELDDMTLWQIVINILSEPPKRKKRKDINTIEDAVK
sirt1-201   (136) RAILKDLLPETVLPPDLDDMTLWQIIINIS-EPPKRKKRKDINTLEDVVR
                  251                                             300
SIRT1-201   (249) LLQECKKIIVLTGAGVSVSCGIPDFRSRDGIYARLAVDFPDLPDPQAMFD
sirt1-201   (185) LLNERKKILVLTGAGVSVSCGIPDFRSRDGIYARLAVDFPDLPDPQAMFD
                  301                                             350
SIRT1-201   (299) IEYFRKDPRPFFKFAKEIYPGQFQPSLCHKFIALSDKEGKLLRNYTQNID
sirt1-201   (235) IDYFRRDPRPFFKFAKEIYPGQFQPSPCHRFISMLDKKGRLLRNYTQNID
                  351                                             400
SIRT1-201   (349) TLEQVAGIQRIIQCHGSFATASCLICKYKVDCEAVRGDIFNQVVPRCPRC
sirt1-201   (285) TLEQVAGIQKIIQCHGSFATASCLICKHKVDCEAIREDIFNQVVPHCPRC
                  401                                             450
SIRT1-201   (399) PADEPLAIMKPEIVFFGENLPEQFHRAMKYDKDEVDLLIVIGSSLKVRPV
sirt1-201   (335) PSDVPYAIMKPDIVFFGENLPEFFHRAMKQDKDEVDLLIVIGSSLKVRPV
                  451                                             500
SIRT1-201   (449) ALIPSSIPHEVPQILINREPLPHLHFDVELLGDCDVIINELCHRLGGEYA
sirt1-201   (385) ALIPSSIPHDVPQVLINREPLPHLNFDVELLGDCDVIVNELCHRLNGDFQ
                  501                                             550
SIRT1-201   (499) KLCCNPVKLSEITEKPPR--------------------------------
sirt1-201   (435) QLCYNSSRLSEITEKPAAPEHTENTSADHSHADAEHIENTSADHSHADAE
                  551                                             600
SIRT1-201   (517) ------TQKELAYLSELPPTPLHVSEDSS--------SPERTSPPDSSVI
sirt1-201   (485) HIENTSADRDDAKHTENTPTDHADAEHTKNTSADHANAEHTENTSAGHVN
                  601                                             650
SIRT1-201   (553) VTLLDQAAKSNDDLDVSESKGCMEEK-------PQEVQTSRNVESIAEQM
sirt1-201   (535) AEHIEHMSKDHANPKDDQSSLSVNEEELASPAAETHALDSTEISAHTERS
                  651                                             700
SIRT1-201   (596) ENPDLKNVGSSTGEKNER---TSVAGTVRKCWPNRVAKEQISRRLDGNQY
sirt1-201   (585) KEADAVNTDDAACVKDEENTDRLRVEMRRRCWRSRICQSPISKRLGASQY
                  701                                             750
SIRT1-201   (643) LFLPPNRYIFHGAEVYSDSEDDVLSSSSCGSNSDSGTCQSPSLEEPMEDE
sirt1-201   (635) LFQAPNRYVFHGAEVYSSSEDESSSS--CGSESDG---------SFQHED
                  751                                             800
SIRT1-201   (693) SEIEEFYNGLEDEPDVPERAGGAGFGTDGDDQEAINEAISVKQEVTDMNY
sirt1-201   (674) SEVEE---------------NGAAMTDKETDTETVQDSEHRRLQTHCTQH
                  801
SIRT1-201   (743) PSNKS
sirt1-201   (709) TQ---
```

Figure 4.4. Protein alignment of human SIRT1 and zebrafish sirt1. *There is 47.0% identity between human SIRT1 and zebrafish sirt1. Yellow highlights identical αα sequences while green highlights conservative substitution. αα, amino acid.*

4.2.2 Design and synthesis of *sirt1* WISH probes

Three *sirt1* WISH probes were synthesised. WISH probe 1 was synthesised using qPCR primers that amplify *sirt1* WT cDNA contained within the EST clone, "BM316937" (**Section 2.11.1.2**). This clone was chosen because it was previously used to synthesise a published *sirt1* WISH probe (Potente *et al.*, 2007). However, BM316937 was not available for purchase, hence the decision to synthesise our *sirt1* WISH probe using PCR products. BM316937's sequence was aligned with *sirt1*'s cDNA sequence, using NCBI's online alignment tool (**Section 2.20**). This revealed that the *sirt1* cDNA sequence within BM316937 spans exons 6-8. Therefore, primers were designed to flank this region (**Figure 4.5**). 2 additional *sirt1* WISH probes were synthesised, using qPCR primers that amplify exons 1-4 of *sirt1* WT cDNA (**Figure 4.5**). Primer sequences are available (**Section 2.11.1.2**).

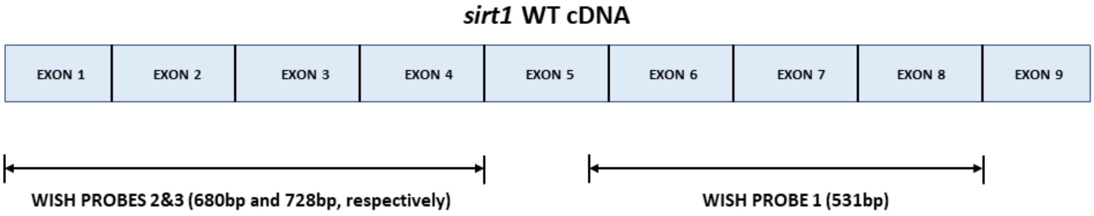

Figure 4.5. Design of sirt1 WISH probes. *3 sirt1 WISH probes were synthesised from PCR products to examine spatial expression of sirt1 mRNA in WT larvae. Probe 1 was designed, by amplifying sirt1 WT cDNA sequence inserted into an EST clone, "BMS316937" utilised by Potente et al., (2007). Probe 1 is 531bp long and contains sirt1 nucleotide sequences spanning exons 5-8 of WT sirt1 cDNA. Probes 2&3 are 680bp and 728bp long, respectively, and contain sirt1 nucleotide sequences spanning exons 1-4 of WT sirt1 cDNA. bp, base pairs; cDNA, complementary DNA; EST, expressed sequence tag; mRNA, messenger RNA; PCR, polymerase chain reaction; WISH, whole-mount in-situ hybridisation; WT, wildtype.*

4.2.3 Generation of the stable *sirt1*$^{-/-}$ zebrafish line

4.2.3.1 sirt1 gRNA efficiency test

The *sirt1* gRNA sequence published by Kim *et al.*, (2019) (TGGACGAGAAACCGGCGCGGA) was used to generate the stable *sirt1*$^{-/-}$ zebrafish line. This gRNA sequence targets exon 1 of *sirt1*.

sirt1 gRNA efficiency was determined by Dr Heba Ismail, using CRISPR-STAT (**Section 2.3.4.2**). A single peak was observed in PCR samples obtained from uninjected embryos (**Figure 4.6**). However, the height of this peak was reduced in CRISPR-injected embryos, in addition to the presence of secondary peaks, indicating genomic editing (**Figure 4.6**).

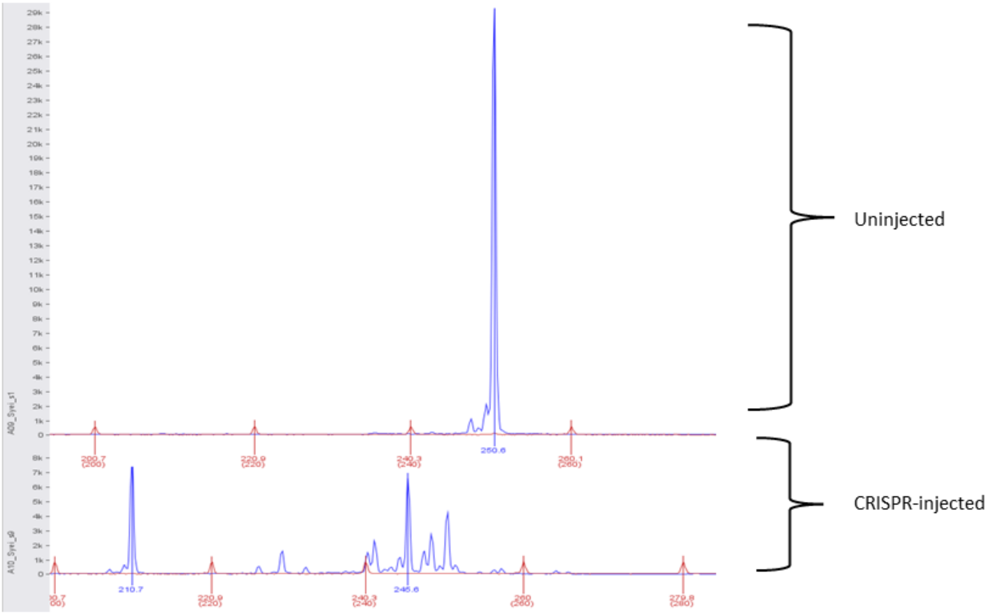

Figure 4.6. sirt1 gRNA efficiency test. *A CRISPR mix containing a gRNA targeting exon 1 of sirt1 (TGGACGAGAAACCGGCGCGGA) was micro-injected into one-cell stage WT zebrafish embryos. DNA was extracted at 24hpf and sirt1 gRNA efficiency was determined using the fluorescent PCR based CRISPR-STAT method. Analysis of the DNA of uninjected embryos revealed a single WT fluorescent PCR peak. However, CRISPR injection reduced this WT peak and resulted in the emergence of secondary peaks, indicating genomic editing. CRISPR, clustered regularly interspaced short palindromic repeats; CRISPR-STAT, CRISPR-somatic tissue activity test; gRNA, guide RNA; hpf, hours post fertilisation; PCR, polymerase chain reaction; WT, wildtype.*

4.2.3.2 Identification of the sirt1 mutant allele

Following confirmation of the high efficiency of *sirt1* gRNA, fresh CRISPR mix containing this gRNA (**Section 2.3.2**) was micro-injected into one-cell stage WT embryos (**Section 2.3.3**), giving an f0 generation. f0 embryos were raised to adulthood then out-crossed to obtain f1$^{+/-}$ embryos. DNA was extracted from 3dpf f1$^{+/-}$ offspring (n =12) obtained from out-crossing a single f0 parent. Non-specific amplification was observed following a PCR reaction using genomic PCR primers provided by Kim *et al.*, (2019) (**data not shown**). Therefore, a new pair of genomic PCR primers were designed to amplify exon 1 of *sirt1* (**Section 2.2.2**). PCR amplification revealed the presence of indel mutations in f1$^{+/-}$ embryos (**Figure 4.7A**). DNA samples extracted from embryos 1, 2 and 3 were sequenced (**Section 2.4**) because they showed indels visible on a gel as double bands; WT DNA sample was also sequenced as control (**Figure 4.7A**). Remaining f1$^{+/-}$ embryos from this out-cross were raised to adulthood.

While f1$^{+/-}$ embryos were being raised to adulthood, sequencing results of DNA samples 1, 2 and 3 were analysed manually by comparison with WT sequence. Embryos 1, 2 and 3 harboured a 2bp deletion, 5bp deletion and 10bp deletion, respectively (**data not shown**). Once f1$^{+/-}$ embryos reached adulthood, DNA was extracted from adult fin clips (**Section 2.2.1.3**), amplified by PCR then sequenced. Again, sequencing results were analysed manually and 2bp deletion, 5bp deletion and 10bp deletion alleles were identified (**data not shown**). An f1$^{+/-}$ adult harbouring a 10bp deletion allele was out-crossed to obtain a stable f2$^{+/-}$ zebrafish line. However, all resulting f2$^{+/-}$ zebrafish were male. Due to time constraints, experiments in this zebrafish line utilised f2$^{+/+}$, f2$^{+/-}$ and f2$^{-/-}$ offspring obtained from a single pair of f1$^{+/-}$ parents, both harbouring the same 10bp deletion allele. In parallel, f2$^{+/-}$ adult zebrafish were out-crossed and offspring were raised to adulthood to obtain f3$^{+/-}$ zebrafish.

Comparison of f2$^{+/+}$ and f2$^{-/-}$ sequences confirmed the presence of a mutant allele harbouring a 10bp deletion of CGGATGGACG (**Figure 4.7B**). This mutation deletes a BccI restriction enzyme site. Therefore, this zebrafish line could be genotyped using BccI restriction digest. PCR products obtained from *sirt1*$^{+/+}$ zebrafish were digested giving 72- and 136bp, while PCR products obtained from *sirt1*$^{-/-}$ zebrafish were undigested, giving 198bp. Due to the presence of a single copy of the WT and mutant allele, PCR products obtained from *sirt1*$^{+/-}$ zebrafish were both digested and undigested, giving 72-, 136- and 198bp (**Figure 4.7C**).

At the protein level, this 10bp deletion induces a premature stop codon (TAA) immediately after 234bp and the predicted protein is truncated, having 78 instead of 710 amino acids. This predicted protein also lacks the conserved catalytic domain (**Figure 4.7D**).

*Figure 4.7. **Generation of the stable sirt1$^{-/-}$ zebrafish line using CRISPR/Cas9 gene editing.** A single highly efficient sirt1 gRNA was injected into one-cell stage WT zebrafish embryos. Injected embryos were raised to adulthood and this founder generation (f0) was out-crossed to obtain f1$^{+/-}$ embryos. DNA was extracted from f1$^{+/-}$ embryos (n = 12) and amplified using PCR, with unrelated WT DNA serving as control. PCR products obtained from individual embryos were loaded into individual lanes of a gel and electrophoresed. Indel mutations were visible in f1$^{+/-}$ embryos, as double and triple DNA bands (A). PCR products in lanes 1, 2 and 3, as well as WT PCR product were sequenced using Genewiz's service. By manually comparing sequences of samples 1, 2 and 3 to WT sequence, they were found to harbour 2bp, 5bp and 10bp deletions, respectively. Remaining f1$^{+/-}$ embryos were raised to adulthood. Once remaining f1$^{+/-}$ embryos reached adulthood, DNA was extracted from fin clips and sequenced. Following sequencing, 2bp, 5bp and 10bp deletions were identified as before. An f1$^{+/-}$ zebrafish with the 10bp allele was out-crossed to obtain a stable f2$^{+/-}$ line. In parallel, a pair of male and female f1$^{+/-}$ zebrafish, both harbouring the 10bp allele were in-crossed. Comparison of f2$^{+/+}$ and f2$^{-/-}$ sequences confirmed the presence of a 10bp deletion of CGGATGGACG (B). For genotyping purposes, the mutation deletes a BccI restriction enzyme site, meaning that PCR products of sirt1$^{+/+}$ zebrafish were digested by BccI, giving 72- and 136bp while PCR products of sirt1$^{-/-}$ zebrafish were undigested, giving 198bp. Due to the presence of a WT and mutant allele, PCR products of sirt1$^{+/-}$ zebrafish were both digested and undigested, giving 72-, 136- and 198bp (C). This 10bp deletion induces a premature stop codon immediately after 234bp. The resulting predicted protein is truncated, having 78 instead of 710αα, and lacks the catalytic domain (D). αα, amino acids; bp, base pairs; CRISPR, clustered regularly interspaced short palindromic repeats; Cas9, CRISPR-associated protein 9; gRNA, guide RNA; Indel, insertion/deletion; PCR, polymerase chain reaction; WT, wildtype.*

4.2.4 Design of *sirt1* qPCR primers

A new pair of qPCR primers (FP2 and RP2) were designed to investigate NMD in *sirt1*$^{-/-}$ larvae, in lieu of qPCR primers obtained from Kim *et al.*, (2019) (FP1 and RP1). This is because the binding sites of FP1 and RP1 flank the mutation site in *sirt1*$^{-/-}$ larvae (**Figure 4.8**), making them unsuitable for comparing *sirt1* expression between *sirt1*$^{+/+}$ and *sirt1*$^{-/-}$ zebrafish, as different transcripts would be detected in *sirt1*$^{+/+}$ and *sirt1*$^{-/-}$ zebrafish. FP2 and RP2 bind *sirt1* cDNA downstream of the mutation and amplify exons 5-6 (**Figure 4.8**).

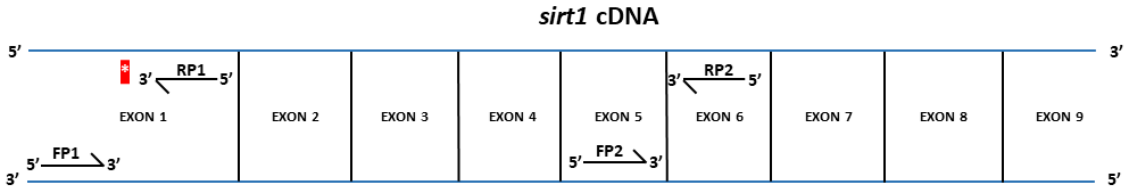

Figure 4.8. Design of a new pair of sirt1 qPCR primers. *To investigate NMD, a new pair of qPCR primers designed (FP2 and RP2) were used in place of qPCR primers obtained from Kim et al., (2019) (FP1 and RP1). This is because FP1 and RP1 flank the sirt1 mutation site (asterisk) in exon 1, thereby they would amplify different transcripts in sirt1*$^{+/+}$ *and sirt1*$^{-/-}$*zebrafish. FP2 and RP2 however flank exons 5 and 6, downstream of the mutation site. cDNA, complementary DNA; FP, forward primer; NMD, nonsense-mediated decay; qPCR, quantitative PCR; RP, reverse primer.*

4.2.5 Generation of the Tg;*sirt1*$^{-/-}$ line

Monoallelic Tg(*eno2*:hsa.*SNCA*-ires-EGFP) zebrafish supplied by the Burton laboratory were crossed with adult *sirt1*$^{+/-}$ zebrafish. Offspring were sorted for GFP expression at 2dpf (**Section 2.1.7**) and GFP-positive offspring were raised to adulthood. Adult offspring were genotyped for the *sirt1* allele and *sirt1*$^{+/-}$ zebrafish were kept, thereby generating a colony of Tg(*eno2*:hsa.SNCA-ires-EGFP);*sirt1*$^{+/-}$ zebrafish (**Figure 4.9**).

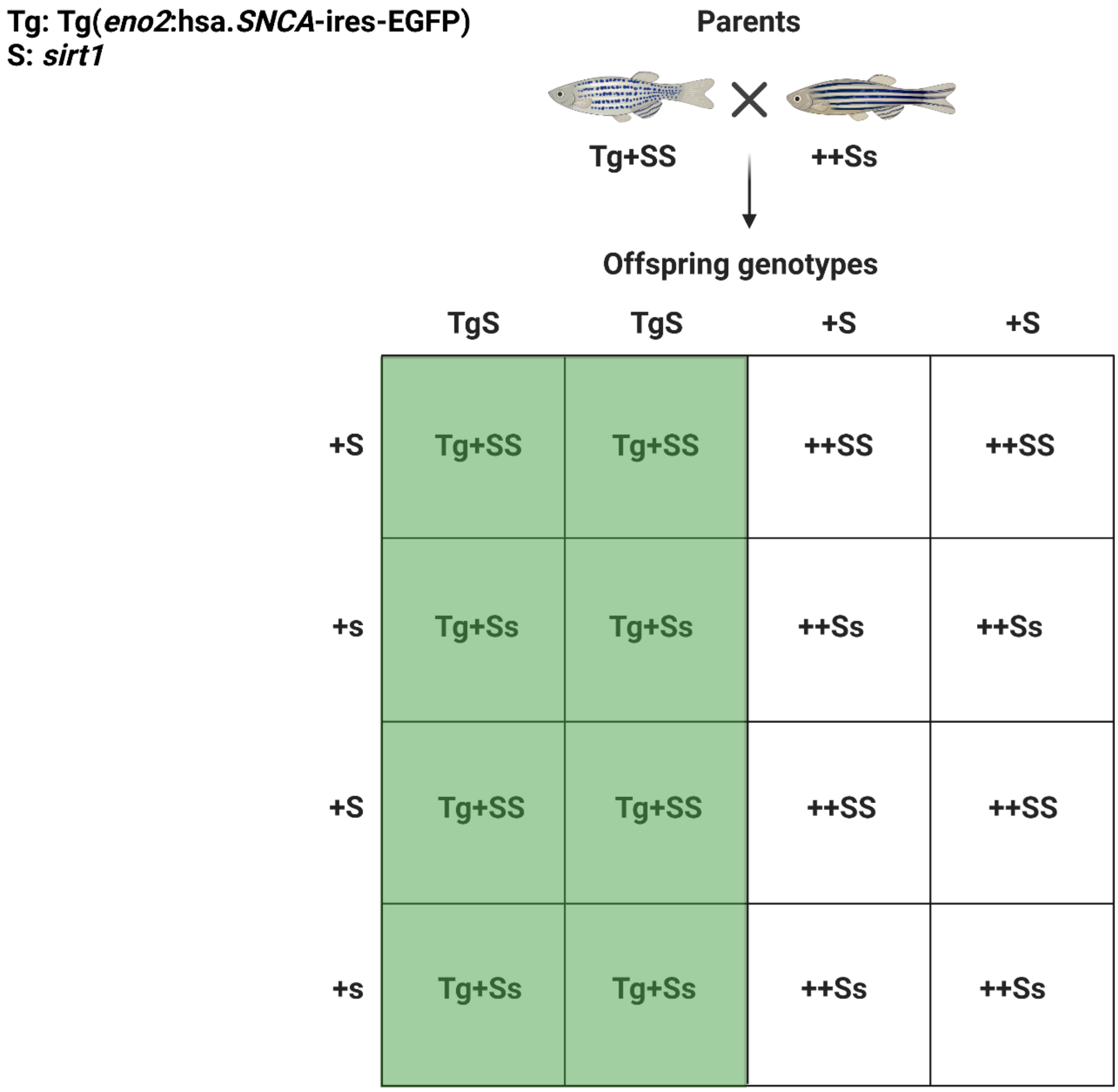

	TgS	TgS	+S	+S
+S	Tg+SS	Tg+SS	++SS	++SS
+s	Tg+Ss	Tg+Ss	++Ss	++Ss
+S	Tg+SS	Tg+SS	++SS	++SS
+s	Tg+Ss	Tg+Ss	++Ss	++Ss

Figure 4.9. A Punnett square of the Tg(eno2:hsa.SNCA-ires-EGFP) x sirt1$^{+/-}$ cross. *Adult monoallelic Tg(eno2:hsa.SNCA-ires-EGFP) zebrafish were crossed with adult sirt1$^{+/-}$ zebrafish. 1/2 of the offspring from this cross expressed GFP (highlighted in green, confirmed by microscopy at 2dpf) and were either sirt1$^{+/+}$ or sirt1$^{+/-}$. GFP-positive embryos were raised to adulthood then genotyped for the sirt1 allele and sirt1$^{+/-}$ zebrafish were kept, generating a colony of Tg(eno2:hsa.SNCA-ires-EGFP);sirt1$^{+/-}$ zebrafish. dpf, days post fertilisation; GFP, green fluorescent protein; s, sirt1; Tg, Tg(eno2:hsa.SNCA-ires-EGFP). Adapted from "Zebrafish Punnett Square (Layout 4x4)", by BioRender.com (2023). Retrieved from https://app.biorender.com/biorender-templates.*

Adult monoallelic Tg(*eno2*:hsa.*SNCA*-ires-EGFP);*sirt1*$^{+/-}$ zebrafish were crossed with adult *sirt1*$^{+/-}$ zebrafish. Offspring were raised to adulthood and genotyped for both *SNCA* and *sirt1* to identify Non-Tg;*sirt1*$^{+/+}$, Non-Tg;*sirt1*$^{-/-}$, Tg;*sirt1*$^{+/+}$ and Tg;*sirt1*$^{-/-}$ zebrafish (**Figure 4.10**).

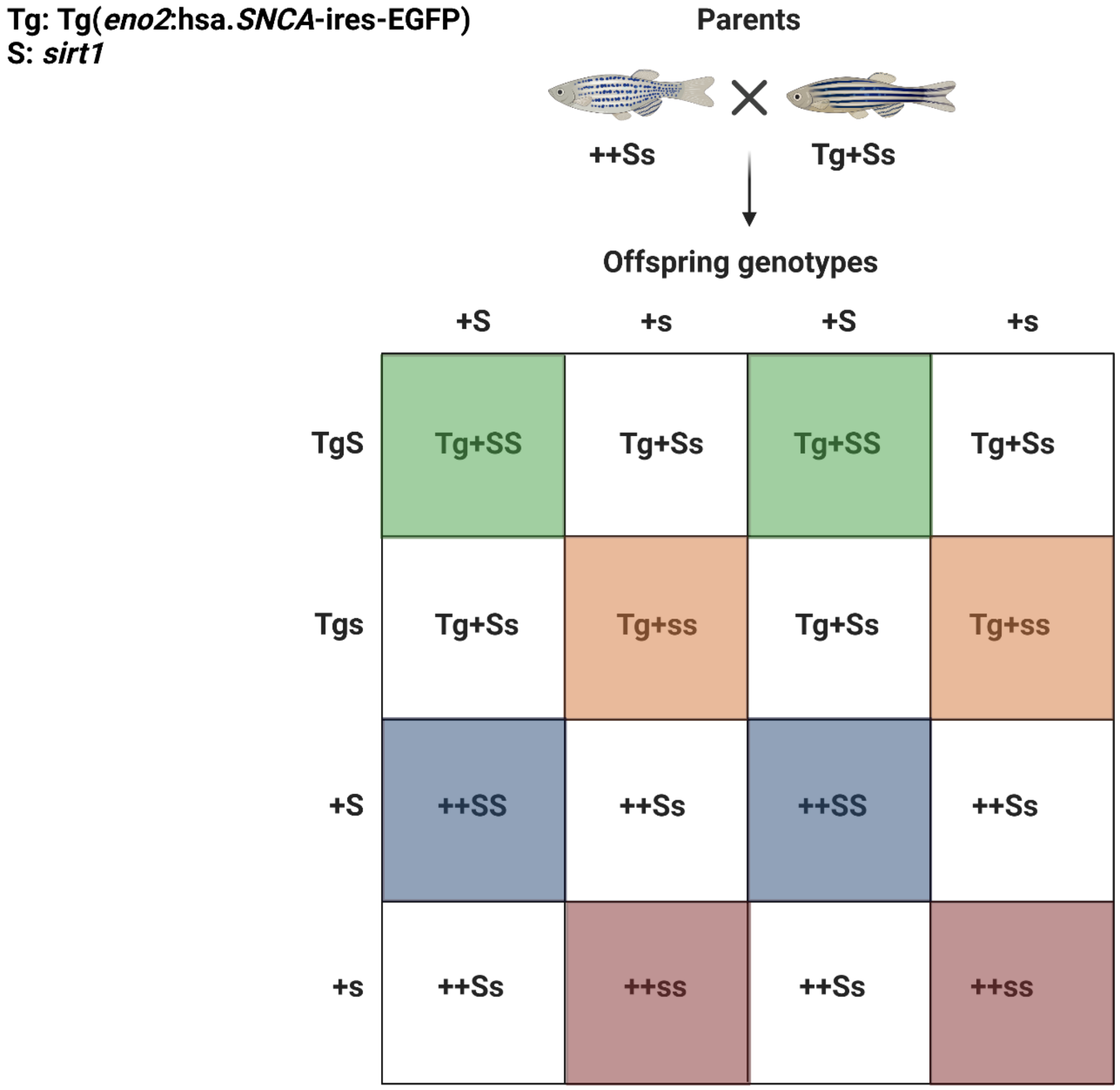

	+S	+s	+S	+s
TgS	Tg+SS	Tg+Ss	Tg+SS	Tg+Ss
Tgs	Tg+Ss	Tg+ss	Tg+Ss	Tg+ss
+S	++SS	++Ss	++SS	++Ss
+s	++Ss	++ss	++Ss	++ss

Figure 4.10. A Punnett square of the Tg(eno2:hsa.SNCA-ires-EGFP);sirt1$^{+/-}$ x sirt1$^{+/-}$ cross. *Adult monoallelic Tg(eno2:hsa.SNCA-ires-EGFP);sirt1$^{+/-}$ zebrafish were crossed with adult sirt1$^{+/-}$ zebrafish. 1/8 of the offspring from this cross were either Non-Tg;sirt1$^{+/+}$ (highlighted in dark blue), Non-Tg;sirt1$^{-/-}$ (highlighted in red), Tg;sirt1$^{+/+}$ (highlighted in green) or Tg;sirt1$^{-/-}$ (highlighted in orange). Non-Tg, non-transgenic; s, sirt1; Tg, Tg(eno2:hsa.SNCA-ires-EGFP). Adapted from "Zebrafish Punnett Square (Layout 4x4)", by BioRender.com (2023). Retrieved from https://app.biorender.com/biorender-templates.*

4.3 Results

4.3.1 Expression of *sirt1* mRNA

4.3.1.1 sirt1 mRNA expression through development

To assess a possible role of *sirt1* in zebrafish development, RT-PCR was employed (**Section 2.9**). RNA was extracted (**Section 2.5**) from WT zebrafish between 0-5dpf. Extracted RNA was reverse transcribed to cDNA (**Section 2.7**) and *sirt1* qPCR primers obtained from Kim *et al.*, (2019) were used to amplify cDNA; *β-actin* served as control.

Although semi-quantitative, RT-PCR can inform changes in gene expression. *sirt1* mRNA expression was first detected at 1dpf and was stably expressed through to 5dpf (**Figure 4.11**), indicating that spatial expression of *sirt1* mRNA could be investigated in 1-5dpf zebrafish. *sirt1* mRNA expression was not investigated in adult tissue.

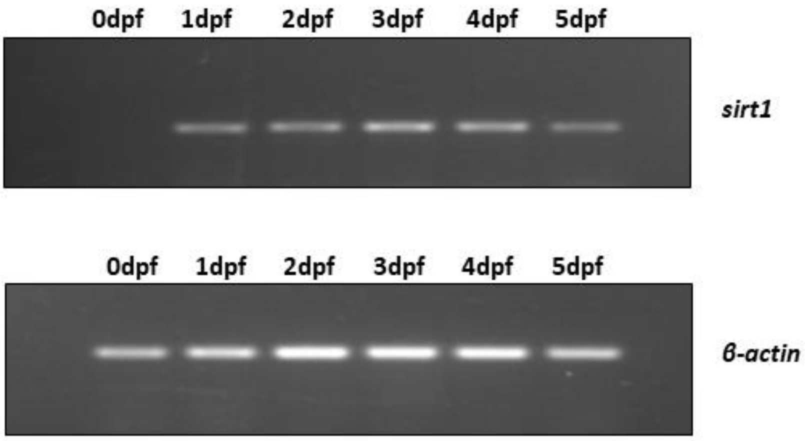

Figure 4.11. sirt1 mRNA expression through development. *RT-PCR was used to investigate sirt1 mRNA expression from 0-5dpf, where; 0dpf refers to the 30% epiboly stage of zebrafish development and β-actin served as loading control. sirt1 expression was first detected at 1dpf and remained unchanged through to 5dpf. β-actin, beta-actin; dpf, days post fertilisation; mRNA, messenger RNA; RT-PCR, reverse transcription PCR.*

4.3.1.2 Spatial expression of sirt1 mRNA

WISH (**Section 2.11**) was employed to investigate spatial *sirt1* expression in WT larvae. 3dpf WT larvae were hybridised with *sirt1* WISH probes (**Section 4.2.2**). However, non-specific staining was consistently observed, as larvae hybridised with both the sense and anti-sense probes were stained in the head and gut (**Figure 4.12**).

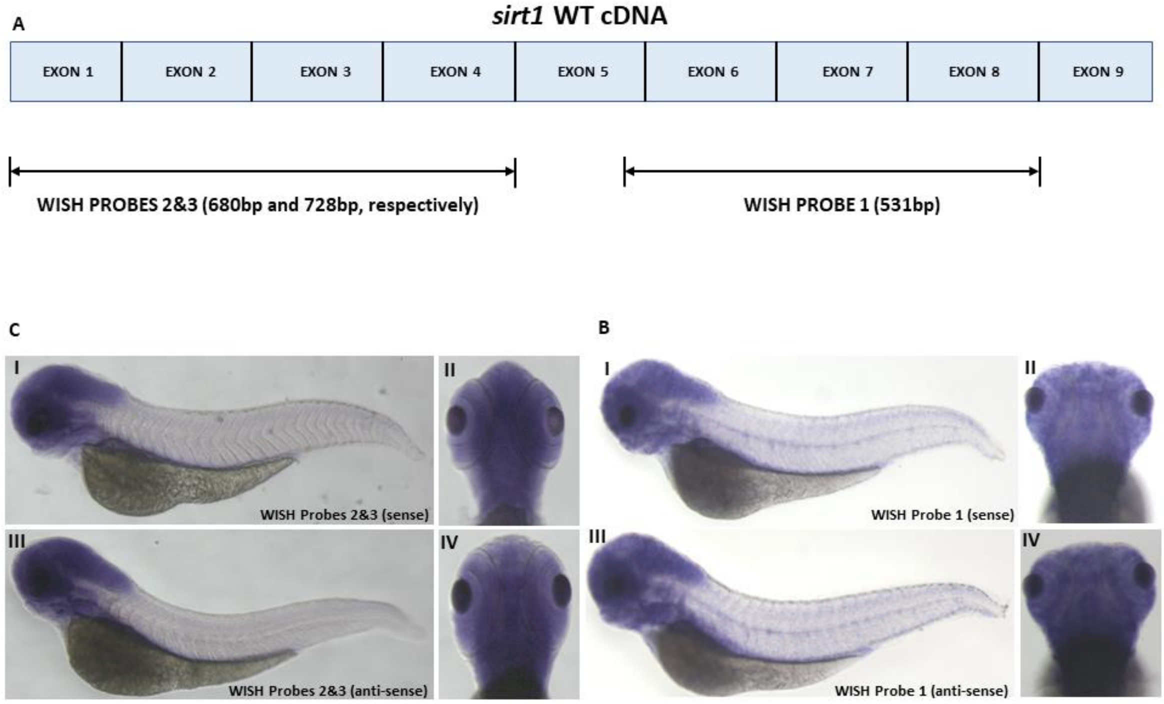

Figure 4.12. Spatial expression of sirt1 mRNA at 3dpf, using WISH. *3 WISH probes were synthesised from PCR products, to examine spatial expression of sirt1 mRNA in WT larvae at 3dpf. Probe 1 was designed, by amplifying sirt1 WT cDNA sequence inserted into an EST clone, "BMS316937" utilised by Potente et al., (2007). Probe 1 is 531bp long and is complementary to cDNA sequence spanning exons 5-8. Probes 2&3 are 680bp and 728bp long, respectively, and are complementary to cDNA sequence spanning exons 1-4 (A). Representative images of 3dpf WT larvae hybridised with probe 1 are provided (B). Representative images of 3dpf WT larvae hybridised with probes 2&3 are also provided (C). I and II are lateral and dorsal images, respectively of larvae hybridised with the sense probe. III and IV are lateral and dorsal images, respectively of larvae hybridised with the anti-sense probe. None of these 3 WISH probes gave specific staining. bp, base pairs; cDNA, complementary DNA; dpf, days post fertilisation; EST, expressed sequence tag; mRNA, messenger RNA; PCR, polymerase chain reaction; WISH, whole-mount in-situ hybridisation; WT, wildtype.*

4.3.2 Characterisation of *sirt1*$^{-/-}$ zebrafish

4.3.2.1 NMD in sirt1$^{-/-}$ *larvae*

Adult *sirt1*$^{+/-}$ zebrafish were crossed, DNA was extracted from larval tail clips of offspring (**Section 2.2.1.2**), and *sirt1*$^{+/+}$ and *sirt1*$^{-/-}$ larvae were identified by genotyping (**Sections 2.2.2 and 2.2.3**). Next, RNA was extracted from pooled *sirt1*$^{+/+}$ and *sirt1*$^{-/-}$ larvae at 5dpf, and extracted RNA was reverse transcribed to cDNA. This was repeated twice to obtain 3 replicates for qPCR experiments (**Section 2.8**).

qPCR showed a trend for NMD of *sirt1* mRNA in *sirt1*$^{-/-}$ larvae at 5dpf with a 66.46% reduction of *sirt1* mRNA levels in *sirt1*$^{-/-}$ larvae compared to age-matched *sirt1*$^{+/+}$ siblings (*sirt1*$^{+/+}$ = 1.08, *sirt1*$^{-/-}$ = 0.36, p = 0.1409, **Figure 4.13**).

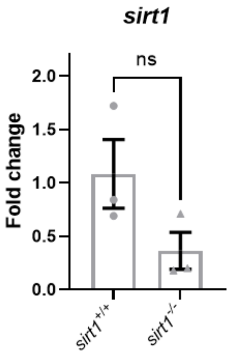

Figure 4.13. Investigation of NMD in sirt1$^{-/-}$ larvae, at 5dpf. *There was a trend for NMD of sirt1 mRNA in the sirt1$^{-/-}$ line at 5dpf. Each replicate was obtained from a single pair of parent f1 sirt1$^{+/-}$ zebrafish. Error bars represent standard error of the mean. Normality was assessed using a Shapiro-Wilk test and data was analysed using a two-way unpaired t-test with Welch's correction. n = 3. p = 0.1409. dpf, days post fertilisation; mRNA, messenger RNA; NMD, nonsense-mediated decay.*

4.3.2.2 Baseline inflammation in sirt1$^{-/-}$ larvae

The only published *sirt1* mutant zebrafish line was characterised by the upregulation of pro-inflammatory genes, such as *il-1β* and *il-6* (Kim *et al.*, 2019). Therefore, *il-1β* and *il-6* mRNA expression were investigated in our *sirt1*$^{-/-}$ zebrafish line. *sirt1*$^{+/+}$ and *sirt1*$^{-/-}$ cDNA samples were obtained as previously detailed (**Section 4.3.2.1**).

There was no significant difference in *il-1β* and *il-6* mRNA expression between *sirt1*$^{+/+}$ and *sirt1*$^{-/-}$ larvae at 5dpf (*il-1β; sirt1*$^{+/+}$ = 1.01667, *sirt1*$^{-/-}$ = 1.2, p = 0.4065, **Figure 4.14A**. *il-6; sirt1*$^{+/+}$ = 1.05333, *sirt1*$^{-/-}$ = 1.11667, p = 0.8526, **Figure 4.14B**), suggesting the absence of a pro-inflammatory phenotype in *sirt1*$^{-/-}$ larvae at 5dpf.

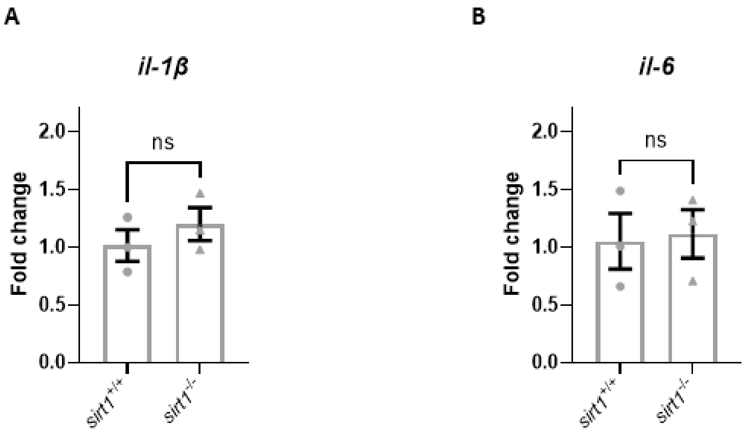

Figure 4.14. Investigation of pro-inflammatory factors in sirt1$^{-/-}$ larvae, at 5dpf. *There was no significant difference in il-1β (A) and il-6 (B) expression between sirt1$^{+/+}$ and sirt1$^{-/-}$ larvae at 5dpf. Each replicate was obtained from a single pair of parent f1 sirt1$^{+/-}$ zebrafish. Error bars represent standard error of the mean. Normality was assessed using a Shapiro-Wilk test and data was analysed using a two-way unpaired t-test with Welch's correction. n = 3. p = 0.4065 (A), p = 0.8526 (B). dpf, days post fertilisation; il-1β, interleukin-1beta; il-6, interleukin-6.*

4.3.2.3 Morphology, morbidity and mortality of sirt1$^{-/-}$ zebrafish

A single pair of adult f1 *sirt1*$^{+/-}$ zebrafish was in-crossed and offspring were carefully monitored to adulthood.

Adult *sirt1*$^{-/-}$ zebrafish did not display an overt phenotype (weight and size were not investigated). Also, the number of adult *sirt1*$^{+/+}$ and *sirt1*$^{-/-}$ zebrafish identified by genotyping was in accordance with Mendelian inheritance (**Table 4.3**), indicating equal viability of *sirt1*$^{+/+}$ and *sirt1*$^{-/-}$ zebrafish to adulthood. Survival was also unaffected in *sirt1*$^{-/-}$ zebrafish; *sirt1*$^{+/+}$ and *sirt1*$^{-/-}$ zebrafish were observed until 12mpf.

Total number of adult *sirt1*$^{+/-}$ in-cross zebrafish = 36			
Zebrafish	***sirt1*$^{+/+}$**	***sirt1*$^{+/-}$**	***sirt1*$^{-/-}$**
Mendelian inheritance	1/4	1/2	1/4
Number of zebrafish predicted by Mendelian inheritance	9	18	9
Number of zebrafish identified by genotyping	6	19	11

Table 4.3. Viability of sirt1$^{-/-}$ zebrafish to adulthood. *Genotyping of 36 adult sirt1$^{+/-}$ in-cross zebrafish revealed that 6 were sirt1$^{+/+}$ zebrafish, 19 were sirt1$^{+/-}$ zebrafish and 11 were sirt1$^{-/-}$ zebrafish, which was in accordance with Mendelian inheritance. Therefore, sirt1$^{-/-}$ zebrafish are viable to adulthood. Genotyping was completed using the Zebrafish Genotyping Service offered by the Biological Services Aquarium.*

4.3.3 Morphology, morbidity and mortality of Tg;*sirt1*$^{-/-}$ zebrafish

Adult Tg;*sirt1*$^{-/-}$ zebrafish did not display an overt phenotype (weight and size were not investigated). The number of adult Non-Tg;*sirt1*$^{+/+}$, Non-Tg;*sirt1*$^{-/-}$, Tg;*sirt1*$^{+/+}$ and Tg;*sirt1*$^{-/-}$ zebrafish identified by genotyping was in accordance with Mendelian inheritance (**Table 4.4**), indicating equal viability of Tg;*sirt1*$^{+/+}$ and Tg;*sirt1*$^{-/-}$ zebrafish to adulthood. Survival was also unaffected in Tg;*sirt1*$^{-/-}$ zebrafish and controls which were monitored until ~12mpf. Due to time constraints, this was the final experiment utilising the *sirt1*$^{-/-}$ line.

Total number of Tg(*eno2*:hsa.*SNCA*-ires-EGFP);*sirt1*$^{+/-}$ x *sirt1*$^{+/-}$ zebrafish = 111				
Zebrafish	**Non-Tg;*sirt1*$^{+/+}$**	**Non-Tg;*sirt1*$^{-/-}$**	**Tg;*sirt1*$^{+/+}$**	**Tg;*sirt1*$^{-/-}$**
Mendelian inheritance	1/8	1/8	1/8	1/8
Number of zebrafish predicted by Mendelian inheritance	14	14	14	14
Number of zebrafish identified by genotyping	9	13	16	18

Table 4.4. Viability of Tg;sirt1$^{-/-}$ zebrafish to adulthood. *Genotyping of 111 adult Tg(eno2:hsa.SNCA-ires-EGFP);sirt1$^{+/-}$ x sirt1$^{+/-}$ zebrafish revealed that 9 were Non-Tg;sirt1$^{+/+}$ zebrafish, 13 were Non-Tg;sirt1$^{-/-}$ zebrafish, 16 were Tg;sirt1$^{+/+}$ zebrafish and 18 were Tg;sirt1$^{-/-}$ zebrafish, which was in accordance with Mendelian inheritance. Therefore, Tg;sirt1$^{-/-}$ zebrafish are viable to adulthood. Non-Tg, non-transgenic; Tg, transgenic.*

4.3.4 Further characterisation of Tg(*eno2*:hsa.*SNCA*-ires-EGFP) zebrafish

Results detailed from this point until the end of this chapter were obtained during my USA placement in the Burton laboratory at the University of Pittsburgh.

To investigate whether chemical inhibition of sirt1 induces/enhances motor impairment in Tg(*eno2*:hsa.*SNCA*-ires-EGFP) larvae, the motor function of EX-527-treated Tg(*eno2*:hsa.*SNCA*-ires-EGFP) out-cross larvae was assessed. First, motor function of Tg(*eno2*:hsa.*SNCA*-ires-EGFP) out-cross larvae was assessed without EX-527 treatment.

4.3.4.1 Movement analysis of Tg(eno2:hsa.SNCA-ires-EGFP) zebrafish

Adult monoallelic Tg(*eno2*:hsa.*SNCA*-ires-EGFP) zebrafish were out-crossed and offspring were sorted for GFP expression at 2dpf (**Section 2.1.7**). Non-Tg siblings and Tg embryos were raised to 6dpf then larval motor function was assessed using a movement assay (**Sections 2.19.1 and 2.19.2**). 6dpf larvae were utilised for this movement assay because robust and reproducible results were previously obtained at this timepoint.

Analysis of the light phase revealed no significant difference in the mean speed (Non-Tg = 0.62 mm/s, Tg = 0.63 mm/s, p = 0.9609, **Figure 4.15A**), % time moving (Non-Tg = 18.52%, Tg = 18.22%, p = 0.8029, **Figure 4.15B**), active duration (Non-Tg = 0.53 s, Tg = 0.54 s, p = 0.7136, **Figure 4.15C**) or rest duration (Non-Tg = 3.87 s, Tg = 3.43 s, p = 0.8349, **Figure 4.15D**) between Non-Tg siblings and Tg larvae.

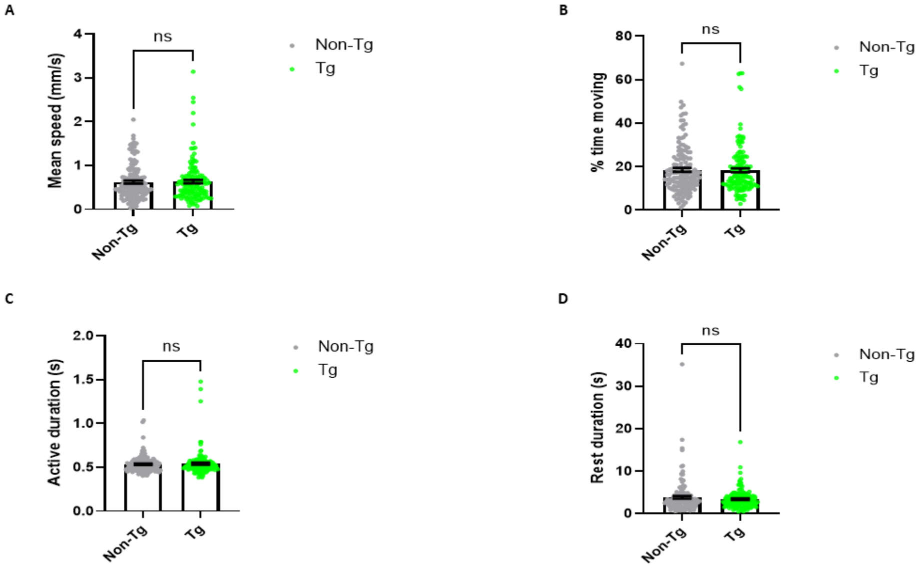

Figure 4.15. Movement of Tg(eno2:hsa.SNCA-ires-EGFP) out-cross larvae in the light phase. *Spontaneous movement of Non-Tg siblings and Tg larvae was assessed during 1 hour of light exposure. There was no significant difference in mean speed (A), % time moving (B), active duration (C) and rest duration (D) between Non-Tg siblings and Tg larvae. Error bars represent standard error of the mean. Data was analysed using a Mann-Whitney test (A-D). Larvae were obtained from 3 clutches of monoallelic Tg(eno2:hsa.SNCA-ires-EGFP) out-cross embryos obtained on different days. n; Non-Tg = 144, Tg = 143. p = 0.9609 (A), p = 0.8029 (B), p = 0.7136 (C), p = 0.8349 (D). Non-Tg, non-transgenic; Tg, transgenic.*

Due to a significant difference between the active speeds of Non-Tg siblings from biological replicates 1, 2 and 3 (**data not shown**), this dataset could not be combined. Instead, active speeds of Non-Tg siblings and Tg larvae from each biological replicate are provided below (**Figure 4.16**). There was no significant difference in the active speed between Non-Tg siblings and Tg larvae in biological replicate 1 (Non-Tg = 3.21 mm/s, Tg = 3.37 mm/s, p = 0.1083, **Figure 4.16A**), biological replicate 2 (Non-Tg = 3.51 mm/s, Tg = 3.56 mm/s, p = 0.6307, **Figure 4.16B**) or biological replicate 3 (Non-Tg = 3.21 mm/s, Tg = 3.10 mm/s, p = 0.1679, **Figure 4.16C**).

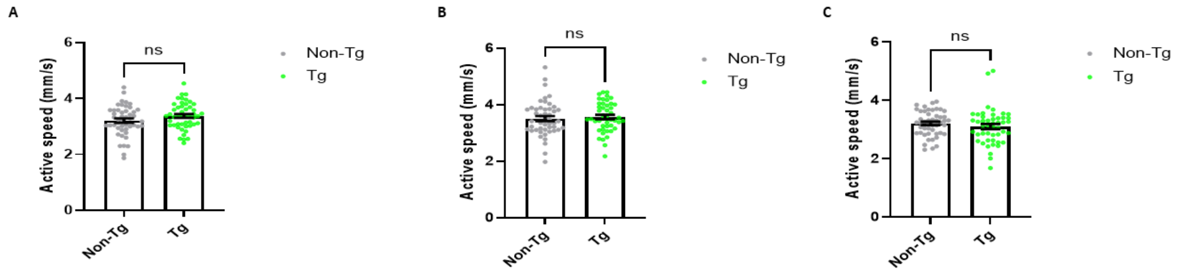

Figure 4.16. Movement of Tg(eno2:hsa.SNCA-ires-EGFP) out-cross larvae in the light phase - active speed. *Spontaneous movement of Non-Tg siblings and Tg larvae was assessed during 1 hour of light exposure. Due to a significant difference in active speeds of Non-Tg siblings between biological replicates, this dataset was not combined. Instead, active speeds were presented for each biological replicate. There was no significant difference in active speed between Non-Tg siblings and Tg larvae in biological replicates 1 (A), 2 (B) and C (3). Error bars represent standard error of the mean. Data was analysed using a two-tailed unpaired t-test with Welch's correction (A-B) and Mann-Whitney test (C). Larvae were obtained from 3 clutches of monoallelic Tg(eno2:hsa.SNCA-ires-EGFP) out-cross embryos obtained on different days. n; Non-Tg = 48, Tg = 48 (A), Non-Tg = 48, Tg = 47 (B), Non-Tg = 48, Tg = 48 (C). p = 0.1083 (A), p = 0.6307 (B), p = 0.1679 (C). Non-Tg, non-transgenic; Tg, transgenic.*

Likewise, analysis of the dark:light cycle showed no significant difference in mean speed between Non-Tg siblings and Tg larvae at any timepoint (**Figure 4.17**). Therefore, expression of human WT α-Synuclein did not induce motor impairment in Tg(*eno2*:hsa.*SNCA*-ires-EGFP) larvae.

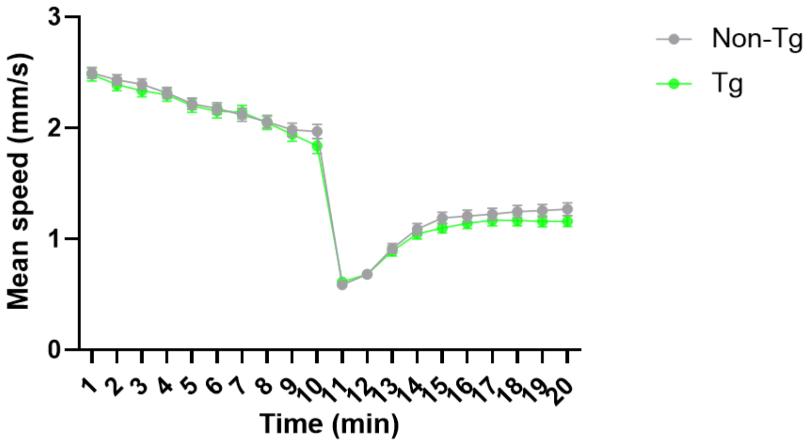

Figure 4.17. Movement of Tg(eno2:hsa.SNCA-ires-EGFP) larvae through the dark:light cycle. *Movement of Non-Tg siblings and Tg larvae was assessed during 10 minute dark:10 minute light cycles (x3). Per replicate, the speed of each larva at each minute was averaged across all 3 cycles. Next, the averaged speeds at each minute were combined across replicates. There was no significant difference between the mean speeds of Non-Tg siblings and Tg larvae. Error bars represent standard error of the mean. Data was analysed using a two-way ANOVA with Šídák's multiple comparisons. Larvae were obtained from 3 clutches of monoallelic Tg(eno2:hsa.SNCA-ires-EGFP) out-cross embryos obtained on different days. n; Non-Tg = 144, Tg = 143. Significance was set at 0.05 level. ANOVA, analysis of variance; Non-Tg, non-transgenic; Tg, transgenic.*

4.3.5 Movement analysis of WT larvae treated with EX-527

To determine toxicity and effective concentrations for subsequent experiments, motor function of WT larvae was investigated, following treatment with a range of EX-527 concentrations (**Section 2.10.2**).

12.5 µM EX-527 was previously shown to worsen motor impairment in a zebrafish model of tauopathy by Dr Qing Bai. Therefore, the highest EX-527 concentration tested in this PhD was 25.0 µM, double of 12.5 µM EX-527.

4.3.5.1. 0-25.0 µM EX-527 dose-response

Analysis of the light phase showed a biphasic dose-response curve, with 1.6 µM EX-527 increasing mean speed and % time moving, while treatment with higher EX-527 concentrations resulted in a dose-dependent decrease of both parameters (**Figure 4.18A and C**). Likewise, biphasic dose-response curves were observed for active speed and active duration (**Figure 4.18 and D**). There was, however, a dose-dependent increase in rest duration (**Figure 4.18E**).

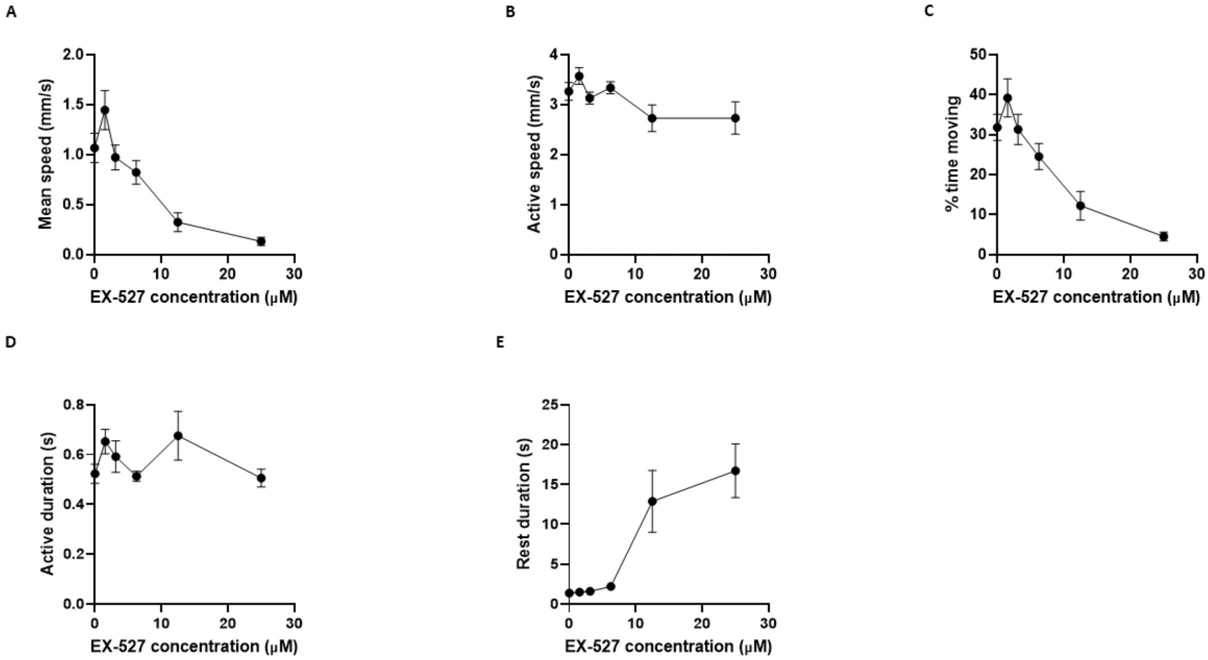

Figure 4.18. Light phase movement of WT larvae treated with EX-527 (0-25.0 µM). *Spontaneous movement of WT larvae following continuous immersion in EX-527 for 96 hours. A biphasic response was observed with 1.6 µM EX-527 for mean speed (A), active speed (B), % time moving (C) and active duration (D) but not rest duration (E). Error bars represent standard error of the mean. n; 0 µM = 11, 1.6 µM = 11, 3.1 µM = 11, 6.2 µM = 11, 12.5 µM = 11, 25.0 µM = 12. EX-527, 6-chloro-2,3,4,9-tetrahydro-1H-carbazole-1-carboxamide; WT, wildtype.*

Further analysis showed that the lowest EX-527 concentration to significantly impair mean speed, % time moving and rest duration was 12.5 µM, with worse motor impairment in larvae treated with 25.0 µM EX-527 (**Figure 4.19A, C and E**). No EX-527 concentration tested in this PhD impaired active speed or active duration (**Figure 4.19B and D**). Higher EX-527 concentrations were not tested because larvae treated with 25.0 µM EX-527 failed to develop swim bladders.

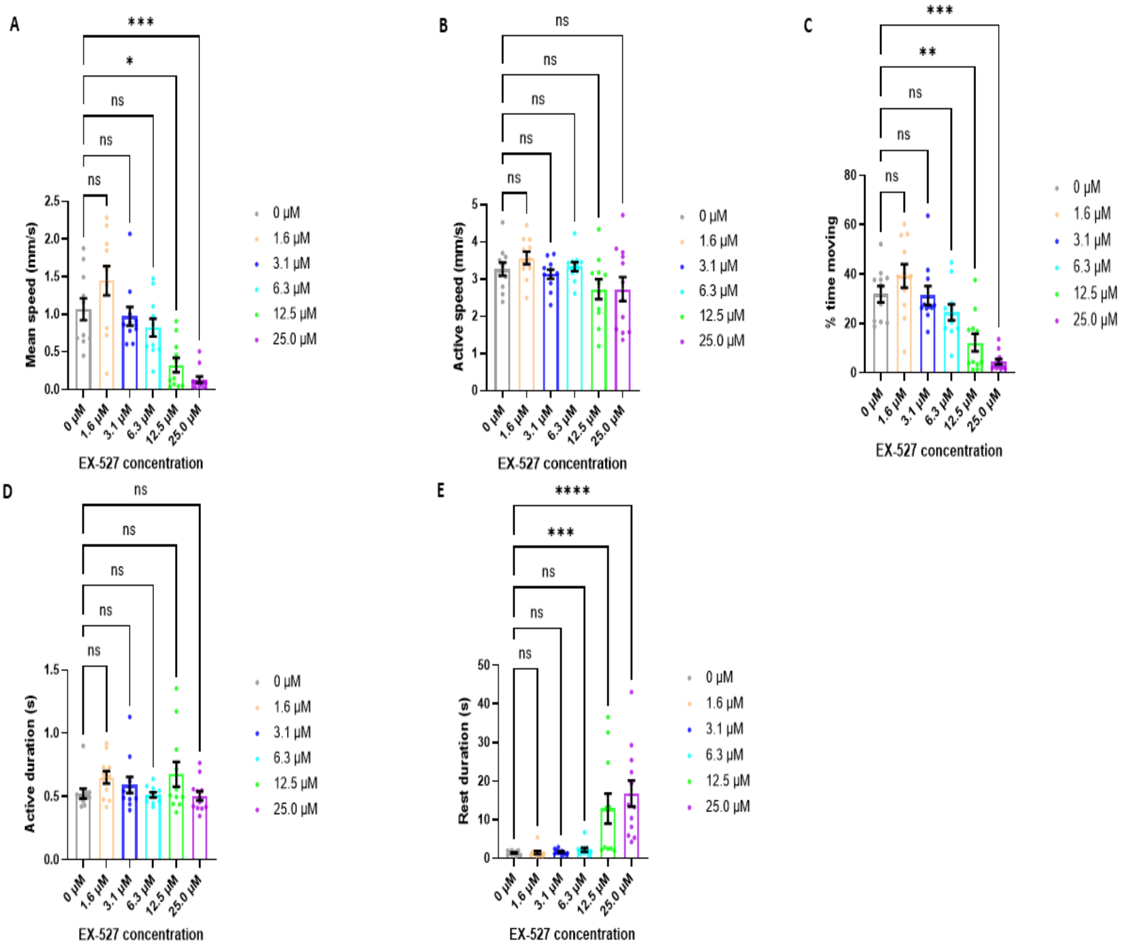

__Figure 4.19. Light phase movement of WT larvae treated with EX-527 (0-25.0 µM)- quantification.__ Spontaneous movement of WT larvae was assessed following continuous immersion in EX-527 for 96 hours. 12.5 µM EX-527 was the lowest concentration to significantly decrease mean speed (A), % time moving (C) and increase rest duration (E). None of the EX-527 concentrations tested effected active speed (B) and active duration (D). Error bars represent standard error of the mean. Data was analysed using a Kruskal-Wallis test with Dunn's multiple comparisons (A,C,D,E) and a Brown-Forsythe and Welch ANOVA test with Dunnett's multiple comparisons (B). n; 0 µM = 11, 1.6 µM = 11, 3.1 µM = 11, 6.2 µM = 11, 12.5 µM = 11, 25.0 µM = 12. Significance was set at 0.05 level. ANOVA, analysis of variance; EX-527, 6-chloro-2,3,4,9-tetrahydro-1H-carbazole-1-carboxamide; WT, wildtype.

Analysis of movement in the dark:light cycle showed that 12.5 µM significantly reduced larval mean speed at minutes 1 and 18 only while 25.0 µM significantly reduced larval mean speed throughout the dark:light cycle, that is, minutes 1-20 (**Figure 4.20**).

It is important to note that due to the small number of larvae utilised in this dose-response experiment, some EX-527 concentrations may induce real motor impairment which would be considered non-significant by statistical analyses.

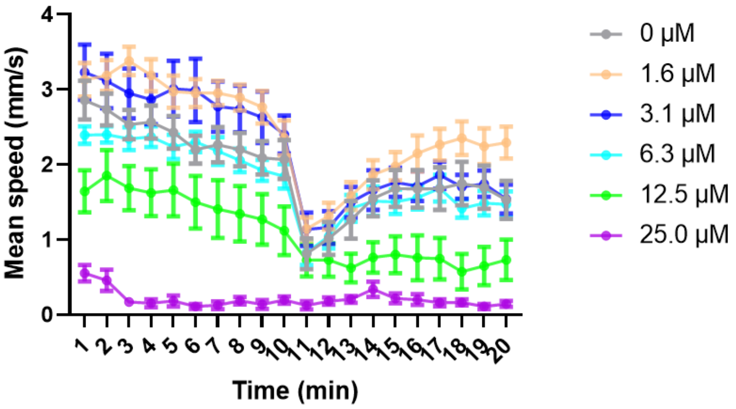

__Figure 4.20. Dark:light cycle movement of WT larvae treated with EX-527 (0-25.0µM).__ Movement of WT larvae during 10 minute dark:10 minute light cycles (x3) was assessed following continuous immersion in EX-527 for 96 hours. Larval speeds at each minute were averaged across all 3 cycles to obtain the dataset presented here. 12.5 µM EX-527 was the lowest concentration to significantly decrease mean speed, at minutes 1 and 18 only. 25.0 µM EX-527 significantly decreased mean speed throughout minutes 1-20. However, larvae exposed to 25.0 µM did not develop swim bladders, indicating toxicity. Error bars represent standard error of the mean. Data was analysed using a two-way ANOVA with Dunnett's multiple comparison. n; 0 µM = 11, 1.6 µM = 11, 3.1 µM = 11, 6.2 µM = 11, 12.5 µM = 11, 25.0 µM = 12. Significance was set at 0.05 level. ANOVA, analysis of variance; EX-527, 6-chloro-2,3,4,9-tetrahydro-1H-carbazole-1-carboxamide; WT, wildtype.

4.3.5.2 0-1.6µM EX-527 dose-response

Due to the above biphasic dose-response curves, another movement assay was run using WT larvae dosed with EX-527 concentrations ranging from 0-1.6 µM. Biphasic dose-response curves were also observed following treatment with 0-1.6 µM EX-527 (**Figure 4.21**).

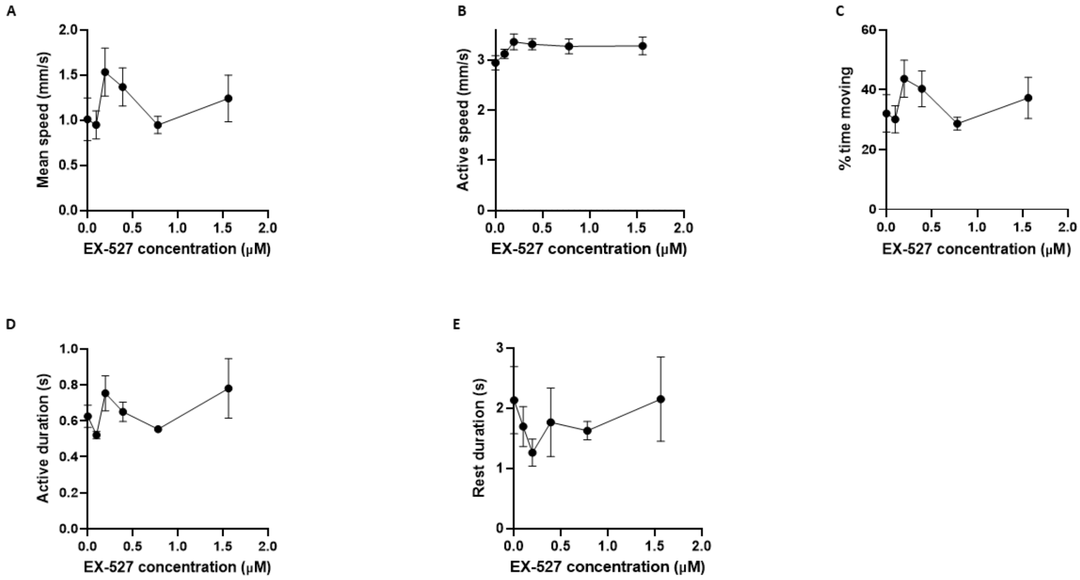

__Figure 4.21. Light phase movement of WT larvae treated with EX-527 (0-1.6 µM).__ Spontaneous movement of WT larvae following continuous immersion in EX-527 for 96 hours. A biphasic response was observed for mean speed (A), % time moving (C), active duration (D), rest duration (E) but not active speed (B). Error bars represent standard error of the mean. n; 0 µM = 10, 0.1 µM = 11, 0.2 µM = 12, 0.4 µM = 12, 0.8 µM = 11, 1.6 µM = 11. EX-527, 6-chloro-2,3,4,9-tetrahydro-1H-carbazole-1-carboxamide; WT, wildtype.

Lower EX-527 concentrations did not have a significant effect on larval movement in the light phase (**Figure 4.22**) and dark:light cycle (**Figure 4.23**). Therefore, only 12.5- and 25.0 µM EX-527 induced significant motor impairment in WT larvae (**Figures 4.19 and 4.20**).

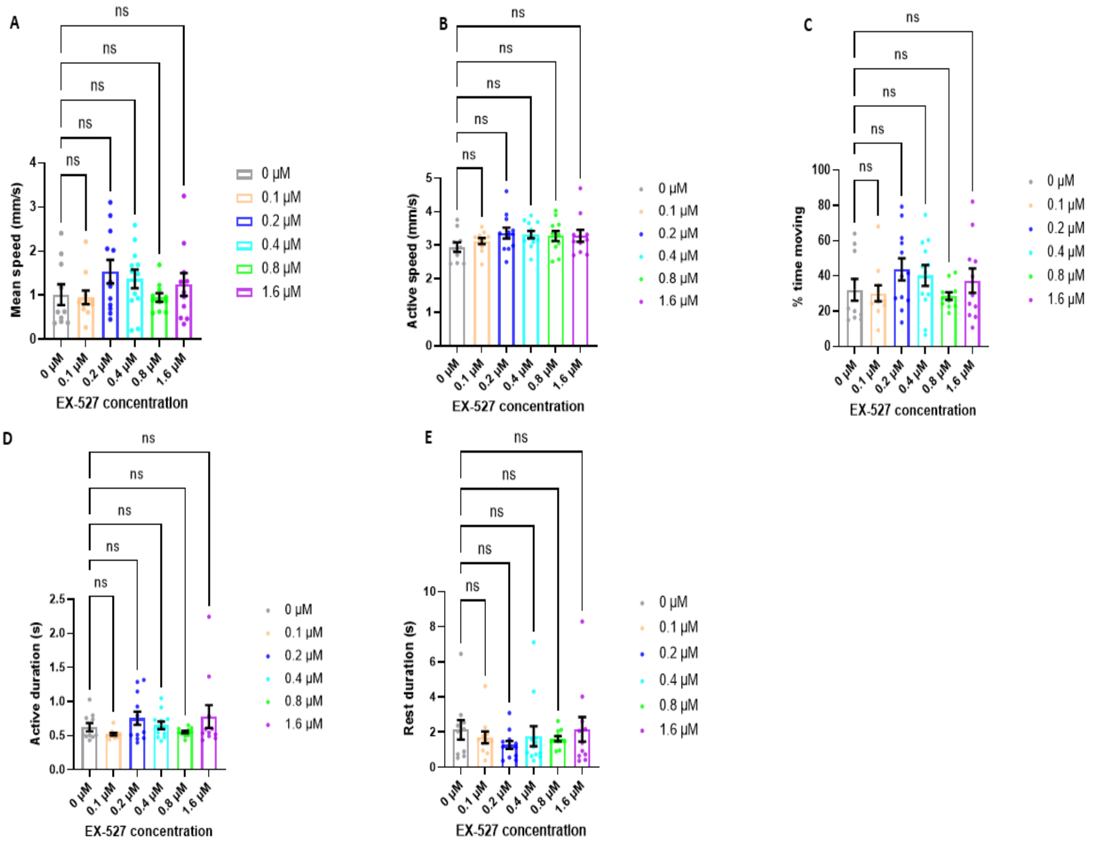

Figure 4.22. Light phase movement of WT larvae treated with EX-527 (0-1.6 µM)- quantification. *Spontaneous movement of WT larvae was assessed following continuous immersion in EX-527 for 96 hours. No EX-527 concentration had a significant effect on mean speed (A), active speed (B), % time moving (C), active duration (D) and rest duration (E). Error bars represent standard error of the mean. Data was analysed using a Kruskal-Wallis test with Dunn's multiple comparisons (A-E). n; 0 µM = 10, 0.1 µM = 11, 0.2 µM = 12, 0.4 µM = 12, 0.8 µM = 11, 1.6 µM = 11. Significance was set at 0.05 level. EX-527, 6-chloro-2,3,4,9-tetrahydro-1H-carbazole-1-carboxamide; WT, wildtype.*

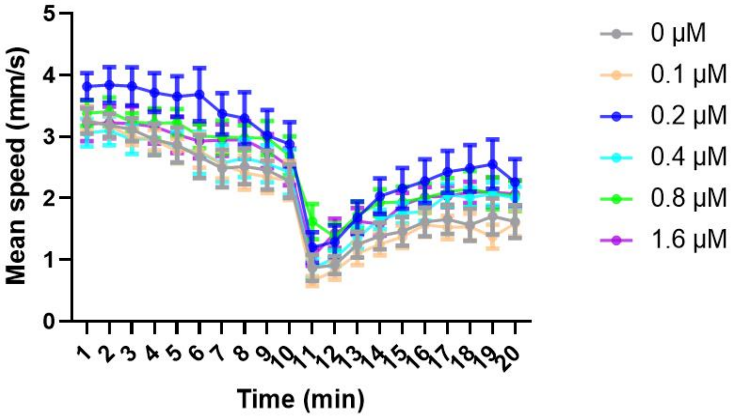

Figure 4.23. Dark:light cycle movement of WT larvae treated with EX-527 (0-1.6 µM). *Movement of WT larvae during 10 minute dark:10 minute light cycles (x3) was assessed following continuous immersion in EX-527 for 96 hours. Larval speeds at each minute were averaged across all 3 cycles to obtain the dataset presented here. No EX-527 concentration had a significant effect on mean speed. Error bars represent standard error of the mean. Data was analysed using a two-way ANOVA with Dunnett's multiple comparison. n; 0 µM = 10, 0.1 µM = 11, 0.2 µM = 12, 0.4 µM = 12, 0.8 µM = 11, 1.6 µM = 11. Significance was set at 0.05 level. ANOVA, analysis of variance; EX-527, 6-chloro-2,3,4,9-tetrahydro-1H-carbazole-1-carboxamide; WT, wildtype.*

4.3.6 Effect of sirt1 inhibition on Tg(*eno2*:hsa.*SNCA*-ires-EGFP) zebrafish

4.3.6.1 Movement analysis of Tg(eno2:hsa.SNCA-ires-EGFP) zebrafish treated with EX-527

Adult monoallelic Tg(*eno2*:hsa.*SNCA*-ires-EGFP) zebrafish were out-crossed and offspring were sorted for GFP expression at 2dpf. Non-Tg siblings and Tg embryos were treated with 6.3- or 12.5 µM EX - 527, or DMSO from 2-6dpf (**Section 2.10.2**). 12.5µM was selected because it was the lowest EX-527 concentration to significantly impair movement in WT larvae (**Figures 4.19 and 4.20**). Although 6.3 µM EX-527 did not induce significant motor impairment in WT larvae (**Figures 4.19 and 4.20**), it was selected to investigate increased susceptibility of Tg larvae to EX-527.

A movement assay was run and although dose-response curves suggested that Non-Tg siblings and Tg larvae have different susceptibilities to EX-527 (**Figure 4.24**), there was no significant difference in mean speed, active speed, % time moving, active duration and rest duration between Non-Tg siblings and Tg larvae, per EX-527 concentration (**Figure 4.25**).

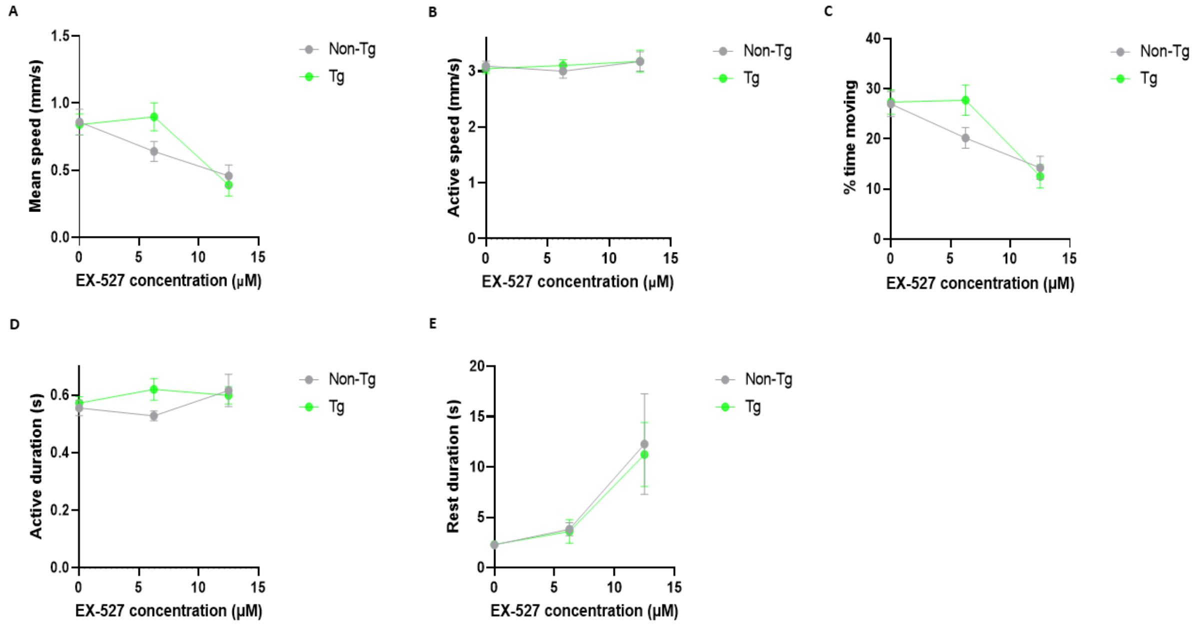

Figure 4.24. Light phase movement of Tg(eno2:hsa.SNCA-ires-EGFP) out-cross larvae treated with 6.3- and 12.5 µM EX-527. *Following continuous immersion in 0-, 6.3- and 12.5 µM EX-527 for 96 hours, spontaneous movement of Non-Tg siblings and Tg larvae was assessed during 1 hour of light exposure. 12.5 µM EX-527 appeared to markedly decrease mean speed (A) and % time moving (C) in both Non-Tg siblings and Tg larvae, slightly increase active speed (B) and active duration (D) in both Non-Tg siblings and Tg larvae, and markedly increase rest duration (E) in both Non-Tg siblings and Tg larvae. 6.3 µM EX-527 appeared to decrease the mean speed (A), active speed (B), % time moving (C) and active duration (D) of Non-Tg siblings only, but increased the rest duration of both Non-Tg siblings and Tg larvae (E). Error bars represent standard error of the mean. Larvae were obtained from 3 clutches of monoallelic Tg(eno2:hsa.SNCA-ires-EGFP) out-cross embryos obtained on different days. n; Non-Tg 0 µM = 35, Non-Tg 6.3 µM = 34, Non-Tg 12.5 µM = 31, Tg 0 µM = 35, Tg 6.3 µM = 34, Tg 12.5 µM = 29. EX-527, 6-chloro-2,3,4,9-tetrahydro-1H-carbazole-1-carboxamide; Non-Tg, non-transgenic; Tg, transgenic.*

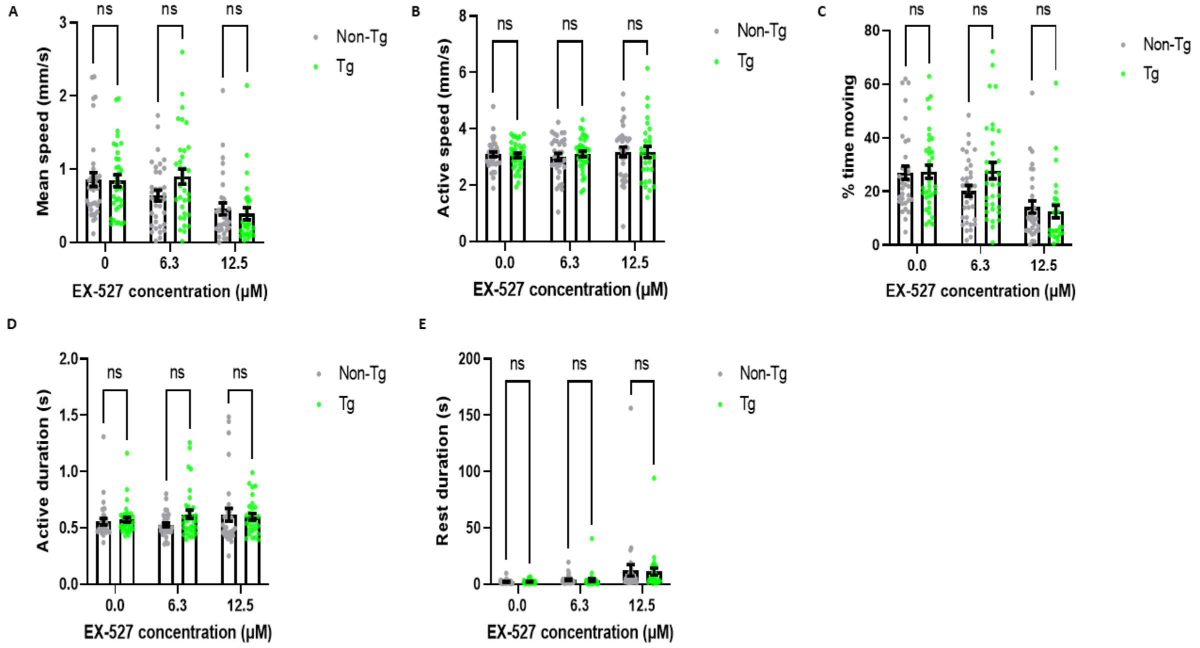

Figure 4.25. Light phase movement of Tg(eno2:hsa.SNCA-ires-EGFP) out-cross larvae treated with 6.3- and 12.5 µM EX-527- quantification. *Following continuous immersion in 0-, 6.3- and 12.5 µM EX-527 for 96 hours, spontaneous movement of Non-Tg siblings and Tg larvae was assessed during 1 hour of light exposure. Per concentration, there was no significant difference in mean speed (A), active speed (B), % time moving (C), active duration (D) and rest duration (E) between Non-Tg siblings and Tg larvae. Error bars represent standard error of the mean. Data was analysed using a two-way ANOVA with Šídák's multiple comparisons (A-E). Larvae were obtained from 3 clutches of monoallelic Tg(eno2:hsa.SNCA-ires-EGFP) out-cross embryos obtained on different days. n; Non-Tg 0 µM = 35, Non-Tg 6.3 µM = 34, Non-Tg 12.5 µM = 31, Tg 0 µM = 35, Tg 6.3 µM = 34, Tg 12.5 µM = 29. Significance was set at 0.05 level. ANOVA, analysis of variance; EX-527, 6-chloro-2,3,4,9-tetrahydro-1H-carbazole-1-carboxamide; Non-Tg, non-transgenic; Tg, transgenic.*

Likewise, larval movement during the dark:light cycle was investigated; dose-response curves for both Non-Tg siblings and Tg larvae are provided below (**Figure 4.26A**). For simplicity, dose-response curves of Non-Tg siblings and Tg larvae per EX-527 concentration are also provided below (**Figure 4.26B-D**). There was no significant difference in mean speed between untreated Non-Tg siblings and Tg larvae (**Figure 4.26B**), as well as between Non-Tg siblings and Tg larvae treated with 6.3 µM (**Figure 4.26C**) and 12.5 µM EX-527 (**Figure 4.26D**). Therefore, Tg larvae do not have increased susceptibility to EX-527, compared to Non-Tg siblings.

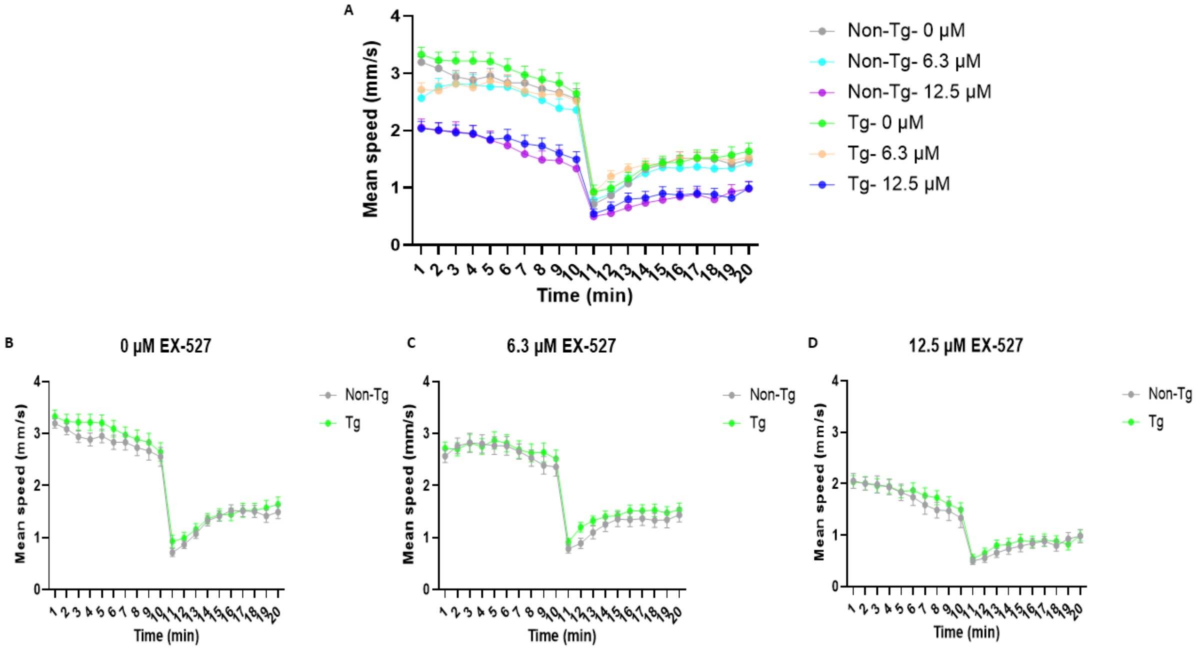

Figure 4.26. Dark:light cycle movement of Tg(eno2:hsa.SNCA-ires-EGFP) out-cross larvae treated with 6.3- and 12.5 µM EX-527. *Movement of Non-Tg siblings and Tg larvae during 10 minute dark:10 minute light cycles (x3) was assessed, following EX-527 treatment. Per replicate, larval speeds at each minute were averaged across all 3 cycles. Next, the averaged speeds at each minute were combined across replicates (A). For statistical analysis, the mean speeds of Non-Tg siblings and Tg larvae were compared per concentration (B-D). There was no significant difference in mean speed between untreated Non-Tg siblings and Tg larvae (B), as well as between Non-Tg siblings and Tg larvae treated with 6.3 µM (C) and 12.5 µM EX-527 (D). Error bars represent standard error of the mean. Data was analysed using a two-way ANOVA with Šídák's multiple comparisons (B-D). Larvae were obtained from 3 clutches of monoallelic Tg(eno2:hsa.SNCA-ires-EGFP) out-cross embryos obtained on different days. n; Non-Tg 0 µM = 35, Non-Tg 6.3 µM = 34, Non-Tg 12.5 µM = 31, Tg 0 µM = 35, Tg 6.3 µM = 34, Tg 12.5 µM = 29. Significance was set at 0.05 level. ANOVA, analysis of variance; EX-527, 6-chloro-2,3,4,9-tetrahydro-1H-carbazole-1-carboxamide; Non-Tg, non-transgenic; Tg, transgenic.*

4.3.6.2 AO staining in Tg(eno2:hsa.SNCA-ires-EGFP) zebrafish treated with EX-527

Cell death was investigated in Tg(*eno2*:hsa.*SNCA*-ires-EGFP) out-cross larvae treated with EX-527, using AO. AO is a DNA intercalating dye that labels degenerating cells due to their permeable plasma membranes (Xie *et al.*, 2020).

Adult monoallelic Tg(*eno2*:hsa.*SNCA*-ires-EGFP) zebrafish were out-crossed, offspring were sorted for GFP expression at 2dpf then treated with 6.3- or 12.5 µM EX-527, or DMSO, as previously detailed (**Section 4.3.6.1**). Following treatment, Non-Tg siblings and Tg larvae were exposed to AO, then AO-stained spinal cord cells were counted (**Section 2.13**). A representative image of AO-stained cells is provided below (**Figure 4.27A**).

There was no significant difference in the number of AO-stained cells between untreated Non-Tg siblings and Tg larvae (Non-Tg = 6.44, Tg = 6.56, p = 0.9996, **Figure 4.27B**). Likewise, there was no significant difference in the number of AO-stained cells between Non-Tg siblings and Tg larvae treated with 6.3 µM (Non-Tg = 7.56, Tg = 8.28, p = 0.9043, **Figure 4.27B**) and 12.5 µM EX-527 (Non-Tg = 7.59, Tg = 9.22, p = 0.4407, **Figure 4.27B**). Therefore, cell death is not exacerbated in the spinal cord of Tg larvae and Tg larvae are not more susceptible to EX-527, compared to Non-Tg siblings.

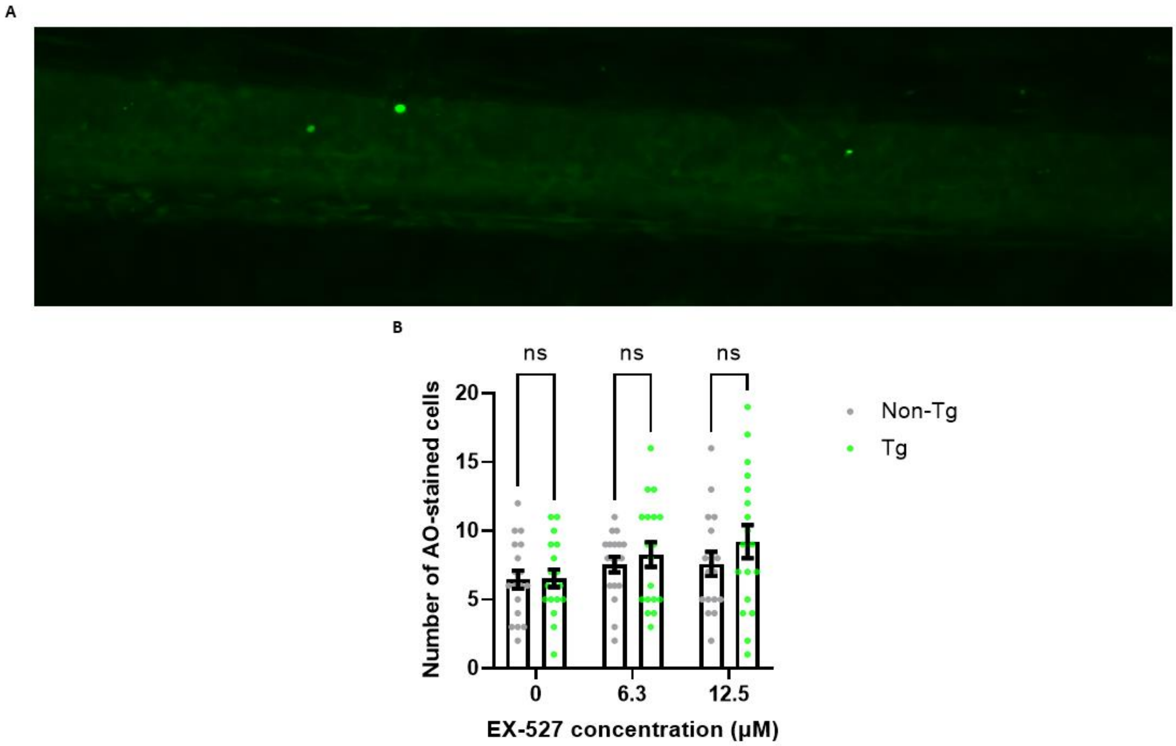

Figure 4.27. AO staining in the spinal cords of Tg(eno2:hsa.SNCA-ires-EGFP) out-cross larvae treated with 6.3- and 12.5 µM EX-527. *Non-Tg siblings and Tg larvae were exposed to AO, following EX-527 treatment. A representative image of AO-stained spinal cord cells is provided. Bright-green dots indicate AO-stained cells (A). There was no significant difference in the number of AO-stained spinal cord cells between untreated Non-Tg siblings and Tg larvae, as well as between Non-Tg siblings and Tg larvae treated with 6.3- and 12.5 µM EX-527 (B). Error bars represent standard error of the mean. Data was analysed using a two-way ANOVA with Šídák's multiple comparisons. Larvae were obtained from 3 clutches of monoallelic Tg(eno2:hsa.SNCA-ires-EGFP) out-cross embryos obtained on different days. n; Non-Tg 0 µM = 18, Non-Tg 6.3 µM = 18, Non-Tg 12.5 µM = 17, Tg 0 µM = 18, Tg 6.3 µM = 18, Tg 12.5 µM = 18. p = 0.9996 (0 µM Non-Tg siblings-Tg larvae), p = 0.9043 (6.3 µM Non-Tg siblings-Tg larvae), p = 0.4407 (12.5 µM Non-Tg siblings-Tg larvae). ANOVA, analysis of variance; AO, acridine orange; EX-527, 6-chloro-2,3,4,9-tetrahydro-1H-carbazole-1-carboxamide; Non-Tg, non-transgenic; Tg, transgenic.*

4.3.7 Macrophage activation in a chemical model for *SIRT1* deficiency

To investigate *sirt1*'s effect on zebrafish microglial activation, Tg(*mpeg1*:EGFP) zebrafish which fluorescently label macrophages with GFP (**Section 2.1.2.7**) were treated with EX-527.

Adult Tg(*mpeg1*:EGFP) zebrafish were out-crossed with adult Casper zebrafish. Embryos were sorted for GFP expression at 2dpf (**Section 2.1.7**), then Tg embryos were treated with 6.3- and 12. 5 µM EX - 527, or DMSO, as previously detailed (**Section 2.10.2**). Next, macrophages were imaged in live larval brains (**Section 2.12.2**) and representative images are provided below (**Figure 4.28**).

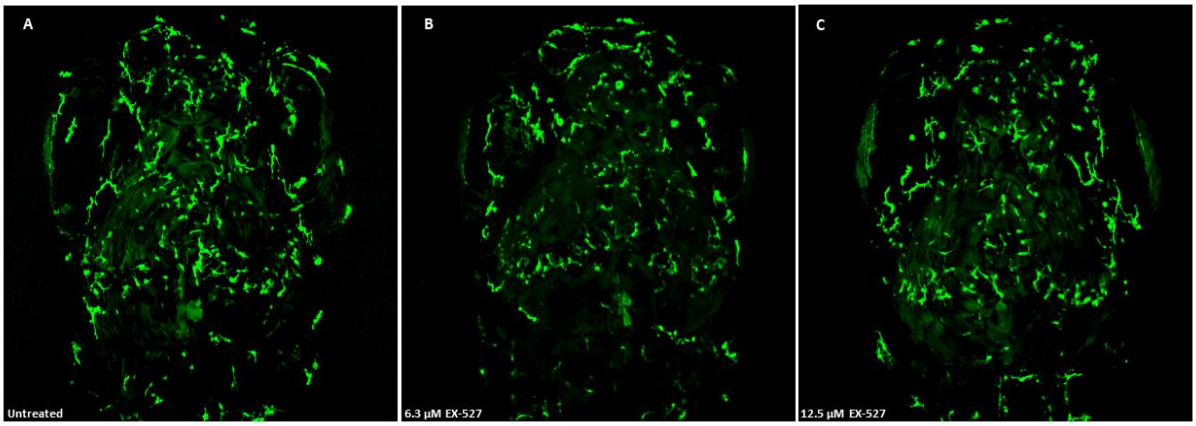

__Figure 4.28. Representative images of macrophages in untreated and EX-527-treated Tg(mpeg1:EGFP) larvae.__ Adult Tg(mpeg1:EGFP) larvae were out-crossed with adult Casper zebrafish. Embryos were sorted for GFP expression and Tg embryos were untreated (A) or treated with 6.3- (B) or 12.5 μM (C) EX-527 from 2-6dpf, then imaged intravitally (20.0x magnification). Larvae were obtained from 3 clutches of Tg(mpeg1:EGFP) out-cross embryos obtained on different days. EX-527, 6-chloro-2,3,4,9-tetrahydro-1H-carbazole-1-carboxamide; GFP, green fluorescent protein; Tg, transgenic.

Microglia are the most abundant macrophages resident in the CNS (Perry and Teeling, 2013; DiSabato, Quan and Godbout, 2016), thereby the number of brain macrophages infers microglial number. EX-527 treatment had no effect on the number of brain macrophages (0 μM = 173.33, 6.3 μM = 190.67, 12.5 μM = 159.56, $p>0.9999$ (0-6.3 μM and 0-12.5 μM), **Figure 4.29**), suggesting that sirt1 inhibition by EX-527 has no effect on microglial number.

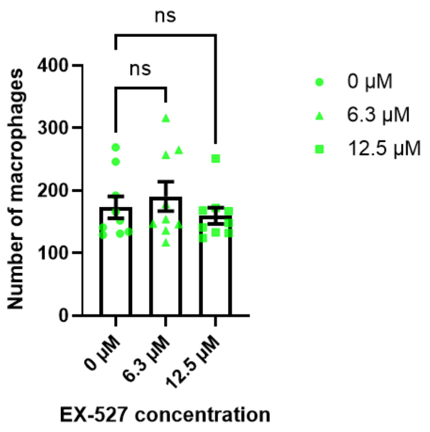

__Figure 4.29. Macrophage counting in untreated and EX-527-treated Tg(mpeg1:EGFP) larvae.__ EX-527 treatment did not affect the number of macrophages in the larval brain. Error bars represent standard error of the mean. Data was analysed using a Kruskal-Wallis test with Dunn's multiple comparisons. Larvae were obtained from 3 clutches of Tg(mpeg1:EGFP) out-cross embryos obtained on different days. n; 0 μM EX-527 = 9, 6.3 μM EX-527 = 9, 12.5 μM EX-527 = 9. $p>0.9999$ (0-6.3 μM EX-527), $p>0.9999$ (0-12.5 μM EX-527). EX-527, 6-chloro-2,3,4,9-tetrahydro-1H-carbazole-1-carboxamide.

Although macrophage activation was not investigated in detail, midbrain macrophages in an untreated larva (**Figure 4.30A-B**) and in a larva treated with 12.5 µM EX-527 (**Figure 4.30C-D**) had similar morphology, with ramified macrophages observed in both groups, suggesting the absence of microglial activation in response to EX-527 treatment.

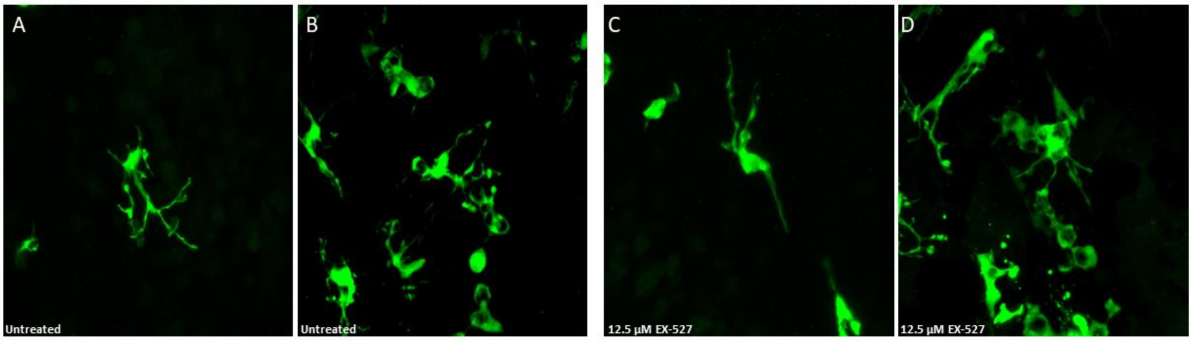

Figure 4.30. Representative images of macrophages in the midbrains of an untreated and an EX-527-treated Tg(mpeg1:EGFP) larva. *Representative images show ramified macrophages in the midbrain of an untreated (A and B) and 12.5 µM EX-527-treated (C and D) Tg(mpeg1:EGFP) larva, suggesting the absence of microglial activation in EX-527-treated larvae. Images A and C were taken in the centre of the midbrain while images B and D were taken in the periphery of the midbrain at 40.0x magnification. EX-527, 6-chloro-2,3,4,9-tetrahydro-1H-carbazole-1-carboxamide.*

4.4 Discussion

The major aims of this chapter were to generate and characterise the *sirt1*$^{-/-}$ zebrafish line, investigate microglial activation in a chemical model for *SIRT1* deficiency, and to investigate whether chemical inhibition of sirt1 induces/enhances motor impairment and cell death in Tg(*eno2*:hsa.*SNCA*-ires-EGFP) zebrafish.

In silico data confirmed *sirt1* to be the zebrafish orthologue of human *SIRT1*. Therefore, the *sirt1*$^{-/-}$ line was generated using the gRNA published by Kim *et al.*, (2019), which targets *sirt1*. In parallel, *sirt1* expression was detected in 1-5dpf larvae, informing that experiments investigating the effect of the *sirt1* mutation in the *sirt1*$^{-/-}$ line could be completed using 1-5dpf larvae.

Unfortunately, WISH probes did not detect specific *sirt1* spatial expression at 3dpf. Spatial expression is valuable because it can be used to confirm *in silico* data, predict phenotypes in mutant zebrafish, and to investigate NMD in mutant zebrafish. Increasing probe hybridisation temperature from 68°C and increasing blocking duration from 2 hours might result in the detection of specific *sirt1* spatial expression.

The non-significant difference in *sirt1* expression between *sirt1*$^{+/+}$ and *sirt1*$^{-/-}$ larvae at 5dpf is likely due to the outlier in the 3rd replicate of *sirt1*$^{+/+}$ and *sirt1*$^{-/-}$ larvae. Additional replicates could have been included to obtain statistical significance but time did not permit this. If *sirt1* WISH probe 1 had worked, it could have been used to further investigate NMD in *sirt1*$^{+/+}$ and *sirt1*$^{-/-}$ larvae, since it does not span the mutation site. However, WISH is not quantitative like qPCR. At the protein level, a western blot could have been used to investigate sirt1 expression in *sirt1*$^{-/-}$ larvae. Furthermore, sirt1's catalytic activity could have been investigated, using a commercial kit. However, due to technical reasons, this assay was not optimised in this PhD.

Unlike the *sirt1* mutant line published by Kim *et al.*, (2019), *il-1β* and *il-6* were not upregulated in *sirt1*$^{-/-}$ larvae, suggesting the absence of a pro-inflammatory phenotype in *sirt1*$^{-/-}$ larvae. NMD of mutant mRNA was recently reported to trigger upregulation of related genes in a process called transcriptional adaptation, thereby compensating for NMD (El-Brolosy *et al.*, 2019). Transcriptional adaptation in the *sirt1*$^{-/-}$ line might be why *il-1β* and *il-6* were not upregulated in *sirt1*$^{-/-}$ larvae. However, since *sirt1*, *il-1β* and *il-6* qPCR experiments utilised *sirt1*$^{+/+}$ and *sirt1*$^{-/-}$ cDNA samples obtained from a single pair of f1 *sirt1*$^{+/-}$ parents, it is possible that qPCR results reported in this thesis are themselves outliers and that *il-1β* and *il-6* may indeed be upregulated in *sirt1*$^{-/-}$ larvae. Also, f1 *sirt1*$^{+/-}$ parents may still harbour background mutations which may influence results. Therefore, *sirt1*, *il-1β* and *il-6* qPCRs would need to be repeated in biological triplicate using *sirt1*$^{+/+}$ and *sirt1*$^{-/-}$ cDNA samples obtained from f2 *sirt1*$^{+/-}$ parents, to ensure the robustness of these datasets.

Although results reported by Kim *et al.*, (2019) support known functions of *sirt1*, as well as phenotypes observed in *Sirt1* mutant mice, they are accompanied by certain concerns. The error bars (which represent standard deviation) for fold changes of pro-inflammatory genes (including *il-1β* and *il-6*) are wide, indicating a large variation in results, thereby reducing the robustness of results. Some experiments using adult tissues, such as qPCRs and Terminal deoxynucleotidyl transferase dUTP nick end labelling (TUNEL) staining, do not specify the exact tissue utilised. Also, although *sirt1* mutant zebrafish survival begins to decrease at 5mpf, survival reaches 50% at 18mpf, implying that the mortality of *sirt1* mutant zebrafish is not due to the *sirt1* mutation, otherwise the mortality of *sirt1* mutant zebrafish would have a fixed timepoint and not span 13 months. Therefore, the effect of *sirt1* KO in zebrafish remains elusive.

Given the presumed absence of accelerated ageing in the *sirt1*$^{-/-}$ larvae and the lack of PD-relevant pathological mechanisms in Tg(*eno2*:hsa.*SNCA*-ires-EGFP) zebrafish (discussed in chapters 3 and 4 of this thesis), it is highly unlikely that PD-relevant pathological mechanisms would be induced in Tg;*sirt1*$^{-/-}$ zebrafish. This was supported by the absence of an overt phenotype in adult Tg;*sirt1*$^{-/-}$ zebrafish raised to adulthood.

Animal husbandry regulations at the University of Pittsburgh require imported zebrafish to be quarantined for 2 generations, making shipment of the *sirt1*$^{-/-}$ and the Tg;*sirt1*$^{-/-}$ lines unfeasible, given the 3-month duration of my laboratory placement, the funding deadline for my PhD and general problems associated with shipments to the USA. Alternatively, EX-527-treated Tg(*eno2*:hsa.*SNCA*-ires-EGFP) zebrafish were used to investigate the interplay between sirt1 and human WT α-Synuclein. Also, EX-527-treated Tg(*mpeg1*:EGFP) zebrafish were used to investigate the effect of sirt1 inhibition on microglial activation.

Decreased mean speed, decreased % time moving, increased rest duration, unaffected active speed and unaffected active duration in dose-response experiments utilising WT larvae imply that EX-527 causes motor impairment by limiting movement initiation and not by affecting motor function itself.

Assessment of baseline motor function of Tg(*eno2*:hsa.*SNCA*-ires-EGFP) out-cross larvae revealed that human WT α-Synuclein expression had no effect on larval motor function. The non-significant difference in motor function and cell death between untreated Non-Tg siblings and Tg larvae, and between EX-527-treated Non-Tg siblings and Tg larvae suggests that chemical inhibition of sirt1 does not induce PD-relevant pathological mechanisms in Tg larvae. On one hand, this is surprising given the negative effect of SIRT1 on α-Synuclein expression (Guo *et al.*, 2016; Singh, Hanson and Morris, 2017). On the other hand, these results are plausible given the lack of a PD phenotype in Tg(*eno2*:hsa.*SNCA*-ires-EGFP) zebrafish. To investigate the validity of these results, future experiments could compare motor function and cell death between Tg;*sirt1*$^{+/+}$ and Tg;*sirt1*$^{-/-}$, using ViewPoint software and TUNEL staining, respectively. However, this is only reasonable provided the *sirt1*$^{-/-}$ line is a KO line.

Although α-Synuclein expression was not investigated in the spinal cords of Tg(*eno2*:hsa.*SNCA*-ires-EGFP) zebrafish, Bai *et al.*, (2007) reported *eno2* expression in the spinal cords of WT larvae and GFP expression in the spinal cords of larvae expressing GFP under the control of the same *eno2* promoter used to generate the Tg(*eno2*:hsa.*SNCA*-ires-EGFP) zebrafish line. Therefore, it is plausible that human WT α-Synuclein is expressed in the spinal cords of Tg(*eno2*:hsa.*SNCA*-ires-EGFP) zebrafish where it may exert a pathogenic effect, thereby explaining why the AO experiment was completed in this PhD.

Lastly, the non-significant effect of EX-527 treatment on microglial activation, does not support the literature which reports that Sirt1 inhibits microglial activation (Lang *et al.*, 2020). As previously stated, the validity of this result could be investigated using the *sirt1*$^{-/-}$ line, assuming that the *sirt1*$^{-/-}$ line is a KO line.

In conclusion, although drug treatment offers an avenue to study the effect of sirt1 inhibition, and the interplay between ageing and PD in zebrafish, stable mutant lines are better suited. However, the use of stable mutant lines may require screening several zebrafish, each harbouring a different mutant allele for the same gene-of-interest, to circumvent transcriptional adaptation which may impact results.

Chapter 5: Zebrafish as a model for *SATB1* deficiency

5.1 Introduction

5.1.1 Background

SATB1 is a nuclear protein that binds to regions of double-stranded DNA where one strand consists of mixed A's, T's and C's, but not G's (ATC sequences). DNA regions containing ATC sequences have a high propensity to unwind under negative superhelical strain, therefore, these regions are called base unpairing regions (BURs). BURs consist of no more than 200bp and are found within matrix attachment regions (MARs), which attach chromatin to the nuclear matrix. SATB1 recruits chromatin remodelling factors, such as brahma-related gene 1 (BRG1), transcription factors, such as MAF, as well as HDACs and histone acetyltransferases (HATs). Therefore, SATB1 functions as a global regulator of gene expression (Kohwi-Shigematsu and Kohwi, 1990; Dickinson *et al.*, 1992; Alvarez *et al.*, 2000; Yasui *et al.*, 2002; Kumar *et al.*, 2005; Cai, Lee and Kohwi-Shigematsu, 2006; Pavan Kumar *et al.*, 2006).

SATB1 is encoded by the *SATB1* gene which is located on chromosome 3 and contains 11 exons (Zelenka and Spilianakis, 2020). SATB1 consists of 763 amino acids. SATB1 contains an N-terminal domain which consists of a nuclear localisation signal (NLS), a ubiquitin-like domain (ULD) and a DNA-binding-like (CUT-like) domain, 2 DNA-binding domains (CUT1 and CUT2 domains) at the centre of the protein and a C-terminal homeodomain (**Figure 5.1**) (Wang *et al.*, 2012, 2017; Ghosh *et al.*, 2019).

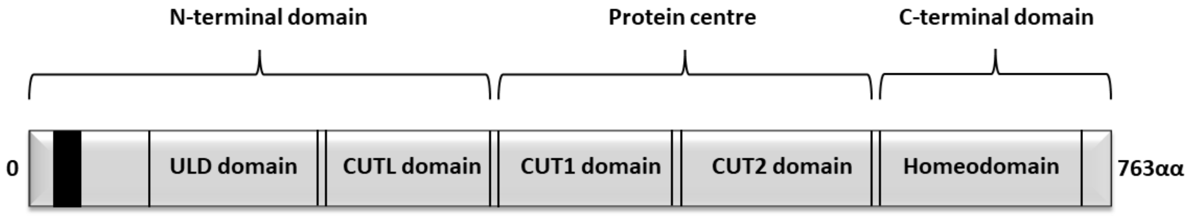

Figure 5.1. SATB1 structure. *SATB1 is a 763αα protein that contains an N-terminal domain consisting of a NLS, a ULD domain and a DNA-binding-like domain (CUTL domain), 2 DNA-binding domains (CUT1 and CUT2 domains) at its centre and a C-terminal homeodomain. The black box indicates the NLS. αα, amino acids; CUTL domain, CUT-like domain; NLS, nuclear localisation signal; SATB1, special AT-rich sequence binding protein 1; ULD, ubiquitin-like domain.*

The ULD domain is responsible for SATB1 dimerisation which is required for DNA binding, as well as interaction between SATB1 and regulatory proteins. SATB1 is also capable of tetramerisation. The CUT-like domain, CUT1 and CUT2 domains, and the homeodomain all contribute to DNA binding but the homeodomain alone contributes to sequence-specific binding of SATB1 to DNA targets (Galande *et al.*, 2001; Wang *et al.*, 2012, 2014; Ghosh *et al.*, 2019; Zelenka and Spilianakis, 2020).

5.1.2 SATB1 regulation

SATB1 is regulated by phosphorylation and acetylation of the ULD domain. SATB1 phosphorylation at serine 185 by protein kinase C (PKC) increases SATB1’s association with histone deacetylase 1 (HDAC1). This increases SATB1’s DNA binding activity and induces SATB1-mediated transcriptional repression (Pavan Kumar *et al.*, 2006; Notani *et al.*, 2010). Also, dephosphorylated SATB1 interacts with and is acetylated at lysine 136 by the HAT, p300/CBP-associated factor (PCAF). This reduces SATB1’s DNA binding activity and induces SATB1-mediated transcriptional activation (Kumar *et al.*, 2005; Pavan Kumar *et al.*, 2006; Purbey *et al.*, 2009).

SATB1 is also regulated by small non-coding RNAs called microRNAs (miRs). For example, microRNA-191 (miR-191) induces senescence in keratinocytes by decreasing SATB1 expression (Lena *et al.*, 2012). miR-191 also decreases SATB1 expression, thereby promoting breast cancer tumorigenesis by regulating genes such as the tumour suppressor gene, *suppressor of cytokine signalling 2* (*SOCS2*) and the oncogene *placenta-specific 1* (*PLAC1*) (Nagpal *et al.*, 2013). microRNA-23a (miR-23a) acts as a tumour suppressor in osteosarcoma by decreasing SATB1 expression (Wang *et al.*, 2015).

5.1.3 SATB1 expression

SATB1 is predominantly expressed in the thymus but is also expressed in the testis, osteoblasts and brain (Dickinson *et al.*, 1992; Alvarez *et al.*, 2000). Specifically, Satb1 is expressed in brain areas such as the cortex, subiculum, SNpc (95.1% of TH-positive neurons were found to express Satb1), ventral tegmental area, deep layers of the superior colliculus, amygdala, supramammillary nucleus, and dorsal nucleus raphe (Balamotis *et al.*, 2011; Huang *et al.*, 2011).

5.1.4 Normal physiological function

Satb1 is involved in the survival of cortical interneurons. Cortical interneuron progenitors are generated during embryogenesis in the medial ganglionic eminence (MGE) and the caudal ganglionic eminence (CGE), and they reach the cortex by tangential migration. The completion of tangential migration signifies the start of terminal differentiation into cortical interneurons and neuronal maturation. There are 3 major types of cortical interneurons, namely PV-expressing, somatostatin (SST)-expressing and ionotropic serotonin receptor (5HT3aR)-expressing interneurons. PV-expressing and SST-expressing interneurons are generated from the MGE while 5HT3aR interneurons are generated from the CGE. Satb1 is expressed in Pv-expressing and Sst-expressing interneurons but not 5HT3aR-expressing interneurons. Satb1 expression begins during the migration of interneuron progenitors into the cortex and continues into adulthood (Close *et al.*, 2012).

Satb1 is essential for the survival of Pv-expressing and Sst-expressing interneurons, as Pv-expressing and Sst-expressing neuronal populations are reduced in the somatosensory cortex of *Satb1* mutant mice and mice with a conditional KO of *Satb1* in cortical interneurons (Close *et al.*, 2012; Denaxa *et al.*, 2012). The number of Sst-expressing neurons is also reduced in the motor and visual cortex of *Satb1* mutant mice (Denaxa *et al.*, 2012), supporting a previous report of downregulated *Sst* expression in the cortex of *Satb1* mutant mice (Balamotis *et al.*, 2011).

Satb1 also regulates the expression of immediate early genes (IEGs) which are transiently and rapidly transcribed in response to external stimuli such as neuronal activity, and are involved in synaptic plasticity, learning and memory (Balamotis *et al.*, 2011). Expression of IEGs, namely *Fos*, *Fosb*, *early growth response 1* (*Egr1*), *early growth response 2* (*Egr2*), *activity-regulated cytoskeleton-associated protein* (*Arc*) and *Bdnf* peaks in the cortex of *Satb1* mutant mice at 10 days after birth then drastically decreases below WT expression levels while IEG expression peaks in the cortex of WT mice at 13 days after birth. Therefore, *Satb1* regulates both temporal and maximal cortical expression of IEGs (Balamotis *et al.*, 2011).

mRNAs encoding Th (*Th*), the growth factor amphiregulin (*Areg*), corticotropin-releasing hormone (*Crh*) and the calcium-binding protein calbindin 2 (*Calb2*) are all downregulated in the cortex of *Satb1* mutant mice. Contrastingly, mRNAs encoding calcium-binding proteins S100 calcium binding protein a8 (*S100a8*) and S100 calcium binding protein a9 (*S100a9*), as well as *Il-6* and *Tnf* are upregulated in the cortex of *Satb1* mutant mice. *Areg* is involved in synaptogenesis, *Crh* is involved in the stress response while *Calb2*, *S100a8* and *S100a9* are involved in inflammation. Despite *Il-6* and *Tnf* upregulation in the cortex of *Satb1* mutant mice, there is no significant difference in cell death between the cortex of WT and *Satb1* mutant mice (Balamotis *et al.*, 2011).

Dendritic spine density of cortical pyramidal neurons is also reduced in *Satb1* mutant mice. Dendritic spines are postsynaptic structures that change shape, size and number in response to neuronal activity. Dendritic spines are implicated in synaptic plasticity, learning and memory. Therefore, Satb1 is involved in neuronal plasticity (Balamotis *et al.*, 2011).

Satb1 expression is increased during the differentiation of haematopoietic stem cells (HSCs) into lymphocytes. HSCs of *Satb1* mutant mice (*Satb1* mutant HSCs) have impaired differentiation into lymphocytes. Contrastingly, Satb1 overexpression in *Satb1* mutant HSCs promotes HSC differentiation into lymphocytes (Y. Satoh *et al.*, 2013).

Satb1 overexpression in WT HSCs upregulates the expression of transcription factors, such as *Sp4*, *Maf*, *Fos* and *inhibitor of DNA binding 3* (*Id3*), as well as cytokines, namely *interleukin-7* (*Il-7*) and *kit* *ligand* (*Kitl*), and *recombination activating gene 1* (*Rag1*), all of which are involved in lymphocyte differentiation. Satb1 overexpression also upregulates *Cd86* expression, which is involved in lymphocyte activation, and downregulates *Colony stimulating factor 3 receptor* (*Csf3r*) which regulates granulopoiesis. Therefore, Satb1 regulates genes to promote lymphocyte differentiation, potentially implicating Satb1 in immunosenescence (Y. Satoh *et al.*, 2013).

Satb1 also represses myeloid differentiation, as *Satb1* mutant HSCs produce more erythroid burst colony forming units (BFU-E), granulocyte-monocyte colony forming units (CFU-GM) and granulocyte-erythrocyte-monocyte-megakaryocyte colony forming units (CFU-GEMM). This may be due to Satb1-mediated repression of *Numb* and *Myc* which are both involved in stem cell fate specification (Will *et al.*, 2013).

5.1.5 *Satb1* and ageing

Satb1 mutant mice are indistinguishable from heterozygous and WT littermates until 3 days after birth when they become emaciated and show age-associated reduction in size. *Satb1* mutant mice have smaller thymi, spleens and lymph nodes compared to WT mice. T-cell development is impaired in *Satb1* mutant mice and *Satb1* mutant mice display signs of neurological deficits, such as incomplete eye opening and the clasping reflex. Survival of *Satb1* mutant mice is reduced to 4 weeks after birth (Alvarez *et al.*, 2000).

Conditional KO of murine *Satb1* in HSCs (*Satb1* cKO) also impairs T-cell development and reduces survival to 60 weeks after birth. *Satb1* cKO mice develop increased serum levels of the autoantibody, anti-double stranded DNA (anti-dsDNA) antibodies, and inflammatory cell infiltration in the lung, liver, stomach and kidney, implicating Satb1 in autoimmunity (Kondo *et al.*, 2016).

5.1.6 Human study

Clinical evaluation of 42 individuals showed that different types of *SATB1* SNPs cause overlapping clinical features such as intellectual disability, hypotonia, spasticity, epilepsy, facial dysmorphisms and dental abnormalities. However, the severity of these clinical features depends on the type of *SATB1* SNP in each individual. Intellectual disability, hypotonia, spasticity and epilepsy were more common in individuals with *SATB1* missense SNPs (for example Q420R) compared to individuals with *SATB1* protein truncating SNPs (for example R410*) (95% versus 80%, 92% versus 42%, 42% versus 0% and 80% versus 18%, respectively). This could be because *SATB1* missense SNPs in the CUT1 and CUT2 domains cause increased transcriptional repression (den Hoed *et al.*, 2021).

5.1.7 *SATB1* and cancer

SATB1 is overexpressed in cancers, such as lymphoma, glioma, colorectal, prostate, liver, bladder and ovarian cancer. Increased SATB1 expression in these tumours is generally associated with cancer progression and poor prognosis (Glatzel-Plucinska *et al.*, 2019). One of the mechanisms by which SATB1 promotes cancer progression is epithelial-to-mesenchymal transition (EMT) (Wan *et al.*, 2015). In contrast, SATB1 expression is reduced in non-small cell lung cancer (NSCLC) but is associated with poor prognosis in NSCLC patients with a history of smoking (Selinger *et al.*, 2011). Differential expression of SATB1 in various cancers could be the result of different pathological mechanisms driving disease progression in each type of cancer.

5.1.8 *SATB1* and PD

SATB1 KO causes senescence and reduces viability in dopaminergic neurons differentiated from human embryonic stem cells (hESCs). *SATB1* KO dopaminergic neurons are characterised by senescence markers such as, increased SA-β-gal staining, upregulation of SASP factors such as *IL-6*, *C-C motif chemokine ligand 2* (*CCL2*) and *IGFBP7*, reduced laminin B1 expression, cytoplasmic lipofuscin accumulation, increased oxidative stress, susceptibility to senolytics, namely azithromycin, fisetin and the dasatinib plus quercetin cocktail, and increased lysosomal-associated membrane protein 1 (LAMP1) expression. *SATB1* represses *CDKN1A* transcription and p21 expression in dopaminergic neurons, explaining the senescence phenotype of *SATB1* KO dopaminergic neurons. *SATB1* KO does not induce senescence in cortical neurons differentiated from hESCs, suggesting a specificity of *SATB1* KO-mediated senescence to dopaminergic neurons. However, other neuronal groups were not investigated (Riessland *et al.*, 2019).

Verma *et al.*, (2021) reported increased p21 expression in rat dopaminergic N27 cells, mouse primary cortical neurons, mouse primary astrocytes and mouse primary microglia treated with murine α-Synuclein PFF. Increased p21 expression was accompanied by decreased Satb1 expression in these cell types with the exception of mouse primary cortical neurons and primary microglia. Although increased ionised calcium-binding adapter molecule-1 (Iba-1) expression indicated microglial activation resulting from α-Synuclein PFF treatment, cell morphology was not investigated.

Satb1 KD in the SNpc of WT mice recapitulates *in vitro* results by reducing dopaminergic neuron number, increasing p21 expression, and upregulating SASP factors in surviving neurons. *Satb1* KD also causes microglial recruitment to and activation in the SNpc (Brichta *et al.*, 2015; Riessland *et al.*, 2019).

A study involving 16 PD patients and 17 controls reported decreased *SATB1* transcriptional activity in the substantia nigra of PD patients (Brichta *et al.*, 2015). Also, p21 expression is increased in surviving

SNpc dopaminergic neurons of PD patients (Riessland *et al.*, 2019). These results support a meta-analysis study between the PDWBS (6,476 PD patients and 302,042 controls) and PDGene (13,708 PD patients and 95,282 controls) studies which identified a *SATB1* SNP, rs4073221, as increasing PD risk (Chang *et al.*, 2017).

Senescent cells induce senescence in neighbouring cells via cell-cell contact and damage their local environment by secreting SASP factors (Nelson *et al.*, 2012; Di Micco *et al.*, 2020). This suggests that the presence of senescent dopaminergic neurons will have deleterious effects on PD patient brains which will be aggravated by age, due to age-associated accumulation of senescent cells (Dimri *et al.*, 1995; Hudgins *et al.*, 2018).

Although SATB1's homolog, special AT-rich sequence binding protein 2 (SATB2), is implicated in neuronal development (Balamotis *et al.*, 2011) and cancers such as pancreatic, breast, colon and rectal cancer (Roy *et al.*, 2020), there is limited data implicating SATB2 in PD (Guo *et al.*, 2019). Satb2 expression is reportedly increased in the substantia nigra of WT mice treated with MPTP for a shorter duration of 10 days but not 15 days, suggesting a neuroprotective effect of Satb2 (Guo *et al.*, 2019). A PubMed search revealed this to be the only publication describing SATB2 involvement in PD.

5.1.9 Chapter-specific aim

This chapter describes the suitability of zebrafish as a model for *SATB1* deficiency, by generating and assessing stable mutant zebrafish lines, for ageing-related mechanisms and PD-relevant pathological mechanisms, namely upregulation of senescence markers, loss of dopaminergic neurons, decreased survival, weight loss and growth retardation.

5.2 Methods

5.2.1 Identification of the zebrafish orthologues of human *SATB1*

Ensembl describes *SATB1* (ENSG00000182568) as a protein-coding gene located on human chromosome 3 (**Figure 5.2B**). Ensembl lists 2 zebrafish orthologues of *SATB1*, namely *satb1a* and *satb1b* (**Figure 5.2A**). 46.40% and 72.87% of *SATB1*'s genomic sequence matched the genomic sequence of *satb1a* and *satb1b*, respectively (**Figure 5.2A**).

satb1a is located on zebrafish chromosome 19 and immediate synteny is conserved between *SATB1* and *satb1a*, with *TBC1D5/tbc1d5* located on nearby loci in both humans and zebrafish (**Figure 5.2B**). *satb1b* is located on zebrafish chromosome 16 but immediate synteny is not conserved between *SATB1* and *satb1b* (**Figure 5.3**).

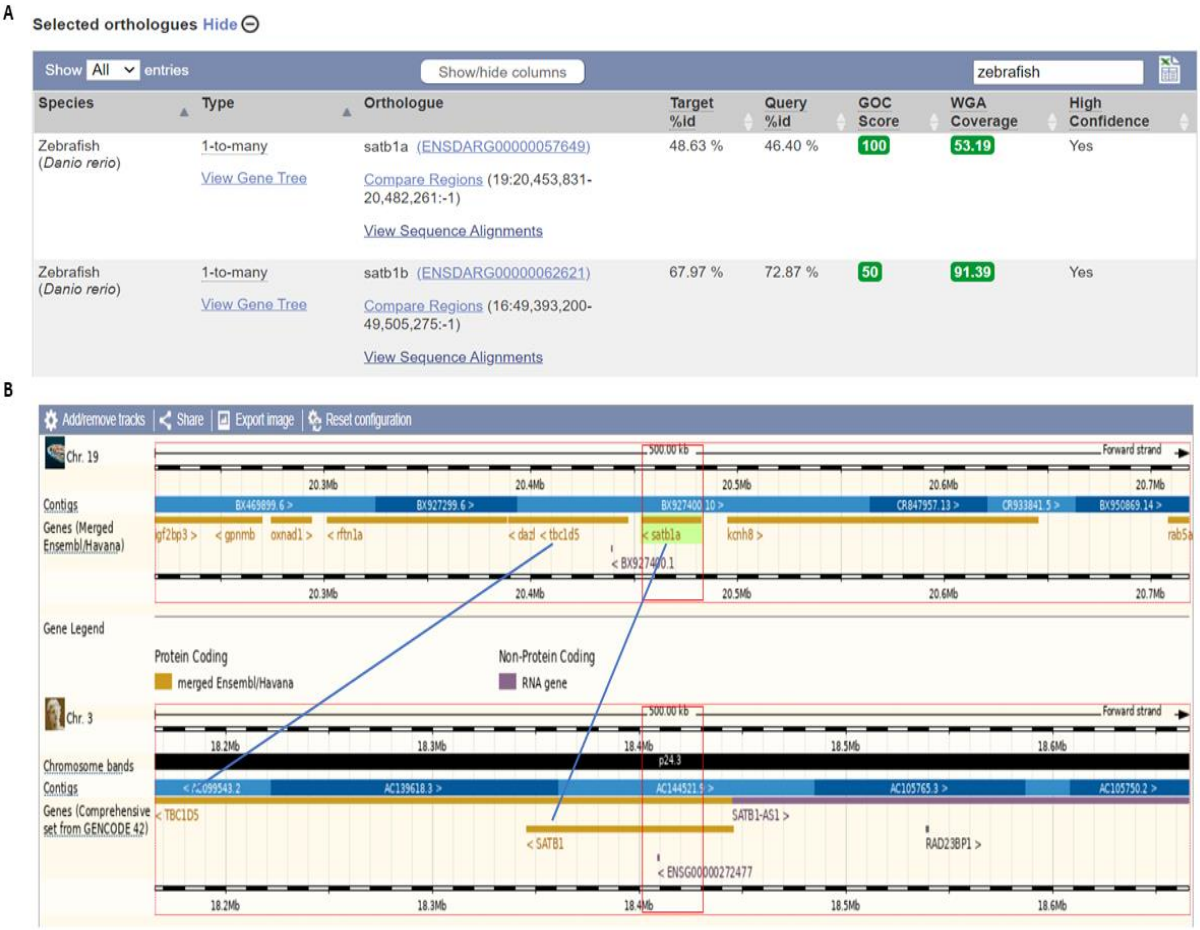

Species	Type	Orthologue	Target %id	Query %id	GOC Score	WGA Coverage	High Confidence
Zebrafish (*Danio rerio*)	1-to-many View Gene Tree	satb1a (ENSDARG00000057649) Compare Regions (19:20,453,831-20,482,261:-1) View Sequence Alignments	48.63 %	46.40 %	100	53.19	Yes
Zebrafish (*Danio rerio*)	1-to-many View Gene Tree	satb1b (ENSDARG00000062621) Compare Regions (16:49,393,200-49,505,275:-1) View Sequence Alignments	67.97 %	72.87 %	50	91.39	Yes

Figure 5.2. ***Zebrafish have two SATB1 orthologues, satb1a and satb1b.*** *Zebrafish have 2 orthologues of human SATB1, namely satb1a and satb1b, with 46.40% of the genomic sequence of human SATB1 matching the genomic sequence of zebrafish satb1a and 72.87% of the genomic sequence of human SATB1 matching the genomic sequence of zebrafish satb1b (A). Immediate synteny is conserved between SATB1 and satb1a, as indicated by the localisation of TBC1D5/tbc1d5 in a nearby locus to SATB1/satb1a (B). SATB1, special AT-rich sequence binding protein 1; TBC1D5, TBC1 Domain Family Member 5.*

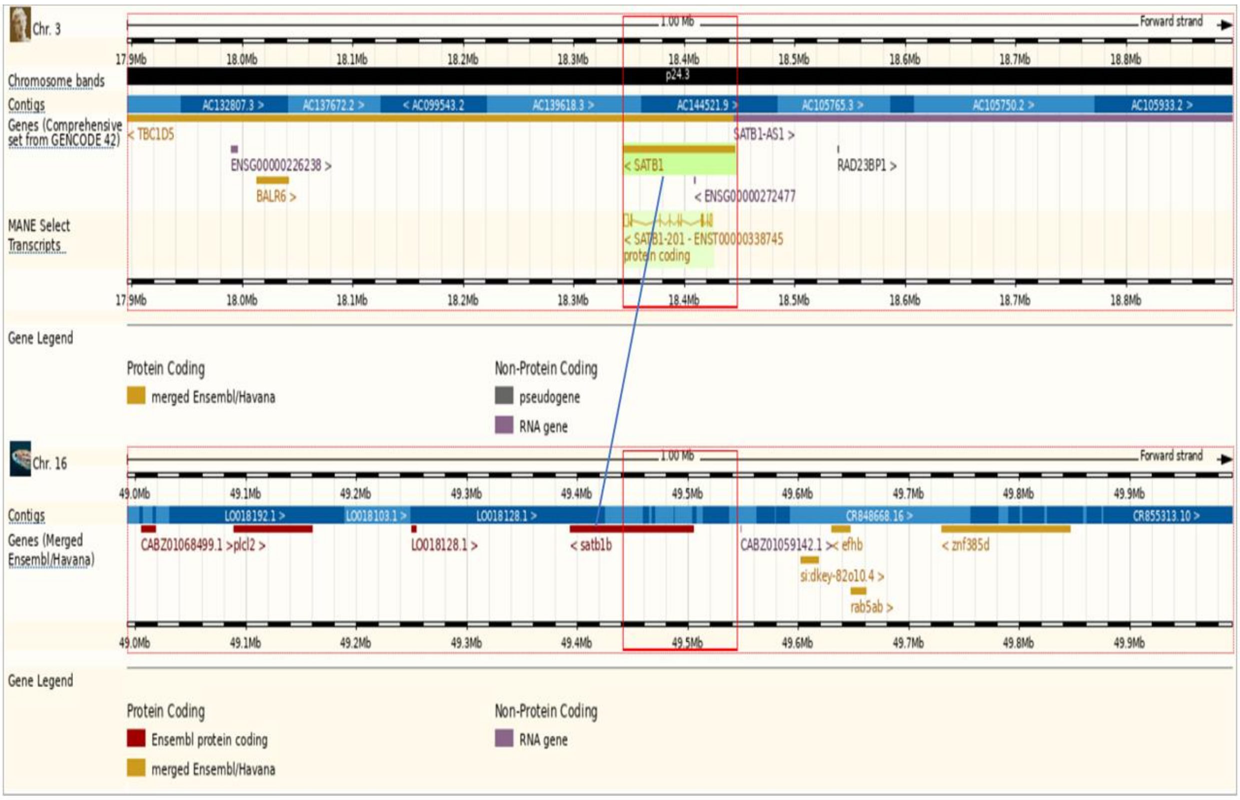

Figure 5.3. ***Synteny between human SATB1 and zebrafish satb1b.*** *Immediate synteny is not conserved between SATB1 and satb1b. SATB1, special AT-rich sequence binding protein 1.*

SATB1 has 23 transcripts (**Table 5.1**), 15 of which encode proteins. However, the most biologically relevant transcript, as identified by Ensembl is *SATB1-201* (ENST00000338745.11). *satb1a* and *satb1b* each have a single annotated protein-coding transcript, namely *satb1a-201* (ENSDART00000056205.7) and *satb1b-201* (ENSDART00000160784.2), respectively (**Table 5.1**). Therefore, *SATB1-201*, *satb1a-201* and *satb1b-201* were used for subsequent *in silico* analyses.

To validate the identification of *satb1a* and *satb1b* as the zebrafish orthologues of *SATB1*, *SATB1* cDNA sequence (ENST00000338745.11) was aligned against the zebrafish transcriptome, using Ensembl's BLASTN tool. *satb1b* (ENSDART00000160784.2) was the top hit with 79.74% identity with *SATB1* and an alignment score of 117 (**data not shown**). Although *satb1a* (ENSDART00000056205.7) had 79.31% identity with *SATB1*, this result had an alignment score of 46, indicating poorer alignment with *SATB1* compared to *satb1b* (**data not shown**).

The *SATB1* transcript contains 11 exons, 10 of which are protein-coding. Likewise, the *satb1a* transcript contains 11 exons, 10 of which are protein-coding, while the *satb1b* transcript contains 12 exons, all of which are protein-coding (**Table 5.1**). The *SATB1* transcript contains 7,822bp while *satb1a* and *satb1b* transcripts contain 2,524bp and 2,457bp, respectively (**Table 5.1**).

Furthermore, SATB1 protein sequence (ENSP00000341024.5) was aligned against the zebrafish proteome, using Ensembl's BLASTP tool. satb1b (ENSDARP00000136225.2) was the top hit with 67.67% identity with SATB1 and an alignment score of 1,017 (**data not shown**). satb1a (ENSDARP00000056204.6) had 54.31% identity with SATB1 and an alignment score of 573, both of which were lower compared to satb1b (**data not shown**).

SATB1 protein contains 763 amino acids while satb1a and satb1b contain 728 and 818 amino acids, respectively (**Table 5.1**). The ULD domain, CUT-like, CUT1 and CUT2 domains are conserved in both satb1a and satb1b. However, the homeodomain is conserved in satb1b only (**Table 5.1, Figures 5.9D and 5.11D**).

Pertinent Information	**Gene**		
	***SATB1* (Human)**	***satb1a* (Zebrafish)**	***satb1b* (Zebrafish)**
Location	Chromosome 3	Chromosome 19	Chromosome 16
Number of exons	11	11	12
Number of protein-coding exons	10	10	12
Length of cDNA	7,822bp	2,524bp	2,457bp
Length of protein	763 amino acids	728 amino acids	818 amino acids
ULD domain present	Yes	Yes	Yes
CUT-like domain present	Yes	Yes	Yes
CUT1 domain present	Yes	Yes	Yes
CUT2 domain present	Yes	Yes	Yes
Homeodomain present	Yes	No	Yes

Table 5.1. Comparison between SATB1, satb1a and satb1b with regards to their respective genomic locations, number of exons in the relevant transcripts, length of cDNA and protein in relevant transcripts, and conservation of protein domains. *bp, base pairs; cDNA, complementary DNA; SATB1, special AT-rich sequence binding protein 1; ULD, ubiquitin-like domain.*

Amino acid sequences of SATB1 were aligned against amino acid sequences of satb1a and satb1b, using CLUSTAL. A 44.9% identity was found between SATB1 and satb1a (**Figure 5.4**) while a 67.7%

identity was found between SATB1 and satb1b (**Figure 5.5**). The difference in % identities between Ensembl BLASTP and CLUSTAL alignment is likely due to differences in programming software, as previously stated (**Section 4.2.1**).

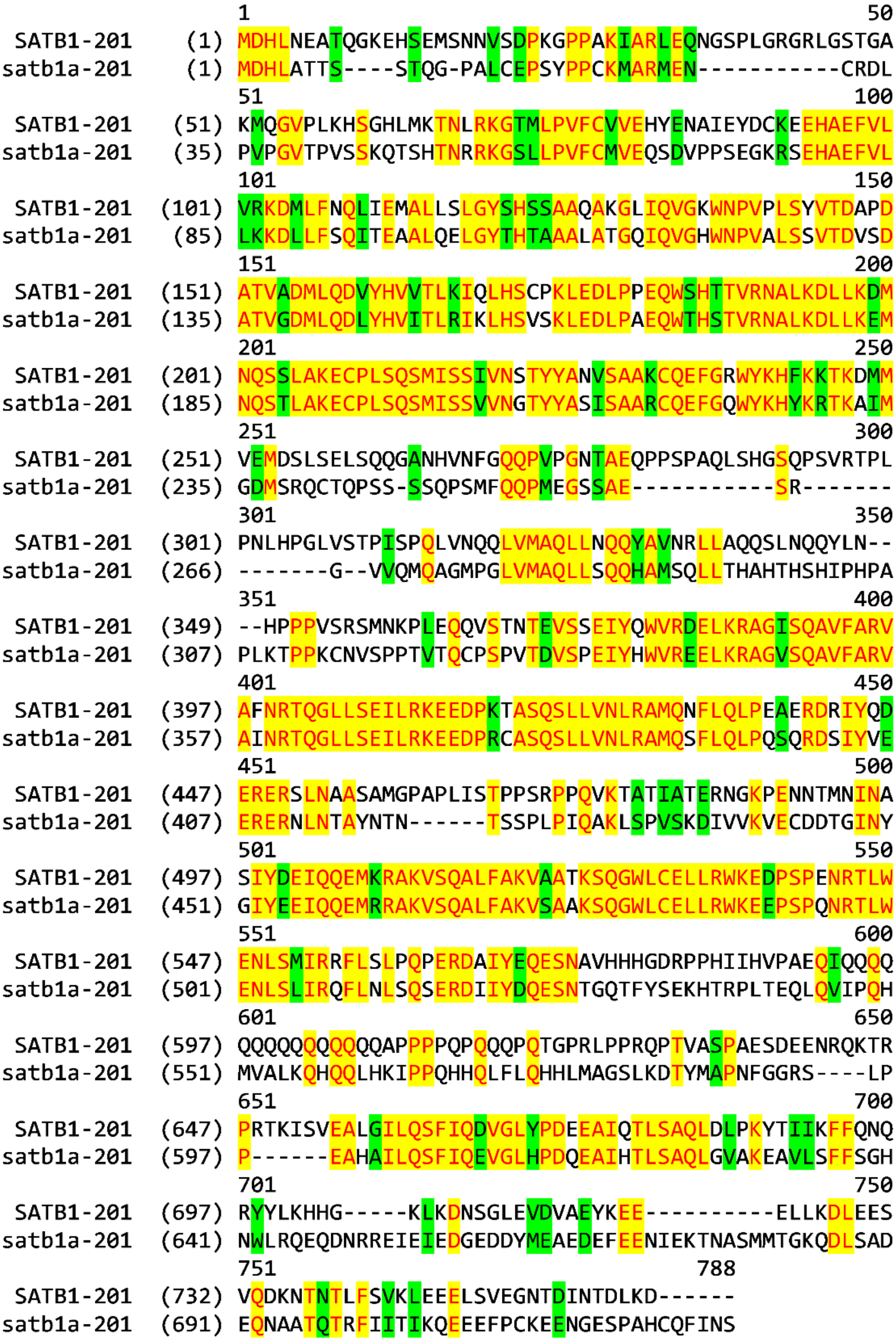

```
                  1                                                50
 SATB1-201    (1) MDHLNEATQGKEHSEMSNNVSDPKGPPAKIARLEQNGSPLGRGRLGSTGA
satb1a-201    (1) MDHLATTS----STQG-PALCEPSYPPCKMARMEN-----------CRDL
                  51                                              100
 SATB1-201   (51) KMQGVPLKHSGHLMKTNLRKGTMLPVFCVVEHYENAIEYDCKEEHAEFVL
satb1a-201   (35) PVPGVTPVSSKQTSHTNRRKGSLLPVFCMVEQSDVPPSEGKRSEHAEFVL
                  101                                             150
 SATB1-201  (101) VRKDMLFNQLIEMALLSLGYSHSSAAQAKGLIQVGKWNPVPLSYVTDAPD
satb1a-201   (85) LKKDLLFSQITEAALQELGYTHTAAALATGQIQVGHWNPVALSSVTDVSD
                  151                                             200
 SATB1-201  (151) ATVADMLQDVYHVVTLKIQLHSCPKLEDLPPEQWSHTTVRNALKDLLKDM
satb1a-201  (135) ATVGDMLQDLYHVITLRIKLHSVSKLEDLPAEQWTHSTVRNALKDLLKEM
                  201                                             250
 SATB1-201  (201) NQSSLAKECPLSQSMISSIVNSTYYANVSAAKCQEFGRWYKHFKKTKDMM
satb1a-201  (185) NQSTLAKECPLSQSMISSVVNGTYYASISAARCQEFGQWYKHYKRTKAIM
                  251                                             300
 SATB1-201  (251) VEMDSLSELSQQGANHVNFGQQPVPGNTAEQPPSPAQLSHGSQPSVRTPL
satb1a-201  (235) GDMSRQCTQPSS-SSQPSMFQQPMEGSSAE-----------SR-------
                  301                                             350
 SATB1-201  (301) PNLHPGLVSTPISPQLVNQQLVMAQLLNQQYAVNRLLAQQSLNQQYLN--
satb1a-201  (266) -------G--VVQMQAGMPGLVMAQLLSQQHAMSQLLTHAHTHSHIPHPA
                  351                                             400
 SATB1-201  (349) --HPPPVSRSMNKPLEQQVSTNTEVSSEIYQWVRDELKRAGISQAVFARV
satb1a-201  (307) PLKTPPKCNVSPPTVTQCPSPVTDVSPEIYHWVREELKRAGVSQAVFARV
                  401                                             450
 SATB1-201  (397) AFNRTQGLLSEILRKEEDPKTASQSLLVNLRAMQNFLQLPEAERDRIYQD
satb1a-201  (357) AINRTQGLLSEILRKEEDPRCASQSLLVNLRAMQSFLQLPQSQRDSIYVE
                  451                                             500
 SATB1-201  (447) ERERSLNAASAMGPAPLISTPPSRPPQVKTATIATERNGKPENNTMNINA
satb1a-201  (407) ERERNLNTAYNTN------TSSPLPIQAKLSPVSKDIVVKVECDDTGINY
                  501                                             550
 SATB1-201  (497) SIYDEIQQEMKRAKVSQALFAKVAATKSQGWLCELLRWKEDPSPENRTLW
satb1a-201  (451) GIYEEIQQEMRRAKVSQALFAKVSAAKSQGWLCELLRWKEEPSPQNRTLW
                  551                                             600
 SATB1-201  (547) ENLSMIRRFLSLPQPERDAIYEQESNAVHHHGDRPPHIIHVPAEQIQQQQ
satb1a-201  (501) ENLSLIRQFLNLSQSERDIIYDQESNTGQTFYSEKHTRPLTEQLQVIPQH
                  601                                             650
 SATB1-201  (597) QQQQQQQQQQQAPPPPQPQQQPQTGPRLPPRQPTVASPAESDEENRQKTR
satb1a-201  (551) MVALKQHQQLHKIPPQHHQLFLQHHLMAGSLKDTYMAPNFGGRS----LP
                  651                                             700
 SATB1-201  (647) PRTKISVEALGILQSFIQDVGLYPDEEAIQTLSAQLDLPKYTIIKFFQNQ
satb1a-201  (597) P------EAHAILQSFIQEVGLHPDQEAIHTLSAQLGVAKEAVLSFFSGH
                  701                                             750
 SATB1-201  (697) RYYLKHHG-----KLKDNSGLEVDVAEYKEE----------ELLKDLEES
satb1a-201  (641) NWLRQEQDNRREIEIEDGEDDYMEAEDEFEENIEKTNASMMTGKQDLSAD
                  751                                 788
 SATB1-201  (732) VQDKNTNTLFSVKLEEELSVEGNTDINTDLKD------
satb1a-201  (691) EQNAATQTRFIITIKQEEEFPCKEENGESPAHCQFINS
```

Figure 5.4. Protein alignment of human SATB1 and zebrafish satb1a. *There is 44.9% identity between human SATB1 and zebrafish satb1a. Yellow highlights identical αα sequences while green highlights conservative substitution. αα, amino acid, SATB1, special AT-rich sequence binding protein 1.*

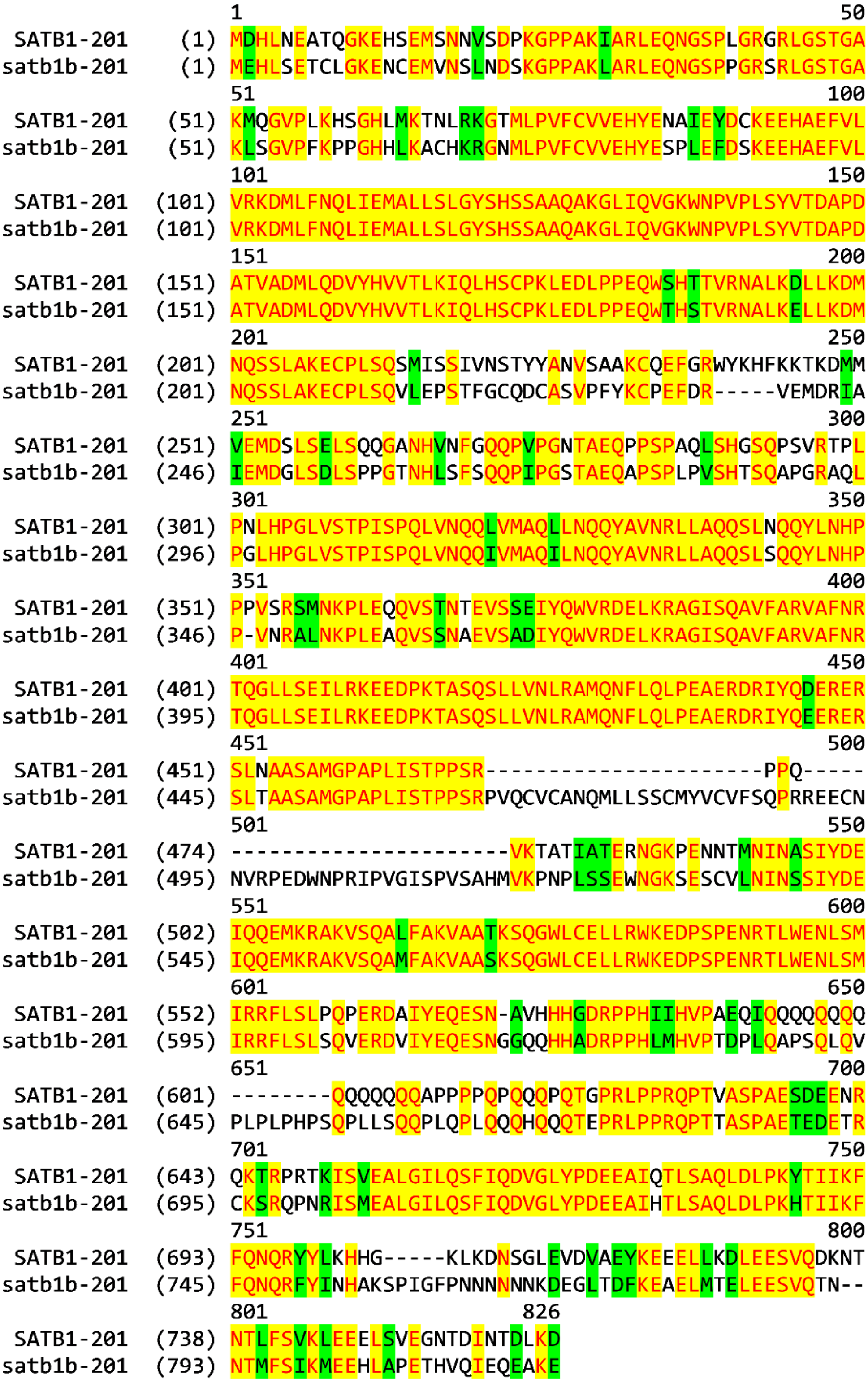

```
                    1                                                50
 SATB1-201    (1)   MDHLNEATQGKEHSEMSNNVSDPKGPPAKIARLEQNGSPLGRGRLGSTGA
satb1b-201    (1)   MEHLSETCLGKENCEMVNSLNDSKGPPAKLARLEQNGSPPGRSRLGSTGA
                    51                                              100
 SATB1-201   (51)   KMQGVPLKHSGHLMKTNLRKGTMLPVFCVVEHYENAIEYDCKEEHAEFVL
satb1b-201   (51)   KLSGVPFKPPGHHLKACHKRGNMLPVFCVVEHYESPLEFDSKEEHAEFVL
                    101                                             150
 SATB1-201  (101)   VRKDMLFNQLIEMALLSLGYSHSSAAQAKGLIQVGKWNPVPLSYVTDAPD
satb1b-201  (101)   VRKDMLFNQLIEMALLSLGYSHSSAAQAKGLIQVGKWNPVPLSYVTDAPD
                    151                                             200
 SATB1-201  (151)   ATVADMLQDVYHVVTLKIQLHSCPKLEDLPPEQWSHTTVRNALKDLLKDM
satb1b-201  (151)   ATVADMLQDVYHVVTLKIQLHSCPKLEDLPPEQWTHSTVRNALKELLKDM
                    201                                             250
 SATB1-201  (201)   NQSSLAKECPLSQSMISSIVNSTYYANVSAAKCQEFGRWYKHFKKTKDMM
satb1b-201  (201)   NQSSLAKECPLSQVLEPSTFGCQDCASVPFYKCPEFDR-----VEMDRIA
                    251                                             300
 SATB1-201  (251)   VEMDSLSELSQQGANHVNFGQQPVPGNTAEQPPSPAQLSHGSQPSVRTPL
satb1b-201  (246)   IEMDGLSDLSPPGTNHLSFSQQPIPGSTAEQAPSPLPVSHTSQAPGRAQL
                    301                                             350
 SATB1-201  (301)   PNLHPGLVSTPISPQLVNQQLVMAQLLNQQYAVNRLLAQQSLNQQYLNHP
satb1b-201  (296)   PGLHPGLVSTPISPQLVNQQIVMAQILNQQYAVNRLLAQQSLSQQYLNHP
                    351                                             400
 SATB1-201  (351)   PPVSRSMNKPLEQQVSTNTEVSSEIYQWVRDELKRAGISQAVFARVAFNR
satb1b-201  (346)   P-VNRALNKPLEAQVSSNAEVSADIYQWVRDELKRAGISQAVFARVAFNR
                    401                                             450
 SATB1-201  (401)   TQGLLSEILRKEEDPKTASQSLLVNLRAMQNFLQLPEAERDRIYQDERER
satb1b-201  (395)   TQGLLSEILRKEEDPKTASQSLLVNLRAMQNFLQLPEAERDRIYQEERER
                    451                                             500
 SATB1-201  (451)   SLNAASAMGPAPLISTPPSR----------------------PPQ-----
satb1b-201  (445)   SLTAASAMGPAPLISTPPSRPVQCVCANQMLLSSCMYVCVFSQPRREECN
                    501                                             550
 SATB1-201  (474)   ----------------------VKTATIATERNGKPENNTMNINASIYDE
satb1b-201  (495)   NVRPEDWNPRIPVGISPVSAHMVKPNPLSSEWNGKSESCVLNINSSIYDE
                    551                                             600
 SATB1-201  (502)   IQQEMKRAKVSQALFAKVAATKSQGWLCELLRWKEDPSPENRTLWENLSM
satb1b-201  (545)   IQQEMKRAKVSQAMFAKVAASKSQGWLCELLRWKEDPSPENRTLWENLSM
                    601                                             650
 SATB1-201  (552)   IRRFLSLPQPERDAIYEQESN-AVHHHGDRPPHIIHVPAEQIQQQQQQQQ
satb1b-201  (595)   IRRFLSLSQVERDVIYEQESNGGQQHHADRPPHLMHVPTDPLQAPSQLQV
                    651                                             700
 SATB1-201  (601)   --------QQQQQQQAPPPPQPQQQPQTGPRLPPRQPTVASPAESDEENR
satb1b-201  (645)   PLPLPHPSQPLLSQQPLQPLQQQHQQQTEPRLPPRQPTTASPAETEDETR
                    701                                             750
 SATB1-201  (643)   QKTRPRTKISVEALGILQSFIQDVGLYPDEEAIQTLSAQLDLPKYTIIKF
satb1b-201  (695)   CKSRQPNRISMEALGILQSFIQDVGLYPDEEAIHTLSAQLDLPKHTIIKF
                    751                                             800
 SATB1-201  (693)   FQNQRYYLKHHG-----KLKDNSGLEVDVAEYKEEELLKDLEESVQDKNT
satb1b-201  (745)   FQNQRFYINHAKSPIGFPNNNNNNKDEGLTDFKEAELMTELEESVQTN--
                    801                      826
 SATB1-201  (738)   NTLFSVKLEEELSVEGNTDINTDLKD
satb1b-201  (793)   NTMFSIKMEEHLAPETHVQIEQEAKE
```

Figure 5.5. Protein alignment of human SATB1 and zebrafish satb1b. *There is 67.7% identity between human SATB1 and zebrafish satb1b. Yellow highlights identical αα sequences while green highlights conservative substitution. αα, amino acid; SATB1, special AT-rich sequence binding protein 1.*

Although *in silico* protein analyses suggest *satb1b* to be the functional zebrafish orthologue of *SATB1*, *satb1a* transcript has an equal number of exons as *SATB1* transcript. Therefore, both *satb1a* and *satb1b* were studied in this PhD.

5.2.2 Synthesis of the *satb1a* WISH probe

The *satb1a* WISH probe was synthesised by transcribing *satb1a* cDNA contained in the "cb955" EST clone (**Section 2.11.1.1**). cb955's sequence was aligned with WT *satb1a* cDNA sequence, using NCBI's online alignment tool (**Section 2.20**). This revealed that the *satb1a* cDNA sequence contained within cb955 spans exons 2-4. Therefore, the *satb1a* WISH probe contains nucleotide sequences spanning exons 2-4 of WT *satb1a* cDNA (**Figure 5.6**).

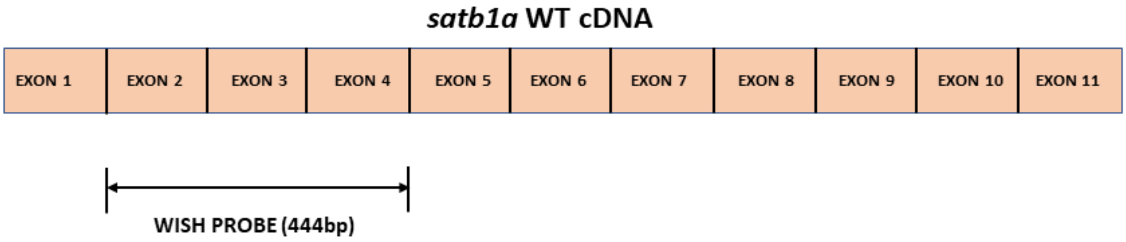

Figure 5.6. Synthesis of the satb1a WISH probe. *The satb1a WISH probe was synthesised from the "cb955" EST clone provided by ZIRC. The satb1a probe is 444bp and contains satb1a nucleotide sequences spanning exons 2-4 of WT satb1a cDNA. bp, base pairs; cDNA, complementary DNA; EST, expressed sequence tag; WISH, whole-mount in-situ hybridisation; WT, wildtype; ZIRC, zebrafish international resource centre.*

5.2.3 Design and synthesis of the *satb1b* WISH probe

The *satb1b* WISH probe was synthesised from PCR product (**Section 2.11.1.2**). qPCR primers were used to amplify exons 1-4 of WT *satb1b* cDNA. Therefore, the *satb1b* WISH probe contains nucleotide sequences spanning exons 1-4 of WT *satb1b* cDNA (**Figure 5.7**). Primer sequences are available (**Section 2.11.1.2**).

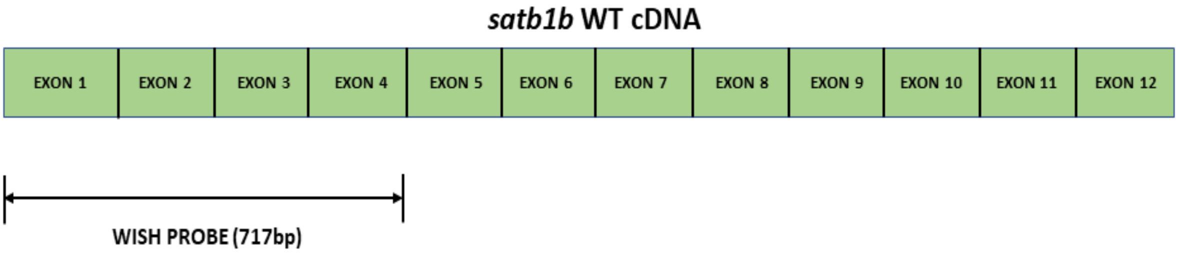

Figure 5.7. Design of the satb1b WISH probe. *The satb1b WISH probe was synthesised from PCR product. This probe is 717bp and contains nucleotide sequences spanning exons 1-4 of WT satb1b cDNA. bp, base pairs; cDNA, complementary DNA; WISH, whole-mount in-situ hybridisation; WT, wildtype.*

5.2.4 Generation of the stable *satb1a*$^{-/-}$ zebrafish line

5.2.4.1 satb1a gRNA efficiency test

gRNA efficiency was tested using RFLP (**Section 2.3.4.1**). Of the 5 *satb1a* gRNAs tested, only 1 gRNA (*satb1a* exon 7a; GTAAATTTCAGGTGACACGT) was highly efficient at inducing mutations; as evidenced by the virtual absence of digested bands in restriction digest products obtained from CRISPR-injected embryos (**Figure 5.8**).

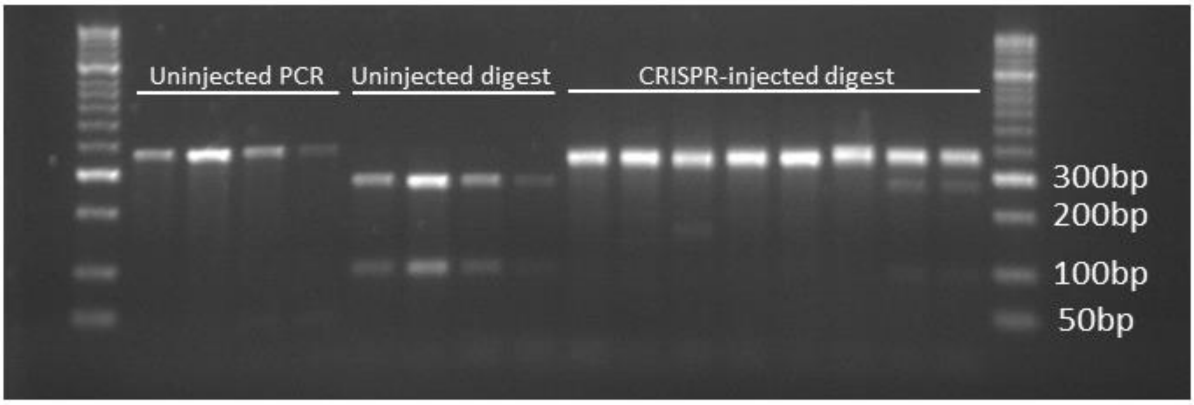

Figure 5.8. satb1a gRNA efficiency test. *A CRISPR mix containing a gRNA targeting exon 7 of satb1a (GTAAATTTCAGGTGACACGT) was micro-injected into one-cell stage WT zebrafish embryos and DNA was extracted at 24hpf. The Cas9 cut-site of this gRNA overlaps an MslI restriction enzyme site. Therefore, gRNA efficiency was inferred from MslI restriction digest efficiency in restriction digest products obtained from CRISPR-injected embryos. A PCR reaction was run to amplify exon 7 of satb1a using DNA samples obtained from 4 uninjected and 8 CRISPR-injected embryos and each PCR product was digested using MslI. PCR products and restriction digest products obtained from uninjected embryos, and restriction digest products obtained from CRISPR-injected embryos were loaded into individual wells of a gel then electrophoresed, with uninjected restriction digest products loaded in the same order as the uninjected PCR products they were derived from. Each well contained the PCR or restriction digest product of a single embryo. PCR products of uninjected embryos were 355bp and restriction digest products of uninjected embryos were 93- and 262bp, as predicted. The restriction digest product of CRISPR-injected embryos was virtually 355bp, indicating high gRNA efficiency. bp, base pairs; Cas9, CRISPR-associated protein 9; CRISPR, clustered regularly interspaced short palindromic repeats; gRNA, guide RNA; hpf, hours post fertilisation; PCR, polymerase chain reaction; WT, wildtype.*

5.2.4.2 Identification of the satb1a mutant allele

Following the identification of a highly efficient *satb1a* gRNA, a fresh CRISPR mix containing this gRNA (**Section 2.3.2**) was micro-injected into one-cell stage WT embryos (**Section 2.3.3**), giving an f0 generation which was raised to adulthood. Adult f0 zebrafish (n = 6) were out-crossed and DNA was extracted from 3dpf f1$^{+/-}$ offspring (n = 8) obtained from each cross. Genomic PCR primers were designed to flank the predicted mutation site and used to amplify exon 7 of *satb1a* (**Section 2.2.2**). PCR amplification revealed the presence of indel mutations in f1$^{+/-}$ embryos obtained from 3 of the 6 f0 out-crosses (**data not shown**). However, for the purpose of this thesis, only indel mutations transmitted from the f0 parent used to generate the *satb1a*$^{-/-}$ line are shown (**Figure 5.9A**).

Remaining f1$^{+/-}$ embryos obtained from the 3 above-mentioned f0 out-crosses were raised to adulthood. DNA was extracted from fin clips (**Section 2.2.1.3**) of individual adult f1$^{+/-}$ zebrafish and amplified using PCR. Samples with indel mutations were sequenced (**Section 2.4**) with WT sample serving as control. Sequencing results were analysed manually by comparing f1$^{+/-}$ sequences to WT sequence. 6bp, 11bp and 12bp deletions, as well as 297bp insertions were identified in adult f1$^{+/-}$ zebrafish obtained from different f0 zebrafish (**data not shown**). An f1$^{+/-}$ zebrafish harbouring an 11bp deletion of GACGTGTCACC (**data not shown**) was out-crossed to obtain a stable f2$^{+/-}$ zebrafish line. Adult f2$^{+/-}$ zebrafish were in-crossed and comparison of f3$^{+/+}$ and f3$^{-/-}$ sequences confirmed the presence of a mutant allele harbouring an 11bp deletion of GACGTGTCACC in exon 7 of *satb1a* (**Figure 5.9B**).

This mutation deletes an MslI restriction enzyme site, meaning this zebrafish line can be genotyped using MslI restriction digest. PCR products obtained from *satb1a*$^{+/+}$ zebrafish were digested giving 93- and 262bp bands, while PCR products obtained from *satb1a*$^{-/-}$ zebrafish were undigested, giving a single 344bp band. Due to the presence of a single copy of the WT and mutant allele, PCR products obtained from *satb1a*$^{+/-}$ zebrafish were both digested and undigested, giving 93-, 262- and 344bp bands (**Figure 5.9C**).

At the protein level, this mutation induces a premature stop codon (TGA) immediately after 987bp. The predicted protein is truncated within its CUT1 domain, having 329 instead of 728 amino acids. Therefore, the predicted protein lacks most of the CUT1 domain and all of the CUT2 domain (**Figure 5.9D**).

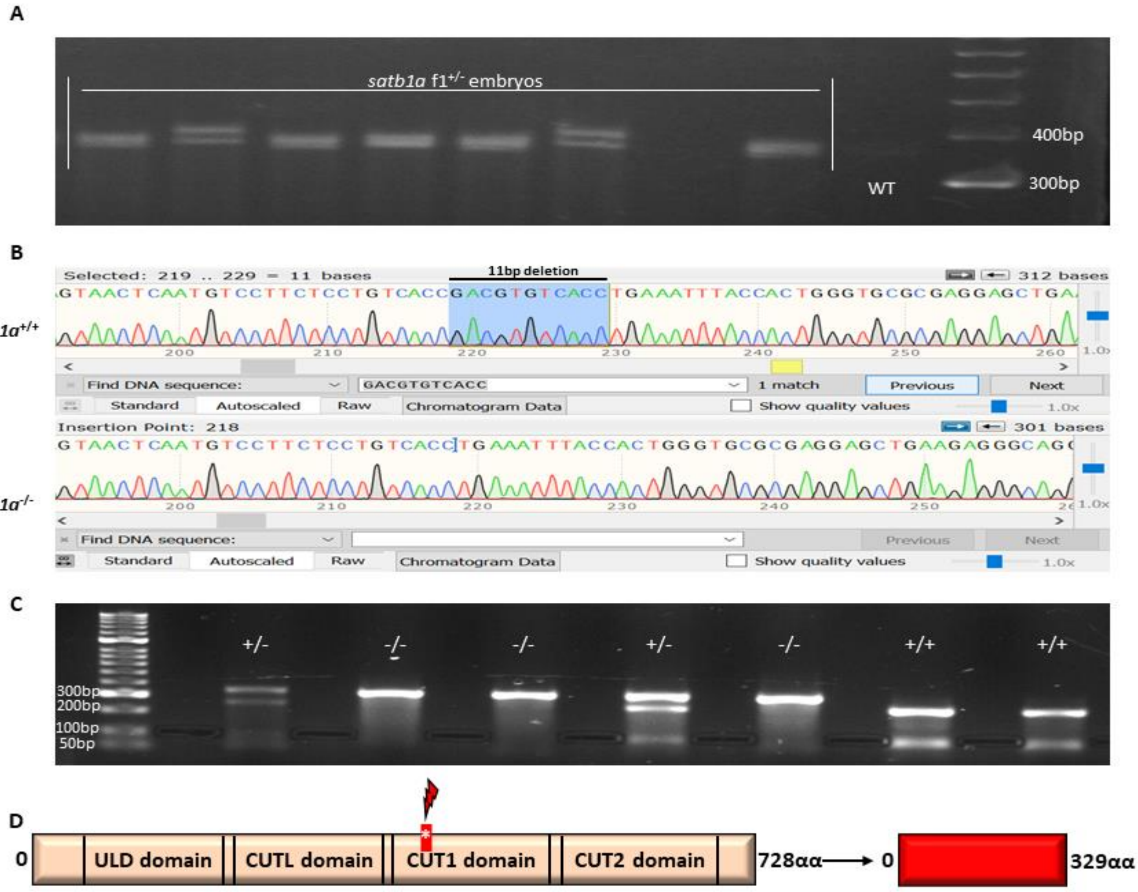

Figure 5.9. Generation of the stable satb1a$^{-/-}$zebrafish line using CRISPR/Cas9 gene editing. *A CRISPR mix containing a single highly efficient sat1ba gRNA was micro-injected into one-cell stage WT zebrafish embryos. Injected embryos were raised to adulthood, then founder (f0) zebrafish were out-crossed to obtain f1$^{+/-}$ embryos. DNA was extracted from f1$^{+/-}$ embryos (n = 8) obtained from a single f0 then amplified using PCR; unrelated WT DNA served as control. PCR products were electrophoresed and indel mutations transmitted from the f0 parent used to generate the satb1a$^{-/-}$ line were identified. WT DNA was not amplified in this PCR reaction (A). Subsequent data refer to offspring of the f0 parent used to generate the satb1a$^{-/-}$ line. Remaining f1$^{+/-}$ embryos were raised to adulthood then DNA was extracted from fin clips and sequenced using Genewiz's service; WT DNA sequence served as control. An 11bp deletion mutation was identified by manually comparing f1$^{+/-}$ sequence to WT sequence. The f1$^{+/-}$ zebrafish harbouring this mutant allele was out-crossed to obtain a stable f2$^{+/-}$ line. Comparison of f3$^{+/+}$ and f3$^{-/-}$ sequences confirmed the presence of an 11bp deletion of GACGTGTCACC (B). For genotyping purposes, this mutation deletes an MslI restriction digest site, meaning that PCR products of satb1a$^{+/+}$ zebrafish were digested by MslI, giving 93- and 262bp bands while PCR products of satb1a$^{-/-}$ zebrafish were undigested, giving a 344bp band. Due to the presence of a WT and mutant allele, PCR products of satb1a$^{+/-}$ zebrafish were both digested and undigested, giving 93-, 262- and 344bp bands (C). This mutation also induces a premature stop codon immediately after 987bp. The predicted protein is truncated, having 329 instead of 728αα, and lacks most of the CUT1 domain and all of the CUT2 domain (D). αα, amino acids; bp, base pairs; Cas9, CRISPR-associated protein 9; CRISPR, clustered regularly interspaced short palindromic repeats; CUTL, CUT-like; gRNA, guide RNA; Indel, insertion/deletion; PCR, polymerase chain reaction; WT, wildtype.*

5.2.5 Generation of the stable *satb1b*$^{-/-}$ zebrafish line

5.2.5.1 satb1b gRNA efficiency test

gRNA efficiency was tested using RFLP and of the 6 *satb1b* gRNAs tested, 1 gRNA (*satb1b* exon 5a; TGTCCGCCGACATCTACCAG) was highly efficient at inducing mutations, as evidenced by reduced intensity of digested bands in restriction digest products obtained from CRISPR-injected embryos (**Figure 5.10**).

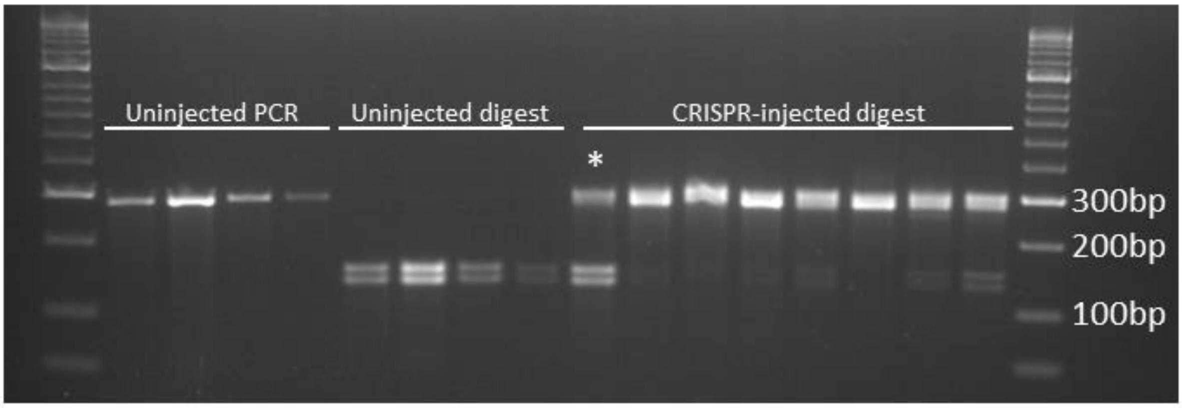

Figure 5.10. satb1b gRNA efficiency test. *A CRISPR mix containing a gRNA targeting exon 5 of satb1b (TGTCCGCCGACATCTACCAG) was micro-injected into one-cell stage WT zebrafish embryos and DNA was extracted at 24hpf. The Cas9 cut-site of this gRNA overlaps a BsrI restriction enzyme site. Therefore, gRNA efficiency was inferred from BsrI restriction digest efficiency in restriction digest products obtained from CRISPR-injected embryos. A PCR reaction was run to amplify exon 5 of satb1b using DNA samples obtained from 4 uninjected and 8 CRISPR-injected embryos and each PCR product was digested using BsrI. PCR products and restriction digest products obtained from uninjected embryos, and restriction digest products obtained from CRISPR-injected embryos were loaded into individual wells of a gel then electrophoresed, with uninjected restriction digest products loaded in the same order as the uninjected PCR products they were derived from. Each well contained the PCR or restriction digest product of a single embryo. PCR products of uninjected embryos were 275bp, and restriction digest products of uninjected embryos were 129- and 146bp, as predicted. Restriction digest products of CRISPR-injected embryos were 129-, 146- and 275bp. However, the intensity of the 275bp band was considerably higher than that of the 129- and 146bp bands, indicating high gRNA efficiency. Suboptimal CRISPR injection is the likely cause of high intensity 129- and 146bp bands in the first CRISPR-injected restriction digest sample denoted by an asterisk, *. bp, base pairs; Cas9, CRISPR-associated protein 9; CRISPR, clustered regularly interspaced short palindromic repeats; gRNA, guide RNA; hpf, hours post fertilisation; PCR, polymerase chain reaction; WT, wildtype.*

5.2.5.2 Identification of the satb1b mutant allele

A fresh CRISPR mix containing the highly efficient *satb1b* gRNA was micro-injected into one-cell stage WT embryos, giving an f0 generation which was raised to adulthood. Adult f0 zebrafish (n = 7) were out-crossed and f1$^{+/-}$ embryos were investigated for indel mutations, as previously detailed (**Section 5.2.4.2**). Indel mutations were identified in f1$^{+/-}$ embryos obtained from 6 of the 7 f0 out-crosses (**data not shown**). For the purpose of this thesis, only indel mutations transmitted from the f0 parent used to generate the *satb1b*$^{-/-}$ line are shown (**Figure 5.11A**).

Remaining f1$^{+/-}$ embryos obtained from the 6 above-mentioned f0 out-crosses were raised to adulthood. DNA was extracted from fin clips of individual adult f1$^{+/-}$ zebrafish and amplified using PCR.

Samples with indel mutations were sequenced; WT sample served as control. Sequencing results were analysed manually, as previously detailed (**Section 5.2.4.2**). 3bp ,4bp, 5bp and 6bp deletions, and a 53bp insertion were identified in adult f1$^{+/-}$ zebrafish obtained from different f0 zebrafish (**data not shown**). An f1$^{+/-}$ zebrafish harbouring a 4bp deletion of TACC (**data not shown**) was out-crossed to obtain a stable f2$^{+/-}$ zebrafish line. Adult f2$^{+/-}$ zebrafish were in-crossed and comparison of f3$^{+/+}$ and f3$^{-/-}$ sequences confirmed the presence of a mutant allele harbouring a 4bp deletion of TACC in exon 5 of *satb1b* (**Figure 5.11B**).

This mutation deletes a BsrI restriction enzyme site, thereby the *satb1b*$^{-/-}$ zebrafish line can be genotyped using BsrI digest. PCR products obtained from *satb1b*$^{+/+}$ zebrafish were digested giving 129- and 146bp bands, while PCR products obtained from *satb1a*$^{-/-}$ zebrafish were undigested, giving a single 271bp band. Due to the presence of a single copy of the WT and mutant allele, PCR products obtained from *satb1a*$^{+/-}$ zebrafish were both digested and undigested, giving 129-, 146- and 271bp bands (**Figure 5.11C**).

At the protein level, this mutation induces a premature stop codon (TGA) immediately after 1,113bp. The predicted protein is truncated within the CUT1 domain, having 371 instead of 818 amino acids. Therefore, the predicted protein lacks most of the CUT1 domain, and all of CUT2 domain and the homeodomain (**Figure 5.11D**).

Figure 5.11. Generation of the stable satb1b$^{-/-}$ zebrafish line using CRISPR/Cas9 gene editing. *A CRISPR mix containing a single highly efficient satb1b gRNA was micro-injected into one-cell stage WT zebrafish embryos. Injected embryos were raised to adulthood, then founder (f0) zebrafish were out-crossed to obtain f1$^{+/-}$ embryos. DNA was extracted from f1$^{+/-}$ embryos (n = 8) obtained from f0 out-crosses (n = 7), and amplified using PCR. Although WT DNA served as control, it and the DNA ladder cannot be shown in this figure due to the order in which samples were loaded in the gel. PCR products were electrophoresed and indel mutations transmitted from the f0 parent used to generate the satb1b$^{-/-}$ line were identified (A). Subsequent data refer to offspring of the f0 parent used to generate the satb1b$^{-/-}$ line. Remaining f1$^{+/-}$ embryos were raised to adulthood then DNA was extracted from fin clips and sequenced using Genewiz's service; WT DNA served as control. A 4bp deletion mutation was identified by manually comparing f1$^{+/-}$ sequence to WT sequence. The f1$^{+/-}$ zebrafish harbouring this mutant allele was out-crossed to obtain a stable f2$^{+/-}$ line. Comparison of f3$^{+/+}$ and f3$^{-/-}$ sequences confirmed the presence of a 4bp deletion of TACC (B). This mutation deletes a BsrI restriction digest site. PCR products obtained from satb1b$^{+/+}$ zebrafish were digested by BsrI, giving 129- and 146bp bands while PCR products obtained from satb1b$^{-/-}$ zebrafish were undigested, giving a single 271bp band. Due to the presence of a WT and mutant allele, PCR products obtained from satb1b$^{+/-}$ zebrafish were both digested and undigested, giving 129-, 146- and 271bp bands (C). This mutation also induces a premature stop codon immediately after 1,113bp. The predicted protein is truncated, having 371 instead of 818αα, and lacks most of the CUT1 domain, all of CUT2 domain and all of the homeodomain (D). αα, amino acids; bp, base pairs; Cas9, CRISPR-associated protein 9; CRISPR, clustered regularly interspaced short palindromic repeats; CUTL, CUT-like; gRNA, guide RNA; Indel, insertion/deletion; PCR, polymerase chain reaction; WT, wildtype.*

5.2.6 Design of *satb1a* qPCR primers

To investigate NMD of *satb1a* mRNA in *satb1a*$^{-/-}$ zebrafish and compensatory upregulation of *satb1a* mRNA in *satb1b*$^{-/-}$ zebrafish, 2 pairs of qPCR primers were designed (FP1 and RP1, and FP2 and RP2). FP1 and RP1 bind upstream of the *satb1a* mutation located in exon 7, and amplify exons 3-4 of *satb1a* cDNA (**Figure 5.12**). FP2 and RP2 bind downstream of the *satb1a* mutation to amplify exons 8-9 of *satb1a* cDNA (**Figure 5.12**). FP1 and RP1 were also utilised for RT-PCR.

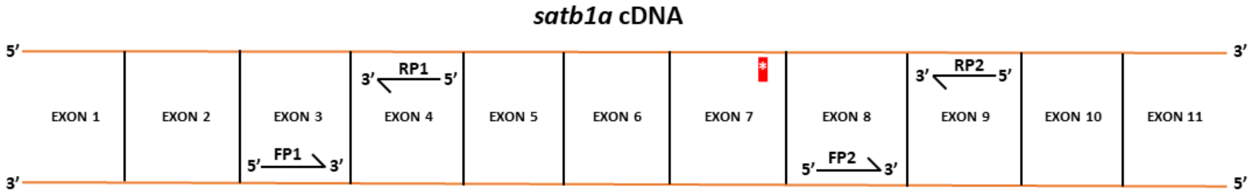

Figure 5.12. Design of satb1a qPCR primers. *2 pairs of satb1a qPCR primers were designed to investigate NMD of satb1a mRNA in satb1a*$^{-/-}$ *zebrafish and compensatory upregulation of satb1a mRNA in satb1b*$^{-/-}$ *zebrafish. FP1 and RP1 bind upstream of the satb1a mutation (asterisk) located in exon 7, and amplify exons 3-4 of satb1a cDNA. FP2 and RP2 bind downstream of the satb1a mutation to amplify exons 8-9 of satb1a cDNA. cDNA, complementary DNA; FP, forward primer; NMD, nonsense-mediated decay; qPCR, quantitative PCR; RP, reverse primer.*

5.2.7 Design of *satb1b* qPCR primers

To investigate NMD of *satb1b* mRNA in *satb1b*$^{-/-}$ zebrafish and compensatory upregulation of *satb1b* mRNA in *satb1a*$^{-/-}$ zebrafish, 2 pairs of qPCR primers were designed (FP1 and RP1, and FP2 and RP2). FP1 and RP1 bind upstream of the *satb1b* mutation located in exon 5, and amplify exons 2-3 of *satb1b* cDNA (**Figure 5.13**). FP2 and RP2 bind downstream of the *satb1b* mutation to amplify exons 8-9 of *satb1b* cDNA (**Figure 5.13**). FP1 and RP1 were also utilised for RT-PCR.

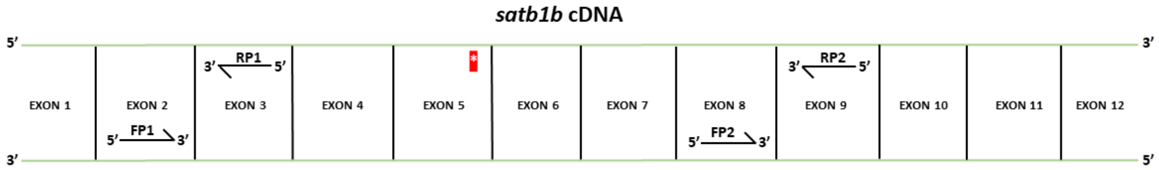

Figure 5.13. Design of satb1b qPCR primers. *2 pairs of satb1b qPCR primers were designed to investigate NMD of satb1b mRNA in satb1b*$^{-/-}$ *zebrafish and compensatory upregulation of satb1b mRNA in satb1a*$^{-/-}$ *zebrafish. FP1 and RP1 bind upstream of the satb1b mutation (asterisk) located in exon 5, and amplify exons 2-3 of satb1b cDNA. FP2 and RP2 bind downstream of the satb1b mutation to amplify exons 8-9 of satb1b cDNA. cDNA, complementary DNA; FP, forward primer; NMD, nonsense-mediated decay; qPCR, quantitative PCR; RP, reverse primer.*

5.3 Results

5.3.1 *satb1a* and *satb1b* mRNA expression

To assess a possible role of *satb1a* and *satb1b* in zebrafish development, mRNA expression of both genes was investigated, using RT-PCR (**Section 2.9**).

5.3.1.1 satb1a mRNA expression

5.3.1.1.1 *satb1a* mRNA expression through development

RNA was extracted (**Section 2.5**) from WT zebrafish between 0-5dpf then reverse transcribed to cDNA (**Section 2.7**). cDNA was amplified using *satb1a* qPCR primers (FP1 and RP1) (**Section 5.2.6**); *β-actin* served as control.

satb1a mRNA was detected as early as 0dpf and was stably expressed through to 5dpf (**Figure 5.14**), indicating that spatial expression of *satb1a* mRNA could be investigated using 0-5dpf zebrafish. *satb1a* mRNA expression was not investigated in adult tissue.

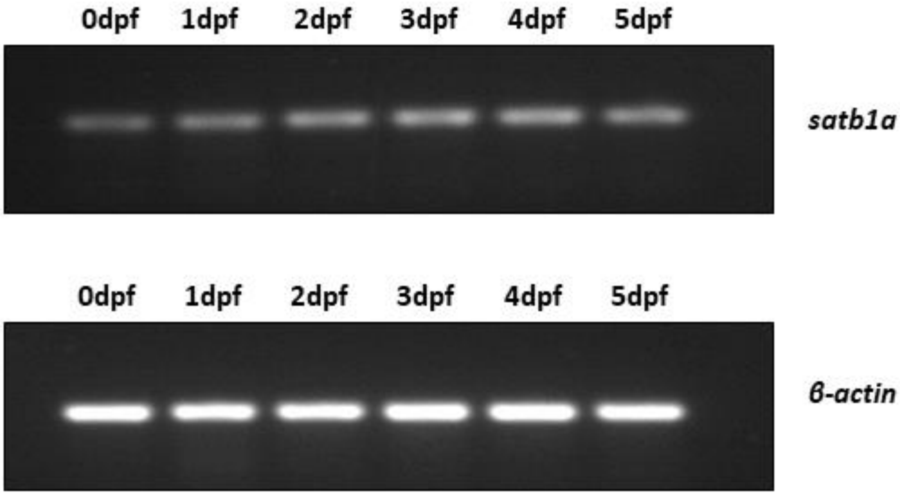

Figure 5.14. satb1a mRNA expression through development. *RT-PCR was used to investigate satb1a mRNA expression in 0-5dpf WT zebrafish, where; 0dpf refers to the 30% epiboly stage of zebrafish development and β-actin served as loading control. satb1a mRNA was steadily expressed from 0-5dpf. β-actin, beta-actin; dpf, days post fertilisation; mRNA, messenger RNA; RT-PCR, reverse transcription PCR; WT, wildtype.*

5.3.1.1.2 Spatial expression of *satb1a* mRNA

WISH (**Section 2.11**) was utilised to investigate spatial *satb1a* expression in 3dpf WT larvae. *satb1a* expression was detected in the tectum, tegmentum, hindbrain, retina and retina ganglion cell layer of larvae hybridised with the anti-sense probe only, indicating specific staining (**Figure 5.15B I-IV**). This mirrored *satb1a* detection recorded in the Zebrafish Information Network (ZFIN) database (**Figure 5.15B V-VI**) and suggests a function of *satb1a* in the zebrafish nervous system.

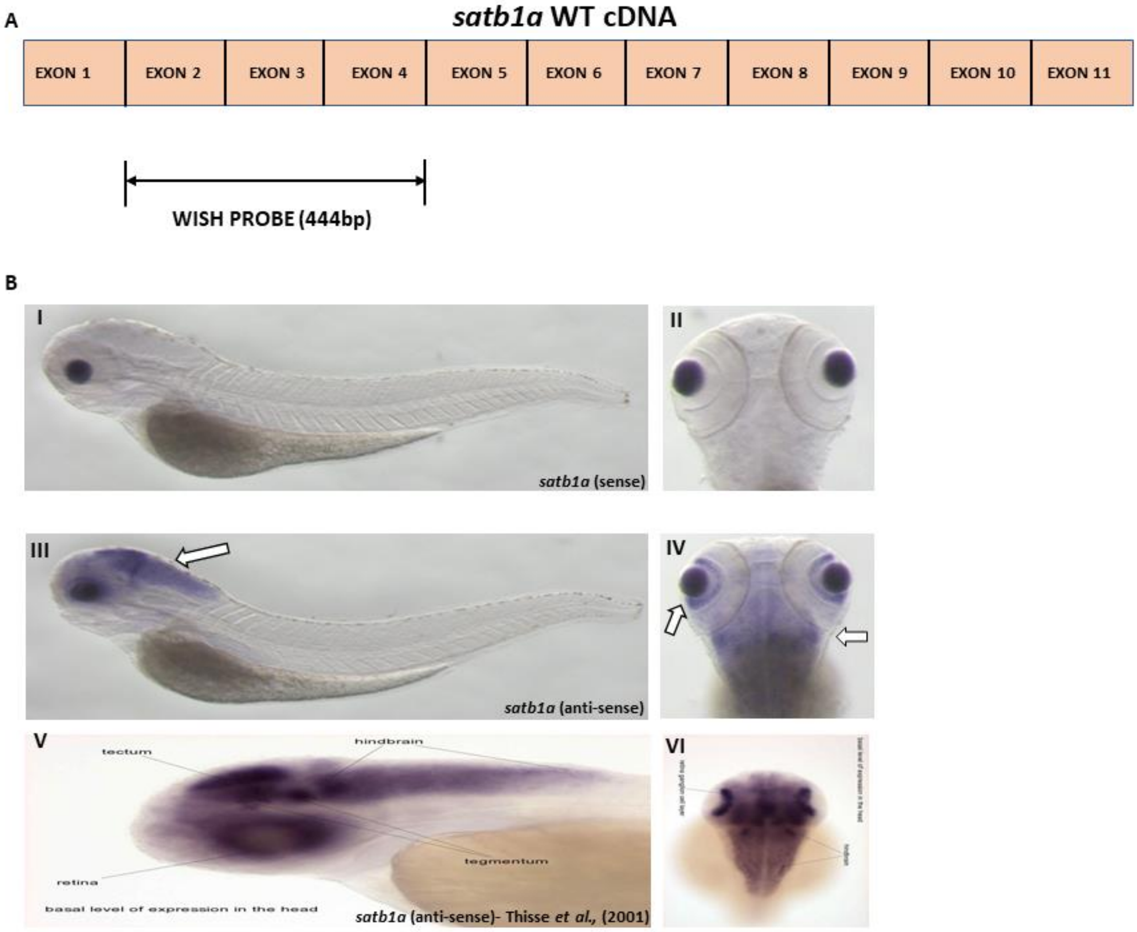

Figure 5.15. Spatial expression of satb1a mRNA at 3dpf, using WISH. *The satb1a WISH probe was transcribed from the "cb955" EST clone. This satb1a WISH probe was used to investigate spatial satb1a mRNA expression by Thisse et al., (2001). This probe is 444bp and contains satb1a nucleotide sequences spanning exons 2-4 of WT satb1a cDNA (A). Representative images of 3dpf larvae hybridised with this satb1a WISH probe are provided (B). I and II are lateral and dorsal images, respectively of larvae hybridised with the sense probe while III and IV are lateral and dorsal images, respectively of larvae hybridised with the anti-sense probe. satb1a is expressed in the tectum, tegmentum, hindbrain, retina and retina ganglion cell layer, as indicated by arrows. V and VI are lateral and dorsal images obtained from Thisse et al., (2001). satb1a spatial expression observed in this PhD resembles that reported by Thisse et al., (2001). bp, base pairs; cDNA, complementary DNA; dpf, days post fertilisation; EST, expressed sequence tag; mRNA, messenger RNA; WISH, whole-mount in-situ hybridisation; WT, wildtype.*

5.3.1.2 *satb1b mRNA expression*

5.3.1.2.1 *satb1b* mRNA expression through development

satb1b expression was investigated in WT zebrafish, as previously detailed (**Section 5.3.1.1.1**). cDNA was amplified using *satb1b* qPCR primers (FP1 and RP1) (**Section 5.2.7**); *β-actin* served as control.

satb1b mRNA was detected as early as 0dpf, was stably expressed to 2dpf, then *satb1b* mRNA expression increased at 3dpf and was stably expressed through to 5dpf (**Figure 5.16**). This indicated that spatial expression of *satb1b* mRNA could be investigated using 0-5dpf zebrafish. *satb1b* mRNA expression was not investigated in adult tissue.

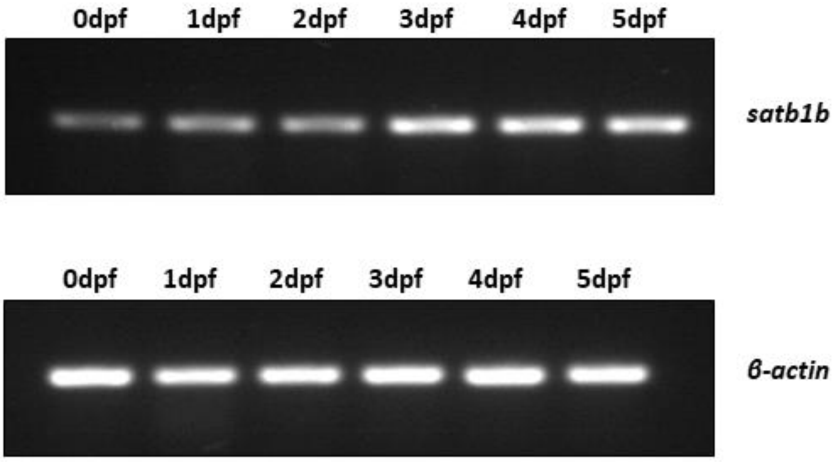

Figure 5.16. satb1b mRNA expression through development. *RT-PCR was used to investigate satb1b mRNA expression in 0-5dpf WT zebrafish, where; 0dpf refers to the 30% epiboly stage of zebrafish development and β-actin served as loading control. satb1b mRNA is steadily expressed from 0-2dpf, then satb1b mRNA expression increased at 3dpf and was steadily expressed through to 5dpf. β-actin, beta-actin; dpf, days post fertilisation; mRNA, messenger RNA; RT-PCR, reverse transcription PCR; WT, wildtype.*

5.3.1.2.2 Spatial expression of *satb1b* mRNA

Spatial *satb1b* expression was investigated in WT larvae, using WISH (**Section 2.11**). *satb1b* expression was detected in the tectum, hindbrain, nasal pit and retinal ganglion cell layer of larvae hybridised with the anti-sense probe only, indicating specific staining (**Figure 5.17B**).

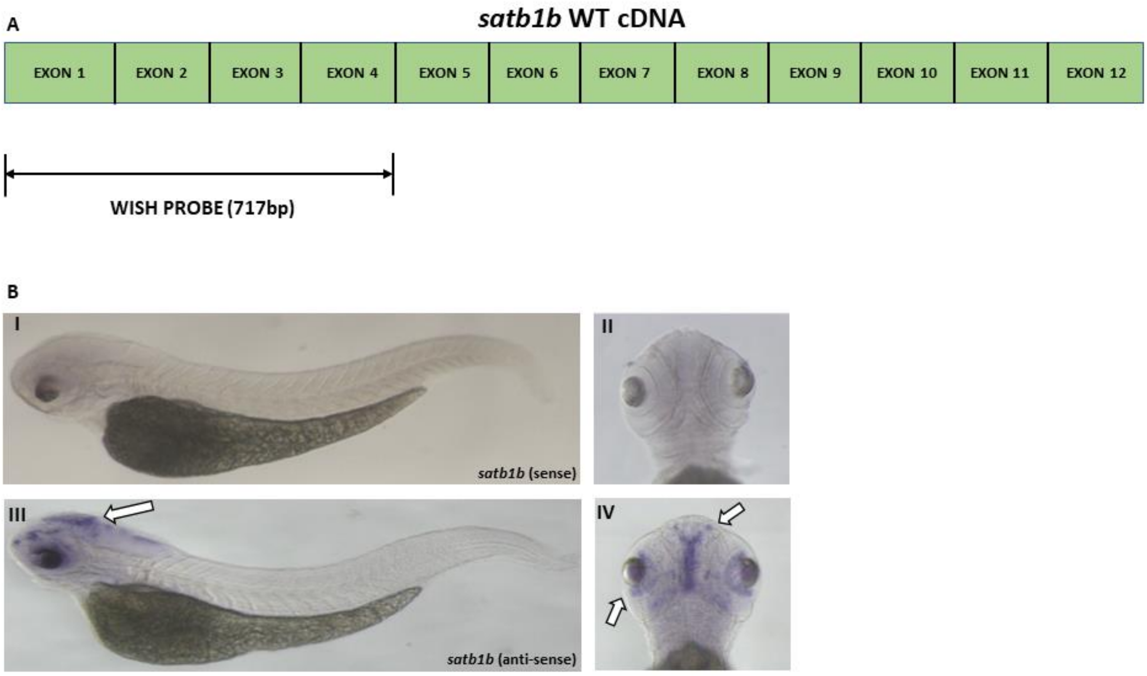

Figure 5.17. Spatial expression of satb1b mRNA at 3dpf, using WISH. *The satb1b WISH probe was synthesised from PCR product. The satb1b WISH probe is 717bp and contains satb1b nucleotide sequences spanning exons 1-4 of WT satb1b cDNA (A). Representative images of 3dpf larvae hybridised with the satb1b WISH probe are provided (B). I and II are lateral and dorsal images, respectively of larvae hybridised with the sense probe while III and IV are lateral and dorsal images, respectively of larvae hybridised with the anti-sense probe. satb1b is expressed in the tectum, hindbrain, nasal pit and retina ganglion cell layer, as indicated by arrows. bp, base pairs; cDNA, complementary DNA; dpf, days post fertilisation; mRNA, messenger RNA; WISH, whole-mount in-situ hybridisation; WT, wildtype.*

5.3.2 Characterisation of *satb1a*$^{-/-}$ and *satb1b*$^{-/-}$ zebrafish

Both the *satb1a*$^{-/-}$ and *satb1b*$^{-/-}$ zebrafish lines were characterised to identify the functional zebrafish orthologue(s) of human *SATB1*.

5.3.2.1 Characterisation of satb1a$^{-/-}$ *zebrafish*

5.3.2.1.1 NMD and compensatory upregulation in *satb1a*$^{-/-}$ larvae

Adult *satb1a*$^{+/-}$ zebrafish were in-crossed, DNA was extracted from larval tail clips of offspring (**Section 2.2.1.2**), and *satb1a*$^{+/+}$ and *satb1a*$^{-/-}$ larvae were identified by genotyping (**Sections 2.2.2 and 2.2.3**). Next, RNA was extracted from pooled *satb1a*$^{+/+}$ and *satb1a*$^{-/-}$ larvae at 5dpf, and extracted RNA was reverse transcribed to cDNA for qPCR experiments (**Section 2.8**).

To investigate NMD of *satb1a* mRNA and compensatory upregulation of *satb1b* mRNA in *satb1a*$^{-/-}$ zebrafish, *satb1a*$^{+/+}$ and *satb1a*$^{-/-}$ cDNA was amplified, using *satb1a* FP1 and RP1 (**Section 5.2.6**), and *satb1b* FP1 and RP1 (**Section 5.2.7**), respectively.

NMD of *satb1a* mRNA was absent in *satb1a*$^{-/-}$ larvae at 5dpf (*satb1a*$^{+/+}$ = 1.40, *satb1a*$^{-/-}$ = 1.68, p = 0.6762, **Figure 5.18A**). Also, there was no compensatory upregulation of *satb1b* mRNA in *satb1a*$^{-/-}$ larvae at 5dpf (*satb1a*$^{+/+}$ = 1.05, *satb1a*$^{-/-}$ = 1.63, p = 0.2305, **Figure 5.18B**).

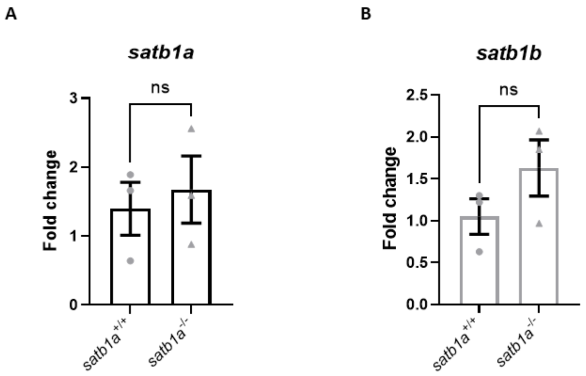

Figure 5.18. Investigation of NMD and compensatory upregulation in satb1a$^{-/-}$ larvae at 5dpf, using the first set of satb1a and satb1b qPCR primers*. NMD of satb1a mRNA was absent in satb1a$^{-/-}$ larvae, at 5dpf (A). There was no compensatory upregulation of satb1b mRNA in satb1a$^{-/-}$ larvae, at 5dpf (B). satb1a FP1 and RP1 (Figure 5.12), and satb1b FP1 and RP1 (Figure 5.13) were utilised. Error bars represent standard error of the mean. Normality was assessed using a Shapiro-Wilk test and datasets were analysed using two-way unpaired t-tests with Welch's correction. n = 3. p = 0.6762 (A), p = 0.2305 (B). dpf, days post fertilisation; FP, forward primer; mRNA, messenger RNA; NMD, nonsense-mediated decay; qPCR, quantitative PCR; RP, reverse primer.*

To further investigate NMD of *satb1a* mRNA and compensatory upregulation of *satb1b* mRNA in *satb1a*$^{-/-}$ zebrafish, *satb1a*$^{+/+}$ and *satb1a*$^{-/-}$ cDNA was amplified, using *satb1a* FP2 and RP2 (**Section 5.2.6**), and *satb1b* FP2 and RP2 (**Section 5.2.7**), respectively. *satb1a*$^{+/+}$ and *satb1a*$^{-/-}$ cDNA was obtained from an additional clutch of *satb1a*$^{+/-}$ in-cross larvae, thereby increasing the number of biological replicates of subsequent qPCR reactions from 3 to 4.

There was a trend for NMD of *satb1a* mRNA in *satb1a*$^{-/-}$ larvae, at 5dpf (*satb1a*$^{+/+}$ = 1.31, *satb1a*$^{-/-}$ = 0.55, p = 0.2448, **Figure 5.19A**). However, there was no compensatory upregulation of *satb1b* mRNA in *satb1a*$^{-/-}$ larvae, at 5dpf (*satb1a*$^{+/+}$ = 1.24, *satb1a*$^{-/-}$ = 1.73, p = 0.5422, **Figure 5.19B**).

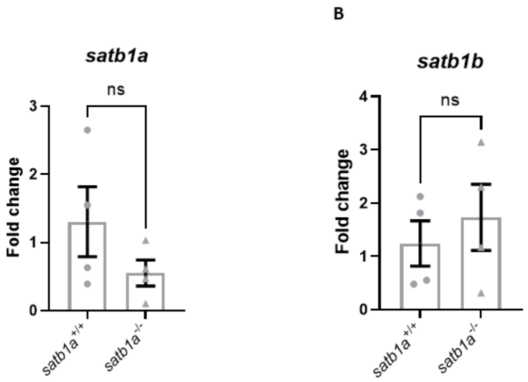

Figure 5.19. Investigation of NMD and compensatory upregulation in satb1a$^{-/-}$ larvae at 5dpf, using the second set of satb1a and satb1b qPCR primers. *There was a trend for NMD of satb1a mRNA in satb1a$^{-/-}$ larvae, at 5dpf (A). There was no compensatory upregulation of satb1b mRNA in satb1a$^{-/-}$ larvae, at 5dpf (B). satb1a FP2 and RP2 (Figure 5.12), and satb1b FP2 and RP2 (Figure 5.13) were utilised. Error bars represent standard error of the mean. Normality was assessed using a Shapiro-Wilk test and datasets were analysed using two-way unpaired t-tests with Welch's correction. n = 4. p = 0.2448 (A), p = 0.5422 (B). dpf, days post fertilisation; FP, forward primer; mRNA, messenger RNA; NMD, nonsense-mediated decay; qPCR, quantitative PCR; RP, reverse primer.*

5.3.2.1.2 mRNA expression of senescence factors *satb1a*$^{-/-}$ larvae

To assess accelerated ageing in *satb1a*$^{-/-}$ larvae, mRNA expression of senescence factors, namely *cdkn1a*, *il-1β* and *il-6* was investigated, using qPCR. *satb1a*$^{+/+}$ and *satb1a*$^{-/-}$ cDNA samples were obtained as previously detailed (**Section 5.3.2.1.1**).

There was no significant difference in *cdkn1a* (*satb1a*$^{+/+}$ = 1.03, *satb1a*$^{-/-}$ = 1.18, p = 0.5178, **Figure 5.20A**), *il-1β* (*satb1a*$^{+/+}$ = 1.25, *satb1a*$^{-/-}$ = 1.37, p = 0.6286, **Figure 5.20B**) and *il-6* expression (*satb1a*$^{+/+}$ = 1.05, *satb1a*$^{-/-}$ = 1.11, p = 0.8857, **Figure 5.20C**) between *satb1a*$^{+/+}$ and *satb1a*$^{-/-}$ larvae at 5dpf, suggesting the absence of accelerated ageing in *satb1a*$^{-/-}$ larvae at 5dpf.

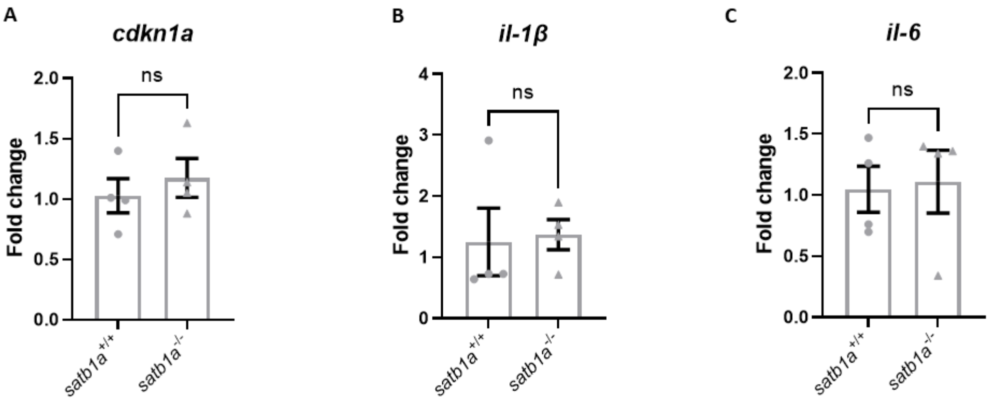

Figure 5.20. Investigation of senescence factors in satb1a$^{-/-}$ larvae, at 5dpf. *There was no upregulation of cdkn1a (A), il-1β (B) and il-6 (C) expression in satb1a$^{-/-}$ larvae at 5dpf. Error bars represent standard error of the mean. Normality was assessed using a Shapiro-Wilk test and data was analysed using a two-way unpaired t-test with Welch's correction (A) and Mann-Whitney tests (B and C). n = 4. p = 0.5178 (A), p = 0.6286 (B), p = 0.8857 (C). cdkn1a, cdk inhibitor 1a; dpf, days post fertilisation; il-1β, interleukin-1beta; il-6, interleukin-6.*

5.3.2.1.3 Dopaminergic neuron number and MPP$^+$ susceptibility in *satb1a*$^{-/-}$ larvae

Adult *satb1a*$^{+/-}$ zebrafish were in-crossed and offspring were exposed to either 3.0 mM MPP$^+$ or MQ from 1-3 dpf (**Section 2.10.1**). 3dpf *satb1a*$^{+/-}$ in-cross larvae were fixed (**Section 2.1.9**) and dopaminergic neurons were visualised using *th1* WISH (**Section 2.11.2**). DC1, DC2, DC4 and DC5 neurons were counted on both hemispheres at 20.0x magnification while larvae were genotyped in parallel (**Section 2.11.4**).

There was no significant difference in the number of dopaminergic neurons between untreated *satb1a*$^{+/+}$ and untreated *satb1a*$^{-/-}$ larvae (*satb1a*$^{+/+}$ = 24.48, *satb1a*$^{-/-}$ = 24.44, p = 0.9990, **Figure 5.21**). Likewise, there was no significant difference in MPP$^+$ susceptibility between *satb1a*$^{+/+}$ and *satb1a*$^{-/-}$ larvae (*satb1a*$^{+/+}$ = 35.93% reduction in dopaminergic neuron number, *satb1a*$^{-/-}$ = 35.17% reduction in dopaminergic neuron number, p = 0.9869, **Figure 5.21**).

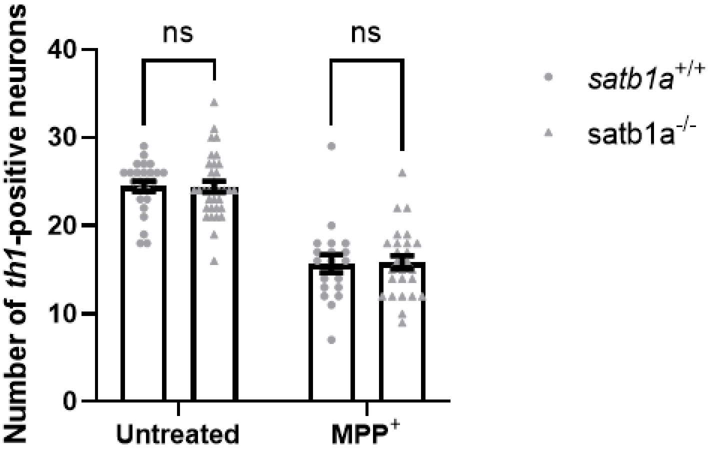

Figure 5.21. Dopaminergic neuron count of 3dpf satb1a$^{+/+}$ and satb1a$^{-/-}$ larvae with and without MPP$^+$ exposure. *Dopaminergic neurons were counted in 3dpf untreated and MPP$^+$-treated satb1a$^{+/+}$ and satb1a$^{-/-}$ larvae. There was no significant difference in the number of dopaminergic neurons between satb1a$^{+/+}$ and satb1a$^{-/-}$ larvae, with and without MPP$^+$ exposure. Error bars represent standard error of the mean. Data was analysed using a two-way ANOVA with Šídák's multiple comparisons. Larvae were obtained from 3 biological replicates of satb1a$^{+/-}$ in-cross embryos. n; untreated satb1a$^{+/+}$ = 25, untreated satb1a$^{-/-}$ = 34, MPP$^+$-treated satb1a$^{+/+}$ = 19 and MPP$^+$-treated satb1a$^{-/-}$ = 26. p = 0.9990 (Untreated satb1a$^{+/+}$-satb1a$^{-/-}$), p = 0.9869 (MPP$^+$ satb1a$^{+/+}$-satb1a$^{-/-}$). ANOVA, analysis of variance; dpf, days post fertilisation; MPP$^+$, 1-methyl-4-phenylpyridinium; th1, tyrosine hydroxylase 1.*

5.3.2.1.4 Morphology, morbidity and mortality of *satb1a*$^{-/-}$ zebrafish

5.3.2.1.4.1 Larval *satb1a*$^{-/-}$ zebrafish

Adult *satb1a*$^{+/-}$ zebrafish were in-crossed and offspring were monitored for morbidity and mortality till 10dpf. Some larvae developed heart oedema and were culled for DNA extraction (**Sections 2.1.10 and 2.2.1.1**) immediately the phenotype was observed, while healthy larvae were culled for DNA extraction at 10dpf.

Genotyping (**Section 2.2**) revealed that heart oedema was displayed by *satb1a*$^{+/+}$, *satb1a*$^{+/-}$ and *satb1a*$^{-/-}$ larvae (**data not shown**). Also, the number of *satb1a*$^{+/+}$, *satb1a*$^{+/-}$ and *satb1a*$^{-/-}$ larvae identified by genotyping was in accordance with Mendelian inheritance (**Table 5.2**), indicating that *satb1a*$^{-/-}$ zebrafish are indistinguishable from *satb1a*$^{+/+}$ siblings, and are equally viable till 10dpf. Likewise, no phenotype was observed in *satb1a*$^{-/-}$ larvae genotyped ahead of RNA extraction at 5dpf (**Sections 5.3.2.1.1 and 5.3.2.1.2**).

Total number of *satb1a*$^{+/-}$ in-cross larvae = 68			
Zebrafish	***satb1a*$^{+/+}$**	***satb1a*$^{+/-}$**	***satb1a*$^{-/-}$**
Mendelian inheritance	1/4	1/2	1/4
Number of larvae predicted by Mendelian inheritance	17	34	17
Number of larvae identified by genotyping	12	39	17

Table 5.2. Viability of satb1a$^{-/-}$ larvae to 10dpf. *Genotyping of 68 satb1a$^{+/-}$ in-cross larvae revealed that 12 were satb1a$^{+/+}$ larvae, 39 were satb1a$^{+/-}$ larvae and 17 were satb1a$^{-/-}$ larvae, which was in accordance with Mendelian inheritance. dpf, days post fertilisation.*

5.3.2.1.4.2 Adult *satb1a*$^{-/-}$ zebrafish

Another clutch of *satb1a*$^{+/-}$ in-cross embryos was obtained and raised to adulthood. At first glance, adult *satb1a*$^{+/+}$ and *satb1a*$^{-/-}$ zebrafish were also indistinguishable from each other (**Figure 5.22**). Likewise, the number of adult *satb1a*$^{+/+}$ and *satb1a*$^{-/-}$ zebrafish identified by genotyping was in accordance with Mendelian inheritance (**Table 5.3**), indicating equal viability of *satb1a*$^{+/+}$ and *satb1a*$^{-/-}$ zebrafish to adulthood. Survival was unaffected in *satb1a*$^{-/-}$ zebrafish. *satb1a*$^{+/+}$ and *satb1a*$^{-/-}$ zebrafish were observed until 5mpf.

Figure 5.22. Representative images of male and female satb1a$^{+/+}$ and satb1a$^{-/-}$ zebrafish, at 4mpf. *Male satb1a$^{+/+}$ (A), male satb1a$^{-/-}$ (B), female satb1a$^{+/+}$ (C) and female satb1a$^{-/-}$ (D) zebrafish were imaged at 4mpf. satb1a$^{-/-}$ zebrafish did not display an overt phenotype. mpf, months post fertilisation.*

Total number of adult *satb1a*$^{+/-}$ in-cross zebrafish = 113			
Zebrafish	***satb1a*$^{+/+}$**	***satb1a*$^{+/-}$**	***satb1a*$^{-/-}$**
Mendelian inheritance	1/4	1/2	1/4
Number of zebrafish predicted by Mendelian inheritance	28	57	28
Number of zebrafish identified by genotyping	24	59	30

Table 5.3. Viability of satb1a$^{-/-}$ zebrafish to adulthood. *Genotyping of 113 adult satb1a$^{+/-}$ in-cross zebrafish revealed that 24 were satb1a$^{+/+}$ zebrafish, 59 were satb1a$^{+/-}$ zebrafish and 30 were satb1a$^{-/-}$ zebrafish, which was in accordance with Mendelian inheritance. Therefore, satb1a$^{-/-}$ zebrafish are viable to adulthood. Genotyping was completed using the Zebrafish Genotyping Service offered by the Biological Services Aquarium.*

5.3.2.1.4.2.1 Weight of adult satb1a$^{-/-}$ zebrafish

To assess emaciation in adult *satb1a*$^{-/-}$ zebrafish at 4mpf, weights were recorded, as previously detailed (**Section 2.14.2.1**).

To investigate a sex-related difference in weight, the weights of male and female zebrafish were analysed for significance, per genotype. There was no significant difference in weight between male and female *satb1a*$^{+/+}$ zebrafish (male *satb1a*$^{+/+}$ = 0.25g, female *satb1a*$^{+/+}$ = 0.25g, p = 0.8486, **Figure 5.23A**), and between male and female *satb1a*$^{-/-}$ zebrafish (male *satb1a*$^{-/-}$ = 0.20g, female *satb1a*$^{-/-}$ = 0.20g, p = 0.9935, **Figure 5.23A**). Therefore, the weights of male and female zebrafish were combined per genotype and re-analysed for significance. There was a significant reduction in weight in *satb1a*$^{-/-}$

zebrafish compared to *satb1a*$^{+/+}$ siblings (*satb1a*$^{+/+}$ = 0.25g, *satb1a*$^{-/-}$ = 0.20g, $p<0.0001$, **Figure 5.23B**), suggesting emaciation of *satb1a*$^{-/-}$ zebrafish.

Further analysis revealed that both male and female *satb1a*$^{-/-}$ zebrafish display weight loss (male *satb1a*$^{+/+}$ = 0.25g, male *satb1a*$^{-/-}$ = 0.20g, p = 0.0001, female *satb1a*$^{+/+}$ = 0.25g, female *satb1a*$^{-/-}$ = 0.20g, p = 0.0002, **Figure 5.23C**).

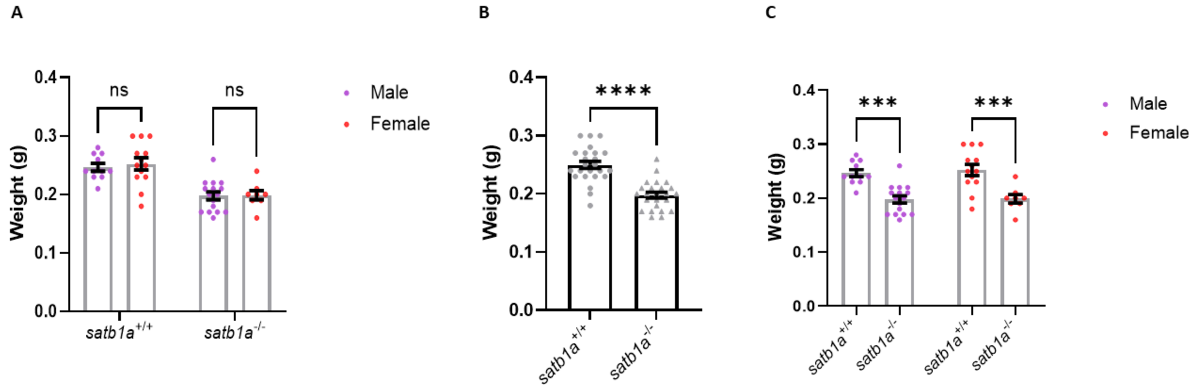

Figure 5.23. Weight of satb1a*$^{+/+}$ *and satb1a*$^{-/-}$ *zebrafish, at 4mpf. *There was no significant difference in weight between male and female satb1a*$^{+/+}$ *zebrafish, and between male and female satb1a*$^{-/-}$ *zebrafish (A). Therefore, weights of male and female zebrafish were combined per genotype and re-analysed for significance. There was a significant reduction in weight in satb1a*$^{-/-}$ *zebrafish (B). satb1a*$^{-/-}$ *zebrafish weighed less than satb1a*$^{+/+}$ *zebrafish, regardless of sex (C). Error bars represent standard error of the mean. Data was analysed using a two-way ANOVA with Šídák's multiple comparisons (A and C) and Welch's t-test (B). n; satb1a*$^{+/+}$ *male = 11, satb1a*$^{+/+}$ *female = 13, satb1a*$^{-/-}$ *male = 16 and satb1a*$^{-/-}$ *female = 8. p = 0.8486 (satb1a*$^{+/+}$ *male-female), p = 0.9935 (satb1a*$^{-/-}$ *male-female), p<0.0001 (satb1a*$^{+/+}$*-satb1a*$^{-/-}$*), p = 0.0001 (male satb1a*$^{+/+}$*-satb1a*$^{-/-}$*) , p = 0.0002 (female satb1a*$^{+/+}$*-satb1a*$^{-/-}$*). ANOVA, analysis of variance; mpf, months post fertilisation.*

5.3.2.1.4.2.2 Size of adult satb1a$^{-/-}$ *zebrafish*

To assess growth defects in adult *satb1a*$^{-/-}$ zebrafish at 4mpf, size was measured and recorded, as previously detailed (**Section 2.14.2.2**).

5.3.2.1.4.2.2.1 Length of adult *satb1a*$^{-/-}$ zebrafish

To investigate a sex-related difference in zebrafish length, the lengths of male and female zebrafish were analysed for significance, per genotype. There was no significant difference in length between male and female *satb1a*$^{+/+}$ zebrafish (male *satb1a*$^{+/+}$ = 2.34cm, female *satb1a*$^{+/+}$ = 2.48cm, p = 0.1974, **Figure 5.24A**), and between male and female *satb1a*$^{-/-}$ zebrafish (male *satb1a*$^{-/-}$ = 2.56cm, female *satb1a*$^{-/-}$ = 2.55cm, p = 0.9883, **Figure 5.24A**). Therefore, the lengths of male and female zebrafish were combined per genotype and re-analysed for significance. There was a significant increase in length in *satb1a*$^{-/-}$ zebrafish compared to *satb1a*$^{+/+}$ siblings (*satb1a*$^{+/+}$ = 2.41cm, *satb1a*$^{-/-}$ = 2.55cm, p = 0.0220, **Figure 5.24B**).

Further analysis revealed that this significant increase in length was contributed by male *satb1a*$^{-/-}$ zebrafish only (male *satb1a*$^{+/+}$ = 2.34cm, male *satb1a*$^{-/-}$ = 2.56cm, p = 0.0170, female *satb1a*$^{+/+}$ = 2.48cm, female *satb1a*$^{-/-}$ = 2.55cm, p = 0.07024, **Figure 5.24C**).

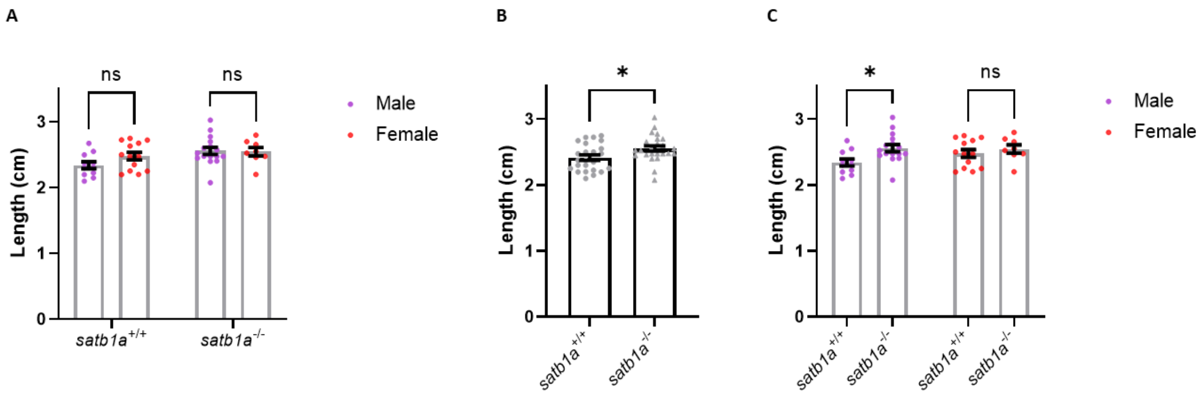

Figure 5.24. Length of satb1a$^{+/+}$ and satb1a$^{-/-}$ zebrafish, at 4mpf. *There was no significant difference in length between male and female satb1a$^{+/+}$ zebrafish, and between male and female satb1a$^{-/-}$ zebrafish (A). Therefore, lengths of male and female zebrafish were combined per genotype and re-analysed for significance. There was a significant increase in length in satb1a$^{-/-}$ zebrafish (B) which was contributed by male satb1a$^{-/-}$ zebrafish only (C). Error bars represent standard error of the mean. Data was analysed using a two-way ANOVA with Šídák's multiple comparisons (A and C) and Welch's t-test (B). n; satb1a$^{+/+}$ male = 11, satb1a$^{+/+}$ female = 13, satb1a$^{-/-}$ male = 16 and satb1a$^{-/-}$ female = 8. p = 0.1974 (satb1a$^{+/+}$ male-female), p = 0.9883 (satb1a$^{-/-}$ male-female), p = 0.0220 (satb1a$^{+/+}$-satb1a$^{-/-}$), p = 0.0170 (male satb1a$^{+/+}$-satb1a$^{-/-}$) , p = 0.07024 (female satb1a$^{+/+}$-satb1a$^{-/-}$). ANOVA, analysis of variance; mpf, months post fertilisation.*

5.3.2.1.4.2.2.2 Width of adult *satb1a*$^{-/-}$ zebrafish

The widths of male and female zebrafish per genotype were also analysed for significance. Although there was no significant difference in width between male and female *satb1a*$^{-/-}$ zebrafish (male *satb1a*$^{-/-}$ = 0.57cm, female *satb1a*$^{-/-}$ = 0.61cm, p = 0.2175, **Figure 5.25A**), female *satb1a*$^{+/+}$ zebrafish were significantly wider than male *satb1a*$^{+/+}$ zebrafish (male *satb1a*$^{+/+}$ = 0.59cm, female *satb1a*$^{+/+}$ = 0.68cm, p = 0.0003, **Figure 5.25A**).

Due to the sex-related difference in widths of *satb1a*$^{+/+}$ zebrafish, this dataset could not be combined per genotype. Instead widths were compared between male *satb1a*$^{+/+}$ and *satb1a*$^{-/-}$ zebrafish, and between female *satb1a*$^{+/+}$ and *satb1a*$^{-/-}$ zebrafish. There was no significant difference in width between male *satb1a*$^{+/+}$ and male *satb1a*$^{-/-}$ zebrafish (male *satb1a*$^{+/+}$ = 0.59cm, male *satb1a*$^{-/-}$ = 0.57cm, p = 0.6512, **Figure 5.25B**). However, there was a significant reduction in width in female *satb1a*$^{-/-}$ zebrafish compared to female *satb1a*$^{+/+}$ zebrafish (female *satb1a*$^{+/+}$ = 0.68cm, female *satb1a*$^{-/-}$ = 0.61cm, p = 0.0093, **Figure 5.25B**).

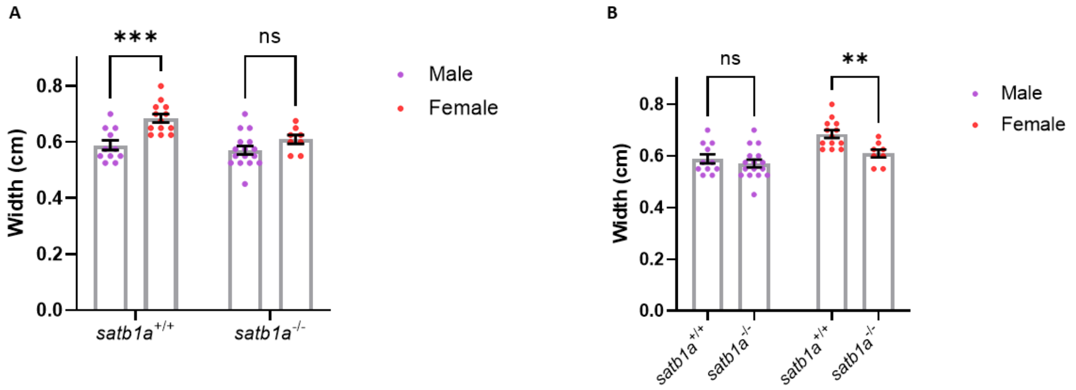

Figure 5.25. Width of satb1a$^{+/+}$ and satb1a$^{-/-}$ zebrafish, at 4mpf. *Due to a significant increase in width in female satb1a$^{+/+}$ zebrafish compared to male satb1a$^{+/+}$ zebrafish (A), the widths of male and female satb1a$^{+/+}$ and satb1a$^{-/-}$ zebrafish were not combined for the subsequent analysis. There was no significant difference in width between male satb1a$^{+/+}$ and male satb1a$^{-/-}$ zebrafish but there was a significant reduction in width in female satb1a$^{-/-}$ zebrafish compared to female satb1a$^{+/+}$ zebrafish (B). Error bars represent standard error of the mean. Data was analysed using a two-way ANOVA with Šídák's multiple comparisons (A and B). n; satb1a$^{+/+}$ male = 11, satb1a$^{+/+}$ female = 13, satb1a$^{-/-}$ male = 16 and satb1a$^{-/-}$ female = 8. p = 0.0003 (satb1a$^{+/+}$ male-female), p = 0.2175 (satb1a$^{-/-}$ male-female), p = 0.6512 (male satb1a$^{+/+}$-satb1a$^{-/-}$) , p = 0.0093 (female satb1a$^{+/+}$-satb1a$^{-/-}$). ANOVA, analysis of variance; mpf, months post fertilisation.*

5.3.2.2 *Characterisation of satb1b$^{-/-}$ zebrafish*

5.3.2.2.1 NMD and compensatory upregulation in *satb1b*$^{-/-}$ larvae

Adult *satb1b*$^{+/-}$ zebrafish were in-crossed, DNA was extracted from larval tail clips of offspring (**Section 2.2.1.2**), and *satb1b*$^{+/+}$ and *satb1b*$^{-/-}$ larvae were identified by genotyping (**Sections 2.2.2 and 2.2.3**). Next, RNA was extracted from pooled *satb1b*$^{+/+}$ and *satb1b*$^{-/-}$ larvae at 5dpf, and extracted RNA was reverse transcribed to cDNA for qPCR experiments (**Section 2.8**).

To investigate NMD of *satb1b* mRNA and compensatory upregulation of *satb1a* mRNA in *satb1b*$^{-/-}$ zebrafish, *satb1b*$^{+/+}$ and *satb1b*$^{-/-}$ cDNA was amplified, using *satb1b* FP1 and RP1 (**Section 5.2.7**), and *satb1a* FP1 and RP1 (**Section 5.2.6**), respectively.

NMD of *satb1b* mRNA was absent in *satb1b*$^{-/-}$ larvae at 5dpf (*satb1b*$^{+/+}$ = 1.09, *satb1b*$^{-/-}$ = 1.02, p = 0.9153, **Figure 5.26A**). Also, there was no compensatory upregulation of *satb1a* mRNA in *satb1b*$^{-/-}$ larvae at 5dpf (*satb1b*$^{+/+}$ = 1.09, *satb1b*$^{-/-}$ = 1.28, p = 0.7203, **Figure 5.26B**).

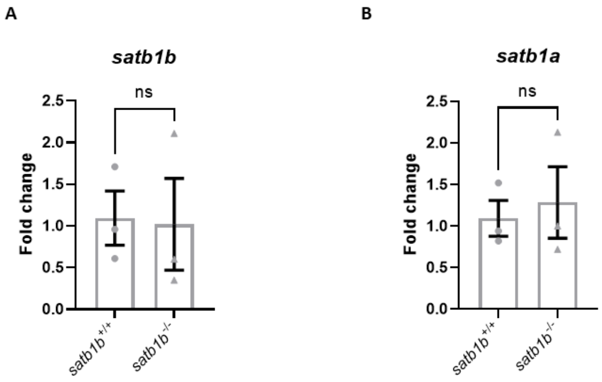

Figure 5.26. Investigation of NMD and compensatory upregulation in satb1b$^{-/-}$ larvae at 5dpf, using the first set of satb1b and satb1a qPCR primers. *NMD of satb1b mRNA was absent in satb1b$^{-/-}$ larvae, at 5dpf (A). Also, there was no compensatory upregulation of satb1a mRNA in satb1b$^{-/-}$ larvae, at 5dpf (B). satb1b FP1 and RP1 (Figure 5.13), and satb1a FP1 and RP1 (Figure 5.12) were utilised. Error bars represent standard error of the mean. Normality was assessed using a Shapiro-Wilk test and datasets were analysed using a two-way unpaired t-test with Welch's correction. n = 3. p = 0.9153 (A). n = 3. p = 0.7203 (B). dpf, days post fertilisation; FP, forward primer; mRNA, messenger RNA; NMD, nonsense-mediated decay; RP, reverse primer.*

To further investigate NMD of *satb1b* mRNA and compensatory upregulation of *satb1a* mRNA in *satb1b*$^{-/-}$ zebrafish, *satb1b*$^{+/+}$ and *satb1b*$^{-/-}$ cDNA was amplified, using *satb1b* FP2 and RP2 (**Section 5.2.7**), and *satb1a* FP2 and RP2 (**Section 5.2.6**). *satb1b*$^{+/+}$ and *satb1b*$^{-/-}$ cDNA was obtained from 2 additional clutches of *satb1b*$^{+/-}$ in-cross larvae, thereby increasing the number of biological replicates of subsequent qPCR reactions from 3 to 5.

Again, NMD of *satb1b* mRNA was absent in *satb1b*$^{-/-}$ larvae at 5dpf (*satb1b*$^{+/+}$ = 1.15, *satb1b*$^{-/-}$ = 0.77, p = 0.3498, **Figure 5.27A**) and there was no compensatory upregulation of *satb1a* mRNA in *satb1b*$^{-/-}$ larvae, at 5dpf (*satb1b*$^{+/+}$ = 1.03, *satb1b*$^{-/-}$ = 0.99, p = 0.8903, **Figure 5.27B**).

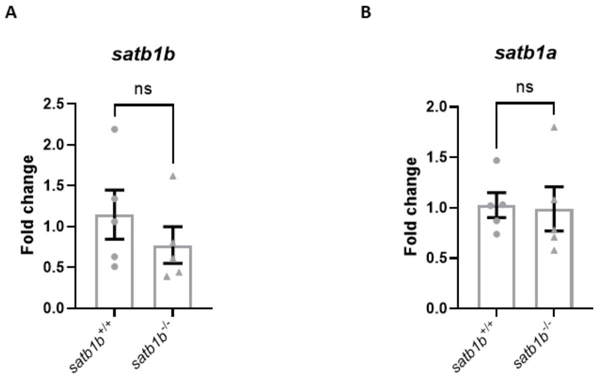

Figure 5.27. Investigation of NMD and compensatory upregulation in satb1b$^{-/-}$ larvae at 5dpf, using the second set of satb1b and satb1a qPCR primers. *NMD of satb1b mRNA was absent in satb1b$^{-/-}$ larvae, at 5dpf (A). Also, there was no compensatory upregulation of satb1a mRNA in satb1b$^{-/-}$ larvae, at 5dpf (B). satb1b FP2 and RP2 (Figure 5.13), and satb1a FP2 and RP2 (Figure 5.12) were utilised. Error bars represent standard error of the mean. Normality was assessed using a Shapiro-Wilk test and datasets were analysed using two-tailed unpaired t-tests with Welch's correction. n = 5. p = 0.3498 (A). n = 5. p = 0.8903 (B). dpf, days post fertilisation; FP, forward primer; mRNA, messenger RNA; NMD, nonsense-mediated decay; RP, reverse primer.*

5.3.2.2.2 mRNA expression of senescence factors in *satb1b*$^{-/-}$ larvae

satb1b$^{-/-}$ larvae were assessed for accelerated ageing by investigating mRNA expression of *cdkn1a*, *il-1β* and *il-6*, using qPCR. *satb1b*$^{+/+}$ and *satb1b*$^{-/-}$ cDNA samples were obtained as previously detailed (**Section 5.3.2.2.1**).

There was no significant difference in *cdkn1a* (*satb1b*$^{+/+}$ = 1.07, *satb1b*$^{-/-}$ = 1.07, p = 0.8889, **Figure 5.28A**), *il-1β* (*satb1b*$^{+/+}$ = 1.56, *satb1b*$^{-/-}$ = 0.54, p = 0.2222, **Figure 5.28B**) and *il-6* expression (*satb1b*$^{+/+}$ = 1.16, *satb1a*$^{-/-}$ = 0.93, p = 0.5202, **Figure 5.28C**) between *satb1b*$^{+/+}$ and *satb1b*$^{-/-}$ larvae at 5dpf, suggesting the absence of accelerated ageing in *satb1b*$^{-/-}$ larvae at 5dpf.

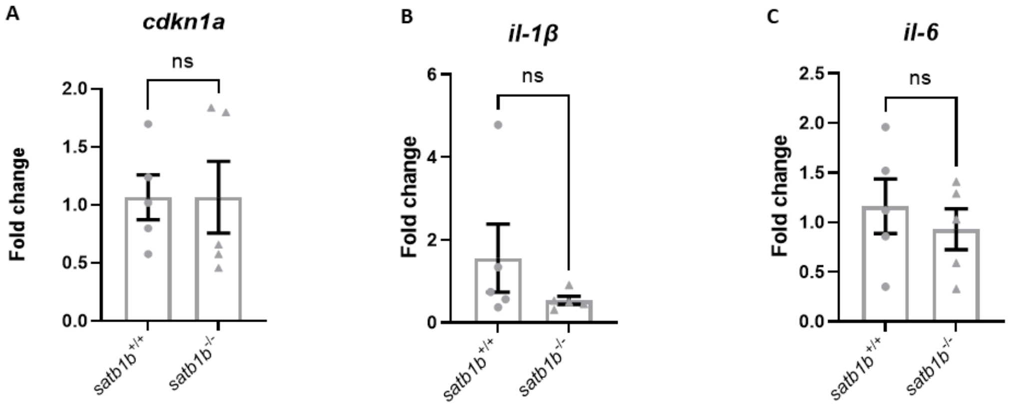

Figure 5.28. Investigation of senescence factors in satb1b$^{-/-}$ larvae, at 5dpf. *There was no significant difference in the expression of cdkn1a (A), il-1β (B) and il-6 (C) mRNA between satb1b$^{+/+}$ and satb1b$^{-/-}$ larvae at 5dpf. Error bars represent standard error of the mean. Normality was assessed using a Shapiro-Wilk test and datasets were analysed using Mann-Whitney tests (A and B) and a two-way unpaired t-test with Welch's correction (C). n = 5. p = 0.8889 (A), p = 0.2222 (B), p = 0.5202 (C). cdkn1a, cdk inhibitor 1a; dpf, days post fertilisation; il-1β, interleukin-1beta; il-6, interleukin-6.*

5.3.2.2.3 Dopaminergic neuron number and MPP$^+$ susceptibility in *satb1b*$^{-/-}$ larvae

Adult *satb1b*$^{+/-}$ zebrafish were in-crossed and offspring were exposed to either 3.0 mM MPP$^+$ or MQ from 1-3 dpf (**Section 2.10.1**). 3dpf *satb1b*$^{+/-}$ in-cross larvae were fixed (**Section 2.1.9**) and dopaminergic neurons were visualised using *th1* WISH (**Section 2.11.2**). DC1, DC2, DC4 and DC5 neurons were counted on both hemispheres at 20.0x magnification while larvae were genotyped in parallel (**Section 2.11.4**).

Although there was no significant difference in MPP$^+$ susceptibility between *satb1b*$^{+/+}$ and *satb1b*$^{-/-}$ larvae (*satb1b*$^{+/+}$ = 43.41% reduction in dopaminergic neuron number, *satb1b*$^{-/-}$ = 34.75% reduction in dopaminergic neuron number, p = 0.9996, **Figure 5.29**), there was a moderate significant decrease in dopaminergic neuron number in *satb1b*$^{-/-}$ larvae compared to *satb1b*$^{+/+}$ larvae (*satb1b*$^{+/+}$ = 25.11, *satb1b*$^{-/-}$ = 21.82, p = 0.0216, **Figure 5.29**).

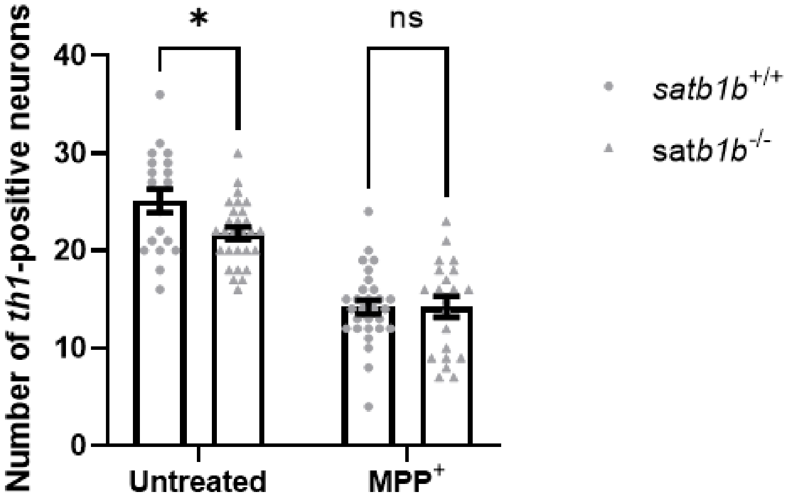

Figure 5.29. Dopaminergic neuron count of 3dpf satb1b$^{+/+}$ and satb1b$^{-/-}$ larvae with and without MPP$^+$ exposure. *Dopaminergic neurons were counted in 3dpf untreated and MPP$^+$-treated satb1b$^{+/+}$ and satb1b$^{-/-}$ larvae. Although there was no significant difference in MPP$^+$ susceptibility between satb1b$^{+/+}$ and satb1b$^{-/-}$ larvae, there was a moderate significant decrease in dopaminergic neuron number in satb1b$^{-/-}$ larvae compared to satb1b$^{+/+}$ larvae (B). Error bars represent standard error of the mean. Data was analysed using a two-way ANOVA with Šídák's multiple comparisons. Larvae were obtained from 3 biological replicates of satb1b$^{+/-}$ in-cross embryos. n; untreated satb1b$^{+/+}$ = 19, untreated satb1b$^{-/-}$ = 29, MPP$^+$-treated satb1b$^{+/+}$ = 29 and MPP$^+$-treated satb1b$^{-/-}$ = 21. p = 0.0216 (Untreated satb1b$^{+/+}$-satb1b$^{-/-}$), p = 0.9996 (MPP$^+$ satb1b$^{+/+}$-satb1b$^{-/-}$). ANOVA, analysis of variance; dpf, days post fertilisation; MPP$^+$, 1-methyl-4-phenylpyridinium; th1, tyrosine hydroxylase 1.*

5.3.2.2.4 Morphology, morbidity and mortality of *satb1b*$^{-/-}$ zebrafish

5.3.2.2.4.1 Larval *satb1b*$^{-/-}$ zebrafish

Adult *satb1b*$^{+/-}$ zebrafish were in-crossed and offspring were monitored for morbidity and mortality till 10dpf. Some larvae developed heart oedema and were immediately culled for DNA extraction (**Sections 2.1.10 and 2.2.1.1**), while healthy larvae were culled for DNA extraction at 10dpf.

Genotyping (**Section 2.2**) revealed that heart oedema was not specific to *satb1b*$^{-/-}$ larvae (**data not shown**). Also, the number of *satb1b*$^{+/+}$, *satb1b*$^{+/-}$ and *satb1b*$^{-/-}$ larvae identified by genotyping was in accordance with Mendelian inheritance (**Table 5.4**), indicating that *satb1b*$^{-/-}$ zebrafish are indistinguishable from *satb1b*$^{+/+}$ siblings, and are equally viable till 10dpf. Likewise, no phenotype was observed in *satb1b*$^{-/-}$ larvae genotyped ahead of RNA extraction at 5dpf (**Sections 5.3.2.2.1 and 5.3.2.2.2**).

Total number of *satb1b*$^{+/-}$ in-cross larvae = 63			
Zebrafish	***satb1b***$^{+/+}$	***satb1b***$^{+/-}$	***satb1b***$^{-/-}$
Mendelian inheritance	1/4	1/2	1/4
Number of larvae predicted by Mendelian inheritance	16	32	16
Number of larvae identified by genotyping	21	32	10

Table 5.4. Viability of satb1b$^{-/-}$ larvae to 10dpf. *Genotyping of 63 satb1b$^{+/-}$ in-cross larvae revealed that 21 were satb1b$^{+/+}$ larvae, 32 were satb1b$^{+/-}$ larvae and 10 were satb1b$^{-/-}$ larvae, which was in accordance with Mendelian inheritance.*

5.3.2.2.4.2 Adult *satb1b*$^{-/-}$ zebrafish

Another clutch of *satb1b*$^{+/-}$ in-cross embryos was obtained and raised to adulthood. Adult *satb1b*$^{-/-}$ zebrafish did not display an overt phenotype (**Figure 5.30**). Also, the number of adult *satb1b*$^{+/+}$ and *satb1b*$^{-/-}$ zebrafish identified by genotyping was in accordance with Mendelian inheritance (**Table 5.5**), indicating equal viability of *satb1b*$^{+/+}$ and *satb1b*$^{-/-}$ zebrafish to adulthood. Survival was unaffected in *satb1b*$^{-/-}$ zebrafish. *satb1b*$^{+/+}$ and *satb1b*$^{-/-}$ zebrafish were observed until 5mpf.

Figure 5.30. Representative images of male and female satb1b$^{+/+}$ and satb1b$^{-/-}$ zebrafish, at 5mpf. *Male satb1b$^{+/+}$ (A), male satb1b$^{-/-}$ (B), female satb1b$^{+/+}$ (C) and female satb1b$^{-/-}$ (D) zebrafish were imaged at 5mpf. satb1b$^{-/-}$ zebrafish did not display an overt phenotype. mpf, months post fertilisation.*

Total number of adult *satb1b*$^{+/-}$ in-cross zebrafish = 102			
Zebrafish	***satb1b***$^{+/+}$	***satb1b***$^{+/-}$	***satb1b***$^{-/-}$
Mendelian inheritance	1/4	1/2	1/4
Number of zebrafish predicted by Mendelian inheritance	26	51	26
Number of zebrafish identified by genotyping	26	52	24

Table 5.5. Viability of satb1b$^{-/-}$ zebrafish to adulthood. *Genotyping of 102 adult satb1b$^{+/-}$ in-cross zebrafish revealed that 26 were satb1b$^{+/+}$ zebrafish, 52 were satb1b$^{+/-}$ zebrafish and 24 were satb1b$^{-/-}$ zebrafish, which was in accordance with Mendelian inheritance. Therefore, satb1b$^{-/-}$ zebrafish are viable to adulthood. Genotyping was completed using the Zebrafish Genotyping Service offered by the Biological Services Aquarium.*

5.3.2.2.4.2.1 Weight of adult satb1b$^{-/-}$ zebrafish

5mpf *satb1b*$^{-/-}$ zebrafish were assessed for emaciation by recording their weights, as previously detailed (**Section 2.14.2.1**).

A sex-related difference in weight was investigated by analysing the weights of male and female *satb1b*$^{+/+}$ and *satb1b*$^{-/-}$ zebrafish for significance. There was no significant difference in weight between male and female *satb1b*$^{+/+}$ zebrafish (male *satb1b*$^{+/+}$ = 0.23g, female *satb1b*$^{+/+}$ = 0.24g, p = 0.9460, **Figure 5.31A**), and between male and female *satb1b*$^{-/-}$ zebrafish (male *satb1b*$^{-/-}$ = 0.21g, female *satb1b*$^{-/-}$ = 0.21g, p = 0.9413, **Figure 5.31A**). Therefore, the weights of male and female zebrafish were combined per genotype and re-analysed for significance. There was no significant difference in weight between *satb1b*$^{+/+}$ and *satb1b*$^{-/-}$ zebrafish (*satb1b*$^{+/+}$ = 0.24g, *satb1b*$^{-/-}$ = 0.21g, p = 0.0548, **Figure 5.31B**).

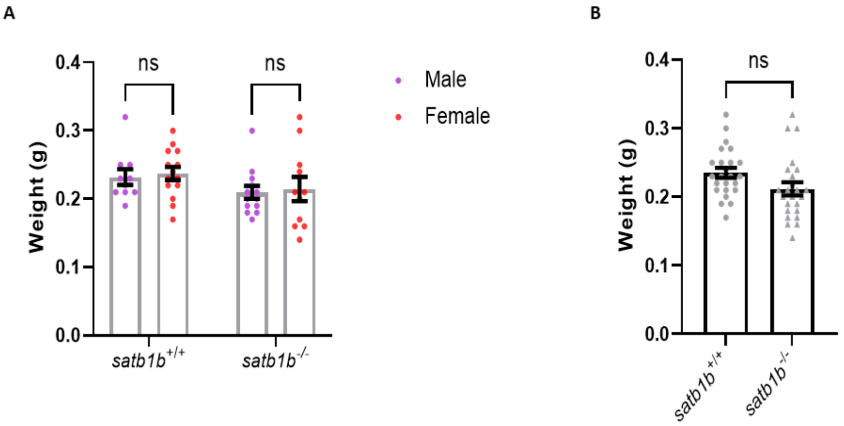

Figure 5.31. Weight of satb1b$^{+/+}$ and satb1b$^{-/-}$ zebrafish, at 5mpf. *There was no significant difference in weight between male and female satb1b$^{+/+}$ zebrafish, and between male and female satb1b$^{-/-}$ zebrafish (A). Therefore, weights of male and female zebrafish were combined per genotype and re-analysed for significance. There was no significant difference in weight between satb1b$^{+/+}$ and satb1b$^{-/-}$ zebrafish (B). Error bars represent standard error of the mean. Data was analysed using a two-way ANOVA with Šídák's multiple comparisons (A) and Welch's t-test (B). n; satb1b$^{+/+}$ male = 10, satb1b$^{+/+}$ female = 14, satb1b$^{-/-}$ male = 13 and satb1b$^{-/-}$ female = 11.p = 0.9460 (satb1b$^{+/+}$ male-female), p = 0.9413 (satb1b$^{-/-}$ male-female), p = 0.0548 (satb1b$^{+/+}$-satb1b$^{-/-}$). ANOVA, analysis of variance; mpf, months post fertilisation.*

5.3.2.2.4.2.2 Size of adult satb1b$^{-/-}$ zebrafish

5mpf *satb1b$^{-/-}$* zebrafish were assessed for growth defects by measuring and recording size, as previously detailed (**Section 2.14.2.2**).

5.3.2.2.4.2.2.1 Length of adult *satb1b$^{-/-}$* zebrafish

A sex-related difference in zebrafish length was investigated by analysing the lengths of male and female *satb1b$^{+/+}$* and *satb1b$^{-/-}$* zebrafish for significance. There was no significant difference in length between male and female *satb1b$^{+/+}$* zebrafish (male *satb1b$^{+/+}$* = 2.04cm, female *satb1b$^{+/+}$* = 2.07cm, p = 0.9053, **Figure 5.32A**), and between male and female *satb1b$^{-/-}$* zebrafish (male *satb1b$^{-/-}$* = 2.10cm, female *satb1b$^{-/-}$* = 2.11cm, p = 0.3857, **Figure 5.32A**). Therefore, the lengths of male and female zebrafish were combined per genotype and re-analysed for significance. There was no significant difference in length between *satb1b$^{+/+}$* and *satb1b$^{-/-}$* zebrafish (*satb1b$^{+/+}$* = 2.06cm, *satb1b$^{-/-}$* = 2.06cm, p = 0.9268, **Figure 5.32B**).

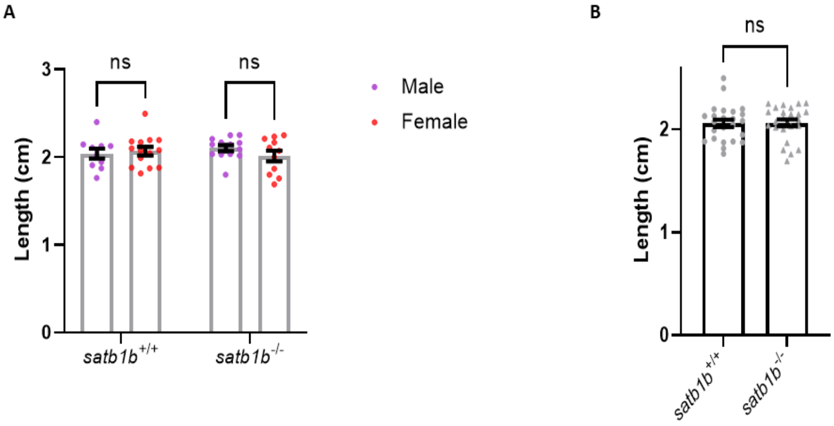

Figure 5.32. Length of satb1b$^{+/+}$ and satb1b$^{-/-}$ zebrafish, at 5mpf. *There was no significant difference in length between male and female satb1b$^{+/+}$ zebrafish, and between male and female satb1b$^{-/-}$ zebrafish (A). Therefore, lengths of male and female zebrafish were combined per genotype and re-analysed for significance. There was no significant difference in length between satb1b$^{+/+}$ and satb1b$^{-/-}$ zebrafish (B). Error bars represent standard error of the mean. Data was analysed using a two-way ANOVA with Šídák's multiple comparisons (A) and Welch's t-test (B). n; satb1b$^{+/+}$ male = 10, satb1b$^{+/+}$ female = 14, satb1b$^{-/-}$ male = 13 and satb1b$^{-/-}$ female = 11. p = 0.9053 (satb1b$^{+/+}$ male-female), p = 0.3857 (satb1b$^{-/-}$ male-female), p = 0.9268 (satb1b$^{+/+}$-satb1b$^{-/-}$). ANOVA, analysis of variance; mpf, months post fertilisation.*

5.3.2.2.4.2.2.2 Width of adult *satb1b*$^{-/-}$ zebrafish

The widths of male and female zebrafish per genotype were also analysed for significance. There was a significant increase in width in female *satb1b*$^{+/+}$ zebrafish compared to male *satb1b*$^{+/+}$ zebrafish (male *satb1b*$^{+/+}$ = 0.53cm, female *satb1b*$^{+/+}$ = 0.61cm, p = 0.0020, **Figure 5.33A**). However, there was no significant difference in width between male and female *satb1b*$^{-/-}$ zebrafish (male *satb1b*$^{-/-}$ = 0.53cm, female *satb1b*$^{-/-}$ = 0.56cm, p = 0.2547, **Figure 5.33A**).

Due to the sex-related difference in widths of *satb1b*$^{+/+}$ zebrafish, this dataset could not be combined per genotype. Instead widths were compared between male *satb1b*$^{+/+}$ and *satb1b*$^{-/-}$ zebrafish, and between female *satb1b*$^{+/+}$ and *satb1b*$^{-/-}$ zebrafish. There was no significant difference in widths between male *satb1b*$^{+/+}$ zebrafish and male *satb1b*$^{-/-}$ zebrafish (male *satb1b*$^{+/+}$ = 0.53cm, male *satb1b*$^{-/-}$ = 0.53cm, p = 0.9988, **Figure 5.33B**). Also, there was no significant difference between the widths of female *satb1b*$^{+/+}$ zebrafish and female *satb1b*$^{-/-}$ zebrafish (female *satb1b*$^{+/+}$ = 0.61cm, female *satb1b*$^{-/-}$ = 0.56cm, p = 0.0945, **Figure 5.33B**).

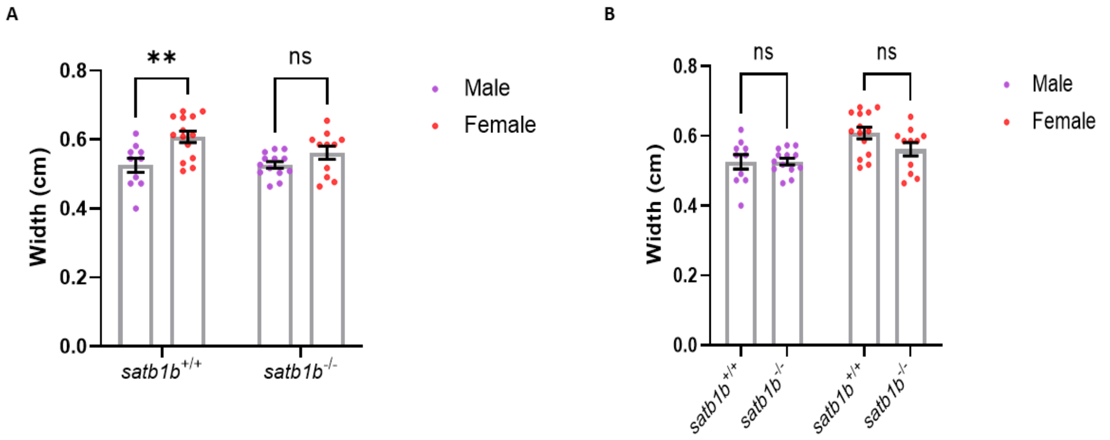

Figure 5.33. Width of satb1b$^{+/+}$ and satb1b$^{-/-}$ zebrafish, at 5mpf. *Due to a significant increase in width in female satb1b$^{+/+}$ zebrafish compared to male satb1b$^{+/+}$ zebrafish (A), the widths of male and female satb1b$^{+/+}$ zebrafish, and of male and female satb1b$^{-/-}$ zebrafish were not combined for subsequent analyses. There was no significant difference in width between male satb1b$^{+/+}$ and male satb1b$^{-/-}$ zebrafish, and between female satb1b$^{+/+}$ and female satb1b$^{-/-}$ zebrafish (B). Error bars represent standard error of the mean. Data was analysed using a two-way ANOVA with Šídák's multiple comparisons (A and B). n; satb1b$^{+/+}$ male = 10, satb1b$^{+/+}$ female = 14, satb1b$^{-/-}$ male = 13 and satb1b$^{-/-}$ female = 11. p = 0.0020 (satb1b$^{+/+}$ male-female), p = 0.2547 (satb1b$^{-/-}$ male-female), p = 0.9988 (male satb1b$^{+/+}$-satb1b$^{-/-}$) , p = 0.0945 (female satb1b$^{+/+}$-satb1b$^{-/-}$). ANOVA, analysis of variance; mpf, months post fertilisation.*

5.3.3 Characterisation of *satb1a*$^{-/-}$;*satb1b*$^{-/-}$ zebrafish

In parallel to characterising both the *satb1a*$^{-/-}$ and *satb1b*$^{-/-}$ zebrafish lines for ageing-related mechanisms and PD-relevant pathological mechanisms, a *satb1a*$^{+/-}$;*satb1b*$^{+/-}$ zebrafish line was generated by crossing an adult *satb1a*$^{+/-}$ zebrafish with an adult *satb1b*$^{+/-}$ zebrafish, and genotyping offspring at adulthood. A Punnett square detailing this cross is provided below (**Figure 5.34**).

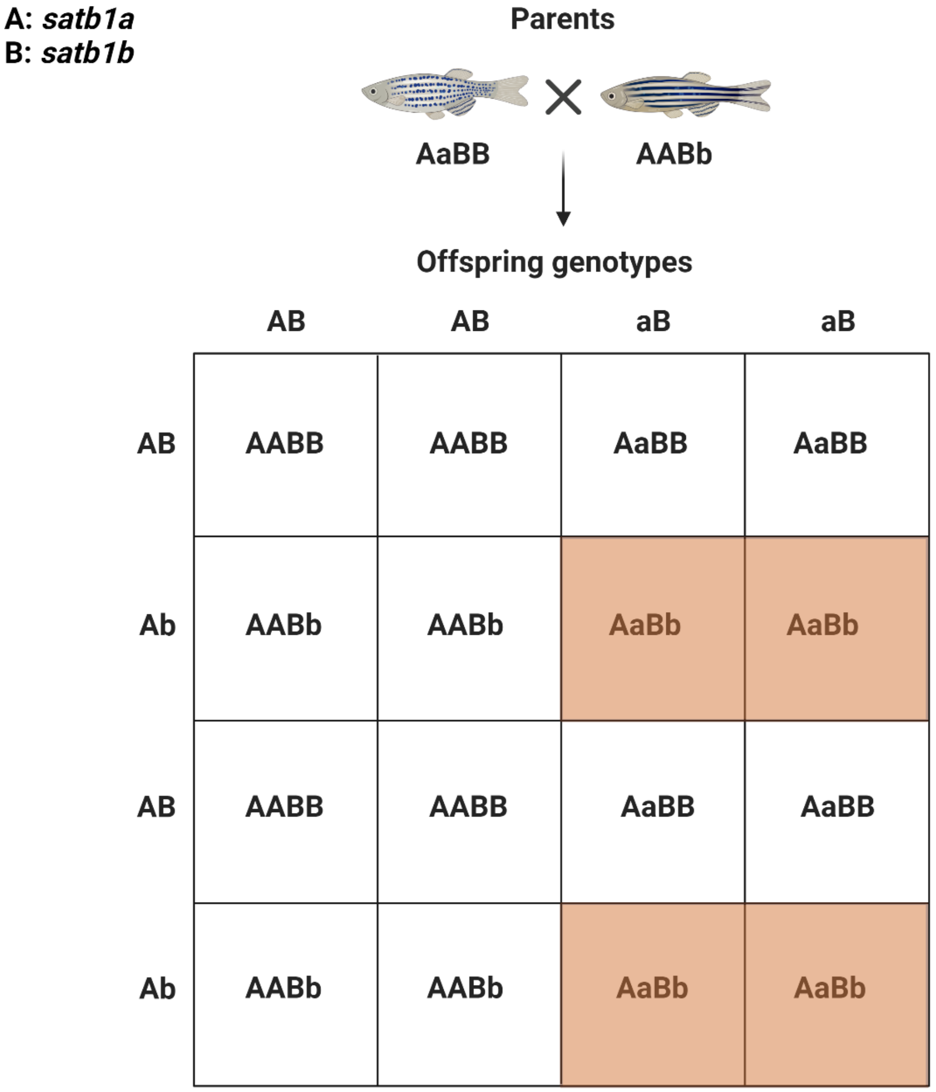

	AB	AB	aB	aB
AB	AABB	AABB	AaBB	AaBB
Ab	AABb	AABb	AaBb	AaBb
AB	AABB	AABB	AaBB	AaBB
Ab	AABb	AABb	AaBb	AaBb

Figure 5.34. A Punnett square of the satb1a$^{+/-}$ x satb1b$^{+/-}$ cross. *A satb1a$^{+/-}$ zebrafish was crossed with a satb1b$^{+/-}$ zebrafish. 1/4 offspring were either satb1a$^{+/+}$;satb1b$^{+/+}$, satb1a$^{+/-}$;satb1b$^{+/+}$, satb1a$^{+/+}$;satb1b$^{+/-}$ or satb1a$^{+/-}$;satb1b$^{+/-}$ (highlighted in orange). satb1a$^{+/-}$;satb1b$^{+/-}$ embryos were raised to adulthood. A, satb1a; B, satb1b. Adapted from "Zebrafish Punnett Square (Layout 4x4)", by BioRender.com (2023). Retrieved from https://app.biorender.com/biorender-templates.*

5.3.3.1 Morphology, morbidity and mortality of *satb1a*$^{-/-}$;*satb1b*$^{-/-}$ zebrafish

5.3.3.1.1 Larval *satb1a*$^{-/-}$;*satb1b*$^{-/-}$ zebrafish

Adult *satb1a*$^{+/-}$;*satb1b*$^{+/-}$ zebrafish were in-crossed and offspring were monitored for morbidity and mortality till 10dpf; a Punnet square detailing this cross is provided below (**Figure 5.35**). Dorsal curvature was observed in some larvae at 10dpf and these larvae together with healthy larvae were culled for DNA extraction at this timepoint (**Sections 2.1.10 and 2.2.1.1**).

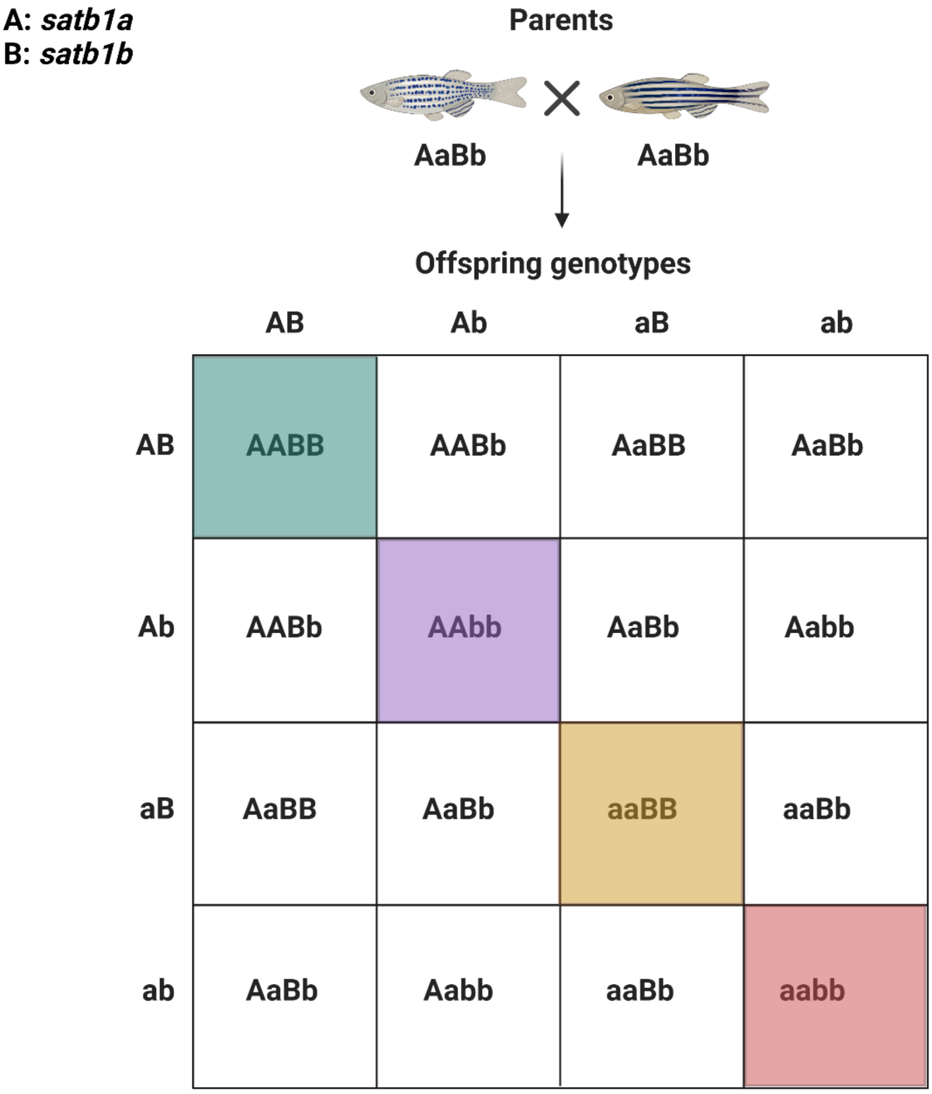

	AB	Ab	aB	ab
AB	AABB	AABb	AaBB	AaBb
Ab	AABb	AAbb	AaBb	Aabb
aB	AaBB	AaBb	aaBB	aaBb
ab	AaBb	Aabb	aaBb	aabb

Figure 5.35. A Punnett square of the satb1a$^{+/-}$;satb1b$^{+/-}$ in-cross. *satb1a$^{+/-}$;satb1b$^{+/-}$ zebrafish were in-crossed and offspring were raised to adulthood. 1/16 offspring were either satb1a$^{+/+}$;satb1b$^{+/+}$ (highlighted in cyan), satb1a$^{+/+}$;satb1b$^{-/-}$ (highlighted in purple), satb1a$^{-/-}$;satb1b$^{+/+}$ (highlighted in yellow) or satb1a$^{-/-}$;satb1b$^{-/-}$ (highlighted in red). A, satb1a; B, satb1b. Adapted from "Zebrafish Punnett Square (Layout 4x4)", by BioRender.com (2023). Retrieved from https://app.biorender.com/biorender-templates.*

Genotyping (**Section 2.2**) revealed that *satb1a*$^{+/+}$;*satb1b*$^{+/+}$, *satb1a*$^{+/+}$;*satb1b*$^{-/-}$, *satb1a*$^{-/-}$;*satb1b*$^{+/+}$ and *satb1a*$^{-/-}$;*satb1b*$^{-/-}$ larvae all displayed dorsal curvature (**data not shown**). Likewise, the number of *satb1a*$^{+/+}$;*satb1b*$^{+/+}$, *satb1a*$^{+/+}$;*satb1b*$^{-/-}$, *satb1a*$^{-/-}$;*satb1b*$^{+/+}$ and *satb1a*$^{-/-}$;*satb1b*$^{-/-}$ larvae identified by genotyping was in accordance with Mendelian inheritance (**Table 5.6**), indicating that *satb1a*$^{-/-}$*;satb1b*$^{-/-}$ larvae are indistinguishable from *satb1a*$^{+/+}$*;satb1b*$^{+/+}$ siblings, and are equally viable till 10dpf.

Total number of *satb1a*$^{+/-}$;*satb1b*$^{+/-}$ in-cross larvae = 70				
Zebrafish	***satb1a*$^{+/+}$*;satb1b*$^{+/+}$**	***satb1a*$^{+/+}$*;satb1b*$^{-/-}$**	***satb1a*$^{-/-}$*;satb1b*$^{+/+}$**	***satb1a*$^{-/-}$*;satb1b*$^{-/-}$**
Mendelian inheritance	1/16	1/16	1/16	1/16
Number of larvae predicted by Mendelian inheritance	4	4	4	4
Number of larvae identified by genotyping	4	4	4	4

Table 5.6. Viability of satb1a*$^{-/-}$*;satb1b*$^{-/-}$ *larvae. *Genotyping of 70 satb1a*$^{+/-}$*;satb1b*$^{+/-}$ *in-cross larvae revealed that 4 were satb1a*$^{+/+}$*;satb1b*$^{+/+}$ *larvae, 4 were satb1a*$^{+/+}$*;satb1b*$^{-/-}$ *larvae, 4 were satb1a*$^{-/-}$*;satb1b*$^{+/+}$ *larvae and 4 were satb1a*$^{-/-}$*;satb1b*$^{-/-}$ *larvae, which was in accordance with Mendelian inheritance.*

5.3.3.1.2 Adult *satb1a*$^{-/-}$;*satb1b*$^{-/-}$ zebrafish

Clutches of *satb1a*$^{+/-}$;*satb1b*$^{+/-}$ in-cross embryos were obtained, raised to adulthood then genotyped. Adult *satb1a*$^{+/+}$;*satb1b*$^{+/+}$, *satb1a*$^{+/+}$;*satb1b*$^{-/-}$, *satb1a*$^{-/-}$;*satb1b*$^{+/+}$ and *satb1a*$^{-/-}$;*satb1b*$^{-/-}$ zebrafish were indistinguishable from one another (**data not shown**).

The number of adult *satb1a*$^{+/+}$;*satb1b*$^{+/+}$ and *satb1a*$^{-/-}$;*satb1b*$^{-/-}$ zebrafish was in accordance with Mendelian inheritance (**Table 5.7**), indicating equal viability of *satb1a*$^{+/+}$;*satb1b*$^{+/+}$ and *satb1a*$^{-/-}$;*satb1b*$^{-/-}$ zebrafish to adulthood. The low number of *satb1a*$^{+/+}$;*satb1b*$^{-/-}$ and *satb1a*$^{-/-}$;*satb1b*$^{+/+}$ zebrafish was attributed to the fact that several adult *satb1a*$^{+/-}$;*satb1b*$^{+/-}$ in-cross zebrafish were not genotyped due to time constraints. This was further supported by the absence of a phenotype in genotyped *satb1a*$^{+/+}$;*satb1b*$^{-/-}$ and *satb1a*$^{-/-}$;*satb1b*$^{+/+}$ zebrafish, and *satb1a*$^{+/-}$;*satb1b*$^{+/-}$ in-cross zebrafish which were not genotyped. Survival was unaffected in *satb1a*$^{+/+}$;*satb1b*$^{-/-}$, *satb1a*$^{-/-}$;*satb1b*$^{+/+}$ and *satb1a*$^{-/-}$;*satb1b*$^{-/-}$ zebrafish.

Total number of adult *satb1a*$^{+/-}$;*satb1b*$^{+/-}$ in-cross zebrafish = 287				
Zebrafish	***satb1a*$^{+/+}$;*satb1b*$^{+/+}$**	***satb1a*$^{+/+}$;*satb1b*$^{-/-}$**	***satb1a*$^{-/-}$;*satb1b*$^{+/+}$**	***satb1a*$^{-/-}$;*satb1b*$^{-/-}$**
Mendelian inheritance	1/16	1/16	1/16	1/16
Number of zebrafish predicted by Mendelian inheritance	18	18	18	18
Number of zebrafish identified by genotyping	13	4	5	10

Table 5.7. Viability of adult satb1a$^{-/-}$;satb1b$^{-/-}$ zebrafish. *Genotyping of 287 adult satb1a$^{+/-}$;satb1b$^{+/-}$ in-cross zebrafish revealed that 13 were satb1a$^{+/+}$;satb1b$^{+/+}$ zebrafish, 4 were satb1a$^{+/+}$;satb1b$^{-/-}$ zebrafish, 5 were satb1a$^{-/-}$;satb1b$^{+/+}$ zebrafish and 10 were satb1a$^{-/-}$;satb1b$^{-/-}$ zebrafish. The number of satb1a$^{+/+}$;satb1b$^{+/+}$ and satb1a$^{-/-}$;satb1b$^{-/-}$ zebrafish was in accordance with Mendelian inheritance. The low number of satb1a$^{+/+}$;satb1b$^{-/-}$ and satb1a$^{-/-}$;satb1b$^{+/+}$ zebrafish was attributed to the fact that several adult satb1a$^{+/-}$;satb1b$^{+/-}$ zebrafish were not genotyped due to time constraints. Some genotyping was completed using the Zebrafish Genotyping Service offered by the Biological Services Aquarium.*

5.4 Discussion

The major aim of this chapter was to investigate ageing-related mechanisms and PD-relevant pathological mechanisms in a zebrafish model for *SATB1* deficiency.

In silico data identified 2 zebrafish orthologues of human *SATB1*, namely *satb1a* and *satb1b*. Due to the exonic similarity between *SATB1* and *satb1a*, and the proteomic similarity between SATB1 and satb1b, both orthologues of human *SATB1* were studied in this PhD. The presence of 2 zebrafish orthologues of human *SATB1* increased the complexity of modelling *SATB1* deficiency using zebrafish, due to the possibility that *satb1a* or *satb1b*, or both *satb1a* and *satb1b* could be the functional orthologue(s) of human *SATB1*.

Both *satb1a* and *satb1b* were expressed as early as 4.66hpf (30% epiboly stage). *satb1a* was stably expressed through to 5dpf while *satb1b* expression increased at 3dpf and remained stably expressed through to 5dpf, suggesting a role for *satb1a* and *satb1b* in zebrafish development.

Overlapping *satb1a* and *satb1b* expression in the tectum, hindbrain and retinal ganglion cell layer (**Figures 5.15 and 5.17**) suggests overlapping function of both paralogues in neuronal development, which is supported by *Satb1*'s function in mice (Balamotis *et al.*, 2011; Close *et al.*, 2012; Denaxa *et al.*, 2012).

The absence of NMD of *satb1a* mRNA and *satb1b* mRNA in *satb1a*$^{-/-}$ and *satb1b*$^{-/-}$ larvae, respectively, suggests that *satb1a* and *satb1b* mRNA escape NMD in the respective stable mutant lines. This would explain the absence of compensatory upregulation of *satb1b* mRNA and *satb1a* mRNA in *satb1a*$^{-/-}$ and *satb1b*$^{-/-}$ larvae, respectively.

A proposed mechanism for escaping NMD is stop codon readthrough; a process whereby a ribosome passes through a stop codon and continues translation to the next stop codon (Dabrowski, Bukowy-Bieryllo and Zietkiewicz, 2015). Another mechanism known to induce escape from NMD is the re-initiation of translation downstream of the premature stop codon. However, this occurs when the premature stop codon is near the start codon (Dyle *et al.*, 2020). Therefore, this cannot apply to the *satb1a*$^{-/-}$ and *satb1b*$^{-/-}$ lines because the premature stop codon is located in exons 7 and 5, respectively. Stop codon readthrough would result in the production of mistranslated satb1a and satb1b, which could possibly disrupt cellular function.

satb1a and *satb1b* WISH probes could have been used to further investigate NMD and compensatory upregulation in *satb1a*$^{-/-}$ and *satb1b*$^{-/-}$ larvae, since neither probe binds to the mutation sites in *satb1a*$^{-/-}$ and *satb1b*$^{-/-}$ zebrafish, respectively. However, WISH is not quantitative like qPCR. A western blot investigating satb1a and satb1b expression in *satb1a*$^{-/-}$ and *satb1b*$^{-/-}$ larvae would help to confirm gene KO. However, there are no commercial satb1a and satb1b antibodies available. Alternatively, RNAseq could be used to investigate NMD and compensatory upregulation in *satb1a*$^{-/-}$ and *satb1b*$^{-/-}$ larvae. Due to its quantitative nature, RNAseq results would either support or disprove the escape of *satb1a* and *satb1b* mRNA from NMD in *satb1a*$^{-/-}$ and *satb1b*$^{-/-}$ larvae, respectively.

cdkn1a, *il-1β* and *il-6* were not upregulated in *satb1a*$^{-/-}$ and *satb1b*$^{-/-}$ larvae at 5dpf, suggesting the absence of accelerated ageing. Understandably, because Riessland *et al.*, (2019) reported that *SATB1* KO specifically induced senescence in dopaminergic neurons and not cortical neurons, it could be argued that *cdkn1a* qPCR using whole larvae might have concealed *cdkn1a* upregulation in dopaminergic neurons. However, since *Satb1* mutant mice display emaciation, an age-associated size reduction and reduced survival, it is unlikely that senescence is restricted solely to dopaminergic neurons. Also, *il-1β* and *il-6* were expected to be upregulated, due to both being SASP factors.

There was no significant difference in the number of dopaminergic neurons and MPP$^+$ susceptibility between *satb1a*$^{+/+}$ and *satb1a*$^{-/-}$ larvae at 3dpf. Although *satb1b*$^{+/+}$ and *satb1b*$^{-/-}$ larvae were equally susceptible to MPP$^+$, there was a moderate reduction in the number of dopaminergic neurons in *satb1b*$^{-/-}$ larvae at 3dpf. However, there was considerable overlap in the number of dopaminergic neurons between *satb1b*$^{+/+}$ and *satb1b*$^{-/-}$ larvae, impacting the robustness of this dataset.

satb1a$^{-/-}$ and *satb1b*$^{-/-}$ larvae were indistinguishable from WT siblings, and equally viable as WT siblings. This together with other larval datasets suggests the absence of ageing-related mechanisms and PD-relevant pathological mechanisms in *satb1a*$^{-/-}$ and *satb1b*$^{-/-}$ larvae.

There was no overt phenotype in adult *satb1a*$^{-/-}$ and *satb1b*$^{-/-}$ zebrafish compared to WT siblings. Likewise, adult *satb1a*$^{-/-}$ and *satb1b*$^{-/-}$ zebrafish were equally viable as WT siblings. Morphological analysis revealed emaciation in adult *satb1a*$^{-/-}$ zebrafish, but not in adult *satb1b*$^{-/-}$ zebrafish. Emaciation was previously reported in *Satb1* mutant mice (Alvarez *et al.*, 2000), suggesting this phenotype in *satb1a*$^{-/-}$ zebrafish might be the result of *satb1a* KO and implicating *satb1a* as a functional orthologue of *SATB1*. However, unlike *Satb1* mutant mice, *satb1a*$^{-/-}$ zebrafish did not display reduced survival, suggesting that emaciation in *satb1a*$^{-/-}$ zebrafish is not the result of *satb1a* KO.

Surprisingly, adult *satb1a*$^{-/-}$ zebrafish, specifically adult male *satb1a*$^{-/-}$ zebrafish were longer than *satb1a*$^{+/+}$ siblings. However, there was no significant difference in length between adult *satb1b*$^{+/+}$ and *satb1b*$^{-/-}$ zebrafish. Strikingly, the widths of adult female *satb1a*$^{-/-}$ zebrafish were smaller than WT siblings, suggesting delayed sexual maturation, which is supported by growth retardation in *Satb1* mutant mice (Alvarez *et al.*, 2000). Alternatively, this could be due to zebrafish husbandry factors beyond the scope of this PhD. Delayed sexual maturation could have been investigated by out-crossing adult female *satb1a*$^{-/-}$ zebrafish and observing breeding efficiency. However, this was not done in this PhD.

The absence of an overt accelerated ageing or PD-relevant phenotype in both the *satb1a*$^{-/-}$ and *satb1b*$^{-/-}$ zebrafish lines, made it more crucial to characterise *satb1a*$^{-/-}$;*satb1b*$^{-/-}$ zebrafish, in the event that both zebrafish *satb1a* and *satb1b* are functional orthologues of human *SATB1.* Both larval and adult *satb1a*$^{+/+}$;*satb1b*$^{+/+}$, *satb1a*$^{-/-}$;*satb1b*$^{+/+}$, *satb1a*$^{+/+}$;*satb1b*$^{-/-}$ and *satb1a*$^{-/-}$;*satb1b*$^{-/-}$ zebrafish were indistinguishable from one another, and equally viable, supporting a previous report by Thyme *et al.*, (2019) who also generated *satb1a*$^{-/-}$ and *satb1b*$^{-/-}$ zebrafish using CRISPR/Cas9 gene editing. Investigation at 6dpf did not reveal any brain structure abnormalities in *satb1a*;*satb1b* double mutant zebrafish while assessment of motor function at 4dpf revealed motor impairment in mutant zebrafish (Thyme *et al.*, 2019). However, it was not specified if larvae utilised for experiments were obtained from biological triplicate. Likewise, it was not specified if mutant zebrafish utilised for behaviour assays were *satb1a* mutant, *satb1b* mutant or *satb1a*;*satb1b* double mutant zebrafish. In addition, the number of larvae per group utilised for behaviour assays was not disclosed.

It is plausible that exon skipping occurs in *satb1a*$^{-/-}$ and *satb1b*$^{-/-}$ pre-mRNA, thereby preventing NMD but also resulting in the production of shorter but functional satb1a and satb1b, potentially explaining the absence of an overt phenotype in *satb1a*$^{-/-}$, *satb1b*$^{-/-}$ and *satb1a*$^{-/-}$;*satb1b*$^{-/-}$ zebrafish.

Due to the absence of an accelerated ageing phenotype in *satb1a*$^{-/-}$, *satb1b*$^{-/-}$ and *satb1a*$^{-/-}$;*satb1b*$^{-/-}$ zebrafish, the effect of the *satb1a* and *satb1b* mutation on Tg(*eno2*:hsa.*SNCA*-ires-EGFP) zebrafish was not investigated.

In conclusion, ageing-related mechanisms and PD-relevant pathological mechanisms were not uncovered in *satb1a*$^{-/-}$, *satb1b*$^{-/-}$ and *satb1a*$^{-/-}$;*satb1b*$^{-/-}$ zebrafish. This was likely due to exon-skipping in *satb1a*$^{-/-}$ and *satb1b*$^{-/-}$ zebrafish to produce functional satb1a and satb1b. However, RNAseq would be needed to confirm escape of *satb1a* mRNA and *satb1b* mRNA from NMD in *satb1a*$^{-/-}$ and *satb1b*$^{-/-}$ lines, respectively.

Chapter 6: General discussion

6.1 Overview

This thesis focused on the generation and assessment of stable zebrafish mutant lines for ageing-related mechanisms and PD-relevant pathological mechanisms. This thesis also focused on the interplay between ageing-related mechanisms and PD-relevant pathological mechanisms. Therefore, zebrafish mutant lines harbouring mutations in ageing-associated genes, namely *klotho*$^{-/-}$, *sirt1*$^{-/-}$, *satb1a*$^{-/-}$, *satb1b*$^{-/-}$ and *satb1a*$^{-/-}$;*satb1b*$^{-/-}$ lines, as well as Tg(*eno2*:hsa.*SNCA*-ires-EGFP) zebrafish which express human WT α-Synuclein were utilised. Although *klotho* mutant, *sirt1* mutant, *satb1a*;*satb1b* double mutant zebrafish and Tg α-Synuclein expressing zebrafish are reported in the literature (A. P. Singh *et al.*, 2019; Kim *et al.*, 2019; Thyme *et al.*, 2019; Ogura *et al.*, 2021; Weston *et al.*, 2021; Lopez *et al.*, 2022), to the best of my knowledge, this thesis represents the first time these zebrafish lines have been utilised for the purpose(s) stated above.

Interestingly, out of 5 stable zebrafish mutant lines generated in this PhD which harbour mutations in ageing-associated genes, only the *klotho*$^{-/-}$ line displayed accelerated ageing, although in adulthood. Potential reasons for the lack of an accelerated ageing phenotype in *sirt1*$^{-/-}$, *satb1a*$^{-/-}$, *satb1b*$^{-/-}$ and *satb1a*$^{-/-}$;*satb1b*$^{-/-}$ lines include transcriptional adaptation and exon skipping (Anderson *et al.*, 2017; El-Brolosy *et al.*, 2019).

El-Brolosy *et al.*, (2019) investigated mutant zebrafish lines such as *heparin-binding EGF-like growth factor a* (*hbegfa*) mutant and *vinculin a* (*vcla*) mutant zebrafish, and showed compensatory upregulation of related genes (termed "adapting genes"), namely *heparin-binding EGF-like growth factor b* (*hbegfb*) and *vinculin b* (*vclb*), respectively. NMD is needed for transcriptional adaptation, as KO of *upstream frameshift 1* (*upf1*), a critical factor in NMD, attenuated NMD and abolished transcriptional adaptation in *hbegfa* mutant and *vcla* mutant zebrafish (El-Brolosy *et al.*, 2019).

Another example of genetic compensation in zebrafish is the *transactive response DNA binding protein* (*tardbp*) mutant. In humans, mutations in *TARDBP* cause amyotrophic lateral sclerosis (ALS). Zebrafish have 2 *TARDBP* orthologues, namely *tardbp* and *tardbp-like* (*tardbpl*). The *tardbp* mutation induced the transcription of a novel *tardbpl* isoform which produced full-length tardbpl protein, which compensated for the *tardbp* mutation. Consequently, *tardbpl* KD in *tardbp* mutant zebrafish induced motor impairment, axonal defects and reduced survival to 10dpf (Hewamaddumal *et al.*, 2013).

Anderson *et al.*, (2017) reported exon skipping in *solute carrier family 27, member 2a* (*slc27a2a*) mutant zebrafish. As a result of exon skipping, the reading frame was maintained and *slc27a2a* mRNA expression was unaffected in *slc27a2a* mutant zebrafish. *slc27a2a* encodes a fatty acid transporter (Anderson *et al.*, 2017).

A potential reason for the lack of PD-relevant pathological mechanisms in the Tg(*eno2*:hsa.*SNCA*-ires-EGFP) line was also suggested to be the lack of α-Synuclein aggregation, in the absence of exogenous human α-Synuclein fibrils, as reported by Matsui and Matsui, (2017). Another example of a Tg zebrafish line which expresses human α-Synuclein is the Tg(*optb*:*gal4*);Tg(*UAS:has.SNCA-p2A-nls-mCherry*) line. However, α-Synuclein expression levels in this line are insufficient to induce neurodegeneration (Van Laar *et al.*, 2020).

Further discussion for each gene-specific chapter of this thesis is detailed below.

6.2 Zebrafish as a model for *KLOTHO* deficiency

The accelerated ageing phenotype of *klotho*$^{-/-}$ zebrafish supports previous zebrafish and mouse publications (Kuro-o *et al.*, 1997; A. P. Singh *et al.*, 2019; Ogura *et al.*, 2021). The reduction of brain NAD^{+} levels in *klotho*$^{-/-}$ zebrafish at 6mpf is potentially interesting as it further validates *klotho*$^{-/-}$ zebrafish as a model for ageing, using a result not published in the literature. It also suggests that the *klotho* mutation would aggravate mitochondrial dysfunction in an effective zebrafish PD model, supporting Klotho's protection against oxidative stress detailed in the literature (Nagai *et al.*, 2003; Yamamoto *et al.*, 2005; Brobey *et al.*, 2015; Sahu *et al.*, 2018).

Due to the presumed inactivation of mechanisms driving accelerated ageing in *klotho*$^{-/-}$ larvae, future experiments will need to utilise adult *klotho*$^{-/-}$ zebrafish. Matsui and Sugie, (2017) published an immunostaining protocol for counting dopaminergic neurons in adult zebrafish brain slices. Perhaps this could be employed for adult *klotho*$^{-/-}$ zebrafish. RNAseq could be used to identify differentially expressed genes in the brains of adult *klotho*$^{-/-}$ zebrafish, which could be compared to differentially expressed genes in the elderly, using publicly available databases. Collaboration with the Hamilton laboratory at the University of York should allow for the assessment of microglial activation in *klotho*$^{-/-}$ zebrafish, as they recently optimised a 4c4 IHC protocol for adult zebrafish brain tissue.

To investigate the effect of the *klotho* mutation on PD-relevant pathological mechanisms, a western blot can be used to compare α-Synuclein expression between brains of adult Tg;*klotho*$^{+/+}$ and Tg;*klotho*$^{-/-}$ zebrafish. Mitochondrial respiratory chain function, mtDNA copy number and expression of pro-inflammatory factors, such as *il-1β* can also be compared between brains of adult Tg;*klotho*$^{+/+}$ and Tg;*klotho*$^{-/-}$ zebrafish. However, given the lack of PD-relevant pathological mechanisms in the Tg(*eno2*:hsa.*SNCA*-ires-EGFP) line, a zebrafish line with α-Synuclein-mediated pathogenesis would need to be generated for future experiments.

6.3 Zebrafish as a model for *SIRT1* deficiency

il-1β and *il-6* expression in *sirt1*$^{-/-}$ larvae, as well as the survival of adult *sirt1*$^{-/-}$ zebrafish suggest the absence of ageing-related mechanisms in *sirt1*$^{-/-}$ zebrafish and do not support the accelerated ageing phenotype of *sirt1* mutant zebrafish reported by Kim *et al.*, (2019). The same gRNA published by Kim *et al.*, (2019) was used to generate the *sirt1*$^{-/-}$ zebrafish line. Also, both the published *sirt1* mutant and our *sirt1*$^{-/-}$ line were generated using AB zebrafish. However, the *sirt1* allele reported by Kim *et al.*, (2019) harboured a 4bp insertion in exon 1 while the Bandmann *sirt1* allele harbours a 10bp deletion in exon 1. The source(s) of discrepancy between results detailed in this thesis and reported by Kim *et al.*, (2019) remain unknown.

Due to the initial negative results obtained using the *sirt1*$^{-/-}$ line, further characterisation for PD-relevant pathological mechanisms, namely dopaminergic neuron loss, MPP^{+} susceptibility and microglial activation was not conducted.

To validate results obtained using the *sirt1*$^{-/-}$ line, qPCR experiments need to be repeated in triplicate. If *il-1β* and *il-6* are found to not be upregulated in *sirt1*$^{-/-}$ zebrafish, RNAseq will need to be employed to investigate transcriptional adaptation. For example, other sirtuin genes, such as *sirt2-7* could be investigated for compensatory upregulation. Should transcriptional adaptation be the reason behind the absence of ageing-related mechanisms in *sirt1*$^{-/-}$ zebrafish , CRISPR/Cas9 gene editing will need to be employed to generate other *sirt1* mutant zebrafish lines, which will need to be screened for transcriptional adaptation. Once a loss-of-function *sirt1* mutant line is obtained, a *sirt1* activity assay kit, for example, Abcam's fluorometric kit (ab156065), would be used to confirm pathogenic effect. A morphology, morbidity and mortality study will also need to be completed to identify the onset of an accelerated ageing phenotype.

Next, experiments completed by Kim *et al.*, (2019), namely *il-1β* and *il-6* qPCRs, investigation of oxidative stress and cell death using dichlorofluorescein (DCF) and TUNEL staining, respectively, will need to be repeated at a timepoint where *sirt1* mutant zebrafish display accelerated ageing. Dopaminergic neuron loss and microglial activation will also need to be investigated. Experiments can also be completed at an earlier timepoint to investigate if the *sirt1* mutation induces oxidative stress and cell death before the onset of an accelerated ageing phenotype. Next, this *sirt1* mutant line will need to be crossed to a zebrafish line with α-Synuclein-mediated pathogenesis to investigate the effect of the *sirt1* mutation on α-Synuclein-mediated motor impairment, cell death, dopaminergic neuron loss, MPP^{+} susceptibility and microglial activation.

6.4 Zebrafish as a model for *SATB1* deficiency

Despite assessment of the *satb1a*$^{-/-}$, *satb1b*$^{-/-}$ and *satb1a*$^{-/-}$;*satb1b*$^{-/-}$ zebrafish lines, the identity of the functional zebrafish orthologue(s) of human *SATB1* remains unknown but more importantly, PD-relevant pathological mechanisms remain largely unassessed in a zebrafish model for *SATB1* deficiency.

Exon skipping could be investigated by comparing satb1a expression between *satb1a*$^{+/+}$ and *satb1a*$^{-/-}$ zebrafish, and satb1b expression between *satb1b*$^{+/+}$ and *satb1b*$^{-/-}$ zebrafish, using a western blot, if antibodies become available. If exon skipping were present, the MWs of mutant satb1a and satb1b might be considerably lower compared to WT satb1a and satb1b. Alternatively, mass spectrometry could be used to investigate exon skipping by comparing satb1a peptide sequences between *satb1a*$^{+/+}$ and *satb1a*$^{-/-}$ zebrafish, and satb1b peptide sequences between *satb1b*$^{+/+}$ and *satb1b*$^{-/-}$ zebrafish.

If exon skipping occurs in *satb1a*$^{-/-}$ and *satb1b*$^{-/-}$ zebrafish, new *satb1a* and *satb1b* mutant lines will need to be generated, using CRISPR/Cas9 gene editing. To ensure loss-of-function, multiple gRNAs targeting multiple exons of each target gene would be micro-injected into one-cell stage embryos to ensure a large KO of genetic material, as reported in the literature for the generation of *smarca2* mutant, *rnf185* mutant and *rnf215* mutant zebrafish lines (Kim and Zhang, 2020).

These new mutant lines will need to be assessed for NMD to investigate the effect of the *satb1a* and *satb1b* mutation on mRNA expression. Expression of related genes, such as *satb2* will also need to be investigated, to assess for transcriptional adaptation. Characterisation will be crucial to discover the functional zebrafish orthologue(s) of human *SATB1*, as this will inform whether single or double mutant zebrafish are required to investigate PD-relevant pathological mechanisms. Collaboration with the Bellantuono laboratory at the University of Sheffield would be beneficial given their recent publication where they validated a Tg p21 zebrafish line as a reporter of senescence. The number of p21:GFP-positive cells increased following ionising radiation, mirroring *cdkn1a* expression observed following WISH using WT larvae. Likewise, the number of p21:GFP-positive cells increased with natural ageing and was attenuated by treatment with senolytics (Morsli *et al.*, 2023). This Tg line should serve as a better method to investigate the functionally relevant zebrafish orthologue(s) of human *SATB1* compared to qPCR, as GFP expression should provide spatial information concerning p21 expression in mutant zebrafish. Given *SATB1*'s role in both ageing and PD, a zebrafish model for *SATB1* deficiency could be used to support results obtained from other zebrafish models used to study the interplay between ageing-related mechanisms and PD-relevant pathological mechanisms.

6.5 Conclusion

In conclusion, questions pertaining to the interplay between ageing-related mechanisms and PD-relevant pathological mechanisms remain unanswered. Does age-related mitochondrial dysfunction enhance α-Synuclein-mediated mitochondrial dysfunction? Does age-related neuroinflammation enhance α-Synuclein-mediated neuroinflammation? If yes, how?

This thesis highlights the limitations of zebrafish as a model for ageing but further highlights the effectiveness of zebrafish as a model for studying PD-relevant pathological mechanisms, thanks to the genetic tractability of zebrafish, and the availability of drug treatment protocols, neuropathological and neurobehavioral tools, albeit for larvae.

References

Aasly, J. O. *et al.* (2010) 'Novel pathogenic LRRK2 p.Asn1437His substitution in familial Parkinson's disease', *Movement Disorders*, 25(13), pp. 2156–2163. doi: 10.1002/MDS.23265.

Abeliovich, A. *et al.* (2000) 'Mice Lacking α-Synuclein Display Functional Deficits in the Nigrostriatal Dopamine System', *Neuron*, 25(1), pp. 239–252. doi: 10.1016/S0896-6273(00)80886-7.

Ahmad, M., Wolberg, A. and Kahwaji, C. I. (2022) 'Biochemistry, Electron Transport Chain', *StatPearls*. Available at: https://www.ncbi.nlm.nih.gov/books/NBK526105/ (Accessed: 7 January 2023).

Ahn, B. H. *et al.* (2008) 'A role for the mitochondrial deacetylase Sirt3 in regulating energy homeostasis', *Proceedings of the National Academy of Sciences of the United States of America*, 105(38), p. 14447. doi: 10.1073/PNAS.0803790105.

Alberts, B. *et al.* (2002) 'Chromosomal DNA and Its Packaging in the Chromatin Fiber'. Available at: https://www.ncbi.nlm.nih.gov/books/NBK26834/ (Accessed: 13 January 2023).

Alvarez, J. D. *et al.* (2000) 'The MAR-binding protein SATB1 orchestrates temporal and spatial expression of multiple genes during T-cell development', *Genes & Development*, 14(5), pp. 521–535. doi: 10.1101/GAD.14.5.521.

Anderson, J. L. *et al.* (2017) 'mRNA processing in mutant zebrafish lines generated by chemical and CRISPR-mediated mutagenesis produces unexpected transcripts that escape nonsense-mediated decay', *PLoS Genetics*, 13(11). doi: 10.1371/JOURNAL.PGEN.1007105.

Andrew D. Napper, *,† *et al.* (2005) 'Discovery of Indoles as Potent and Selective Inhibitors of the Deacetylase SIRT1', *Journal of Medicinal Chemistry*, 48(25), pp. 8045–8054. doi: 10.1021/JM050522V.

Arking, D. E. *et al.* (2002) 'Association of human aging with a functional variant of klotho', *Proceedings of the National Academy of Sciences of the United States of America*, 99(2), p. 856. doi: 10.1073/PNAS.022484299.

Arking, D. E. *et al.* (2005) 'Association between a functional variant of the KLOTHO gene and high-density lipoprotein cholesterol, blood pressure, stroke, and longevity', *Circulation research*, 96(4), pp. 412–418. doi: 10.1161/01.RES.0000157171.04054.30.

Arroyo-Olarte, R. D., Bravo Rodríguez, R. and Morales-Ríos, E. (2021) 'Genome Editing in Bacteria: CRISPR-Cas and Beyond', *Microorganisms*, 9(4). doi: 10.3390/MICROORGANISMS9040844.

Ashrafi, G. *et al.* (2014) ‘Mitophagy of damaged mitochondria occurs locally in distal neuronal axons and requires PINK1 and Parkin’, *The Journal of Cell Biology*, 206(5), p. 655. doi: 10.1083/JCB.201401070.

Bae, Y. K. *et al.* (2009) ‘Anatomy of zebrafish cerebellum and screen for mutations affecting its development’, *Developmental Biology*, 330(2), pp. 406–426. doi: 10.1016/J.YDBIO.2009.04.013.

Bai, Q. *et al.* (2007) ‘Generation of a transgenic zebrafish model of Tauopathy using a novel promoter element derived from the zebrafish eno2 gene’, *Nucleic Acids Research*, 35(19), p. 6501. doi: 10.1093/NAR/GKM608.

Balamotis, M. A. *et al.* (2011) ‘Satb1 Ablation Alters Temporal Expression of Immediate Early Genes and Reduces Dendritic Spine Density during Postnatal Brain Development’, *Molecular and Cellular Biology*, 32(2), pp. 333–347. doi: 10.1128/MCB.05917-11.

Banati, R. B., Myers, R. and Kreutzberg, G. W. (1997) ‘PK ('peripheral benzodiazepine’)--binding sites in the CNS indicate early and discrete brain lesions: microautoradiographic detection of [3H]PK11195 binding to activated microglia’, *Journal of neurocytology*, 26(2), pp. 77–82. doi: 10.1023/A:1018567510105.

Banks, A. S. *et al.* (2008) ‘SirT1 gain-of-function increases energy efficiency and prevents diabetes in mice’, *Cell metabolism*, 8(4), p. 333. doi: 10.1016/J.CMET.2008.08.014.

Barba, L. *et al.* (2022) ‘Alpha and Beta Synucleins: From Pathophysiology to Clinical Application as Biomarkers’, *Movement Disorders*, 37(4), pp. 669–683. doi: 10.1002/mds.28941.

Barrett, J. C. *et al.* (2008) ‘Genome-wide association defines more than thirty distinct susceptibility loci for Crohn’s disease’, *Nature genetics*, 40(8), p. 955. doi: 10.1038/NG.175.

Barthel, T. K. *et al.* (2007) ‘1,25-Dihydroxyvitamin D3/VDR-mediated induction of FGF23 as well as transcriptional control of other bone anabolic and catabolic genes that orchestrate the regulation of phosphate and calcium mineral metabolism’, *The Journal of steroid biochemistry and molecular biology*, 103(3–5), pp. 381–388. doi: 10.1016/J.JSBMB.2006.12.054.

Baumgartner, M. R. *et al.* (2001) ‘The molecular basis of human 3-methylcrotonyl-CoA carboxylase deficiency’, *Journal of Clinical Investigation*, 107(4), p. 495. doi: 10.1172/JCI11948.

Belloy, M. E. *et al.* (2020) ‘Association of Klotho-VS Heterozygosity With Risk of Alzheimer Disease in Individuals Who Carry APOE4’, *JAMA Neurology*, 77(7), pp. 849–862. doi:

10.1001/JAMANEUROL.2020.0414.

Ben-Dov, I. Z. *et al.* (2007) 'The parathyroid is a target organ for FGF23 in rats', *The Journal of clinical investigation*, 117(12), pp. 4003–4008. doi: 10.1172/JCI32409.

Béraud, D. *et al.* (2011) 'α-Synuclein Alters Toll-Like Receptor Expression', *Frontiers in Neuroscience*, 5. doi: 10.3389/fnins.2011.00080.

Berdichevsky, A. *et al.* (2006) 'C. elegans SIR-2.1 interacts with 14-3-3 proteins to activate DAF-16 and extend life span', *Cell*, 125(6), pp. 1165–1177. doi: 10.1016/J.CELL.2006.04.036.

Bergo, M. O. *et al.* (2002) 'Zmpste24 deficiency in mice causes spontaneous bone fractures, muscle weakness, and a prelamin A processing defect'. Available at: www.pnas.orgcgidoi10.1073pnas.192460799 (Accessed: 3 March 2023).

Betarbet, R. *et al.* (2000) 'Chronic systemic pesticide exposure reproduces features of Parkinson's disease', *Nature Neuroscience*, 3(12), pp. 1301–1306. doi: 10.1038/81834.

Beutler, E. *et al.* (2017) 'Gaucher Disease : New Molecular Approaches to Diagnosis and Treatment Published by : American Association for the Advancement of Science Gaucher Disease : New Molecular Approaches to Diagnosis and Treatment', 256(5058), pp. 794–799.

Bezard, E. *et al.* (2001) 'Relationship between the Appearance of Symptoms and the Level of Nigrostriatal Degeneration in a Progressive 1-Methyl-4-Phenyl-1,2,3,6-Tetrahydropyridine-Lesioned Macaque Model of Parkinson's Disease', *The Journal of Neuroscience*, 21(17), p. 6853. doi: 10.1523/JNEUROSCI.21-17-06853.2001.

Billingsley, K. J. *et al.* (2018) 'Genetic risk factors in Parkinson's disease', *Cell and tissue research*, 373(1), p. 9. doi: 10.1007/S00441-018-2817-Y.

Bindoff, L. A. *et al.* (1991) 'Respiratory chain abnormalities in skeletal muscle from patients with Parkinson's disease', *Journal of the Neurological Sciences*, 104(2), pp. 203–208. doi: 10.1016/0022-510X(91)90311-T.

Bisi, N. *et al.* (2021) 'α-Synuclein: An All-Inclusive Trip Around its Structure, Influencing Factors and Applied Techniques', *Frontiers in Chemistry*, 9(July), pp. 1–28. doi: 10.3389/fchem.2021.666585.

Blander, G. and Guarente, L. (2004) 'The Sir2 Family of Protein Deacetylases', *https://doi.org/10.1146/annurev.biochem.73.011303.073651*, 73, pp. 417–435. doi:

10.1146/ANNUREV.BIOCHEM.73.011303.073651.

Blasiak, J. *et al.* (2013) ‘Mitochondrial and Nuclear DNA Damage and Repair in Age-Related Macular Degeneration’, *International Journal of Molecular Sciences*, 14(2), p. 2996. doi: 10.3390/IJMS14022996.

Bloch, L. *et al.* (2009) ‘Klotho is a substrate for alpha-, beta- and gamma-secretase’, *FEBS letters*, 583(19), pp. 3221–3224. doi: 10.1016/J.FEBSLET.2009.09.009.

Boecker, C. A. *et al.* (2021) ‘Increased LRRK2 kinase activity alters neuronal autophagy by disrupting the axonal transport of autophagosomes’, *Current Biology*, 31(10), pp. 2140-2154.e6. doi: 10.1016/J.CUB.2021.02.061.

Boengler, K. *et al.* (2017) ‘Mitochondria and ageing: role in heart, skeletal muscle and adipose tissue’, *Journal of Cachexia, Sarcopenia and Muscle*, 8(3), p. 349. doi: 10.1002/JCSM.12178.

Bonifati, V. *et al.* (2003) ‘Mutations in the DJ-1 gene associated with autosomal recessive early-onset parkinsonism’, *Science*, 299(5604), pp. 256–259. doi: 10.1126/SCIENCE.1077209/SUPPL_FILE/1077209S.PDF.

Bordone, L. *et al.* (2007) ‘SIRT1 transgenic mice show phenotypes resembling calorie restriction’, *Aging Cell*, 6(6), pp. 759–767. doi: 10.1111/J.1474-9726.2007.00335.X.

Borra, M. T., Smith, B. C. and Denu, J. M. (2005) ‘Mechanism of Human SIRT1 Activation by Resveratrol’, *Journal of Biological Chemistry*, 280(17), pp. 17187–17195. doi: 10.1074/JBC.M501250200.

Bouhouche, A. *et al.* (2017) ‘LRRK2 G2019S Mutation: Prevalence and Clinical Features in Moroccans with Parkinson’s Disease’, *Parkinson’s Disease*, 2017. doi: 10.1155/2017/2412486.

Bowman, G. D. and Poirier, M. G. (2015) ‘Post-translational modifications of histones that influence nucleosome dynamics’, *Chemical Reviews*, 115(6), pp. 2274–2295. doi: 10.1021/CR500350X/ASSET/IMAGES/LARGE/CR-2014-00350X_0015.JPEG.

Braak, H. *et al.* (2003) ‘Staging of brain pathology related to sporadic Parkinson’s disease’, *Neurobiology of Aging*, 24(2), pp. 197–211. doi: 10.1016/S0197-4580(02)00065-9.

Braidy, N. *et al.* (2011) ‘Age Related Changes in NAD+ Metabolism Oxidative Stress andSirt1 Activity in Wistar Rats’, *PLoS ONE*, 6(4), p. 19194. doi: 10.1371/JOURNAL.PONE.0019194.

Brichta, L. *et al.* (2015) ‘Identification of Neurodegenerative Factors Using Translatome-Regulatory Network Analysis’, *Nature neuroscience*, 18(9), p. 1325. doi: 10.1038/NN.4070.

Brobey, R. K. *et al.* (2015) ‘Klotho protects dopaminergic neuron oxidant-induced degeneration by modulating ASK1 and p38 MAPK signaling pathways’, *PLoS ONE*, 10(10). doi: 10.1371/journal.pone.0139914.

Brooks, A. I. *et al.* (1999) ‘Paraquat elicited neurobehavioral syndrome caused by dopaminergic neuron loss’, *Brain Research*, 823(1–2), pp. 1–10. doi: 10.1016/S0006-8993(98)01192-5.

Brown, T. A. (2002) ‘Mutation, Repair and Recombination’. Available at: https://www.ncbi.nlm.nih.gov/books/NBK21114/ (Accessed: 12 January 2023).

Brownstein, C. A. *et al.* (2008) ‘A translocation causing increased α-Klotho level results in hypophosphatemic rickets and hyperparathyroidism’, *Proceedings of the National Academy of Sciences of the United States of America*, 105(9), p. 3455. doi: 10.1073/PNAS.0712361105.

Brunet, A. *et al.* (2004) ‘Stress-dependent regulation of FOXO transcription factors by the SIRT1 deacetylase’, *Science (New York, N.Y.)*, 303(5666), pp. 2011–2015. doi: 10.1126/SCIENCE.1094637.

Buchman, A. S. *et al.* (2012) ‘Nigral Pathology and Parkinsonian Signs in Elders without Parkinson’s Disease’, *Annals of Neurology*, 71(2), p. 258. doi: 10.1002/ANA.22588.

Burnett, C. *et al.* (2011) ‘Absence of effects of Sir2 over-expression on lifespan in C. elegans and Drosophila’, *Nature*, 477(7365), p. 482. doi: 10.1038/NATURE10296.

Burns, R. S. *et al.* (1983) ‘A primate model of parkinsonism: selective destruction of dopaminergic neurons in the pars compacta of the substantia nigra by N-methyl-4-phenyl-1,2,3,6-tetrahydropyridine’, *Proceedings of the National Academy of Sciences of the United States of America*, 80(14), pp. 4546–4550. doi: 10.1073/PNAS.80.14.4546.

Cai, S., Lee, C. C. and Kohwi-Shigematsu, T. (2006) ‘SATB1 packages densely looped, transcriptionally active chromatin for coordinated expression of cytokine genes’, *Nature Genetics 2006 38:11*, 38(11), pp. 1278–1288. doi: 10.1038/ng1913.

Van Campenhout, C. *et al.* (2019) ‘Guidelines for optimized gene knockout using CRISPR/Cas9’, *BioTechniques*, 66(6), pp. 295–302. doi: 10.2144/BTN-2018-0187/ASSET/IMAGES/LARGE/FIGURE4B.JPEG.

Campigli, D. *et al.* (2013) ‘Article PARP1 Represses PAP and Inhibits Polyadenylation during Heat Shock’. doi: 10.1016/j.molcel.2012.11.005.

Cao, K. *et al.* (2018) ‘Reduced expression of SIRT1 and SOD-1 and the correlation between these levels in various regions of the brains of patients with Alzheimer’s disease’, *Journal of Clinical Pathology*, 71(12), pp. 1090–1099. doi: 10.1136/JCLINPATH-2018-205320.

Carrington, B. *et al.* (2015) ‘CRISPR-STAT: an easy and reliable PCR-based method to evaluate target-specific sgRNA activity’, *Nucleic Acids Research*, 43(22), p. e157. doi: 10.1093/NAR/GKV802.

Cerutti, R. *et al.* (2014) ‘NAD+-Dependent Activation of Sirt1 Corrects the Phenotype in a Mouse Model of Mitochondrial Disease’, *Cell Metabolism*, 19(6), pp. 1042–1049. doi: 10.1016/J.CMET.2014.04.001.

Chaib, S., Tchkonia, T. and Kirkland, J. L. (2022) ‘Cellular senescence and senolytics: the path to the clinic’, *Nature medicine*, 28(8), p. 1556. doi: 10.1038/S41591-022-01923-Y.

Chang, D. *et al.* (2017) ‘A meta-analysis of genome-wide association studies identifies 17 new Parkinson’s disease risk loci’. doi: 10.1038/ng.3955.

Chang, S. *et al.* (2004) ‘Essential role of limiting telomeres in the pathogenesis of Werner syndrome’, *Nature Genetics 2004 36:8*, 36(8), pp. 877–882. doi: 10.1038/ng1389.

Chartier-Harlin, M. C. *et al.* (2004) ‘α-synuclein locus duplication as a cause of familial Parkinson’s disease’, *The Lancet*, 364(9440), pp. 1167–1169. doi: 10.1016/S0140-6736(04)17103-1.

Château, M. T. *et al.* (2010) ‘Klotho interferes with a novel FGF-signalling pathway and insulin/Igf-like signalling to improve longevity and stress resistance in *Caenorhabditis elegans*’, *Aging*, 2(9), pp. 567–581. doi: 10.18632/AGING.100195.

Chatterjee, N. and Walker, G. C. (2017) ‘Mechanisms of DNA damage, repair and mutagenesis’, *Environmental and molecular mutagenesis*, 58(5), p. 235. doi: 10.1002/EM.22087.

Chaudhuri, K. R., Yates, L. and Martinez-Martin, P. (2005) ‘The non-motor symptom complex of Parkinson’s disease: A comprehensive assessment is essential’, *Current Neurology and Neuroscience Reports*, 5(4), pp. 275–283. doi: 10.1007/s11910-005-0072-6.

Chen, C. Di *et al.* (2007) ‘Insulin stimulates the cleavage and release of the extracellular domain of Klotho by ADAM10 and ADAM17’, *Proceedings of the National Academy of Sciences of the United States of America*, 104(50), p. 19796. doi: 10.1073/PNAS.0709805104.

Chen, G. *et al.* (2018) ‘α-Klotho is a non-enzymatic molecular scaffold for FGF23 hormone signalling’, *Nature*, 553(7689), pp. 461–466. doi: 10.1038/NATURE25451.

Chen, J. H., Hales, C. N. and Ozanne, S. E. (2007) ‘DNA damage, cellular senescence and organismal ageing: causal or correlative?’, *Nucleic Acids Research*, 35(22), p. 7417. doi: 10.1093/NAR/GKM681.

Chen, W., Rezaizadehnajafi, L. and Wink, M. (2013) ‘Influence of resveratrol on oxidative stress resistance and life span in Caenorhabditis elegans’, *Journal of Pharmacy and Pharmacology*, 65(5), pp. 682–688. doi: 10.1111/JPHP.12023.

Chen, Xiongjin *et al.* (2019) ‘Rs2015 Polymorphism in miRNA Target Site of Sirtuin2 Gene Is Associated with the Risk of Parkinson’s Disease in Chinese Han Population’, *BioMed Research International*, 2019. doi: 10.1155/2019/1498034.

Cheng, H. C., Ulane, C. M. and Burke, R. E. (2010) ‘Clinical Progression in Parkinson’s Disease and the Neurobiology of Axons’, *Annals of neurology*, 67(6), p. 715. doi: 10.1002/ANA.21995.

Cheng, H. L. *et al.* (2003) ‘Developmental defects and p53 hyperacetylation in Sir2 homolog (SIRT1)-deficient mice’, *Proceedings of the National Academy of Sciences of the United States of America*, 100(19), p. 10794. doi: 10.1073/PNAS.1934713100.

Chiba, K., Trevor, A. and Castagnoli, N. (1984) ‘Metabolism of the neurotoxic tertiary amine, MPTP, by brain monoamine oxidase’, *Biochemical and Biophysical Research Communications*, 120(2), pp. 574–578. doi: 10.1016/0006-291X(84)91293-2.

Childs, B. G. *et al.* (2017) ‘Senescent cells: an emerging target for diseases of ageing’, *Nature reviews. Drug discovery*, 16(10), pp. 718–735. doi: 10.1038/NRD.2017.116.

Choi, T. Y. *et al.* (2021) ‘Zebrafish as an animal model for biomedical research’, *Experimental & Molecular Medicine 2021 53:3*, 53(3), pp. 310–317. doi: 10.1038/s12276-021-00571-5.

Christensen, C. *et al.* (2020) ‘Multi-parameter Behavioral Phenotyping of the MPP+ Model of Parkinson’s Disease in Zebrafish’, *Frontiers in Behavioral Neuroscience*, 14. doi: 10.3389/FNBEH.2020.623924.

Chu, Y. and Kordower, J. H. (2007) ‘Age-associated increases of α-synuclein in monkeys and humans are associated with nigrostriatal dopamine depletion: Is this the target for Parkinson’s disease?’, *Neurobiology of Disease*, 25(1), pp. 134–149. doi: 10.1016/J.NBD.2006.08.021.

Church, F. C. (2021) 'Treatment Options for Motor and Non-Motor Symptoms of Parkinson's Disease', *Biomolecules*, 11(4). doi: 10.3390/BIOM11040612.

Clarke, C. E. (2007) 'Parkinson's disease', *BMJ : British Medical Journal*, 335(7617), p. 441. doi: 10.1136/BMJ.39289.437454.AD.

Close, J. *et al.* (2012) 'Satb1 Is an Activity-Modulated Transcription Factor Required for the Terminal Differentiation and Connectivity of Medial Ganglionic Eminence-Derived Cortical Interneurons', *Journal of Neuroscience*, 32(49), pp. 17690–17705. doi: 10.1523/JNEUROSCI.3583-12.2012.

Cohen, H. Y. *et al.* (2004) 'Acetylation of the C terminus of Ku70 by CBP and PCAF controls Bax-mediated apoptosis', *Molecular cell*, 13(5), pp. 627–638. doi: 10.1016/S1097-2765(04)00094-2.

Collado, M., Blasco, M. A. and Serrano, M. (2007) 'Cellular Senescence in Cancer and Aging', *Cell*, 130(2), pp. 223–233. doi: 10.1016/J.CELL.2007.07.003.

Cooper, A. A. *et al.* (2006) 'α-Synuclein Blocks ER-Golgi Traffic and Rab1 Rescues Neuron Loss in Parkinson's Models', *Science (New York, N.Y.)*, 313(5785), p. 324. doi: 10.1126/SCIENCE.1129462.

Cooper, G. M. (2000) 'The Mechanism of Oxidative Phosphorylation'. Available at: https://www.ncbi.nlm.nih.gov/books/NBK9885/ (Accessed: 7 January 2023).

Coppé, J.-P. *et al.* (2010) 'The Senescence-Associated Secretory Phenotype: The Dark Side of Tumor Suppression', *Annual Review of Pathology: Mechanisms of Disease*, 5(1), pp. 99–118. doi: 10.1146/annurev-pathol-121808-102144.

Covarrubias, A. J. *et al.* (2020) 'NAD+ metabolism and its roles in cellular processes during ageing', *Nature Reviews Molecular Cell Biology 2020 22:2*, 22(2), pp. 119–141. doi: 10.1038/s41580-020-00313-x.

Crouch, J. *et al.* (2022) 'Epigenetic Regulation of Cellular Senescence', *Cells*, 11(4). doi: 10.3390/CELLS11040672.

Csiszar, A. *et al.* (2003) 'Aging-induced proinflammatory shift in cytokine expression profile in coronary arteries', *FASEB journal : official publication of the Federation of American Societies for Experimental Biology*, 17(9), pp. 1183–1185. doi: 10.1096/FJ.02-1049FJE.

D'amours, D. *et al.* (1999) 'Poly(ADP-ribosyl)ation reactions in the regulation of nuclear functions', *Biochem. J*, 342, pp. 249–268.

Dabrowski, M., Bukowy-Bieryllo, Z. and Zietkiewicz, E. (2015) ‘Translational readthrough potential of natural termination codons in eucaryotes – The impact of RNA sequence’, *RNA Biology*, 12(9), p. 950. doi: 10.1080/15476286.2015.1068497.

Dauer, W. *et al.* (2002) ‘From the Cover: Resistance of α-synuclein null mice to the parkinsonian neurotoxin MPTP’, *Proceedings of the National Academy of Sciences of the United States of America*, 99(22), p. 14524. doi: 10.1073/PNAS.172514599.

David, A. *et al.* (2017) ‘Werner Syndrome: Clinical Features, Pathogenesis and Potential Therapeutic Interventions’, *Ageing research reviews*, 33(5), p. 105. doi: 10.1016/J.ARR.2016.03.002.

Denaxa, M. *et al.* (2012) ‘Maturation-Promoting Activity of SATB1 in MGE-Derived Cortical Interneurons’, *Cell Reports*, 2(5), p. 1351. doi: 10.1016/J.CELREP.2012.10.003.

Deng, H., Wang, P. and Jankovic, J. (2018) ‘The genetics of Parkinson disease’, *Ageing Research Reviews*. Elsevier Ireland Ltd, pp. 72–85. doi: 10.1016/j.arr.2017.12.007.

Van Deursen, J. M. (2014) ‘The role of senescent cells in ageing’, *Nature*, 509(7501), p. 439. doi: 10.1038/NATURE13193.

Devi, L. *et al.* (2008) ‘Mitochondrial import and accumulation of α-synuclein impair complex I in human dopaminergic neuronal cultures and Parkinson disease brain’, *Journal of Biological Chemistry*, 283(14), pp. 9089–9100. doi: 10.1074/jbc.M710012200.

Dickinson, L. A. *et al.* (1992) ‘A tissue-specific MARSAR DNA-binding protein with unusual binding site recognition’, *Cell*, 70(4), pp. 631–645. doi: 10.1016/0092-8674(92)90432-C.

Dickson, D. W. (2012) ‘Parkinson’s Disease and Parkinsonism: Neuropathology’, *Cold Spring Harbor Perspectives in Medicine*, 2(8), p. a009258. doi: 10.1101/CSHPERSPECT.A009258.

Dimri, G. P. *et al.* (1995) ‘A biomarker that identifies senescent human cells in culture and in aging skin in vivo’, *Proceedings of the National Academy of Sciences of the United States of America*, 92(20), pp. 9363–9367. doi: 10.1073/pnas.92.20.9363.

DiSabato, D. J., Quan, N. and Godbout, J. P. (2016) ‘Neuroinflammation: the devil is in the details’, *Journal of Neurochemistry*, 139, pp. 136–153. doi: 10.1111/jnc.13607.

Dölle, C. *et al.* (2016) ‘Defective mitochondrial DNA homeostasis in the substantia nigra in Parkinson disease’, *Nature communications*, 7. doi: 10.1038/NCOMMS13548.

Dongiovanni, P. *et al.* (2020) ‘β-Klotho gene variation is associated with liver damage in children with NAFLD’, *Journal of Hepatology*, 72(3), pp. 411–419. doi: 10.1016/j.jhep.2019.10.011.

Du, G. J. *et al.* (2012) ‘Epigallocatechin Gallate (EGCG) Is the Most Effective Cancer Chemopreventive Polyphenol in Green Tea’, *Nutrients*, 4(11), p. 1679. doi: 10.3390/NU4111679.

Du, Y. *et al.* (2016) ‘Spatial and temporal distribution of dopaminergic neurons during development in zebrafish’, *Frontiers in Neuroanatomy*, 10(NOV), p. 115. doi: 10.3389/FNANA.2016.00115/BIBTEX.

Dubal, D. B. *et al.* (2014) ‘Life extension factor klotho enhances cognition’, *Cell reports*, 7(4), p. 1065. doi: 10.1016/J.CELREP.2014.03.076.

Duffy, P. E. and Tennyson, V. M. (1965) ‘Phase and Electron Microscopic Observations of Lewy Bodies and Melanin Granules in the Substantia Nigra and Locus Caeruleus in Parkinson’s Disease’, *Journal of Neuropathology & Experimental Neurology*, 24(3), pp. 398–414. doi: 10.1097/00005072-196507000-00003.

Dyle, M. C. *et al.* (2020) ‘How to get away with nonsense: Mechanisms and consequences of escape from nonsense-mediated RNA decay’, *Wiley Interdisciplinary Reviews: RNA*, 11(1), p. e1560. doi: 10.1002/WRNA.1560.

Earls, R. H. *et al.* (2019) ‘Intrastriatal injection of preformed alpha-synuclein fibrils alters central and peripheral immune cell profiles in non-transgenic mice’, *Journal of Neuroinflammation*, 16(1), pp. 1–15. doi: 10.1186/S12974-019-1636-8/FIGURES/7.

El-Brolosy, M. A. *et al.* (2019) ‘Genetic compensation triggered by mutant mRNA degradation’, *Nature*, 568(7751), p. 193. doi: 10.1038/S41586-019-1064-Z.

Ellett, F. *et al.* (2011) ‘mpeg1 promoter transgenes direct macrophage-lineage expression in zebrafish’, *Blood*, 117(4), p. e49. doi: 10.1182/BLOOD-2010-10-314120.

Emborg, M. E. (2007) ‘Nonhuman Primate Models of Parkinson’s Disease’, *ILAR Journal*, 48(4), pp. 339–355. doi: 10.1093/ILAR.48.4.339.

Emmanouilidou, E., Stefanis, L. and Vekrellis, K. (2010) ‘Cell-produced α-synuclein oligomers are targeted to, and impair, the 26S proteasome’, *Neurobiology of Aging*, 31(6), pp. 953–968. doi: 10.1016/J.NEUROBIOLAGING.2008.07.008.

Engeland, K. (2022) ‘Cell cycle regulation: p53-p21-RB signaling’, *Cell Death & Differentiation 2022*

29:5, 29(5), pp. 946–960. doi: 10.1038/s41418-022-00988-z.

Ettig, R. *et al.* (2011) ‘Dissecting DNA-Histone Interactions in the Nucleosome by Molecular Dynamics Simulations of DNA Unwrapping’, *Biophysical Journal*, 101(8), pp. 1999–2008. doi: 10.1016/J.BPJ.2011.07.057.

Fargnoli, J. *et al.* (1990) ‘Decreased expression of heat shock protein 70 mRNA and protein after heat treatment in cells of aged rats.’, *Proceedings of the National Academy of Sciences of the United States of America*, 87(2), p. 846. doi: 10.1073/PNAS.87.2.846.

Fearnley, J. M. and Lees, A. J. (1991) ‘AGEING AND PARKINSON’S DISEASE: SUBSTANTIA NIGRA REGIONAL SELECTIVITY’, *Brain*, 114, pp. 2283–2301. Available at: https://academic.oup.com/brain/article/114/5/2283/399854 (Accessed: 29 November 2022).

Feige, J. N. and Johan, A. (2008) ‘Transcriptional targets of sirtuins in the coordination of mammalian physiology’, *Current opinion in cell biology*, 20(3), p. 303. doi: 10.1016/J.CEB.2008.03.012.

Feng, J. Q. *et al.* (2006) ‘Loss of DMP1 causes rickets and osteomalacia and identifies a role for osteocytes in mineral metabolism’, *Nature genetics*, 38(11), pp. 1310–1315. doi: 10.1038/NG1905.

Ferrington, D. A., Husom, A. D. and Thompson, L. V. (2005) ‘Altered proteasome structure, function, and oxidation in aged muscle’, *The FASEB Journal*, 19(6), pp. 1–24. doi: 10.1096/FJ.04-2578FJE.

Ferrucci, L. and Fabbri, E. (2018) ‘Inflammageing: chronic inflammation in ageing, cardiovascular disease, and frailty’, *Nature reviews. Cardiology*, 15(9), p. 505. doi: 10.1038/S41569-018-0064-2.

Flik, G., Verbost, P. M. and Bonga, S. E. W. (1995) ‘12 Calcium Transport Processes in Fishes’, *Fish Physiology*, 14(C), pp. 317–342. doi: 10.1016/S1546-5098(08)60251-4.

Flinn, L. *et al.* (2009) ‘Complex I deficiency and dopaminergic neuronal cell loss in parkin-deficient zebrafish (Danio rerio)’, *Brain*, 132(6), pp. 1613–1623. doi: 10.1093/BRAIN/AWP108.

Di Fonzo, A. *et al.* (2005) ‘A frequent LRRK2 gene mutation associated with autosomal dominant Parkinson’s disease’, *The Lancet*, 365(9457), pp. 412–415. doi: 10.1016/S0140-6736(05)17829-5.

Ford, E. *et al.* (2006) ‘Mammalian Sir2 homolog SIRT7 is an activator of RNA polymerase I transcription’. doi: 10.1101/gad.1399706.

Forster, R. E. *et al.* (2011) ‘Vitamin D Receptor Controls Expression of the Anti-aging Klotho Gene in

Mouse and Human Renal Cells', *Biochemical and biophysical research communications*, 414(3), p. 557. doi: 10.1016/J.BBRC.2011.09.117.

Frank-Cannon, T. C. *et al.* (2008) 'Parkin Deficiency Increases Vulnerability to Inflammation-Related Nigral Degeneration', *The Journal of Neuroscience*, 28(43), p. 10825. doi: 10.1523/JNEUROSCI.3001-08.2008.

Freathy, R. M. *et al.* (2006) 'The functional "KL-VS" variant of KLOTHO is not associated with type 2 diabetes in 5028 UK Caucasians', *BMC Medical Genetics*, 7, pp. 1–6. doi: 10.1186/1471-2350-7-51.

Frye, R. A. (1999) 'Characterization of Five Human cDNAs with Homology to the Yeast SIR2 Gene: Sir2-like Proteins (Sirtuins) Metabolize NAD and May Have Protein ADP-Ribosyltransferase Activity', *Biochemical and Biophysical Research Communications*, 260(1), pp. 273–279. doi: 10.1006/BBRC.1999.0897.

Frye, R. A. (2000) 'Phylogenetic classification of prokaryotic and eukaryotic Sir2-like proteins', *Biochemical and Biophysical Research Communications*, 273(2), pp. 793–798. doi: 10.1006/BBRC.2000.3000.

Fulton, M. D. *et al.* (2021) 'The macromolecular complexes of histones affect protein arginine methyltransferase activities', *The Journal of Biological Chemistry*, 297(4), p. 101123. doi: 10.1016/J.JBC.2021.101123.

Furlan, S. *et al.* (2020) 'Calsequestrins New Calcium Store Markers of Adult Zebrafish Cerebellum and Optic Tectum', *Frontiers in Neuroanatomy*, 14, p. 15. doi: 10.3389/FNANA.2020.00015/BIBTEX.

Galande, S. *et al.* (2001) 'SATB1 Cleavage by Caspase 6 Disrupts PDZDomain-Mediated Dimerization, Causing Detachment from Chromatin Early in T-Cell Apoptosis', *Molecular and Cellular Biology*, 21(16), p. 5591. doi: 10.1128/MCB.21.16.5591-5604.2001.

Gámez-Valero, A. and Beyer, K. (2018) 'Alternative Splicing of Alpha- and Beta-Synuclein Genes Plays Differential Roles in Synucleinopathies', *Genes*, 9(2). doi: 10.3390/GENES9020063.

Ganjam, G. K. *et al.* (2019) 'Mitochondrial damage by α-synuclein causes cell death in human dopaminergic neurons', *Cell Death and Disease*, 10(11), pp. 1–16. doi: 10.1038/s41419-019-2091-2.

Gao, H. M. *et al.* (2008) 'Neuroinflammation and Oxidation/Nitration of α-Synuclein Linked to Dopaminergic Neurodegeneration', *The Journal of Neuroscience*, 28(30), p. 7687. doi: 10.1523/JNEUROSCI.0143-07.2008.

Garringer, H. J. *et al.* (2006) ‘The Role of Mutant UDP-N-Acetyl-α-d-Galactosamine-Polypeptide N-Acetylgalactosaminyltransferase 3 in Regulating Serum Intact Fibroblast Growth Factor 23 and Matrix Extracellular Phosphoglycoprotein in Heritable Tumoral Calcinosis’, *The Journal of Clinical Endocrinology & Metabolism*, 91(10), pp. 4037–4042. doi: 10.1210/JC.2006-0305.

Gerhard, A. *et al.* (2006) ‘In vivo imaging of microglial activation with [11C](R)-PK11195 PET in idiopathic Parkinson’s disease’, *Neurobiology of disease*, 21(2), pp. 404–412. doi: 10.1016/J.NBD.2005.08.002.

Gerhard, G. S. *et al.* (2002) ‘Life spans and senescent phenotypes in two strains of Zebrafish (Danio rerio)’, *Experimental Gerontology*, 37(8–9), pp. 1055–1068. doi: 10.1016/S0531-5565(02)00088-8.

Gerhart-Hines, Z. *et al.* (2007) ‘Metabolic control of muscle mitochondrial function and fatty acid oxidation through SIRT1/PGC-1α’, *The EMBO Journal*, 26(7), p. 1913. doi: 10.1038/SJ.EMBOJ.7601633.

Gertz, M. *et al.* (2013) ‘Ex-527 inhibits Sirtuins by exploiting their unique NAD+-dependent deacetylation mechanism’, *Proceedings of the National Academy of Sciences of the United States of America*, 110(30), pp. E2772–E2781. doi: 10.1073/PNAS.1303628110/SUPPL_FILE/PNAS.201303628SI.PDF.

Geut, H. *et al.* (2020) ‘Neuropathological correlates of parkinsonian disorders in a large Dutch autopsy series’, *Acta Neuropathologica Communications*, 8(1), pp. 1–14. doi: 10.1186/S40478-020-00914-9/TABLES/3.

Ghosh, R. P. *et al.* (2019) ‘Satb1 integrates DNA binding site geometry and torsional stress to differentially target nucleosome-dense regions’, *Nature Communications 2019 10:1*, 10(1), pp. 1–16. doi: 10.1038/s41467-019-11118-8.

Gibney, E. R. and Nolan, C. M. (2010) ‘Epigenetics and gene expression’, *Heredity 2010 105:1*, 105(1), pp. 4–13. doi: 10.1038/hdy.2010.54.

Giguère, N., Nanni, S. B. and Trudeau, L. E. (2018) ‘On cell loss and selective vulnerability of neuronal populations in Parkinson’s disease’, *Frontiers in Neurology*. Frontiers Media S.A., p. 455. doi: 10.3389/fneur.2018.00455.

Gilbert, M. J. H., Zerulla, T. C. and Tierney, K. B. (2013) ‘Zebrafish (Danio rerio) as a model for the study of aging and exercise: Physical ability and trainability decrease with age’, *Experimental Gerontology*, 50(1), pp. 106–113. doi: 10.1016/j.exger.2013.11.013.

Glatzel-Plucinska, N. *et al.* (2019) 'The Role of SATB1 in Tumour Progression and Metastasis', *International Journal of Molecular Sciences*, 20(17). doi: 10.3390/IJMS20174156.

Goetz, C. G. *et al.* (2008) 'Movement Disorder Society-sponsored revision of the Unified Parkinson's Disease Rating Scale (MDS-UPDRS): Scale presentation and clinimetric testing results', *Movement Disorders*, 23(15), pp. 2129–2170. doi: 10.1002/MDS.22340.

Goldman, J. E. *et al.* (1983) 'Lewy bodies of Parkinson's disease contain neurofilament antigens', *Science (New York, N.Y.)*, 221(4615), pp. 1082–1084. doi: 10.1126/SCIENCE.6308771.

Gómez-Benito, M. *et al.* (2020) 'Modeling Parkinson's Disease With the Alpha-Synuclein Protein', *Frontiers in Pharmacology*, 11, p. 356. doi: 10.3389/FPHAR.2020.00356/BIBTEX.

Van Gool, F. *et al.* (2009) 'INTRACELLULAR NAD LEVELS REGULATE TNF-α PROTEIN SYNTHESIS IN A SIRTUIN-DEPENDENT MANNER', *Nature medicine*, 15(2), p. 206. doi: 10.1038/NM.1906.

Gottlieb, S. and Esposito, R. E. (1989) 'A new role for a yeast transcriptional silencer gene, SIR2, in regulation of recombination in ribosomal DNA', *Cell*, 56(5), pp. 771–776. doi: 10.1016/0092-8674(89)90681-8.

Grabowska, W., Sikora, E. and Bielak-Zmijewska, A. (2017) 'Sirtuins, a promising target in slowing down the ageing process', *Biogerontology*, 18(4), p. 447. doi: 10.1007/S10522-017-9685-9.

Grandinetti, A. *et al.* (1994) 'Prospective Study of Cigarette Smoking and the Risk of Developing Idiopathic Parkinson's Disease', *American Journal of Epidemiology*, 139(12), pp. 1129–1138. doi: 10.1093/OXFORDJOURNALS.AJE.A116960.

Greenamyre, J. T. *et al.* (2009) 'Lessons from the rotenone model of Parkinson's disease'. doi: 10.1016/j.tips.2009.12.006.

Greene, J. C. *et al.* (2003) 'Mitochondrial pathology and apoptotic muscle degeneration in Drosophila parkin mutants', *Proceedings of the National Academy of Sciences of the United States of America*, 100(7), p. 4078. doi: 10.1073/PNAS.0737556100.

Gregg, S. Q. *et al.* (2012) 'A mouse model of accelerated liver aging due to a defect in DNA repair', *Hepatology (Baltimore, Md.)*, 55(2), p. 609. doi: 10.1002/HEP.24713.

Guo, H. M. *et al.* (2019) 'Investigation of the roles of dysbindin-1 and SATB2 in the progression of Parkinson's disease', *European review for medical and pharmacological sciences*, 23(17), pp. 7510–

7516. doi: 10.26355/EURREV_201909_18865.

Guo, J. *et al.* (2022) 'Aging and aging-related diseases: from molecular mechanisms to interventions and treatments', *Signal Transduction and Targeted Therapy 2022 7:1*, 7(1), pp. 1–40. doi: 10.1038/s41392-022-01251-0.

Guo, X. and García, L. R. (2014) 'SIR-2.1 integrates metabolic homeostasis with the reproductive neuromuscular excitability in early aging male Caenorhabditis elegans', *eLife*, 2014(3). doi: 10.7554/ELIFE.01730.

Guo, Y. J. *et al.* (2016) 'Resveratrol alleviates MPTP-induced motor impairments and pathological changes by autophagic degradation of α-synuclein via SIRT1-deacetylated LC3', *Molecular nutrition & food research*, 60(10), p. 2161. doi: 10.1002/MNFR.201600111.

'Guyton and Hall Textbook of Medical Physiology' (no date). Available at: http://avaxho.me/blogs/ChrisRedfield (Accessed: 18 January 2023).

Haigis, M. C. *et al.* (2006) 'SIRT4 inhibits glutamate dehydrogenase and opposes the effects of calorie restriction in pancreatic beta cells', *Cell*, 126(5), pp. 941–954. doi: 10.1016/J.CELL.2006.06.057.

Haigis, M. C. and Sinclair, D. A. (2010) 'Mammalian Sirtuins: Biological Insights and Disease Relevance', *Annual review of pathology*, 5, p. 253. doi: 10.1146/ANNUREV.PATHOL.4.110807.092250.

Hall, B., Limaye, A. and Kulkarni, A. B. (2009) 'Overview: Generation of Gene Knockout Mice', *Current protocols in cell biology / editorial board, Juan S. Bonifacino ... [et al.]*, CHAPTER(SUPPL. 44), p. Unit. doi: 10.1002/0471143030.CB1912S44.

Hall, D. M. *et al.* (2000) 'Aging reduces adaptive capacity and stress protein expression in the liver after heat stress', *Journal of applied physiology (Bethesda, Md. : 1985)*, 89(2), pp. 749–759. doi: 10.1152/JAPPL.2000.89.2.749.

Harfe, B. D. and Jinks-Robertson, S. (1999) 'Removal of Frameshift Intermediates by Mismatch Repair Proteins in Saccharomyces cerevisiae', *Molecular and Cellular Biology*, 19(7), p. 4766. doi: 10.1128/MCB.19.7.4766.

HARMAN, D. (1956) 'Aging: A Theory Based on Free Radical and Radiation Chemistry', *Journal of Gerontology*, 11(3), pp. 298–300. doi: 10.1093/GERONJ/11.3.298.

Hayflick, L. and Moorhead, P. S. (1961) 'The serial cultivation of human diploid cell strains', *Experimental cell research*, 25(3), pp. 585–621. doi: 10.1016/0014-4827(61)90192-6.

Heikkila, R. E. *et al.* (1984) ‘Protection against the dopaminergic neurotoxicity of 1-methyl-4-phenyl-1,2,5,6-tetrahydropyridine by monoamine oxidase inhibitors’, *Nature*, 311(5985), pp. 467–469. doi: 10.1038/311467A0.

Heikkila, R. E. *et al.* (1985) ‘Dopaminergic toxicity of rotenone and the 1-methyl-4-phenylpyridinium ion after their stereotaxic administration to rats: implication for the mechanism of 1-methyl-4-phenyl-1,2,3,6-tetrahydropyridine toxicity’, *Neuroscience letters*, 62(3), pp. 389–394. doi: 10.1016/0304-3940(85)90580-4.

Henriques, C. M. *et al.* (2013) ‘Telomerase Is Required for Zebrafish Lifespan’, *PLoS Genetics*. Edited by S. E. Artandi, 9(1), p. e1003214. doi: 10.1371/journal.pgen.1003214.

Herculano-Houzel, S. (2012) ‘The remarkable, yet not extraordinary, human brain as a scaled-up primate brain and its associated cost’, *Proceedings of the National Academy of Sciences of the United States of America*, 109(SUPPL.1), pp. 10661–10668. doi: 10.1073/PNAS.1201895109.

Herranz, D. *et al.* (2010) ‘Sirt1 improves healthy ageing and protects from metabolic syndrome-associated cancer syndrome’, *Nature communications*, 1(1), p. 3. doi: 10.1038/NCOMMS1001.

Hertzman, C. *et al.* (1990) ‘Parkinson’s disease: A case-control study of occupational and environmental risk factors’, *American Journal of Industrial Medicine*, 17(3), pp. 349–355. doi: 10.1002/AJIM.4700170307.

Hewamaddumal, C. A. A. *et al.* (2013) ‘Tardbpl splicing rescues motor neuron and axonal development in a mutant tardbp zebrafish’, *Human Molecular Genetics*, 22(12), p. 2376. doi: 10.1093/HMG/DDT082.

den Hoed, J. *et al.* (2021) ‘Mutation-specific pathophysiological mechanisms define different neurodevelopmental disorders associated with SATB1 dysfunction’, *The American Journal of Human Genetics*, 108(2), pp. 346–356. doi: 10.1016/j.ajhg.2021.01.007.

Hoeijmakers, J. H. J. (2009) ‘DNA damage, aging, and cancer’, *The New England journal of medicine*, 361(15), pp. 1475–1485. doi: 10.1056/NEJMRA0804615.

Hou, J. G. G. and Lai, E. C. (2007) ‘Non-motor symptoms of Parkinson’s disease’, *International Journal of Gerontology*, 1(2), pp. 53–64. doi: 10.1016/S1873-9598(08)70024-3.

Van Houten, B., Woshner, V. and Santos, J. H. (2006) ‘Role of mitochondrial DNA in toxic responses to oxidative stress’, *DNA repair*, 5(2), pp. 145–152. doi: 10.1016/J.DNAREP.2005.03.002.

Huang, Y. *et al.* (2011) ‘Distribution of Satb1 in the central nervous system of adult mice’, *Neuroscience Research*, 71(1), pp. 12–21. doi: 10.1016/J.NEURES.2011.05.015.

Hudgins, A. D. *et al.* (2018) ‘Age- and tissue-specific expression of senescence biomarkers in mice’, *Frontiers in Genetics*, 9(FEB), p. 59. doi: 10.3389/FGENE.2018.00059/BIBTEX.

Hurtado-Bagès, S. *et al.* (2020) ‘The taming of PARP1 and its impact on NAD+ metabolism’, *Molecular Metabolism*, 38, p. 100950. doi: 10.1016/J.MOLMET.2020.01.014.

Ichikawa, S. *et al.* (2007) ‘A homozygous missense mutation in human KLOTHO causes severe tumoral calcinosis’, *Journal of Clinical Investigation*, 117(9), pp. 2684–2691. doi: 10.1172/JCI31330.

Imai, S. I. *et al.* (2000) ‘Transcriptional silencing and longevity protein Sir2 is an NAD-dependent histone deacetylase’, *Nature 2000 403:6771*, 403(6771), pp. 795–800. doi: 10.1038/35001622.

Imura, A. *et al.* (2004) ‘Secreted Klotho protein in sera and CSF: implication for post-translational cleavage in release of Klotho protein from cell membrane’, *FEBS Letters*, 565(1–3), pp. 143–147. doi: 10.1016/J.FEBSLET.2004.03.090.

Isakova, T. *et al.* (2011) ‘Fibroblast growth factor 23 is elevated before parathyroid hormone and phosphate in chronic kidney disease’, *Kidney international*, 79(12), pp. 1370–1378. doi: 10.1038/KI.2011.47.

Ito, S. *et al.* (2000) ‘Molecular cloning and expression analyses of mouse βklotho, which encodes a novel Klotho family protein’, *Mechanisms of Development*, 98(1–2), pp. 115–119. doi: 10.1016/S0925-4773(00)00439-1.

Itoh, N. and Konishi, M. (no date) ‘The Zebrafish fgf Family’. Available at: www.liebertpub.com (Accessed: 22 January 2023).

Jacobson, S. *et al.* (2019) ‘Parkinson’s Disease and the Environment’, *Frontiers in Neurology | www.frontiersin.org*, 1, p. 218. doi: 10.3389/fneur.2019.00218.

Jankovic, J. and Tan, E. K. (2020) ‘Parkinson’s disease: etiopathogenesis and treatment’, *Journal of Neurology, Neurosurgery & Psychiatry*, 91(8), pp. 795–808. doi: 10.1136/JNNP-2019-322338.

Javitch, J. A. and Snyder, S. H. (1984) 'Uptake of MPP(+) by dopamine neurons explains selectivity of parkinsonism-inducing neurotoxin, MPTP', *European Journal of Pharmacology*, 106(2), pp. 455–456. doi: 10.1016/0014-2999(84)90740-4.

Jellinger, K. A. (2019) 'Is Braak staging valid for all types of Parkinson's disease?', *Journal of neural transmission (Vienna, Austria : 1996)*, 126(4), pp. 423–431. doi: 10.1007/S00702-018-1898-9.

Jeong, H. *et al.* (2011) 'Sirt1 mediates neuroprotection from mutant huntingtin by activation of the TORC1 and CREB transcriptional pathway', *Nature Medicine 2011 18:1*, 18(1), pp. 159–165. doi: 10.1038/nm.2559.

Jiang, M. *et al.* (2011) 'Neuroprotective role of Sirt1 in mammalian models of Huntington's disease through activation of multiple Sirt1 targets', *Nature Medicine 2011 18:1*, 18(1), pp. 153–158. doi: 10.1038/nm.2558.

Jun, J. Il and Lau, L. F. (2010) 'The Matricellular Protein CCN1/CYR61 Induces Fibroblast Senescence and Restricts Fibrosis in Cutaneous Wound Healing', *Nature cell biology*, 12(7), p. 676. doi: 10.1038/NCB2070.

Kaeberlein, M., McVey, M. and Guarente, L. (1999) 'The SIR2/3/4 complex and SIR2 alone promote longevity in Saccharomyces cerevisiae by two different mechanisms', *Genes & Development*, 13(19), p. 2570. doi: 10.1101/GAD.13.19.2570.

Kahle, P. J., Waak, J. and Gasser, T. (2009) 'DJ-1 and prevention of oxidative stress in Parkinson's disease and other age-related disorders', *Free Radical Biology and Medicine*, 47(10), pp. 1354–1361. doi: 10.1016/J.FREERADBIOMED.2009.08.003.

Kakar, R. S. *et al.* (2021) 'Peripheral Klotho and Parkinson's Disease', *Movement Disorders*, 36(5), pp. 1274–1276. doi: 10.1002/MDS.28530.

Kakefuda, K. *et al.* (2009) 'Sirtuin 1 overexpression mice show a reference memory deficit, but not neuroprotection', *Biochemical and Biophysical Research Communications*, 387(4), pp. 784–788. doi: 10.1016/J.BBRC.2009.07.119.

Kamel, C. *et al.* (2006) 'SirT1 fails to affect p53-mediated biological functions', *Aging Cell*, 5(1), pp. 81–88. doi: 10.1111/J.1474-9726.2006.00191.X.

Karperien, A., Ahammer, H. and Jelinek, H. F. (2013) 'Quantitating the subtleties of microglial morphology with fractal analysis', *Frontiers in Cellular Neuroscience*, 7(JANUARY 2013), pp. 1–34. doi:

10.3389/FNCEL.2013.00003/BIBTEX.

Kassebaum, N. J. (2022) ‘Global, regional, and national burden of diseases and injuries for adults 70 years and older: systematic analysis for the Global Burden of Disease 2019 Study’, *BMJ*, 376. doi: 10.1136/BMJ-2021-068208.

Kawahara, T. L. A. *et al.* (2009) ‘SIRT6 links histone H3 lysine 9 deacetylation to control of NF-κB dependent gene expression and organismal lifespan’, *Cell*, 136(1), p. 62. doi: 10.1016/J.CELL.2008.10.052.

Kawale, A. S. and Povirk, L. F. (2018) ‘Tyrosyl–DNA phosphodiesterases: rescuing the genome from the risks of relaxation’, *Nucleic Acids Research*, 46(2), p. 520. doi: 10.1093/NAR/GKX1219.

Kazak, L., Reyes, A. and Holt, I. J. (2012) ‘Minimizing the damage: repair pathways keep mitochondrial DNA intact’, *Nature reviews. Molecular cell biology*, 13(10), pp. 659–671. doi: 10.1038/NRM3439.

Kim, B. H. and Zhang, G. (2020) ‘Generating Stable Knockout Zebrafish Lines by Deleting Large Chromosomal Fragments Using Multiple gRNAs’. doi: 10.1534/g3.119.401035.

Kim, Do Hee *et al.* (2019) ‘Knockout of longevity gene Sirt1 in zebrafish leads to oxidative injury, chronic inflammation, and reduced life span’, *PLoS ONE*, 14(8). doi: 10.1371/journal.pone.0220581.

Kim, H. J. *et al.* (2012) ‘Increased expression of α-synuclein by SNCA duplication is associated with resistance to toxic stimuli’, *Journal of molecular neuroscience : MN*, 47(2), pp. 249–255. doi: 10.1007/S12031-012-9732-6.

Kim, J. *et al.* (2013) ‘PINK1 Deficiency Enhances Inflammatory Cytokine Release from Acutely Prepared Brain Slices’, *Experimental Neurobiology*, 22(1), p. 38. doi: 10.5607/EN.2013.22.1.38.

Kishi, S. *et al.* (2003) ‘The zebrafish as a vertebrate model of functional aging and very gradual senescence’, *Experimental Gerontology*, 38(7), pp. 777–786. doi: 10.1016/S0531-5565(03)00108-6.

Kishi, S. *et al.* (2009) ‘Zebrafish as a Genetic Model in Biological and Behavioral Gerontology: Where Development Meets Aging in Vertebrates – A Mini-Review’, *Gerontology*, 55(4), p. 430. doi: 10.1159/000228892.

Kitada, T. *et al.* (1998) ‘Mutations in the parkin gene cause autosomal recessive juvenile parkinsonism’, *Nature 1998 392:6676*, 392(6676), pp. 605–608. doi: 10.1038/33416.

Kitao, Y. *et al.* (2015) 'Transgenic supplementation of SIRT1 fails to alleviate acute loss of nigrostriatal dopamine neurons and gliosis in a mouse model of MPTP-induced parkinsonism', *F1000Research*, 4. doi: 10.12688/F1000RESEARCH.6386.1/DOI.

Kohwi-Shigematsu, T. and Kohwi, Y. (1990) 'Torsional Stress Stabilizes Extended Base Unpairing in Suppressor Sites Flanking Immunoglobulin Heavy Chain Enhancer', *Biochemistry*, 29(41), pp. 9551–9560. doi: 10.1021/BI00493A009/ASSET/BI00493A009.FP.PNG_V03.

Kõks, S. *et al.* (2016) 'Mouse models of ageing and their relevance to disease', *Mechanisms of Ageing and Development*. Elsevier Ireland Ltd, pp. 41–53. doi: 10.1016/j.mad.2016.10.001.

Kondo, M. *et al.* (2016) 'SATB1 Plays a Critical Role in Establishment of Immune Tolerance', *The Journal of Immunology*, 196(2), pp. 563–572. doi: 10.4049/JIMMUNOL.1501429.

Konnova, E. A. and Swanberg, M. (2018) 'Animal Models of Parkinson's Disease', *Parkinson's Disease: Pathogenesis and Clinical Aspects*, pp. 83–106. doi: 10.15586/CODONPUBLICATIONS.PARKINSONSDISEASE.2018.CH5.

Kosaka, K. *et al.* (1976) 'Presenile dementia with Alzheimer-, Pick- and Lewy-body changes', *Acta Neuropathologica 1976 36:3*, 36(3), pp. 221–233. doi: 10.1007/BF00685366.

Kosakai, A. *et al.* (2011) 'Degeneration of mesencephalic dopaminergic neurons in klotho mouse related to vitamin D exposure', *Brain Research*, 1382, pp. 109–117. doi: 10.1016/j.brainres.2011.01.056.

Krige, D. *et al.* (1992) 'Platelet mitochondria function in Parkinson's disease', *Annals of Neurology*, 32(6), pp. 782–788. doi: 10.1002/ANA.410320612.

Krizhanovsky, V. *et al.* (2008) 'Senescence of activated stellate cells limits liver fibrosis', *Cell*, 134(4), p. 657. doi: 10.1016/J.CELL.2008.06.049.

Krüger, R. *et al.* (1998) 'Ala30Pro mutation in the gene encoding alpha-synuclein in Parkinson's disease', *Nature genetics*, 18(2), pp. 106–108. doi: 10.1038/NG0298-106.

Kujoth, C. C. *et al.* (2005) 'Medicine: Mitochondrial DNA mutations, oxidative stress, and apoptosis in mammalian aging', *Science*, 309(5733), pp. 481–484. doi: 10.1126/SCIENCE.1112125.

Kumar, P. P. *et al.* (2005) 'Displacement of SATB1-Bound Histone Deacetylase 1 Corepressor by the Human Immunodeficiency Virus Type 1 Transactivator Induces Expression of Interleukin-2 and Its

Receptor in T Cells', *Molecular and Cellular Biology*, 25(5), p. 1620. doi: 10.1128/MCB.25.5.1620-1633.2005.

Kuro-o, M. *et al.* (1997) 'Mutation of the mouse klotho gene leads to a syndrome resembling ageing', *Nature*, 390(6655), pp. 45–51. doi: 10.1038/36285.

Kurosu, H. *et al.* (2005) 'Physiology: Suppression of aging in mice by the hormone Klotho', *Science*, 309(5742), pp. 1829–1833. doi: 10.1126/science.1112766.

Kurosu, H. *et al.* (2006) 'Regulation of Fibroblast Growth Factor-23 Signaling by Klotho', *The Journal of biological chemistry*, 281(10), p. 6120. doi: 10.1074/JBC.C500457200.

Kuzuhara, S. *et al.* (1988) 'Lewy bodies are ubiquitinated. A light and electron microscopic immunocytochemical study', *Acta neuropathologica*, 75(4), pp. 345–353. doi: 10.1007/BF00687787.

Van Laar, V. S. *et al.* (2020) 'α-Synuclein amplifies cytoplasmic peroxide flux and oxidative stress provoked by mitochondrial inhibitors in CNS dopaminergic neurons in vivo', *Redox Biology*, 37. doi: 10.1016/j.redox.2020.101695.

Lajoie, A. C., Lafontaine, A. L. and Kaminska, M. (2021) 'The Spectrum of Sleep Disorders in Parkinson Disease: A Review', *Chest*, 159(2), pp. 818–827. doi: 10.1016/J.CHEST.2020.09.099.

Lamis, A. *et al.* (2022) 'Hutchinson-Gilford Progeria Syndrome: A Literature Review', *Cureus*, 14(8). doi: 10.7759/CUREUS.28629.

Landry, J. *et al.* (2000) 'The silencing protein SIR2 and its homologs are NAD-dependent protein deacetylases', *Proceedings of the National Academy of Sciences of the United States of America*, 97(11), pp. 5807–5811. doi: 10.1073/PNAS.110148297.

Lang, X. *et al.* (2020) 'Treadmill exercise mitigates neuroinflammation and increases BDNF via activation of SIRT1 signaling in a mouse model of T2DM', *Brain Research Bulletin*, 165, pp. 30–39. doi: 10.1016/J.BRAINRESBULL.2020.09.015.

Langston, J. W. *et al.* (1984) '1-Methyl-4-phenylpyridinium ion (MPP+): Identification of a metabolite of MPTP, a toxin selective to the substantia nigra', *Neuroscience Letters*, 48(1), pp. 87–92. doi: 10.1016/0304-3940(84)90293-3.

Langston, J. W. *et al.* (1999) 'Evidence of active nerve cell degeneration in the substantia nigra of humans years after 1-methyl-4-phenyl-1,2,3,6-tetrahydropyridine exposure.', *Annals of Neurology*, 46(4), pp. 598–605. doi: 10.1002/1531-8249(199910)46:4<598::aid-ana7>3.0.co;2-f.

Laranjeiro, R. *et al.* (2013) ‘Cyclin-dependent kinase inhibitor p20 controls circadian cell-cycle timing’, *Proceedings of the National Academy of Sciences of the United States of America*, 110(17), pp. 6835–6840. doi: 10.1073/pnas.1217912110.

Larbalestier, H. *et al.* (2022) ‘GCH1 Deficiency Activates Brain Innate Immune Response and Impairs Tyrosine Hydroxylase Homeostasis’, *Journal of Neuroscience*, 42(4), pp. 702–716. doi: 10.1523/JNEUROSCI.0653-21.2021.

Larbi, A. *et al.* (2008) ‘Aging of the immune system as a prognostic factor for human longevity’, *Physiology (Bethesda, Md.)*, 23(2), pp. 64–74. doi: 10.1152/PHYSIOL.00040.2007.

Lavi-Moshayoff, V. *et al.* (2010) ‘PTH increases FGF23 gene expression and mediates the high-FGF23 levels of experimental kidney failure: A bone parathyroid feedback loop’, *American Journal of Physiology - Renal Physiology*, 299(4). doi: 10.1152/AJPRENAL.00360.2010.

Lebel, M. and Leder, P. (1998) ‘A deletion within the murine Werner syndrome helicase induces sensitivity to inhibitors of topoisomerase and loss of cellular proliferative capacity’, *Genetics*, 95, pp. 13097–13102. Available at: www.pnas.org. (Accessed: 3 March 2023).

Lee, H. M. and Koh, S.-B. (2015) ‘Many Faces of Parkinson’s Disease: Non-Motor Symptoms of Parkinson’s Disease’, *Journal of Movement Disorders*, 8(2), pp. 92–97. doi: 10.14802/jmd.15003.

Lena, A. M. *et al.* (2012) ‘MicroRNA-191 triggers keratinocytes senescence by SATB1 and CDK6 downregulation’, *Biochemical and Biophysical Research Communications*, 423(3), pp. 509–514. doi: 10.1016/J.BBRC.2012.05.153.

Leon, J. *et al.* (2017) ‘Peripheral Elevation of a Klotho Fragment Enhances Brain Function and Resilience in Young, Aging, and α-Synuclein Transgenic Mice’, *Cell Reports*, 20(6), pp. 1360–1371. doi: 10.1016/j.celrep.2017.07.024.

Lesage, S. *et al.* (2013) ‘G51D α-synuclein mutation causes a novel Parkinsonian–pyramidal syndrome’, *Annals of Neurology*, 73(4), pp. 459–471. doi: 10.1002/ANA.23894.

Lesage, S. *et al.* (2016) ‘Loss of VPS13C Function in Autosomal-Recessive Parkinsonism Causes Mitochondrial Dysfunction and Increases PINK1/Parkin-Dependent Mitophagy’, *The American Journal of Human Genetics*, 98(3), pp. 500–513. doi: 10.1016/J.AJHG.2016.01.014.

Li, S. A. *et al.* (2004) ‘Immunohistochemical localization of Klotho protein in brain, kidney, and reproductive organs of mice’, *Cell structure and function*, 29(4), pp. 91–99. doi: 10.1247/CSF.29.91.

Li, W. W. *et al.* (2007) ‘Localization of alpha-synuclein to mitochondria within midbrain of mice’, *Neuroreport*, 18(15), pp. 1543–1546. doi: 10.1097/WNR.0B013E3282F03DB4.

Li, Z., Yang, J. and Huang, H. (2006) ‘Oxidative stress induces H2AX phosphorylation in human spermatozoa’, *FEBS Letters*, 580(26), pp. 6161–6168. doi: 10.1016/J.FEBSLET.2006.10.016.

Lim, K. *et al.* (2015) ‘α-Klotho Expression in Human Tissues’, *The Journal of Clinical Endocrinology & Metabolism*, 100(10), pp. E1308–E1318. doi: 10.1210/JC.2015-1800.

Lin, C. H., Hu, H. J. and Hwang, P. P. (2017) ‘Molecular Physiology of the Hypocalcemic Action of Fibroblast Growth Factor 23 in Zebrafish (Danio rerio)’, *Endocrinology*, 158(5), pp. 1347–1358. doi: 10.1210/EN.2016-1883.

Liu, H. *et al.* (2021) ‘A Novel SNCA A30G Mutation Causes Familial Parkinson’s Disease’, *Movement Disorders*, 36(7), pp. 1624–1633. doi: 10.1002/MDS.28534.

Liu, T. *et al.* (2017) ‘NF-κB signaling in inflammation’, *Signal Transduction and Targeted Therapy*. Springer Nature, p. 17023. doi: 10.1038/sigtrans.2017.23.

Liu, Z. *et al.* (2011) ‘Leucine-rich repeat kinase 2 (LRRK2) regulates inflammatory bowel disease through the Nuclear Factor of Activated T cells (NFAT)’, *Nature immunology*, 12(11), p. 1063. doi: 10.1038/NI.2113.

Loewe, L. and Hill, W. G. (2010) ‘The population genetics of mutations: good, bad and indifferent’, *Philosophical Transactions of the Royal Society B: Biological Sciences*, 365(1544), p. 1153. doi: 10.1098/RSTB.2009.0317.

Lombard, D. B. *et al.* (2007) ‘Mammalian Sir2 Homolog SIRT3 Regulates Global Mitochondrial Lysine Acetylation’, *Molecular and Cellular Biology*, 27(24), p. 8807. doi: 10.1128/MCB.01636-07.

López-Otín, C. *et al.* (2013) ‘The hallmarks of aging’, *Cell*. Cell Press, p. 1194. doi: 10.1016/j.cell.2013.05.039.

Lopez, A. *et al.* (2022) ‘A New Zebrafish Model to Measure Neuronal α-Synuclein Clearance In Vivo’, *Genes*, 13(5). doi: 10.3390/GENES13050868/S1.

López Nadal, A. *et al.* (2018) 'Exposure to Antibiotics Affects Saponin Immersion-Induced Immune Stimulation and Shift in Microbial Composition in Zebrafish Larvae', *Frontiers in Microbiology*, 9, p. 2588. doi: 10.3389/FMICB.2018.02588/BIBTEX.

Lubomski, M., Davis, R. L. and Sue, C. M. (2021) 'Health-Related Quality of Life for Parkinson's Disease Patients and Their Caregivers', *Journal of Movement Disorders*, 14(1), p. 42. doi: 10.14802/JMD.20079.

Luk, K. C., Kehm, V. M., *et al.* (2012) 'Intracerebral inoculation of pathological α-synuclein initiates a rapidly progressive neurodegenerative α-synucleinopathy in mice', *The Journal of Experimental Medicine*, 209(5), p. 975. doi: 10.1084/JEM.20112457.

Luk, K. C., Kehm, V., *et al.* (2012) 'Pathological α-Synuclein Transmission Initiates Parkinson-like Neurodegeneration in Non-transgenic Mice', *Science (New York, N.Y.)*, 338(6109), p. 949. doi: 10.1126/SCIENCE.1227157.

Luo, J. *et al.* (2001) 'Negative control of p53 by Sir2alpha promotes cell survival under stress', *Cell*, 107(2), pp. 137–148. doi: 10.1016/S0092-8674(01)00524-4.

Luo, X. and Lee Kraus, W. (2012) 'On PAR with PARP: cellular stress signaling through poly(ADP-ribose) and PARP-1', *Genes & Development*, 26(5), p. 417. doi: 10.1101/GAD.183509.111.

Ma, S. Y. *et al.* (1999) 'Unbiased morphometrical measurements show loss of pigmented nigral neurones with ageing', *Neuropathology and Applied Neurobiology*, 25(5), pp. 394–399. doi: 10.1046/J.1365-2990.1999.00202.X.

Ma, W. *et al.* (2007) 'GCIP/CCNDBP1, a helix-loop-helix protein, suppresses tumorigenesis', *Journal of cellular biochemistry*, 100(6), pp. 1376–1386. doi: 10.1002/JCB.21140.

Mackenzie I. R. (2001). Available at: https://bcmj.org/articles/pathology-parkinson's-disease (Accessed: 29 November 2022).

MacMahon Copas, A. N. *et al.* (2021) 'The Pathogenesis of Parkinson's Disease: A Complex Interplay Between Astrocytes, Microglia, and T Lymphocytes?', *Frontiers in Neurology*, 12, p. 771. doi: 10.3389/FNEUR.2021.666737/BIBTEX.

De Magalhães, J. P. *et al.* (2002) 'Stress-induced premature senescence in BJ and hTERT-BJ1 human foreskin fibroblasts', *FEBS Letters*, 523(1–3), pp. 157–162. doi: 10.1016/S0014-5793(02)02973-3.

de Magalhães, J. P., Curado, J. and Church, G. M. (2009) 'Meta-analysis of age-related gene expression profiles identifies common signatures of aging', *Bioinformatics*, 25(7), p. 875. doi: 10.1093/BIOINFORMATICS/BTP073.

Mangos, S. *et al.* (2012) 'Expression of fgf23 and αklotho in developing embryonic tissues and adult kidney of the zebrafish, Danio rerio', *Nephrology Dialysis Transplantation*, 27(12), pp. 4314–4322. doi: 10.1093/NDT/GFS335.

Manning-Bog, A. B. *et al.* (2002) 'The herbicide paraquat causes up-regulation and aggregation of α-synuclein in mice: Paraquat and α-synuclein', *Journal of Biological Chemistry*, 277(3), pp. 1641–1644. doi: 10.1074/jbc.C100560200.

Marras, C. *et al.* (2018) 'Prevalence of Parkinson's disease across North America', *npj Parkinson's Disease*, 4(1). doi: 10.1038/S41531-018-0058-0.

Massip, L. *et al.* (2006) 'Increased insulin, triglycerides, reactive oxygen species, and cardiac fibrosis in mice with a mutation in the helicase domain of the Werner syndrome gene homologue', *Experimental Gerontology*, 41(2), pp. 157–168. doi: 10.1016/J.EXGER.2005.10.011.

Masuyama, R. *et al.* (2006) 'Vitamin D receptor in chondrocytes promotes osteoclastogenesis and regulates FGF23 production in osteoblasts', *Journal of Clinical Investigation*, 116(12), p. 3150. doi: 10.1172/JCI29463.

Maszlag-Török, R. *et al.* (2021) 'Gene variants and expression changes of SIRT1 and SIRT6 in peripheral blood are associated with Parkinson's disease', *Scientific Reports 2021 11:1*, 11(1), pp. 1–10. doi: 10.1038/s41598-021-90059-z.

Matsui, H. and Matsui, N. (2017) 'Cerebrospinal fluid injection into adult zebrafish for disease research', *Journal of Neural Transmission*, 124(12), pp. 1627–1633. doi: 10.1007/s00702-017-1787-7.

Matsui, H. and Sugie, A. (2017) 'An optimized method for counting dopaminergic neurons in zebrafish', *PLoS ONE*, 12(9). doi: 10.1371/JOURNAL.PONE.0184363.

Matsumura, Y. *et al.* (1998) 'Identification of the human klotho gene and its two transcripts encoding membrane and secreted klotho protein', *Biochemical and Biophysical Research Communications*, 242(3), pp. 626–630. doi: 10.1006/bbrc.1997.8019.

Maynard, S. *et al.* (2015) 'DNA damage, DNA repair, aging, and neurodegeneration', *Cold Spring Harbor Perspectives in Medicine*, 5(10). doi: 10.1101/cshperspect.a025130.

McBurney, M. W. *et al.* (2003) ‘The Mammalian SIR2α Protein Has a Role in Embryogenesis and Gametogenesis’, *Molecular and Cellular Biology*, 23(1), p. 38. doi: 10.1128/MCB.23.1.38-54.2003.

Mcdonald, C. *et al.* (2018) ‘200 Years of Parkinson’s disease: what have we learnt from James Parkinson?’, *Age and Ageing*, 47(2), pp. 209–214. doi: 10.1093/AGEING/AFX196.

McGeer, P. L. *et al.* (1988) ‘Reactive microglia are positive for HLA-DR in the substantia nigra of Parkinson’s and Alzheimer’s disease brains’, *Neurology*, 38(8), pp. 1285–1291. doi: 10.1212/WNL.38.8.1285.

Meade, R. M., Fairlie, D. P. and Mason, J. M. (2019) ‘Alpha-synuclein structure and Parkinson’s disease – lessons and emerging principles’, *Molecular Neurodegeneration 2019 14:1*, 14(1), pp. 1–14. doi: 10.1186/S13024-019-0329-1.

Meiser, J., Weindl, D. and Hiller, K. (2013) ‘Complexity of dopamine metabolism’, *Cell Communication and Signaling*, 11(1), pp. 1–18. doi: 10.1186/1478-811X-11-34/FIGURES/5.

Melchinger, H. *et al.* (2019) ‘Role of Platelet Mitochondria: Life in a Nucleus-Free Zone’, *Frontiers in Cardiovascular Medicine*, 6, p. 153. doi: 10.3389/FCVM.2019.00153/BIBTEX.

Meredith, G. E. and Rademacher, D. J. (2011) ‘MPTP Mouse Models of Parkinson’s Disease: An Update’, *Journal of Parkinson’s disease*, 1(1), p. 19. doi: 10.3233/JPD-2011-11023.

Mian, I. S. (1998) ‘Sequence, structural, functional, and phylogenetic analyses of three glycosidase families’, *Blood cells, molecules & diseases*, 24(2), pp. 83–100. doi: 10.1006/BCMD.1998.9998.

Di Micco, R. *et al.* (2020) ‘Cellular senescence in ageing: from mechanisms to therapeutic opportunities’, *Nature Reviews Molecular Cell Biology 2020 22:2*, 22(2), pp. 75–95. doi: 10.1038/s41580-020-00314-w.

Michishita, E. *et al.* (2005) ‘Evolutionarily conserved and nonconserved cellular localizations and functions of human SIRT proteins’, *Molecular Biology of the Cell*, 16(10), pp. 4623–4635. doi: 10.1091/MBC.E05-01-0033.

Milanese, C. *et al.* (2012) ‘Hypokinesia and reduced dopamine levels in zebrafish lacking β- and γ1-synucleins’, *The Journal of biological chemistry*, 287(5), pp. 2971–2983. doi: 10.1074/JBC.M111.308312.

Miller, D. W. *et al.* (2004) ‘α-Synuclein in blood and brain from familial Parkinson disease with SNCA locus triplication', *Neurology*, 62(10), pp. 1835–1838. doi: 10.1212/01.WNL.0000127517.33208.F4.

Moehle, M. S. *et al.* (2012) 'LRRK2 Inhibition Attenuates Microglial Inflammatory Responses', *The Journal of Neuroscience*, 32(5), p. 1602. doi: 10.1523/JNEUROSCI.5601-11.2012.

Moniot, S., Weyand, M. and Steegborn, C. (2012) 'Structures, Substrates, and Regulators of Mammalian Sirtuins – Opportunities and Challenges for Drug Development', *Frontiers in Pharmacology*, 3. doi: 10.3389/FPHAR.2012.00016.

Di Monte, D. *et al.* (1986) 'Comparative studies on the mechanisms of paraquat and 1-methyl-4-phenylpyridine (MPP+) cytotoxicity', *Biochemical and Biophysical Research Communications*, 137(1), pp. 303–309. doi: 10.1016/0006-291X(86)91210-6.

Montgomery, E. B. (1995) 'Heavy metals and the etiology of Parkinson's disease and other movement disorders', *Toxicology*, 97(1–3), pp. 3–9. doi: 10.1016/0300-483X(94)02962-T.

Morais, V. A. *et al.* (2009) 'Parkinson's disease mutations in PINK1 result in decreased Complex I activity and deficient synaptic function', *EMBO Molecular Medicine*, 1(2), p. 99. doi: 10.1002/EMMM.200900006.

Moreno-García, A. *et al.* (2018) 'An overview of the role of lipofuscin in age-related neurodegeneration', *Frontiers in Neuroscience*, 12(JUL), p. 464. doi: 10.3389/FNINS.2018.00464/BIBTEX.

Morimoto, R. I. and Cuervo, A. M. (2009) 'Protein Homeostasis and Aging: Taking Care of Proteins From the Cradle to the Grave', *The Journals of Gerontology Series A: Biological Sciences and Medical Sciences*, 64A(2), p. 167. doi: 10.1093/GERONA/GLN071.

Morsli, S. *et al.* (2023) 'A p21-GFP zebrafish model of senescence for rapid testing of senolytics in vivo', *Aging Cell*, p. e13835. doi: 10.1111/ACEL.13835.

Mostoslavsky, R. *et al.* (2006) 'Genomic instability and aging-like phenotype in the absence of mammalian SIRT6', *Cell*, 124(2), pp. 315–329. doi: 10.1016/J.CELL.2005.11.044.

Motta, M. C. *et al.* (2004) 'Mammalian SIRT1 Represses Forkhead Transcription Factors by Sir2p results in silencing of mating type genes, telo-meres, and ribosomal DNA (Shore, 2000). Silencing in the ribosomal DNA promotes longevity (Kennedy et al., 1997; Sinclair and Guarente, 1997), and increased dos', *Cell*, 116, pp. 551–563.

Motyl, J. *et al.* (2018) ‘Alpha-synuclein alters differently gene expression of Sirts, PARPs and other stress response proteins: implications for neurodegenerative disorders’, *Molecular Neurobiology*, 55(1), p. 727. doi: 10.1007/S12035-016-0317-1.

Mudò, G. *et al.* (2012) ‘Transgenic expression and activation of PGC-1α protect dopaminergic neurons in the MPTP mouse model of Parkinsons disease’, *Cellular and Molecular Life Sciences*, 69(7), pp. 1153–1165. doi: 10.1007/S00018-011-0850-Z/FIGURES/7.

Muñoz-Espín, D. *et al.* (2013) ‘Programmed cell senescence during mammalian embryonic development’, *Cell*, 155(5), p. 1104. doi: 10.1016/J.CELL.2013.10.019.

Murer, H., Forster, I. and Biber, J. (2004) ‘The sodium phosphate cotransporter family SLC34’, *Pflugers Archiv : European journal of physiology*, 447(5), pp. 763–767. doi: 10.1007/S00424-003-1072-5.

Murga, M. *et al.* (2009) ‘A mouse model of the ATR-Seckel Syndrome reveals that replicative stress during embryogenesis limits mammalian lifespan’, *Nature genetics*, 41(8), p. 891. doi: 10.1038/NG.420.

Nagai, T. *et al.* (2003) ‘Cognition impairment in the genetic model of aging klotho gene mutant mice: a role of oxidative stress.’, *The FASEB journal : official publication of the Federation of American Societies for Experimental Biology*, 17(1), pp. 50–52. doi: 10.1096/fj.02-0448fje.

Nagai, Y. *et al.* (2011) ‘α-Synuclein Transgenic Drosophila As a Model of Parkinson’s Disease and Related Synucleinopathies’, *Parkinson’s Disease*, 2011. doi: 10.4061/2011/212706.

Nagpal, N. *et al.* (2013) ‘MicroRNA-191, an estrogen-responsive microRNA, functions as an oncogenic regulator in human breast cancer’, *Carcinogenesis*, 34(8), pp. 1889–1899. doi: 10.1093/CARCIN/BGT107.

Nakagawa, T. *et al.* (2009) ‘SIRT5 Deacetylates Carbamoyl Phosphate Synthetase 1 and Regulates the Urea Cycle’, *Cell*, 137(3), p. 560. doi: 10.1016/J.CELL.2009.02.026.

Nakamura, A. J. *et al.* (2010) ‘The complexity of phosphorylated H2AX foci formation and DNA repair assembly at DNA double-strand breaks’, *Cell cycle (Georgetown, Tex.)*, 9(2), p. 389. doi: 10.4161/CC.9.2.10475.

Nakatani, T. *et al.* (2009) ‘In vivo genetic evidence for klotho-dependent, fibroblast growth factor 23 (Fgf23) -mediated regulation of systemic phosphate homeostasis’, *The FASEB Journal*, 23(2), p. 433. doi: 10.1096/FJ.08-114397.

Nalls, M. A. *et al.* (2011) ‘Imputation of sequence variants for identification of genetic risks for Parkinson’s disease: a meta-analysis of genome-wide association studies’, *Lancet*, 377(9766), p. 641. doi: 10.1016/S0140-6736(10)62345-8.

Nalls, M. A. *et al.* (2014) ‘Large-scale meta-analysis of genome-wide association data identifies six new risk loci for Parkinson’s disease’, *Nature genetics*, 46(9), p. 989. doi: 10.1038/NG.3043.

Nalls, M. A. *et al.* (2019) ‘Identification of novel risk loci, causal insights, and heritable risk for Parkinson’s disease: a meta-genome wide association study’, *The Lancet. Neurology*, 18(12), p. 1091. doi: 10.1016/S1474-4422(19)30320-5.

Nelson, G. *et al.* (2012) ‘A senescent cell bystander effect: senescence-induced senescence’, *Aging Cell*, 11(2), p. 345. doi: 10.1111/J.1474-9726.2012.00795.X.

Nemani, V. M. *et al.* (2010) ‘Increased Expression of Alpha-Synuclein Reduces Neurotransmitter Release by Inhibiting Synaptic Vesicle Reclustering After Endocytosis’, *Neuron*, 65(1), p. 66. doi: 10.1016/J.NEURON.2009.12.023.

Nemoto, S., Fergusson, M. M. and Finkel, T. (2005) ‘SIRT1 Functionally Interacts with the Metabolic Regulator and Transcriptional Coactivator PGC-1*’. doi: 10.1074/jbc.M501485200.

Nguyen, A. P. T. *et al.* (2020) ‘Dopaminergic neurodegeneration induced by Parkinson’s disease-linked G2019S LRRK2 is dependent on kinase and GTPase activity’, *Proceedings of the National Academy of Sciences of the United States of America*, 117(29), pp. 17296–17307. doi: 10.1073/PNAS.1922184117/-/DCSUPPLEMENTAL.

Niccoli, T. and Partridge, L. (2012) ‘Ageing as a risk factor for disease’, *Current Biology*. doi: 10.1016/j.cub.2012.07.024.

North, B. J. *et al.* (2003) ‘The human Sir2 ortholog, SIRT2, is an NAD+-dependent tubulin deacetylase’, *Molecular cell*, 11(2), pp. 437–444. doi: 10.1016/S1097-2765(03)00038-8.

Notani, D. *et al.* (2010) ‘Phosphorylation-dependent regulation of satb1, the higher-order chromatin organizer and global gene regulator’, *Methods in Molecular Biology*, 647, pp. 317–335. doi: 10.1007/978-1-60761-738-9_20/FIGURES/4.

Oberdoerffer, P. *et al.* (2008) ‘DNA damage-induced alterations in chromatin contribute to genomic integrity and age-related changes in gene expression’, *Cell*, 135(5), p. 907. doi: 10.1016/J.CELL.2008.10.025.

Ogura, Y. *et al.* (2021) ‘Loss of αklotho causes reduced motor ability and short lifespan in zebrafish’, *Scientific Reports 2021 11:1*, 11(1), pp. 1–7. doi: 10.1038/s41598-021-93909-y.

Olauson, H. *et al.* (2013) ‘Parathyroid-specific deletion of Klotho unravels a novel calcineurin-dependent FGF23 signaling pathway that regulates PTH secretion’, *PLoS genetics*, 9(12). doi: 10.1371/JOURNAL.PGEN.1003975.

Old, J. (2013) ‘Hemoglobinopathies and Thalassemias’, *Emery and Rimoin’s Principles and Practice of Medical Genetics*, pp. 1–44. doi: 10.1016/B978-0-12-383834-6.00075-6.

Osorio, F. G. *et al.* (2011) ‘Hutchinson-Gilford progeria: Splicing-directed therapy in a new mouse model of human accelerated aging’, *Science Translational Medicine*, 3(106). doi: 10.1126/SCITRANSLMED.3002847.

Ou, Z. *et al.* (2021) ‘Global Trends in the Incidence, Prevalence, and Years Lived With Disability of Parkinson’s Disease in 204 Countries/Territories From 1990 to 2019’, *Frontiers in Public Health*, 9, p. 1994. doi: 10.3389/FPUBH.2021.776847/BIBTEX.

Outeiro, T. F., Marques, O. and Kazantsev, A. (2008) ‘Therapeutic role of sirtuins in neurodegenerative disease’, *Biochimica et Biophysica Acta (BBA) - Molecular Basis of Disease*, 1782(6), pp. 363–369. doi: 10.1016/J.BBADIS.2008.02.010.

Pahlavani, M. A. *et al.* (1995) ‘The expression of heat shock protein 70 decreases with age in lymphocytes from rats and rhesus monkeys’, *Experimental cell research*, 218(1), pp. 310–318. doi: 10.1006/EXCR.1995.1160.

Palacino, J. J. *et al.* (2004) ‘Mitochondrial Dysfunction and Oxidative Damage in parkin-deficient Mice’, *Journal of Biological Chemistry*, 279(18), pp. 18614–18622. doi: 10.1074/JBC.M401135200.

Pandey, K. B. and Rizvi, S. I. (2009) ‘Plant polyphenols as dietary antioxidants in human health and disease’, *Oxidative Medicine and Cellular Longevity*, 2(5), p. 270. doi: 10.4161/OXIM.2.5.9498.

Pang, S. Y. Y. *et al.* (2019) ‘The interplay of aging, genetics and environmental factors in the pathogenesis of Parkinson’s disease’, *Translational neurodegeneration*, 8(1). doi: 10.1186/S40035-019-0165-9.

Panula, P. *et al.* (2010) ‘The comparative neuroanatomy and neurochemistry of zebrafish CNS systems of relevance to human neuropsychiatric diseases’, *Neurobiology of Disease*, 40(1), pp. 46–57. doi: 10.1016/J.NBD.2010.05.010.

Pardridge, W. M. *et al.* (1989) 'Predominant low-molecular-weight proteins in isolated brain capillaries are histones', *Journal of neurochemistry*, 53(4), pp. 1014–1018. doi: 10.1111/J.1471-4159.1989.TB07388.X.

Parkinson's UK (2017). Available at: https://www.parkinsons.org.uk/news/whats-cost-living-parkinsons (Accessed: 28 November 2022).

Pavan Kumar, P. *et al.* (2006) 'Phosphorylation of SATB1, a Global Gene Regulator, Acts as a Molecular Switch Regulating Its Transcriptional Activity In Vivo', *Molecular Cell*, 22(2), pp. 231–243. doi: 10.1016/J.MOLCEL.2006.03.010.

Pedrosa Carrasco, A. J., Timmermann, L. and Pedrosa, D. J. (2018) 'Management of constipation in patients with Parkinson's disease', *NPJ Parkinson's Disease*, 4(1), p. 6. doi: 10.1038/S41531-018-0042-8.

Pendás, A. M. *et al.* (2002) 'Defective prelamin A processing and muscular and adipocyte alterations in Zmpste24 metalloproteinase–deficient mice', *Nature Genetics 2002 31:1*, 31(1), pp. 94–99. doi: 10.1038/ng871.

Pérez, V. I. *et al.* (2009) 'The overexpression of major antioxidant enzymes does not extend the lifespan of mice', *Aging Cell*, 8(1), p. 73. doi: 10.1111/J.1474-9726.2008.00449.X.

Perry, V. H. and Teeling, J. (2013) 'Microglia and macrophages of the central nervous system: the contribution of microglia priming and systemic inflammation to chronic neurodegeneration', *Seminars in Immunopathology*, 35(5), p. 601. doi: 10.1007/S00281-013-0382-8.

Pfluger, P. T. *et al.* (2008) 'Sirt1 protects against high-fat diet-induced metabolic damage', *Proceedings of the National Academy of Sciences of the United States of America*, 105(28), p. 9793. doi: 10.1073/PNAS.0802917105.

Picard, F. *et al.* (2004) 'Sirt1 promotes fat mobilization in white adipocytes by repressing PPAR-γ', *Nature 2004 429:6993*, 429(6993), pp. 771–776. doi: 10.1038/nature02583.

Podbielska, M. *et al.* (2016) 'Neuron-microglia interaction induced bi-directional cytotoxicity associated with calpain activation', *Journal of Neurochemistry*, 139(3), pp. 440–455. doi: 10.1111/JNC.13774.

Polymeropoulos, M. H. *et al.* (1997) 'Mutation in the alpha-synuclein gene identified in families with Parkinson's disease', *Science (New York, N.Y.)*, 276(5321), pp. 2045–2047. doi:

10.1126/SCIENCE.276.5321.2045.

Postuma, R. B. *et al.* (2015) ‘MDS clinical diagnostic criteria for Parkinson’s disease’, *Movement Disorders*, 30(12), pp. 1591–1601. doi: 10.1002/mds.26424.

Potente, M. *et al.* (2007) ‘SIRT1 controls endothelial angiogenic functions during vascular growth’, *Genes & Development*, 21(20), p. 2644. doi: 10.1101/GAD.435107.

Przedborski, S. *et al.* (2001) ‘Oxidative post-translational modifications of α-synuclein in the 1-methyl-4-phenyl-1,2,3,6-tetrahydropyridine (MPTP) mouse model of Parkinson’s disease’, *Journal of Neurochemistry*, 76(2), pp. 637–640. doi: 10.1046/J.1471-4159.2001.00174.X.

Pucci, L. *et al.* (2007) ‘Tissue expression and biochemical characterization of human 2-amino 3-carboxymuconate 6-semialdehyde decarboxylase, a key enzyme in tryptophan catabolism’, *The FEBS Journal*, 274(3), pp. 827–840. doi: 10.1111/J.1742-4658.2007.05635.X.

Purbey, P. K. *et al.* (2009) ‘Acetylation-Dependent Interaction of SATB1 and CtBP1 Mediates Transcriptional Repression by SATB1’, *Molecular and Cellular Biology*, 29(5), p. 1321. doi: 10.1128/MCB.00822-08.

Qin, W. *et al.* (2006) ‘Neuronal SIRT1 Activation as a Novel Mechanism Underlying the Prevention of Alzheimer Disease Amyloid Neuropathology by Calorie Restriction’, *Journal of Biological Chemistry*, 281(31), pp. 21745–21754. doi: 10.1074/JBC.M602909200.

Radak, Z. *et al.* (2011) ‘Age-dependent changes in 8-oxoguanine-DNA-glycosylase activity is modulated by adaptive responses to physical exercise in human skeletal muscle’, *Free radical biology & medicine*, 51(2), p. 417. doi: 10.1016/J.FREERADBIOMED.2011.04.018.

Ramachandiran, S. *et al.* (2007) ‘Divergent Mechanisms of Paraquat, MPP+, and Rotenone Toxicity: Oxidation of Thioredoxin and Caspase-3 Activation’, *Toxicological Sciences*, 95(1), pp. 163–171. doi: 10.1093/TOXSCI/KFL125.

Ramirez, A. *et al.* (2006) ‘Hereditary parkinsonism with dementia is caused by mutations in ATP13A2, encoding a lysosomal type 5 P-type ATPase’, *Nature Genetics 2006 38:10*, 38(10), pp. 1184–1191. doi: 10.1038/ng1884.

Ramsay, R. R., Salach, J. I. and Singer, T. P. (1986) ‘Uptake of the neurotoxin 1-methyl-4-phenylpyridine (MPP+) by mitochondria and its relation to the inhibition of the mitochondrial oxidation of NAD+-linked substrates by MPP+’, *Biochemical and Biophysical Research Communications*, 134(2), pp. 743–

748. doi: 10.1016/S0006-291X(86)80483-1.

Ran, F. A. *et al.* (2013) ‘Genome engineering using the CRISPR-Cas9 system’, *Nature Protocols 2013 8:11*, 8(11), pp. 2281–2308. doi: 10.1038/nprot.2013.143.

Rango, M. and Bresolin, N. (2018) ‘Brain Mitochondria, Aging, and Parkinson’s Disease’, *Genes*, 9(5). doi: 10.3390/GENES9050250.

Razali, K. *et al.* (2021) ‘The Promise of the Zebrafish Model for Parkinson’s Disease: Today’s Science and Tomorrow’s Treatment’, *Frontiers in Genetics*, 12(April). doi: 10.3389/fgene.2021.655550.

Recasens, A. *et al.* (2014) ‘Lewy body extracts from Parkinson disease brains trigger α-synuclein pathology and neurodegeneration in mice and monkeys’, *Annals of Neurology*, 75(3), pp. 351–362. doi: 10.1002/ANA.24066.

Recasens, A. *et al.* (2017) ‘In vivo models of alpha-synuclein transmission and propagation’, *Cell and Tissue Research*, 373(1), pp. 183–193. doi: 10.1007/S00441-017-2730-9/FIGURES/1.

Van Remmen, H. *et al.* (2003) ‘Life-long reduction in MnSOD activity results in increased DNA damage and higher incidence of cancer but does not accelerate aging’, *Physiological genomics*, 16(1), pp. 29–37. doi: 10.1152/PHYSIOLGENOMICS.00122.2003.

Riachi, N. J., LaManna, J. C. and Harik, S. I. (1989) ‘Entry of 1-methyl-4-phenyl-1,2,3,6-tetrahydropyridine into the rat brain.’, *Journal of Pharmacology and Experimental Therapeutics*, 249(3).

Richardson, J. R. *et al.* (no date) ‘Paraquat Neurotoxicity is Distinct from that of MPTP and Rotenone’. doi: 10.1093/toxsci/kfi304.

Riessland, M. *et al.* (2019) ‘Loss of SATB1 Induces p21-Dependent Cellular Senescence in Post-mitotic Dopaminergic Neurons’, *Cell Stem Cell*, 25(4), pp. 514-530.e8. doi: 10.1016/j.stem.2019.08.013.

Rink, E. and Wullimann, M. F. (2001) ‘The teleostean (zebrafish) dopaminergic system ascending to the subpallium (striatum) is located in the basal diencephalon (posterior tuberculum)’, *Brain Research*, 889(1–2), pp. 316–330. doi: 10.1016/S0006-8993(00)03174-7.

Rink, E. and Wullimann, M. F. (2002) ‘Development of the catecholaminergic system in the early zebrafish brain: an immunohistochemical study’, *Developmental Brain Research*, 137(1), pp. 89–100. doi: 10.1016/S0165-3806(02)00354-1.

Rogina, B. and Helfand, S. L. (2004) ‘Sir2 mediates longevity in the fly through a pathway related to calorie restriction’, *Proceedings of the National Academy of Sciences of the United States of America*, 101(45), p. 15998. doi: 10.1073/PNAS.0404184101.

Ross, G. W. *et al.* (2000) ‘Association of Coffee and Caffeine Intake With the Risk of Parkinson Disease’, *JAMA*, 283(20), pp. 2674–2679. doi: 10.1001/JAMA.283.20.2674.

Roy, S. K. *et al.* (2020) ‘SATB2 is a novel biomarker and therapeutic target for cancer’, *Journal of Cellular and Molecular Medicine*, 24(19), p. 11064. doi: 10.1111/JCMM.15755.

Royal College of Physicians (UK) (2006) ‘Parkinson’s Disease’, *Parkinson’s Disease: National Clinical Guideline for Diagnosis and Management in Primary and Secondary Care*, pp. 59–100. Available at: https://www.ncbi.nlm.nih.gov/books/NBK48513/ (Accessed: 21 December 2022).

Sahu, A. *et al.* (2018) ‘Age-related declines in α-Klotho drive progenitor cell mitochondrial dysfunction and impaired muscle regeneration’, *Nature communications*, 9(1), p. 4859. doi: 10.1038/s41467-018-07253-3.

Sakai, C., Ijaz, S. and Hoffman, E. J. (2018) ‘Zebrafish Models of Neurodevelopmental Disorders: Past, Present, and Future’, *Frontiers in Molecular Neuroscience*, 11, p. 294. doi: 10.3389/FNMOL.2018.00294/BIBTEX.

Salim, S. (2017) ‘Oxidative Stress and the Central Nervous System’, *The Journal of Pharmacology and Experimental Therapeutics*, 360(1), p. 201. doi: 10.1124/JPET.116.237503.

Salminen, A., Kaarniranta, K. and Kauppinen, A. (2012) ‘Inflammaging: disturbed interplay between autophagy and inflammasomes’, *Aging (Albany NY)*, 4(3), p. 166. doi: 10.18632/AGING.100444.

Sancesario, G. M. *et al.* (2021) ‘Biofluids profile of α-Klotho in patients with Parkinson’s disease’, *Parkinsonism & Related Disorders*, 90, pp. 62–64. doi: 10.1016/J.PARKRELDIS.2021.08.004.

Sanders, B. D., Jackson, B. and Marmorstein, R. (2010) ‘Structural Basis for Sirtuin Function: What We Know and What We Don’t’, *Biochimica et biophysica acta*, 1804(8), p. 1604. doi: 10.1016/J.BBAPAP.2009.09.009.

Satake, W. *et al.* (2009) ‘Genome-wide association study identifies common variants at four loci as genetic risk factors for Parkinson’s disease’, *Nature Genetics 2009 41:12*, 41(12), pp. 1303–1307. doi: 10.1038/ng.485.

Satoh, A. *et al.* (2013) ‘Sirt1 extends life span and delays aging in mice through the regulation of Nk2 homeobox 1 in the DMH and LH’, *Cell metabolism*, 18(3), p. 416. doi: 10.1016/J.CMET.2013.07.013.

Satoh, Y. *et al.* (2013) ‘The Satb1 protein directs hematopoietic stem cell differentiation toward lymphoid lineages’, *Immunity*, 38(6), p. 1105. doi: 10.1016/J.IMMUNI.2013.05.014.

Sawada, M. *et al.* (2003) ‘Ku70 suppresses the apoptotic translocation of Bax to mitochondria’, *Nature Cell Biology 2003 5:4*, 5(4), pp. 320–329. doi: 10.1038/ncb950.

Schapira, A. H. V. *et al.* (1989) ‘MITOCHONDRIAL COMPLEX I DEFICIENCY IN PARKINSON’S DISEASE’, *The Lancet*, 333(8649), p. 1269. doi: 10.1016/S0140-6736(89)92366-0.

Schlicker, C. *et al.* (2008) ‘Substrates and Regulation Mechanisms for the Human Mitochondrial Sirtuins Sirt3 and Sirt5’, *Journal of Molecular Biology*, 382(3), pp. 790–801. doi: 10.1016/J.JMB.2008.07.048.

Schniertshauer, D., Gebhard, D. and Bergemann, J. (2018) ‘Age-Dependent Loss of Mitochondrial Function in Epithelial Tissue Can Be Reversed by Coenzyme Q10’, *Journal of Aging Research*, 2018. doi: 10.1155/2018/6354680.

Schrag, A. *et al.* (2015) ‘Prediagnostic presentations of Parkinson’s disease in primary care: A case-control study’, *The Lancet Neurology*, 14(1), pp. 57–64. doi: 10.1016/S1474-4422(14)70287-X.

Schwer, B. *et al.* (2006) ‘Reversible lysine acetylation controls the activity of the mitochondrial enzyme acetyl-CoA synthetase 2’, *Proceedings of the National Academy of Sciences*, 103(27), pp. 10224–10229. doi: 10.1073/PNAS.0603968103.

Sedelnikova, O. A. *et al.* (2004) ‘Senescing human cells and ageing mice accumulate DNA lesions with unrepairable double-strand breaks’, *Nature cell biology*, 6(2), pp. 168–170. doi: 10.1038/NCB1095.

Seirafi, M., Kozlov, G. and Gehring, K. (2015) ‘Parkin structure and function’, *The Febs Journal*, 282(11), p. 2076. doi: 10.1111/FEBS.13249.

Selinger, C. I. *et al.* (2011) ‘Loss of Special AT-Rich Binding Protein 1 Expression is a Marker of Poor Survival in Lung Cancer’, *Journal of Thoracic Oncology*, 6(7), pp. 1179–1189. doi: 10.1097/JTO.0B013E31821B4CE0.

Semba, R. D. *et al.* (2014) ‘Klotho in the cerebrospinal fluid of adults with and without Alzheimer’s disease’, *Neuroscience letters*, 558, p. 37. doi: 10.1016/J.NEULET.2013.10.058.

Seto, E. and Yoshida, M. (2014) ‘Erasers of Histone Acetylation: The Histone Deacetylase Enzymes’, *Cold Spring Harbor Perspectives in Biology*, 6(4). doi: 10.1101/CSHPERSPECT.A018713.

Shi, T. *et al.* (2005) ‘SIRT3, a mitochondrial sirtuin deacetylase, regulates mitochondrial function and thermogenesis in brown adipocytes’, *The Journal of biological chemistry*, 280(14), pp. 13560–13567. doi: 10.1074/JBC.M414670200.

Shim, J. H. *et al.* (2011) ‘The antioxidant Trolox helps recovery from the familial Parkinson’s disease-specific mitochondrial deficits caused by PINK1- and DJ-1-deficiency in dopaminergic neuronal cells’, *Mitochondrion*, 11(5), pp. 707–715. doi: 10.1016/J.MITO.2011.05.013.

Shimada, T. *et al.* (2001) ‘Cloning and characterization of FGF23 as a causative factor of tumor-induced osteomalacia’, *Proceedings of the National Academy of Sciences of the United States of America*, 98(11), p. 6500. doi: 10.1073/PNAS.101545198.

Shimada, T. *et al.* (2004) ‘FGF-23 Is a Potent Regulator of Vitamin D Metabolism and Phosphate Homeostasis’, *Journal of Bone and Mineral Research*, 19(3), pp. 429–435. doi: 10.1359/JBMR.0301264.

Shiraki-Iida, T. *et al.* (1998) ‘Structure of the mouse klotho gene and its two transcripts encoding membrane and secreted protein’, *FEBS Letters*, 424(1–2), pp. 6–10. doi: 10.1016/S0014-5793(98)00127-6.

Shore, D., Squire, M. and Nasmyth, K. A. (1984) ‘Characterization of two genes required for the position-effect control of yeast mating-type genes.’, *The EMBO journal*, 3(12), pp. 2817–2823. doi: 10.1002/J.1460-2075.1984.TB02214.X.

Simpson, B., Tupper, C. and Al Aboud, N. M. (2022) ‘Genetics, DNA Packaging’, *StatPearls*. Available at: https://www.ncbi.nlm.nih.gov/books/NBK534207/ (Accessed: 6 March 2023).

Singh, A. P. *et al.* (2019) ‘αKlotho Regulates Age-Associated Vascular Calcification and Lifespan in Zebrafish’, *Cell Reports*, 28(11), pp. 2767-2776.e5. doi: 10.1016/j.celrep.2019.08.013.

Singh, P., Hanson, P. S. and Morris, C. M. (2017) ‘SIRT1 ameliorates oxidative stress induced neural cell death and is down-regulated in Parkinson’s disease’, *BMC neuroscience*, 18(1). doi: 10.1186/S12868-017-0364-1.

Singh, P. P. *et al.* (2019) ‘The Genetics of Aging: A Vertebrate Perspective’, *Cell*, 177(1), p. 200. doi: 10.1016/J.CELL.2019.02.038.

Singleton, A. B. *et al.* (2003) ‘α-Synuclein Locus Triplication Causes Parkinson’s Disease’, *Science*, 302(5646), p. 841. doi: 10.1126/SCIENCE.1090278/SUPPL_FILE/SINGLETON.SOM.PDF.

Slanzi, A. *et al.* (2020) ‘In vitro Models of Neurodegenerative Diseases’, *Frontiers in Cell and Developmental Biology*, 8(May). doi: 10.3389/fcell.2020.00328.

Smith, E. R. *et al.* (2013) ‘Fetuin-A-containing calciprotein particles reduce mineral stress in the macrophage’, *PloS one*, 8(4). doi: 10.1371/JOURNAL.PONE.0060904.

Smith, L. and Schapira, A. H. V. (2022) ‘GBA Variants and Parkinson Disease: Mechanisms and Treatments’, *Cells*, 11(8). doi: 10.3390/CELLS11081261.

Snyder, H. *et al.* (2003) ‘Aggregated and Monomeric α-Synuclein Bind to the S6′ Proteasomal Protein and Inhibit Proteasomal Function’, *Journal of Biological Chemistry*, 278(14), pp. 11753–11759. doi: 10.1074/JBC.M208641200.

Song, D. D. *et al.* (2004) ‘Enhanced substantia nigra mitochondrial pathology in human α-synuclein transgenic mice after treatment with MPTP’, *Experimental Neurology*, 186(2), pp. 158–172. doi: 10.1016/S0014-4886(03)00342-X.

Soong, N. W. *et al.* (1992) ‘Mosaicism for a specific somatic mitochondrial DNA mutation in adult human brain’, *Nature Genetics*, 2(4), pp. 318–323. doi: 10.1038/ng1292-318.

Soto, C. and Pritzkow, S. (2018) ‘Protein misfolding, aggregation, and conformational strains in neurodegenerative diseases’, *Nature neuroscience*, 21(10), p. 1332. doi: 10.1038/S41593-018-0235-9.

Sousa, V. L. *et al.* (2009) ‘α-Synuclein and Its A30P Mutant Affect Actin Cytoskeletal Structure and Dynamics’, *Molecular Biology of the Cell*, 20(16), p. 3725. doi: 10.1091/MBC.E08-03-0302.

Spillantini, M. G. *et al.* (1997) ‘α-Synuclein in Lewy bodies’, *Nature 1997 388:6645*, 388(6645), pp. 839–840. doi: 10.1038/42166.

Spillantini, M. G. *et al.* (1998) ‘α-Synuclein in filamentous inclusions of Lewy bodies from Parkinson’s disease and dementia with Lewy bodies’, *Proceedings of the National Academy of Sciences of the United States of America*, 95(11), pp. 6469–6473. doi: 10.1073/PNAS.95.11.6469/ASSET/8C2E99A7-7759-4BFA-BDCB-4D2193913746/ASSETS/GRAPHIC/PQ1181054005.JPEG.

Stefanis, L. *et al.* (2019) ‘How is alpha-synuclein cleared from the cell?’, *Journal of Neurochemistry*, 150(5), pp. 577–590. doi: 10.1111/JNC.14704.

Storer, M. *et al.* (2013) ‘Senescence is a developmental mechanism that contributes to embryonic growth and patterning’, *Cell*, 155(5), p. 1119. doi: 10.1016/J.CELL.2013.10.041.

Sugano, Y. and Lardelli, M. (2011) ‘Identification and expression analysis of the zebrafish orthologue of Klotho’, *Development Genes and Evolution*, 221(3), pp. 179–186. doi: 10.1007/s00427-011-0367-3.

Surmeier, D. J. (2018) ‘Determinants of dopaminergic neuron loss in Parkinson’s disease’, *The FEBS journal*, 285(19), p. 3657. doi: 10.1111/FEBS.14607.

Sveinbjornsdottir, S. (2016) ‘The clinical symptoms of Parkinson’s disease’, *Journal of Neurochemistry*, 139, pp. 318–324. doi: 10.1111/jnc.13691.

Swygert, S. G. and Peterson, C. L. (2014) ‘Chromatin dynamics: Interplay between remodeling enzymes and histone modifications’, *Biochimica et biophysica acta*, 1839(8), p. 728. doi: 10.1016/J.BBAGRM.2014.02.013.

Tan, B. L. *et al.* (2018) ‘Antioxidant and oxidative stress: A mutual interplay in age-related diseases’, *Frontiers in Pharmacology*, 9(OCT), p. 1162. doi: 10.3389/FPHAR.2018.01162/BIBTEX.

Tang, Q. *et al.* (2021) ‘Alpha-Synuclein defects autophagy by impairing SNAP29-mediated autophagosome-lysosome fusion’, *Cell Death & Disease 2021 12:10*, 12(10), pp. 1–16. doi: 10.1038/s41419-021-04138-0.

Tanner, K. G. *et al.* (2000) ‘Silent information regulator 2 family of NAD-dependent histone/protein deacetylases generates a unique product, 1-O-acetyl-ADP-ribose’, *Proceedings of the National Academy of Sciences of the United States of America*, 97(26), pp. 14178–14182. doi: 10.1073/PNAS.250422697/ASSET/C42665DE-1FF4-41DD-9780-3DE4D5B4CE61/ASSETS/GRAPHIC/PQ2504226004.JPEG.

Tanny, J. C. and Moazed, D. (2001) ‘Coupling of histone deacetylation to NAD breakdown by the yeast silencing protein Sir2: Evidence for acetyl transfer from substrate to an NAD breakdown product’, *Proceedings of the National Academy of Sciences of the United States of America*, 98(2), pp. 415–420. doi: 10.1073/PNAS.98.2.415.

Taormina, G. *et al.* (2019) ‘Longevity: Lesson from Model Organisms’, *Genes*, 10(7). doi: 10.3390/GENES10070518.

Thöny, B., Auerbach, G. and Blau, N. (2000) ‘Tetrahydrobiopterin biosynthesis, regeneration and functions.’, *Biochemical Journal*, 347(Pt 1), p. 1. doi: 10.1042/0264-6021:3470001.

Thyme, S. B. *et al.* (2019) ‘Phenotypic Landscape of Schizophrenia-Associated Genes Defines Candidates and Their Shared Functions’, *Cell*, 177(2), pp. 478-491.e20. doi: 10.1016/j.cell.2019.01.048.

Tissenbaum, H. A. and Guarente, L. (2001) ‘Increased dosage of a sir-2 gene extends lifespan in Caenorhabditis elegans’, *Nature 2001 410:6825*, 410(6825), pp. 227–230. doi: 10.1038/35065638.

Tolosa, E. *et al.* (2021) ‘Challenges in the diagnosis of Parkinson’s disease’, *The Lancet. Neurology*, 20(5), p. 385. doi: 10.1016/S1474-4422(21)00030-2.

Tong, Y. *et al.* (no date) ‘R1441C mutation in LRRK2 impairs dopaminergic neurotransmission in mice’. Available at: www.pnas.orgcgidoi10.1073pnas.0906334106 (Accessed: 22 December 2022).

Torres-Lista, V. *et al.* (2014) ‘Neophobia, NQO1 and SIRT1 as premorbid and prodromal indicators of AD in 3xTg-AD mice’, *Behavioural Brain Research*, 271, pp. 140–146. doi: 10.1016/J.BBR.2014.04.055.

Tran, T. A. *et al.* (2011) ‘Lipopolysaccharide and Tumor Necrosis Factor Regulate Parkin Expression via Nuclear Factor-Kappa B’, *PLoS ONE*, 6(8), p. 23660. doi: 10.1371/JOURNAL.PONE.0023660.

Trifunovic, A. *et al.* (2004) ‘Premature ageing in mice expressing defective mitochondrial DNA polymerase’, *Nature*, 429(6990), pp. 417–423. doi: 10.1038/NATURE02517.

Trudler, D. *et al.* (2014) ‘DJ-1 deficiency triggers microglia sensitivity to dopamine toward a pro-inflammatory phenotype that is attenuated by rasagiline’, *Journal of Neurochemistry*, 129(3), pp. 434–447. doi: 10.1111/JNC.12633.

Tsujikawa, H. *et al.* (2003) ‘Klotho, a Gene Related to a Syndrome Resembling Human Premature Aging, Functions in a Negative Regulatory Circuit of Vitamin D Endocrine System’, *Molecular Endocrinology*, 17(12), pp. 2393–2403. doi: 10.1210/ME.2003-0048.

Uemura, N. *et al.* (2018) ‘Inoculation of α-synuclein preformed fibrils into the mouse gastrointestinal tract induces Lewy body-like aggregates in the brainstem via the vagus nerve’, *Molecular neurodegeneration*, 13(1). doi: 10.1186/S13024-018-0257-5.

Valente, E. M. *et al.* (2004) ‘PINK1 mutations are associated with sporadic early-onset parkinsonism’, *Annals of Neurology*, 56(3), pp. 336–341. doi: 10.1002/ANA.20256.

Vandamme, T. (2014) ‘Use of rodents as models of human diseases’, *Journal of Pharmacy and Bioallied Sciences*. Medknow Publications, pp. 2–9. doi: 10.4103/0975-7406.124301.

Vaquero, A. *et al.* (2006) 'SirT2 is a histone deacetylase with preference for histone H4 Lys 16 during mitosis'. doi: 10.1101/gad.1412706.

Venkateshappa, C. *et al.* (2012) 'Increased oxidative damage and decreased antioxidant function in aging human substantia nigra compared to striatum: implications for Parkinson's disease', *Neurochemical research*, 37(2), pp. 358–369. doi: 10.1007/S11064-011-0619-7.

Verma, D. K. *et al.* (2021) 'Alpha-synuclein preformed fibrils induce cellular senescence in parkinson's disease models', *Cells*, 10(7). doi: 10.3390/CELLS10071694/S1.

Vermulst, M. *et al.* (2008) 'DNA deletions and clonal mutations drive premature aging in mitochondrial mutator mice', *Nature genetics*, 40(4), pp. 392–394. doi: 10.1038/NG.95.

Vilchez, D., Saez, I. and Dillin, A. (2014) 'The role of protein clearance mechanisms in organismal ageing and age-related diseases', *Nature Communications 2014 5:1*, 5(1), pp. 1–13. doi: 10.1038/ncomms6659.

Villa-Bellosta, R. *et al.* (2013) 'Defective extracellular pyrophosphate metabolism promotes vascular calcification in a mouse model of Hutchinson-Gilford progeria syndrome that is ameliorated on pyrophosphate treatment', *Circulation*, 127(24), pp. 2442–2451. doi: 10.1161/CIRCULATIONAHA.112.000571.

Viswanathan, M. *et al.* (2005) 'A Role for SIR-2.1 Regulation of ER Stress Response Genes in Determining C. elegans Life Span', *Developmental Cell*, 9(5), pp. 605–615. doi: 10.1016/J.DEVCEL.2005.09.017.

Wan, F. *et al.* (2015) 'SATB1 Overexpression Regulates the Development and Progression in Bladder Cancer through EMT', *PLOS ONE*, 10(2), p. e0117518. doi: 10.1371/JOURNAL.PONE.0117518.

Wang, C. *et al.* (2009) 'DNA damage response and cellular senescence in tissues of aging mice', *Aging cell*, 8(3), pp. 311–323. doi: 10.1111/J.1474-9726.2009.00481.X.

Wang, G. *et al.* (2015) 'miR-23a suppresses proliferation of osteosarcoma cells by targeting SATB1', *Tumour biology : the journal of the International Society for Oncodevelopmental Biology and Medicine*, 36(6), pp. 4715–4721. doi: 10.1007/S13277-015-3120-0.

Wang, R. H. *et al.* (2008) 'Impaired DNA damage response, genome instability, and tumorigenesis in SIRT1 mutant mice', *Cancer cell*, 14(4), p. 312. doi: 10.1016/J.CCR.2008.09.001.

Wang, W. *et al.* (2016) ‘Caspase-1 causes truncation and aggregation of the Parkinson’s disease-associated protein α-synuclein’, *Proceedings of the National Academy of Sciences of the United States of America*, 113(34), pp. 9587–9592. doi: 10.1073/pnas.1610099113.

Wang, X. *et al.* (2017) ‘Expression and clinical significance of SATB1 and TLR4 in breast cancer’, *Oncology Letters*, 14(3), p. 3611. doi: 10.3892/OL.2017.6571.

Wang, Z. *et al.* (2012) ‘The structural basis for the oligomerization of the N-terminal domain of SATB1’, *Nucleic Acids Research*, 40(9), p. 4193. doi: 10.1093/NAR/GKR1284.

Wang, Z. *et al.* (2014) ‘Crystal Structure of the Ubiquitin-like Domain-CUT Repeat-like Tandem of Special AT-rich Sequence Binding Protein 1 (SATB1) Reveals a Coordinating DNA-binding Mechanism’, *The Journal of Biological Chemistry*, 289(40), p. 27376. doi: 10.1074/JBC.M114.562314.

Weiner, W. J. (2008) ‘There Is No Parkinson Disease’, *Archives of Neurology*, 65(6), pp. 705–708. doi: 10.1001/ARCHNEUR.65.6.705.

Westerheide, S. D. *et al.* (2009) ‘Stress-inducible regulation of heat shock factor 1 by the deacetylase SIRT1’, *Science (New York, N.Y.)*, 323(5917), pp. 1063–1066. doi: 10.1126/SCIENCE.1165946.

Weston, L. J. *et al.* (2021) ‘In vivo aggregation of presynaptic alpha-synuclein is not influenced by its phosphorylation at serine-129’, *Neurobiology of Disease*, 152, p. 105291. doi: 10.1016/J.NBD.2021.105291.

Whitaker, R. *et al.* (2013) ‘Increased expression of Drosophila Sir 2 extends life span in a dose-dependent manner’, *Aging (Albany NY)*, 5(9), p. 682. doi: 10.18632/AGING.100599.

White, K. E. *et al.* (2000) ‘Autosomal dominant hypophosphataemic rickets is associated with mutations in FGF23’, *Nature genetics*, 26(3), pp. 345–348. doi: 10.1038/81664.

Wilk, A. *et al.* (2020) ‘Extracellular NAD+ enhances PARP-dependent DNA repair capacity independently of CD73 activity’, *Scientific Reports 2020 10:1*, 10(1), pp. 1–21. doi: 10.1038/s41598-020-57506-9.

Wilkinson, R. N. *et al.* (2013) ‘A method for high-throughput PCR-based genotyping of larval zebrafish tail biopsies’, *BioTechniques*, 55(6), pp. 314–316. doi: 10.2144/000114116.

Will, B. *et al.* (2013) ‘Satb1 regulates hematopoietic stem cell self-renewal by promoting quiescence and repressing differentiation commitment’, *Nature immunology*, 14(5), p. 437. doi: 10.1038/NI.2572.

William Langston, J. *et al.* (1983) ‘Chronic parkinsonism in humans due to a product of meperidine-analog synthesis’, *Science*, 219(4587), pp. 979–980. doi: 10.1126/SCIENCE.6823561.

William Langston, J. *et al.* (1984) ‘Selective nigral toxicity after systemic administration of 1-methyl-4-phenyl-1,2,5,6-tetrahydropyrine (MPTP) in the squirrel monkey’, *Brain research*, 292(2), pp. 390–394. doi: 10.1016/0006-8993(84)90777-7.

Williams-Gray, C. H. and Worth, P. F. (2016) ‘Parkinson’s disease’, *Medicine (United Kingdom)*, 44(9), pp. 542–546. doi: 10.1016/j.mpmed.2016.06.001.

Wills, E. J. (2009) ‘Ultrastructural Pathology The Powerhouse of the Cell’. doi: 10.3109/01913129209061353.

World Health Organisation (2022). Available at: https://www.who.int/news-room/fact-sheets/detail/parkinson-disease (Accessed: 28 November 2022).

World Health Organisation (2022). Available at: https://www.who.int/news-room/fact-sheets/detail/ageing-and-health (Accessed: 11 January 2023).

Xie, W. *et al.* (2020) ‘Chemoptogenetic ablation of neuronal mitochondria in vivo with spatiotemporal precision and controllable severity’, *eLife*, 9. doi: 10.7554/ELIFE.51845.

Xie, Y. *et al.* (2019) ‘Glucocorticoids inhibit macrophage differentiation towards a pro-inflammatory phenotype upon wounding without affecting their migration’, *DMM Disease Models and Mechanisms*, 12(5). doi: 10.1242/DMM.037887/VIDEO-2.

Xilouri, M. *et al.* (2009) ‘Abberant alpha-synuclein confers toxicity to neurons in part through inhibition of chaperone-mediated autophagy’, *PloS one*, 4(5). doi: 10.1371/JOURNAL.PONE.0005515.

Xu, Y. and Sun, Z. (2015) ‘Molecular basis of klotho: From gene to function in aging’, *Endocrine Reviews*. Endocrine Society, pp. 174–193. doi: 10.1210/er.2013-1079.

Yamamoto, M. *et al.* (2005) ‘Regulation of oxidative stress by the anti-aging hormone klotho’, *Journal of Biological Chemistry*, 280(45), pp. 38029–38034. doi: 10.1074/jbc.M509039200.

Yang, S. H. *et al.* (2005) ‘Blocking protein farnesyltransferase improves nuclear blebbing in mouse fibroblasts with a targeted Hutchinson-Gilford progeria syndrome mutation’. Available at: www.pnas.orgcgidoi10.1073pnas.0504641102 (Accessed: 3 March 2023).

Yang, S. H. *et al.* (2008) ‘Progerin elicits disease phenotypes of progeria in mice whether or not it is farnesylated', *The Journal of Clinical Investigation*, 118. doi: 10.1172/JCI35876.

Yang, W. *et al.* (2020) 'Current and projected future economic burden of Parkinson's disease in the U.S.', *npj Parkinson's Disease 2020 6:1*, 6(1), pp. 1–9. doi: 10.1038/s41531-020-0117-1.

Yang, Y. *et al.* (2022) 'Regulation of SIRT1 and Its Roles in Inflammation', *Frontiers in Immunology*, 13, p. 872. doi: 10.3389/FIMMU.2022.831168/BIBTEX.

Yasui, D. *et al.* (2002) 'SATB1 targets chromatin remodelling to regulate genes over long distances', *Nature 2002 419:6907*, 419(6907), pp. 641–645. doi: 10.1038/nature01084.

Ye, Q. *et al.* (2012) 'Epigallocatechin-3-gallate suppresses 1-methyl-4-phenyl-pyridine-induced oxidative stress in PC12 cells via the SIRT1/PGC-1α signaling pathway', *BMC Complementary and Alternative Medicine*, 12(1), pp. 1–7. doi: 10.1186/1472-6882-12-82/FIGURES/4.

Yerbury, J. J. *et al.* (2016) 'Walking the tightrope: proteostasis and neurodegenerative disease', *Journal of Neurochemistry*, 137(4), pp. 489–505. doi: 10.1111/JNC.13575.

Yeung, F. *et al.* (2004) 'Modulation of NF-κB-dependent transcription and cell survival by the SIRT1 deacetylase', *EMBO Journal*, 23(12), pp. 2369–2380. doi: 10.1038/SJ.EMBOJ.7600244.

Yu, X. and White, K. E. (2005) 'FGF23 and disorders of phosphate homeostasis', *Cytokine & growth factor reviews*, 16(2), pp. 221–232. doi: 10.1016/J.CYTOGFR.2005.01.002.

Zarranz, J. J. *et al.* (2004) 'The new mutation, E46K, of α-synuclein causes parkinson and Lewy body dementia', *Annals of Neurology*, 55(2), pp. 164–173. doi: 10.1002/ANA.10795.

Zeldich, E. *et al.* (2015) 'The Anti-Aging Protein Klotho Enhances Remyelination Following Cuprizone-Induced Demyelination', *Journal of Molecular Neuroscience*, 57(2), pp. 185–196. doi: 10.1007/S12031-015-0598-2/FIGURES/4.

Zelenka, T. and Spilianakis, C. (2020) 'SATB1-mediated chromatin landscape in T cells', *Nucleus*, 11(1), p. 117. doi: 10.1080/19491034.2020.1775037.

Zhang, C. X. *et al.* (2005) 'Multiple Roles for Cyclin G-Associated Kinase in Clathrin-Mediated Sorting Events', *Traffic*, 6(12), pp. 1103–1113. doi: 10.1111/J.1600-0854.2005.00346.X.

Zhang, J., Li, X. and Li, J. Da (2019) 'The Roles of Post-translational Modifications on α-Synuclein in the Pathogenesis of Parkinson's Diseases', *Frontiers in Neuroscience*, 13(APR), pp. 1–11. doi:

10.3389/fnins.2019.00381.

Zhang, Q. *et al.* (2018) 'Cdk5 suppression blocks SIRT1 degradation via the ubiquitin-proteasome pathway in Parkinson's disease models', *Biochimica et Biophysica Acta (BBA) - General Subjects*, 1862(6), pp. 1443–1451. doi: 10.1016/J.BBAGEN.2018.03.021.

Zhang, W. *et al.* (2005) 'Aggregated α-synuclein activates microglia: a process leading to disease progression in Parkinson's disease', *The FASEB Journal*, 19(6), pp. 533–542. doi: 10.1096/FJ.04-2751COM.

Zhao, R. Z. *et al.* (2019) 'Mitochondrial electron transport chain, ROS generation and uncoupling (Review)', *International Journal of Molecular Medicine*, 44(1), pp. 3–15. doi: 10.3892/IJMM.2019.4188/HTML.

Zhao, Y. *et al.* (2020) 'Klotho overexpression improves amyloid-β clearance and cognition in the APP/PS1 mouse model of Alzheimer's disease', *Aging Cell*, 19(10). doi: 10.1111/ACEL.13239.

Zhou, Y. *et al.* (2014) 'Quantification of larval zebrafish motor function in multiwell plates using open-source MATLAB applications', *Nature Protocols*, 9(7), pp. 1533–1548. doi: 10.1038/nprot.2014.094.

Zhu, L. *et al.* (2018) 'Klotho controls the brain–immune system interface in the choroid plexus', *Proceedings of the National Academy of Sciences of the United States of America*, 115(48), pp. E11388–E11396. doi: 10.1073/pnas.1808609115.

Zhu, Y. *et al.* (2021) 'Reduced serum SIRT1 levels in patients with Parkinson's disease: a cross-sectional study in China', *Neurological Sciences*, 42(5), pp. 1835–1841. doi: 10.1007/S10072-020-04711-Z/TABLES/5.

Zhuang, N. *et al.* (2016) 'PINK1-dependent phosphorylation of PINK1 and Parkin is essential for mitochondrial quality control', *Cell death & disease*, 7(12). doi: 10.1038/CDDIS.2016.396.

Zimmermann, M. *et al.* (2021) 'The longevity gene Klotho and its cerebrospinal fluid protein profiles as a modifier for Parkinson´s disease', *European Journal of Neurology*, 28(5), pp. 1557–1565. doi: 10.1111/ENE.14733.

Zimprich, A. *et al.* (2004) 'Mutations in LRRK2 Cause Autosomal-Dominant Parkinsonism with Pleomorphic Pathology', *Neuron*, 44(4), pp. 601–607. doi: 10.1016/J.NEURON.2004.11.005.

Zou, D. *et al.* (2018) 'The role of klotho in chronic kidney disease', *BMC Nephrology*, 19(1). doi:

10.1186/S12882-018-1094-Z.